University of California
Santa Barbara

Slip in the presence of surfactants: application to superhydrophobic drag reduction

A dissertation submitted in partial satisfaction
of the requirements for the degree

Doctor of Philosophy
in
Mechanical Engineering

by

Fernando Temprano-Coleto

Committee in charge:

Professor Paolo Luzzatto-Fegiz, co-Chair
Professor Frédéric G. Gibou, co-Chair
Professor Igor Mezić
Professor Todd M. Squires

March 2021

The dissertation of Fernando Temprano-Coleto is approved.

Professor Igor Mezić

Professor Todd M. Squires

Professor Paolo Luzzatto-Fegiz, Committee co-Chair

Professor Frédéric G. Gibou, Committee co-Chair

March 2021

Slip in the presence of surfactants:

application to superhydrophobic drag reduction

Fernando Temprano-Coleto

Acknowledgements

I would first like to thank my PhD advisors, Professor Paolo Luzzatto-Fegiz and Professor Frédéric Gibou, for their constant support and crucial guidance during the past five years. When they offered me to be a part of their joint project, they provided me with the greatest opportunity of my professional life.

I am also grateful to Professors Igor Mezić and Todd M. Squires for agreeing to serve in my doctoral committee. It has been a true privilege to have the opportunity to discuss dynamical systems and surfactant chemistry with such experts in their respective fields.

I am particularly indebted to Dr. Juan Pérez-Mercader, my first research mentor and the main responsible of my commitment to Science.

Many thanks to Julien R. Landel and François J. Peaudecerf, who have been a fundamental part of this research with their advice from the distance. Thanks also to Scott M. Smith for the tremendous amount of dedication that he put into this project as an undergraduate student.

I must also thank all my colleagues over the years in the CASL and FESLab, and especially to Raphael Egan and Daniil Bochkov for their guidance. I would also like to acknowledge all faculty and staff that have helped along the way, both in the Mechanical Engineering Department and in the rest of the UC Santa Barbara campus.

In addition, this thesis would not have been possible without the support of my friends, both in Madrid and in Santa Barbara. Special thanks to Amir Tahmasebipour, Alejandro Chamorro, Xavier López, Ivana Bagarić, Petra Peršolja and Fernando Luna for their friendship, which endures through wildfires and pandemics.

Finally, my most profound gratitude goes to my family —and particularly to my parents— who are almost entirely responsible for who I am today.

Curriculum Vitæ

Fernando Temprano-Coleto

Education

2021	PhD in Mechanical Engineering, University of California Santa Barbara.
2018	MS in Mechanical Engineering, University of California Santa Barbara.
2015	Grado en Ingeniería en Tecnologías Industriales, Universidad Politécnica de Madrid.

Publications

- **F. Temprano-Coleto**, S.M. Smith, F.J. Peaudecerf, J.R. Landel, F. Gibou, P. Luzzatto-Fegiz, *Slip on three-dimensional surfactant-contaminated superhydrophobic gratings* (in preparation).
- **F. Temprano-Coleto**, P. Luzzatto-Fegiz, F. Gibou, *On the accuracy of implicit methods for surface advection-diffusion equations on moving interfaces* (in preparation).
- P. Luzzatto-Fegiz, **F. Temprano-Coleto**, F.J. Peaudecerf, J.R. Landel, Y.Zhu, J.A. McMurry, *UVB radiation alone may not explain sunlight inactivation of SARS-CoV-2*, Journal of Infectious Diseases, in press (2021).
- P. Luzzatto-Fegiz, **F. Temprano-Coleto**, F.J. Peaudecerf, J.R. Landel, Y.Zhu, J.A. McMurry, *Existing data suggest that UVA radiation could be the principal contributor to sunlight inactivation of SARS-CoV-2*, bioRXiv preprint (2020).
- R. Egan, A. Guittet, **F. Temprano-Coleto**, T. Isaac, F.J. Peaudecerf, J.R. Landel, P. Luzzatto-Fegiz, C. Burstedde, F. Gibou, *Direct numerical simulation of incompressible flows on parallel octree grids*, Journal of Computational Physics 428 110084 (2021).
- J.R. Landel, F.J. Peaudecerf, **F. Temprano-Coleto**, F. Gibou, R.E. Goldstein, P. Luzzatto-Fegiz, *A theory for the slip and drag of superhydrophobic surfaces with surfactant*, Journal of Fluid Mechanics 883 A18 (2020).
- **F. Temprano-Coleto**, F.J. Peaudecerf, J.R. Landel, F. Gibou, P. Luzzatto-Fegiz, *Soap opera in the maze: Geometry matters in Marangoni flows*, Physical Review Fluids 3 (10) 100507 (2018).
- C. C. de Langavant, A. Guittet, M. Theillard, **F. Temprano-Coleto**, F. Gibou, *Level-set simulations of soluble surfactant driven flows*, Journal of Computational Physics 348 271-297 (2017).
- J. K. Szymański, **F. Temprano-Coleto**, J. Pérez-Mercader, *Unusual kinetics of poly(ethylene glycol) oxidation with cerium(IV) ions in sulfuric acid medium and implications for copolymer synthesis*, Physical Chemistry Chemical Physics 17 6713-6717 (2015).

Honors and Awards

- ▷ WAGS/ProQuest **Distinguished Master's Thesis Award**, STEM category (2019).
- ▷ UCSB Graduate Division **Dissertation Fellowship** (2019).
- ▷ **First Place** in the UCSB Mechanical Engineering Annual **Grad Slam Competition** (2018).
- ▷ APS Division of Fluid Dynamics **Gallery of Fluid Motion Award** (2017). See bit.ly/flowmaze.
- ▷ Spanish Ministry of Education **Collaboration Grant** (2014).
- ▷ Harvard Origins of Life Initiative **Summer Undergraduate Research Grant** (2014).
- ▷ Harvard Origins of Life Initiative **Summer Undergraduate Research Grant** (2013).

Abstract

Slip in the presence of surfactants:
application to superhydrophobic drag reduction

by

Fernando Temprano-Coleto

Surfactants —molecules with a tendency to adsorb to interfaces between fluids— have been known to critically affect the behavior of multiphase flows for decades. They slow the rise of air bubbles in water, increase the thickness of liquid coating films, and trigger the motion of the so-called "tears" in a glass of wine, to name a few examples. In recent years, it has been shown that these substances also play a central role in the performance of *superhydrophobic surfaces* (SHS), textures designed to reduce friction by retaining a layer of air while immersed in water. Indeed, the presence of even small traces of surfactants, unavoidable not only in the environment but also in nominally clean conditions, inevitably leads to adverse Marangoni forces that substantially inhibit drag reduction. Quantifying and predicting these effects would have far-reaching technological implications in energy efficiency, yet it is extremely challenging due to the underlying mathematical complexity and the difficulty in the detection and control of surfactants in experiments.

The first part of this dissertation introduces two numerical methods: one is designed for the surfactant transport problem in deforming geometries, while the other solves the incompressible Navier-Stokes equations for the fluid flow in parallel multi-processor environments. The computational framework is based on a level-set representation of moving interfaces and the utilization of adaptive Cartesian grids, providing a unique tool to efficiently tackle the full problem in relatively general scenarios. We then describe the first theoretical model for laminar flows over superhydrophobic surfaces inclusive of surfactant, based on simplifying physical assumptions that apply in the specific case of two-dimensional SHS gratings. In practice, how-

ever, flows over realistic SHS textures have key three-dimensional features. To overcome this limitation, a new model for three-dimensional gratings is presented, allowing for the first time to compare theoretical predictions with experimental measurements, which we perform using confocal microscopy in microfluidic devices. Additionally, this thesis presents (i) a striking experimental demonstration of maze-solving by surfactants in the context of free-surface flows, and (ii) a concise theoretical study on the sunlight inactivation of the SARS-CoV-2 virus, with potential applications in UV disinfection technology.

Contents

Chapter 1

Introduction

Surfactants, molecules with a tendency to adsorb to interfaces between fluids, are well-known to have drastic effects in multiphase flows [1, 2] through the capillary and Marangoni effects. Bubble motion [3], drop breakup and coalescence [4, 5], capillary waves [6] or dip coating [7] are just a few examples of fluid-mechanical problems where these substances can dramatically affect the *slip* between different fluids, deeply altering the flow dynamics.

In order to study these and many other instances of flows with surfactants, one must consider a complex problem with four coupled partial differential equations defined on irregular, deforming geometries. Such a problem can rarely be addressed in its general form by approaches other than numerical methods. It is thus unsurprising that many different computational tools for flows with surfactants have emerged in the last three decades [4, 8, 9, 10, 11, 12, 13], each with its advantages and disadvantages. However, a method with (i) the ability to address the full problem including the surfactant *solubility*, (ii) a sharp representation —i.e. without any numerical smearing— of the moving interface, (iii) the flexibility to adapt to large deformations and changes in topology, (iv) adaptive grid refinement and (v) parallel computing capabilities is yet to be developed. Such a computational approach would constitute a unique resource in the investigation of these flows, allowing for a fine tuning of the problem parameters that is often impossible to achieve in experimental settings in which the surfactant is an unknown

contaminant present only in small amounts.

Within the general problem of fluid flows with surfactant, we take special interest in their effect on flows over superhydrophobic surfaces (SHS). These materials are textures aimed at achieving drag reduction by means of retaining a layer of air when immersed in water, by virtue of the slip between these two fluids. Despite initial observations that agreed with surfactant-free theory [14, 15], many subsequent experimental studies reported a reduced or even nonexistent slip [16, 17, 18]. Very recently, it has been shown [19, 20] that even trace amounts of surfactants can render these coatings unusable, triggering adverse Marangoni forces at the air-water interface that are responsible for this reduction of fluid slip. Although a quantitative understanding of this phenomenon would be invaluable to develop effective SHSs with real impact on energy efficiency, the development of theories is still in its infancy due to the novelty of these findings. Similarly, there are no direct comparisons between theory and experiments that specifically account for the effects of surfactants, and thus efforts in this direction would be particularly useful for the definitive adoption of this technology.

This PhD thesis compiles a series of results produced to date to address these challenges, combining computational, experimental and theoretical work. Each chapter is self-contained and corresponds to a journal article that has either been published or is currently under review.

Chapters 2 and 3 are reprints from [21][1] and [22] [2], and detail two computational tools developed in-house. The first one solves the surfactant transport equations, while the second is focused on the incompressible Navier-Stokes equations for the flow field. The numerical framework is based on Finite-Difference and Finite-Volume schemes on adaptive Quad/Oc-tree cartesian grids, combined with an implicit interface representation via the level-set method. Additionally, the Navier-Stokes solver incorporates parallel multi-processor capabilities based on the `p4est` library, essential to tackle large problems and to explore the turbulent regime in future work. These numerical methods provide access to accurate solutions of the problem in relatively general situations, a key requirement to inform the development of theory and

[1] DOI: 10.1016/j.jcp.2017.07.003
[2] DOI: 10.1016/j.jcp.2020.110084

to systematically investigate the fine-tuning of the problem parameters, which are typically impossible to accurately infer in experimental settings.

Chapter 4 reproduces the results in [23][3], describing the experimental observation of Marangoni maze-solving in open-channel flows and postulating a physical mechanism for such behavior. The visual appeal and striking dynamics of this maze-solving flow[4] earned the Gallery of Fluid Motion Award in the 70th Annual Meeting of the American Physical Society Division of Fluid Dynamics. It was also featured in prime-time national television in Spain[5], with an audience estimated in 2.4 million viewers.

Chapter 5, a reprint from [24][6], describes a theory for laminar flows with surfactant over an array of infinite SHS gratings *transverse* to the flow. We deliberately choose this two-dimensional scenario because it is the simplest case in which the SHS geometry displays stagnation points, which are necessary to produce surfactant accumulation and the subsequent Marangoni forces. We combine a scaling theory for the surfactant transport with a modified solution of the Stokes equations in this geometry, obtaining a semi-analytical model that agrees with simulations of the full problem over a wide range of the large parameter space. This is the first model for the apparent slip produced by SHS in the presence of surfactants.

Chapter 6, which is in the process of being submitted for publication as this thesis is written, is a study of laminar flows over realistic three-dimensional SHS gratings. Making use of the theory of matched asymptotic expansions, we present a novel theory that takes into account the leading order three-dimensional effect that slender longitudinal SHS gratings have on laminar fluid flows. Combining this flow solution with scaling theory similar to the one in [24], we obtain a model that can, for the first time, be compared to experimental results in realistic conditions. We also perform experiments based on confocal microscopy in microfluidic devices, using micro-particle image velocimetry to obtain flow measurements and confirm the trends predicted by the theory. The results confirm that this model is a powerful predictive tool with

[3]DOI: 10.1103/PhysRevFluids.3.100507
[4]See bit.ly/flowmaze
[5]See bit.ly/flowmazeonTV
[6]DOI: 10.1017/jfm.2019.857

immediate application in the design of effective superhydrophobic coatings.

Chapters 7 and 8 are outside of the realms of surfactants or fluid mechanics, yet they are timely works of applied mathematics as well. They are reprints of [25][7] and [26][8], respectively, and contain theoretical studies on the inactivation of the SARS-CoV-2 virus by ultraviolet (UV) light. Chapter 7 presents evidence that suggests that the UVB segment of the spectrum (with wavelengths from 280 to 315 nm) may not be enough to explain the rates observed in the sunlight inactivation of the virus, which is responsible for the current COVID-19 global pandemic. Instead, the less energetic UVA light (315 to 400 nm), traditionally neglected due to its inability to directly damage enveloped viruses, could justify this disagreement through an indirect mechanism of damage involving intermediate chemical species present in the medium. Chapter 8 presents a simple mathematical model that takes into account these effects, bridging the gap between the observed and predicted inactivation rates. These results have the potential to lead to novel and inexpensive technologies of viral disinfection.

1.1 Permissions and Attributions

1. The reprint of [21] and [22] in Chapters 2 and 3 is considered by Elsevier as "Personal Use" by a co-author[9], and therefore permitted.

2. The reprint of [23] and [26] in Chapters 4 and 8 is allowed as well, since these two articles are published under a Creative Commons Attribution 4.0 international License[10].

3. The reprint of [24] in Chapter 5 is also permitted without a license[11] by Cambridge University Press.

4. The reprint of [25] in Chapter 7 has been authorized for this dissertation through a license[12] granted by Oxford University Press.

[7] DOI: 10.1093/infdis/jiab070
[8] DOI: 10.1101/2020.09.07.286666
[9] See https://www.elsevier.com/about/policies/copyright/personal-use.
[10] See https://creativecommons.org/licenses/by/4.0/
[11] See "Rights & Permissions" in https://doi.org/10.1017/jfm.2019.857
[12] License number: 5022511113429

Chapter 2

A numerical method for the transport of soluble surfactant

2.1 Abstract

We present an approach to simulate the diffusion, advection and adsorption-desorption of a material quantity defined on an interface in two and three spatial dimensions. We use a level-set approach to capture the interface motion and a Quad-/Oc-tree data structure to efficiently solve the equations describing the underlying physics. Coupling with a Navier-Stokes solver enables the study of the effect of soluble surfactants that locally modify the parameters of surface tension on different types of flows. The method is tested on several benchmarks and applied to three typical examples of flows in the presence of surfactant: a bubble in a shear flow, the well-known phenomenon of tears of wine, and the Landau-Levich coating problem.

2.2 Introduction

Many problems in fluid dynamics exhibit a different behavior in the presence of surfactants at the interface between two phases or at a free surface. Surfactants are amphiphilic molecules, i.e. they possess both hydrophilic and hydrophobic groups, giving them properties that can

affect the flow through two different mechanisms that have the same origin. First, surfactants at an interface lower its surface tension, thus altering the pressure jump at the interface. Second, when the surfactant concentration is not constant along the interface, it generates the so-called Marangoni forces, which are tangential stresses that can critically perturb the flow near the interface.

The computational modeling of the diffusion, the advection, the adsorption and the desorption processes of a material quantity on a moving interface, as well as its possible effects on a fluid flow, is a challenging task. Several computational studies have been undertaken since the early 1990s, involving more or less sophisticated numerical methods and more or less comprehensive physical models depending, for example, on whether or not the surfactant is considered soluble, which implies the presence of adsorption-desorption coupling between the bulk and the interface; whether the effect of surfactants on the surface tension are modeled by a linear or a nonlinear equation of state; or whether the full Navier-Stokes equations or the Stokes equations are considered.

In 1989, Stone and Leal [4] developed a boundary integral method for studying the effects of insoluble surfactant on drop deformation and breakup. One year later, He, Dagan and Maldarelli [27] investigated, using uniform retardation perturbation schemes, the retarding effect of the Marangoni forces due to soluble surfactant on the motion of a fluid sphere in creeping translation inside a tube. In 1992, Borhan and Mao [8] developed a boundary element method to study the effects of surfactant on drop deformation. The same year, Milliken, Stone and Leal [28] developed a boundary integral method for studying the evolution of viscous drops under the hypothesis of Stokes flow with arbitrary viscosity ratios in the presence of surfactant and using a nonlinear equation of state for the interfacial tension. In 1994, Leveque and Li [29] designed an immersed interface method for elliptic equations with discontinuous coefficients and singular source terms, which could be applied to the study of the effects of Marangoni forces on fluid flows. In 1998, Eggleton and Stebe [30] investigated the effects of a soluble surfactant on the deformation of a droplet using a boundary integral method for

Stokes flows. In 2003, Drumright-Clarke and Renardy [31] used the full Navier-Stokes equations to study the effects of insoluble surfactant on the motion and breakup of viscous drops in a shear flow, using a volume-of-fluid method. In 2004, James and Lowengrub [32] developed a finite-elements solver using a surfactant-conserving volume-of-fluid interface-capturing method to investigate the effects of insoluble surfactant on various interfacial flows. In 2006, Xu, Li, Lowengrub and Zhao [11] developed a level-set method on uniform grids for solving the surfactant equation coupled to an external Stokes flow solver, and applied it to investigate the effects of insoluble surfactant on single drops, on drop-drop interactions and on the interactions of many drops. It was the first time the level-set method was used to simulate fluid interfaces with surfactant. In 2007, Muradoglu and Tryggvason [12] developed a front tracking method to investigate the axisymmetric motion and deformation of a viscous drop with soluble surfactant moving in a circular tube. This approach introduced an adsorption layer in order to model the adsorption/desorption terms. In 2009, Teigen *et al.* [33] presented a diffuse-interface approach for modeling the advection, the diffusion and the adsorption-desorption of material quantities on a deformable interface, using finite-difference schemes on a block-structured adaptive grid.

In this paper, we present a level-set method on adaptive Quad/Oc-tree grids to study the effects of both soluble and insoluble surfactant on free surface flows in two and three spatial dimensions. We use the full Navier-Stokes equations and a nonlinear equation of state for the surface tension. After describing the governing equations in section 2.3 we will describe the numerical approach in section 2.4. Section 2.5 is dedicated to the verification in both in two and three spatial dimensions, mainly using variants of the test examples proposed in [12]. In Section 2.6, we present three examples of application of our method: the deformation of a bubble in a shear flow in the presence of soluble surfactant, the well-known phenomenon of tears of wine, and the effect of the presence of surfactant on the flow near the meniscus in the Landau-Levich coating problem. Section 2.7 gathers a few concluding remarks on the topic of the simulation of surfactant-driven flows using our method.

2.3 Governing equations

The governing equations are those describing the evolution of the surfactant concentration, both at the interface and in the bulk as well as their coupling. In addition, the surfactant concentration and the fluid's velocity field are coupled through the surfactant's advection and the surface tension effects.

2.3.1 Evolution of a material quantity defined on an interface

A scalar quantity Γ, here the surface surfactant concentration, diffusing along an interface Σ and being advected by an external velocity field $\mathbf{u}$ is described by the following time-dependent equation [34]:

$$\Gamma_t + \nabla_s \cdot (\Gamma \mathbf{u}) = D_s \Delta_s \Gamma, \tag{2.1}$$

where D_s is the diffusion constant of Γ along Σ. Using the definition of the surface divergence $\nabla_s \cdot \mathbf{v} = \nabla \cdot \mathbf{v} - \mathbf{n} \cdot [(\nabla\ \mathbf{v}) \cdot \mathbf{n}]$, where $\mathbf{n}$ is the outward normal to Σ, and that of the surface Laplacian $\Delta_s f = \Delta f - \frac{\partial^2 f}{\partial n^2} - \kappa \frac{\partial f}{\partial n}$, where $\kappa = \nabla \cdot \mathbf{n} = \nabla_s \cdot \mathbf{n}$ is the mean curvature of the interface, Equation (2.1) yields:

$$\Gamma_t + \mathbf{u} \cdot \nabla_s \Gamma + \Gamma \nabla \cdot \mathbf{u} - \Gamma \mathbf{n} \cdot [(\nabla \mathbf{u}) \cdot \mathbf{n}] = D_s \left(\Delta \Gamma - \frac{\partial^2 \Gamma}{\partial n^2} - \kappa \frac{\partial \Gamma}{\partial n} \right). \tag{2.2}$$

Splitting the velocity into its normal u_n and its tangential $\mathbf{u}_s$ components and using the fact that $\mathbf{n} \cdot \nabla_s f = 0$ for any scalar quantity f, Equation (2.1) can be further written as:

$$\Gamma_t + \mathbf{u}_s \cdot \nabla_s \Gamma + \Gamma \nabla \cdot \mathbf{u}_s - \Gamma \mathbf{n} \cdot [(\nabla \mathbf{u}_s) \cdot \mathbf{n}] + \Gamma \kappa u_n = D_s \left(\Delta \Gamma - \frac{\partial^2 \Gamma}{\partial n^2} - \kappa \frac{\partial \Gamma}{\partial n} \right).$$

Such relations and their variants, along with their rigorous demonstration, can also be found in [35] and [36].

2.3.2 Coupling with a quantity defined in the bulk

When considering the problem of how the surfactant concentration evolves in time on an interface immersed in a fluid bulk, it often occurs that the surfactants, despite its tendency to accumulate preferentially on the interface, can also dissolve in the bulk Ω^-. The surfactant concentration at the interface $\Gamma(\mathbf{x}, t)$ is then coupled with a surfactant concentration in the bulk, $c(\mathbf{x}, t)$, with a diffusion constant D. The exchange of material between the interface and the bulk is usually modeled by an adsorption-desorption source/sink term S that depends on the kinetics considered (see [37]). For the case of Langmuir kinetics:

$$S\left(c, \Gamma\right) = k_a c\left(\Gamma_\infty - \Gamma\right) - k_b \Gamma, \tag{2.3}$$

where k_a and k_b are namely the adsorption and desorption coefficients, and Γ_∞ represents the saturation level of surfactant on the interface. The system of governing equations for the evolution of the surfactant concentration in the entire domain can thereafter be written as:

$$\begin{cases} \Gamma_t + \mathbf{u}\cdot\nabla_s\Gamma + \Gamma\nabla\cdot\mathbf{u} - \Gamma\mathbf{n}\cdot\left[(\nabla\mathbf{u})\cdot\mathbf{n}\right] &= D_s\left(\Delta\Gamma - \partial^2\Gamma/\partial n^2 - \kappa\partial\Gamma/\partial n\right) + S \quad \forall x \in \Sigma, \\ c_t + \mathbf{u}\cdot\nabla c &= D\Delta c \quad \forall x \in \Omega, \\ D\ \nabla c\cdot\mathbf{n} &= -S \quad \forall x \in \Sigma. \end{cases} \tag{2.4}$$

2.3.3 Coupling with the Navier-Stokes equations

The evolution of the concentration of surfactant governed by (2.4) and the fluid velocity, described by the Navier-Stokes equations, have reciprocal influences: On the one hand, the incompressible Navier-Stokes equations give the fluid's velocity $\mathbf{u}$ and pressure p, under which the interface is stretched and distorted, and under which the quantities c and Γ are advected. On the other hand the presence of surfactant influences the fluid velocity by modifying the surface

tension along the interface, and therefore the boundary conditions for the Navier-Stokes solver.

A common model for describing the effect on the surface tension γ by the interface concentration Γ is the Szyszkowski equation:

$$\gamma(\Gamma) = \gamma_0 + n\ R\ T\ \Gamma_\infty\ \ln\left(1 - \frac{\Gamma}{\Gamma_\infty}\right), \tag{2.5}$$

where R is the ideal gas constant, T is the absolute temperature, γ_0 is the surface tension of a clean interface, and n is a constant that depends on the type of surfactant and on the presence of excess electrolytes.

It is important to note that both the equation of state and the adsorption-desorption term must be congruent. For instance, the equation of state (2.5) and the kinetic term (2.3) are both derived from Langmuir isotherm, and are therefore congruent. Other choices for this pair are also possible (see [37] for a detailed review of different equations of state and kinetics). For instance, in the case of Frumkin kinetics:

$$\begin{cases} \gamma(\Gamma) & = \ \gamma_0 + n\ R\ T\ \Gamma_\infty\ \left[\ln\left(1 - \dfrac{\Gamma}{\Gamma_\infty}\right) + \dfrac{A}{2}\left(\dfrac{\Gamma}{\Gamma_\infty}\right)^2\right], \\ \\ S\left(c, \Gamma\right) & = \ k_a c\left(\Gamma_\infty - \Gamma\right) - k_b \Gamma \exp\left(-A\left(\Gamma/\Gamma_\infty\right)\right)\ , \end{cases} \tag{2.6}$$

where A is an interaction parameter that depends on the surfactant considered. Other alternatives (like, for example, the 'generalized Frumkin' pair reported in [38] for some nonionic polyoxyethylene surfactants and alcohols) can be found in specialized literature. While in our implementation it is possible to consider any pair of kinetic term and equation of state, in what follows we will assume Langmuir kinetics $\big($Equations (2.3) and (2.5)$\big)$, unless otherwise indicated.

The presence of a varying surface tension implies the following boundary condition on the

jump of the stress tensor $\underline{\underline{\sigma}} = -p\mathbb{1} + \mu\left(\nabla\mathbf{u} + (\nabla\mathbf{u})^T\right)$ across the interface :

$$\left[\underline{\underline{\sigma}}\right] \cdot \mathbf{n} = \gamma\kappa\mathbf{n} - \nabla_s\gamma.$$

The last term in the above boundary condition, whose consequences are only made visible when the surface tension is non constant, is at the origin of the Marangoni force [11]. The complete system of equations describing a surfactant-driven incompressible flow, with a soluble surfactant in the bulk, as well as the coupling between the interface and the bulk, is given by the following system of partial differential equations:

$$\begin{cases} \rho\left(\mathbf{u}_t + \mathbf{u}\cdot\nabla\mathbf{u}\right) &= \nabla\cdot\underline{\underline{\sigma}} + \mathbf{f} \quad \forall x \in \Omega^-, \\ \nabla\cdot\mathbf{u} &= 0 \quad \forall x \in \Omega^-, \\ \Gamma_t + \mathbf{u}\cdot\nabla_s\Gamma + \Gamma\nabla\cdot\mathbf{u} - \Gamma\mathbf{n}\cdot\left[(\nabla\mathbf{u})\cdot\mathbf{n}\right] &= D_s\left(\Delta\Gamma - \partial^2\Gamma/\partial n^2 - \kappa\partial\Gamma/\partial n\right) + S \quad \forall x \in \Sigma, \\ c_t + \mathbf{u}\cdot\nabla c &= D\Delta c \quad \forall x \in \Omega^-, \end{cases} \tag{2.7}$$

completed by the following interface conditions on Σ:

$$\begin{cases} S &= k_a c\,(\Gamma_\infty - \Gamma) - k_b \Gamma, \\ \gamma &= \gamma_0 + n\ R\ T\ \Gamma_\infty\ \ln\left(1 - \dfrac{\Gamma}{\Gamma_\infty}\right), \\ D\ \nabla c \cdot \mathbf{n} &= -S, \\ \left[\underline{\underline{\sigma}}\right] \cdot \mathbf{n} &= \gamma\kappa\mathbf{n} - \nabla_s \gamma. \end{cases} \tag{2.8}$$

2.4 Numerical Method

2.4.1 General framework: the level-set approach on Quad-/Oc-trees

Overview

The level-set method is a general computational method to capture efficiently an interface. It is based on the use of a level-set function ϕ that divides the computational domain Ω into (at most) three parts : $\Omega^+ = \{\mathbf{x} \in \Omega \mid \phi(\mathbf{x}) > 0\}$, $\Omega^- = \{\mathbf{x} \in \Omega \mid \phi(\mathbf{x}) < 0\}$ and the interface $\Sigma = \{\mathbf{x} \in \Omega \mid \phi(\mathbf{x}) = 0\}$. As a convention, the domain of interest for our computation will be Ω^-. The main great advantage of this method is that it naturally captures the changes in the topology of the interface that can occur in many physical situations, such as the pinching of a droplet. The main level-set equation, which evolves the interface according to a velocity field $\mathbf{u}$, is:

$$\phi_t + \mathbf{u} \cdot \nabla\phi = 0. \tag{2.9}$$

Although the algorithms we propose could be employed on a uniform Cartesian mesh, we employ here a Quadtree data structure in two spatial dimensions and an Octree data structure

in three spatial dimensions for increased efficiency. The construction of the Quad-/Oc-tree is recursive: starting from the root cell, which represents the whole computational domain, children are added to the different cells: four of them in the case of a Quadtree data structure (eight for an Octree data structure), corresponding to the splitting of the cell in four (eight for Octrees) new smaller cells. The level of a cell is defined as the depth of the leaf characterizing the corresponding cell in the tree. Graded grids limit the difference of level between two adjacent cells in the grid to one, whereas in non-graded grids, this difference can be arbitrary. The advantage of using non-graded grids is that they are more straightforward to build, and for a same maximum level (corresponding to the depth of the tree), the number of necessary nodes is smaller. An illustration of the principle of the application of Quadtrees to the storage of non-graded adaptive grids in two dimensions is given in Figure 2.1.

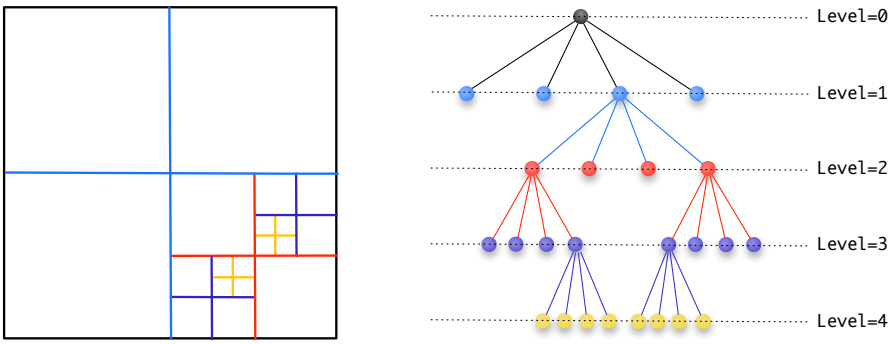

Figure 2.1: An example of the partition of a square into a non-graded adaptive grid (left) and the Quadtree used for its storage.

Refinement criteria

Being mainly interested in refining the grid close to where the interface lies, we apply the following simple refinement criteria proposed in [39, 40]: Split any cell $\mathcal{C}$ if

$$\min_{v \in \text{vertices}(\mathcal{C})} |\phi(v)| \leq \text{Lip}\,(\phi) \times \text{diag-size}(\mathcal{C}),$$

where diag-size($\mathcal{C}$) is the length of the diagonal of the current cell $\mathcal{C}$, Lip (ϕ) is the Lipschitz constant of ϕ and v refers to a vertex (i.e. a node) of the current cell.

Reinitialization of the level-set function

Any Lipschitz continuous function can be chosen for the level-set function ϕ; however, the numerical results are known to be more robust, to induce less mass loss and to provide better geometrical information when computing geometrical quantities when ϕ is taken as the so-called signed distance function. An arbitrary level-set function ϕ_0 can be reinitialized into a signed distance function that describes the same interface Σ by iterating a few steps in fictitious time τ (using a TVD RK-2 scheme) the following reinitialization equation [41]:

$$\phi_\tau + \text{sgn}\,(\phi_0)\,(|\nabla\phi| - 1) = 0. \tag{2.10}$$

Here τ is a fictitious time. The outward normal $\mathbf{n}$ to the interface Σ and the mean curvature κ are defined as:

$$\mathbf{n} = \frac{\nabla\phi}{|\nabla\phi|} \quad \text{and} \quad \kappa = \nabla \cdot \mathbf{n}.$$

In this work, we use the algorithms described in [40] to solve Equations (2.9), (2.10), and to compute the normal and curvature.

Computation of spatial derivatives

In order to compute such spatial derivatives using standard finite-difference formulas, we are bound to introduce ghost nodes where the mesh is locally non uniform (the so called T-junctions; see Figure 2.2). We use the framework of [40]. Considering a node-sampled function $f : v_i \longrightarrow \mathbb{R}$, its value at the ghost node v_4 in two dimensions is defined by the following third-order interpolation (denoting by f_i the value of $f(v_i)$ and by s_i the distance between grid

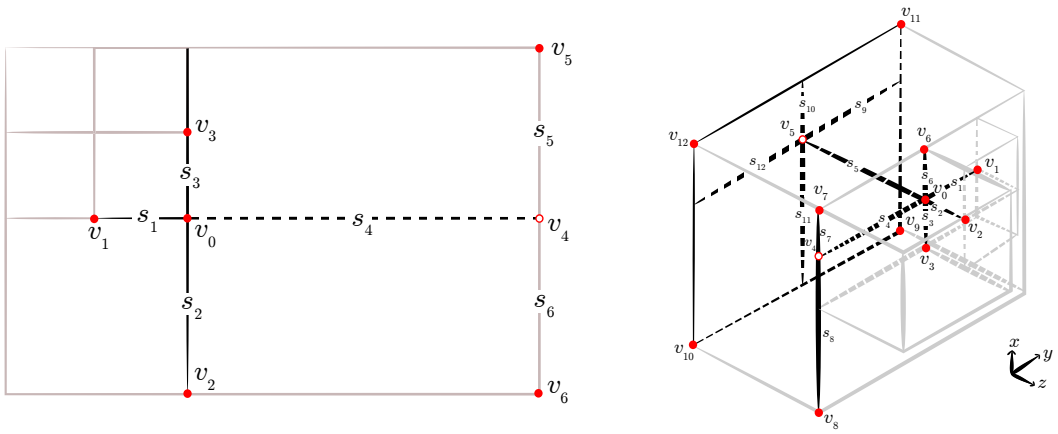

Figure 2.2: General configuration of a T-junction centered on the node v_0 in two (left) and three (right) spatial dimensions

nodes as given in Figure 2.2):

$$f_4^G = \frac{f_5 s_6 + f_6 s_5}{s_5 + s_6} - \frac{s_5 s_6}{s_2 + s_3}\left(\frac{f_2 - f_0}{s_2} + \frac{f_3 - f_0}{s_3}\right),$$

whereas in three spatial dimensions, the definition of the, at most two, ghost nodes are:

$$f_4^G = \frac{f_7 s_8 + f_8 s_7}{s_7 + s_8} - \frac{s_7 s_8}{s_3 + s_6}\left(\frac{f_3 - f_0}{s_3} + \frac{f_6 - f_0}{s_6}\right),$$

and

$$\begin{aligned} f_5^G =& \frac{s_{11}s_{12}f_{11} + s_{11}s_9 f_{12} + s_{10}s_{12}f_9 + s_{10}s_9 f_{10}}{(s_{10} + s_{11})(s_9 + s_{12})} \\ &- \frac{s_{10}s_{11}}{s_3 + s_6}\left(\frac{f_3 - f_0}{s_3} + \frac{f_6 - f_0}{s_6}\right) \\ &- \frac{s_9 s_{12}}{s_1 + s_4}\left(\frac{f_1 - f_0}{s_1} + \frac{f_4^G - f_0}{s_4}\right). \end{aligned}$$

From these ghost nodes definitions, second order accurate discretizations of the standard differential operators can be derived following [40].

Extrapolation Procedures

The algorithms described in the next sections depend on the ability to extrapolate a scalar quantity f from Ω^- to Ω^+, which is performed by iterating a few steps in fictitious time τ (using a TVD RK-2 scheme) of the following equation:

$$\frac{\partial f}{\partial \tau} + H(\phi)\ \mathbf{n} \cdot \nabla f = 0, \tag{2.11}$$

where H is the Heaviside function defined for every node v as follows:

$$H(\phi(\mathbf{x})) = \begin{cases} 1 & \text{if } \ \phi(\mathbf{x}) \geq 0, \\ 0 & \text{otherwise.} \end{cases}$$

Likewise, extrapolating a scalar quantity f from the interface Σ to the entire domain in the normal direction is performed by solving in fictitious time τ the following equation:

$$\frac{\partial f}{\partial \tau} + \delta(\phi)\ \mathbf{n} \cdot \nabla f = 0, \tag{2.12}$$

where δ is the indicator function of the interface, defined by:

$$\delta(\phi(\mathbf{x})) = \begin{cases} 0 & \text{if } \ \phi(\mathbf{x}) = 0, \\ 1 & \text{otherwise.} \end{cases}$$

We refer the interested reader to [42] for the discretization formulas of H and δ, as well as how to discretize Equations (2.11)-(2.12).

2.4.2 Evolution of the surfactant concentration

In this section, we present how we solve the time-dependent evolution of the interfacial concentration of a soluble material quantity, including the advection, the surface diffusion and the adsorption-desorption on the interface. Coupling this solver with a Navier-Stokes solver [43] enables to complete the resolution of the full flow problem described in the previous section.

Solving the equation for the concentration in the bulk

The equation for the surfactant concentration in the bulk, assuming that $\mathbf{u}$ is divergence free, is given by $\big($see (2.4)$\big)$:

$$\frac{\partial c}{\partial t} + \mathbf{u} \cdot \nabla c = D\Delta c \quad \text{in } \Omega^-, \quad \text{with} \quad D\ \nabla c \cdot \mathbf{n} = -S(c, \Gamma) \quad \text{on } \Sigma. \tag{2.13}$$

The advective part of this equation is solved by a non-conservative semi-Lagrangian method discretized using a backward differentiation formula, while the diffusive part is solved implicitly:

$$\alpha\ \frac{c^{n+1} - c_d^n}{\Delta t_n} + \beta\ \frac{c_d^n - c_d^{n-1}}{\Delta t_{n-1}} = D\Delta c^{n+1},$$

where:

$$\alpha = \frac{2\Delta t_n + \Delta t_{n-1}}{\Delta t_n + \Delta t_{n-1}}\,,$$

$$\beta = -\frac{\Delta t_n}{\Delta t_n + \Delta t_{n-1}}\,,$$

and where c_d^n and c_d^{n-1} are the values of c at time t^n and t^{n-1}, respectively, taken at the departure points $\mathbf{x}_d^n$ and $\mathbf{x}_d^{n-1}$, i.e. following the characteristics back from the current node's location $\mathbf{x}^{n+1}$ under the velocity field $\mathbf{u}$ during Δt_n and $\Delta t_n + \Delta t_{n-1}$. Specifically, these points are constructed as

$$\begin{aligned}
\mathbf{x}^* &= \mathbf{x}^{n+1} - \frac{\Delta t_n}{2}\mathbf{u^n}(\mathbf{x^{n+1}}),\\
\mathbf{u}^* &= \frac{2\Delta t_{n-1} + \Delta t_n}{2\Delta t_{n-1}}\mathbf{u^n}(\mathbf{x}^*) - \frac{\Delta t_n}{2\Delta t_{n-1}}\mathbf{u^{n-1}}(\mathbf{x}^*),\\
\mathbf{x_d^n} &= \mathbf{x^{n+1}} - \Delta t_n \mathbf{u}^*,
\end{aligned}$$

and

$$\begin{aligned} \mathbf{x}^* &= \mathbf{x^{n+1}} - \Delta t_n \mathbf{u^n}(\mathbf{x^{n+1}}), \\ \mathbf{x_d^{n-1}} &= \mathbf{x^{n+1}} - (\Delta t_n + \Delta t_{n-1})\, \mathbf{u^n}(\mathbf{x}^*). \end{aligned}$$

Since $\mathbf{x}_d^n$, $\mathbf{x}_d^{n-1}$, $\mathbf{x}^*$ are not in general located on a grid point, we use quadratic interpolation procedures to interpolate the velocity fields at these points [40].

Note that for the case of a constant timestep $\Delta t_n = \Delta t_{n-1} = \Delta t$, the above discretization reduces to:

$$\frac{1}{\Delta t}\left(\frac{3}{2}c^{n+1} - 2c_d^n + \frac{1}{2}c_d^{n-1}\right) = D\Delta c^{n+1}.$$

The equation for solving c^{n+1} implicitly is therefore:

$$\frac{\alpha}{\Delta t_n}\, c^{n+1} - D\Delta c^{n+1} = \left(\frac{\alpha}{\Delta t_n} - \frac{\beta}{\Delta t_{n-1}}\right) c_d^n + \frac{\beta}{\Delta t_{n-1}}\, c_d^{n-1}, \tag{2.14}$$

supplemented with the boundary condition:

$$D\ \nabla c^{n+1} \cdot \mathbf{n} = -S(c^n, \Gamma^n) \quad \forall x \in \Sigma. \tag{2.15}$$

Far away from the interface Σ, Equation (2.14) is discretized using the finite differences framework presented in section 2.4.1. Close to the interface, where the non-homogeneous Neumann boundary condition (2.15) needs to be enforced, a finite volume approach is employed as in [44, 45, 46]. In two spatial dimensions, considering a cell $\mathcal{C}_{i,j}$ in Ω^- centered at the node (i,j) and cut by the interface Σ, and using the divergence theorem on the Laplace operator of Equation (2.14), we have:

$$\frac{\alpha}{\Delta t_n}\int_{\mathcal{C}_{i,j}\cap\Omega^-} c^{n+1}\, d\mathbf{x} - D\int_{\partial C_{i,j}\cap\Omega^-} \nabla c^{n+1}\cdot\mathbf{n}\, dl = \int_{\mathcal{C}_{i,j}\cap\Omega^-} f_{i,j}\, d\mathbf{x} - \int_{\mathcal{C}_{i,j}\cap\Sigma} S(c^n,\Gamma^n)\, dl, \tag{2.16}$$

where $f_{i,j} = \left[\left(\frac{\alpha}{\Delta t_n} - \frac{\beta}{\Delta t_{n-1}}\right) c_d^n + \frac{\beta}{\Delta t_{n-1}}\, c_d^{n-1}\right]_{i,j}$ and where we have used the boundary condition (2.15). We approximate the integrals using the methods detailed in [47]. These approximations yield the filling of the row of the linear system corresponding to the node (i, j). The linear system is symmetric positive definite.

Solving the equation for the interface concentration

Assuming that the velocity field is divergence free, the interface concentration satisfies the following equation:

$$\frac{\partial \Gamma}{\partial t} + \mathbf{u} \cdot \nabla \Gamma - \Gamma \mathbf{n} \cdot [(\nabla\ \mathbf{u}) \cdot \mathbf{n}] = D_s \left(\Delta \Gamma - \frac{\partial^2 \Gamma}{\partial n^2} - \kappa \frac{\partial \Gamma}{\partial n}\right) + S(c, \Gamma), \tag{2.17}$$

which is discretized in time using a modified non-conservative semi-Lagrangian combined with a semi-implicit backward-differentiation-formula scheme [48], treating diffusion implicitly as well:

$$\begin{aligned} \alpha\ \frac{\Gamma^{n+1} - \Gamma_d^n}{\Delta t_n} + \beta\ \frac{\Gamma_d^n - \Gamma_d^{n-1}}{\Delta t_{n-1}} = D_s \Delta \Gamma^{n+1} + \\ \eta\ \left(\Gamma_d^n \Big\{\mathbf{n} \cdot [(\nabla\ \mathbf{u}) \cdot \mathbf{n}]\Big\}_d^n + S(c_d^n, \Gamma_d^n) + A_d^n\right) + \\ \zeta\ \left(\Gamma_d^{n-1} \Big\{\mathbf{n} \cdot [(\nabla\ \mathbf{u}) \cdot \mathbf{n}]\Big\}_d^{n-1} + S(c_d^{n-1}, \Gamma_d^{n-1}) + A_d^{n-1}\right), \end{aligned} \tag{2.18}$$

where $A = D_s \left(-\frac{\partial^2 \Gamma}{\partial n^2} - \kappa \frac{\partial \Gamma}{\partial n}\right)$ is the specific interfacial term of the surface Laplace operator, and where all the quantities evaluated explicitly in the right-hand side are computed at the

departure points (subindex d). Also:

$$\eta = \frac{\Delta t_n + \Delta t_{n-1}}{\Delta t_{n-1}},$$

$$\zeta = -\frac{\Delta t_n}{\Delta t_{n-1}}.$$

Note that for the case of a constant timestep $\Delta t_n = \Delta t_{n-1} = \Delta t$, (2.18) reduces to the implicit-explicit extrapolated Gear scheme [49]:

$$\frac{1}{\Delta t}\left(\frac{3}{2}\Gamma^{n+1} - 2\Gamma_d^n + \frac{1}{2}\Gamma_d^{n-1}\right) = D_s\Delta\Gamma^{n+1} + 2\left(\Gamma_d^n\Big\{\mathbf{n}\cdot[(\nabla\ \mathbf{u})\cdot\mathbf{n}]\Big\}_d^n + S(c_d^n,\Gamma_d^n) + A_d^n\right) - \left(\Gamma_d^{n-1}\Big\{\mathbf{n}\cdot[(\nabla\ \mathbf{u})\cdot\mathbf{n}]\Big\}_d^{n-1} + S(c_d^{n-1},\Gamma_d^{n-1}) + A_d^{n-1}\right).$$

Following the idea of [31], all the quantities of interest are constantly extrapolated to a tube surrounding the interface Σ (see Figure 2.3, left). The new surfactant concentration Γ^{n+1} is then obtained by solving the above equation in this tube with homogeneous Neumann boundary conditions. Constant extrapolation is performed following the procedures presented in [50]. A level-set function χ describing a tube of width 2δ around the interface can easily be obtained from the level-set function ϕ describing the domain, once it has been reinitialized as described in section 2.4.1, by taking simply: $\chi(\mathbf{x}) = |\phi(\mathbf{x})| - \delta$. One of the advantages of this method is that the same grid is used to solve the concentration in the bulk and the concentration on the interface (see Figure 2.3, right).

Note that the specific interfacial terms of the surface Laplace operator $\left(-\frac{\partial^2\Gamma}{\partial n^2} - \kappa\frac{\partial\Gamma}{\partial n}\right)$ are here taken into account in an explicit way. However, by extending Γ from the interface to the whole domain before solving the equation, we have ensured that Γ is almost constant in the normal direction and therefore those terms are very small (here, we take them to be zero).

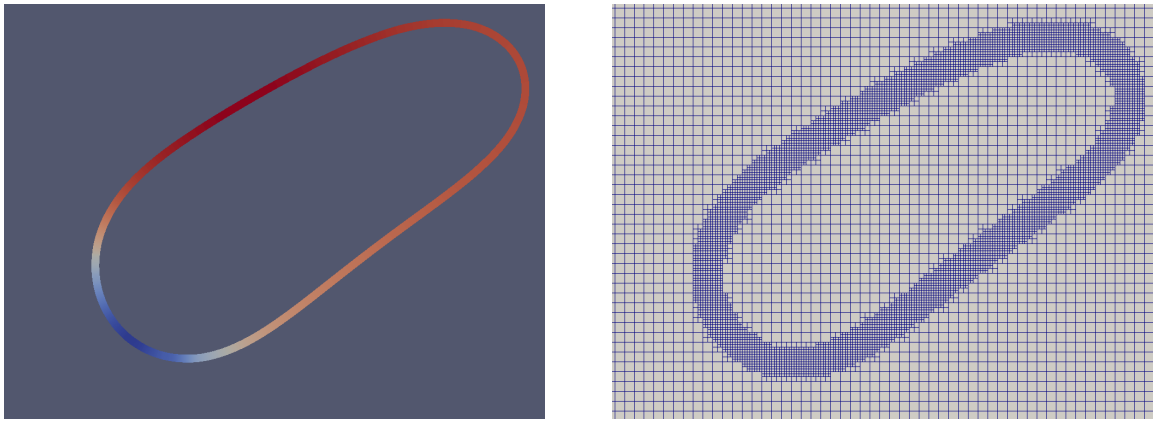

Figure 2.3: Left: visualization of the geometry of the tube used to solve the equation governing the evolution of the concentration Γ of surfactant on the interface (2.18), in the case of a bubble in a shear flow. The tube is colored according to interface concentration (with increasing concentration from blue to red). Right: grid used to perform this simulation.

2.4.3 Coupling with a Navier-Stokes solver

A Navier-Stokes solver, described below, is used at each time step, alternating with the resolution of the governing equations for the interface concentration and the bulk concentration of surfactant. The velocity field given by the Navier-Stokes equations is used to advect c and Γ, whereas the value of Γ obtained using the procedure described in the section 2.4.2 is used to compute the value of the surface tension γ and its gradient $\nabla\gamma$, which intervene at the next iteration in the boundary conditions for the Navier-Stokes solver.

The projection method

The Navier-Stokes equations

$$\begin{cases} \rho\left(\mathbf{u}_t + \mathbf{u}\cdot\nabla\ \mathbf{u}\right) &= \nabla p + \mu\Delta\mathbf{u} + \mathbf{f} \\ \\ \nabla\cdot\mathbf{u} &= 0 \end{cases}$$

are solved using a projection method [51]. We first solve for an auxiliary velocity $\mathbf{u}^*$ using again a semi-Lagrangian/backward-differentiation-formula discretization of the momentum equation

from which the pressure term has been removed:

$$\rho\left(\alpha\,\frac{\mathbf{u}^*-\mathbf{u}_d^n}{\Delta t_n}+\beta\,\frac{\mathbf{u}_d^n-\mathbf{u}_d^{n-1}}{\Delta t_{n-1}}\right)=\mu\Delta\mathbf{u}^*+\mathbf{f}.$$

Here the velocity components are stored at the nodes on the corners of the cells, as in [52], from which the semi-Lagrangian updates are computed. To treat the viscosity implicitly, a linear system for $\mathbf{u}^*$ is built using the finite differences techniques described in section 2.4.1 and solved using a BiCGSTAB solver and the multigrid method presented in [53] as a preconditioner. The velocity components (u, v) are then interpolated to the cells faces as in the standard MAC grid arrangement. The projection is then performed on that grid, i.e. we write $\mathbf{u}^{n+1}=\mathbf{u}^*-\nabla\Phi$ and solve the following linear system for the Hodge variable Φ:

$$\nabla\cdot\nabla\Phi=\nabla\cdot\mathbf{u}^*. \tag{2.19}$$

Following the standard MAC grid projection method, the Hodge variable is stored at the center of the grid cells. The gradient operator appearing in the above equation is approximated using the second order discretizations in [54]. To ensure the stability of the projection step, the divergence operator D is constructed following [43], in particular it is related to the discrete gradient G through

$$L_F G=-(L_C D)^T,$$

where L_F and L_C are two diagonal matrices. We refer the interested reader to [43] for more details about the stability. The velocity components are then interpolated back to the nodes with least-squares interpolations in order to proceed to the advection of the different quantities of interest [43].

Also, even though our algorithm does not require the pressure to be computed, we note that it is given by $p=\alpha\frac{\rho}{\Delta t_n}\Phi-\mu\Delta\Phi=\alpha\frac{\rho}{\Delta t_n}\Phi-\mu\nabla\cdot\mathbf{u}^*$.

Boundary conditions

Free surface boundary conditions are implemented in order to enforce the exact boundary conditions in velocity and pressure that are imposed by the presence of surfactant:

$$\left[\underline{\underline{\sigma}}\right] \cdot \mathbf{n} = \gamma\kappa\mathbf{n} - \nabla_s\gamma \ , \tag{2.20}$$

where the surface tension γ is computed as a function of the interface concentration Γ. Even though the coupling with the Navier-Stokes solver admits any regime, in our computational examples we will limit ourselves to Stokes flows for simplicity of the boundary conditions. Indeed, in this case the treatment is considerably more straightforward, since there is a decoupling between the pressure and the velocity (we refer the interested reader to the original derivation in [55]). The jump boundary conditions read as follows [11]:

$$\begin{cases} [p] = -\gamma\kappa, \\ [\nabla p \cdot \mathbf{n}] = \Delta_s\,\gamma, \\ [\mathbf{u}] = 0, \\ [\mu\,\nabla\mathbf{u} \cdot \mathbf{n}] = \nabla_s\gamma. \end{cases} \tag{2.21}$$

Furthermore, in our computational examples we will assume that one of the phases is dynamically negligible (i.e. the shear stress in that phase is much smaller than the shear stress in the other phase, and its pressure is constant and taken as zero). This allows for the utilization of a monophase Navier-Stokes solver, and the above four boundary conditions reduce to two (imposing the four of them with only one phase would be overconstraining the problem). Additionally, the jump boundary conditions reduce to Dirichlet (for the pressure) and Neumann

(for the velocity) boundary conditions:

$$\begin{cases} p &= \gamma\kappa, \\ \\ \mu\nabla\mathbf{u}\cdot\mathbf{n} &= -\nabla_s\gamma. \end{cases} \tag{2.22}$$

The boundary conditions for the velocities are enforced on $\mathbf{u}^*$ during the first step of the projection algorithm (2.4.3), taking into account the fact that $\mathbf{u}^*$ is different from $\mathbf{u}^{n+1}$ by adding the gradient of the Hodge variable obtained at the previous iteration to the conditions enforced (assuming that $\nabla\Phi^{n+1}$ is not far from $\nabla\Phi^n$, which proves to be a good approximation).

The boundary condition for the pressure is enforced during the second step of the projection method, i.e. when solving for the Hodge variable (2.19) using the expression $p = \alpha\dfrac{\rho}{\Delta t_n}\Phi - \mu\nabla\cdot\mathbf{u}^*$.

Time step restriction

As suggested by Brackbill *et al.* in [56], the simulation of free surface flows is stable if it is able to resolve the capillary waves along the interface. Denoting by c the velocity of those capillary waves, this induces a restriction of:

$$c\frac{\Delta t}{\Delta x} < \frac{1}{2}, \tag{2.23}$$

where here Δx refers to the smallest grid size. However, the velocities c_k of those capillary waves are given as a function of the wave number k by:

$$c_k = \sqrt{\frac{\gamma k}{\rho}}. \tag{2.24}$$

The maximum time step allowed can be estimated in Equation (2.23) using the maximum wave velocity. Equation (2.24) shows that this maximum velocity is reached for maximum wave

numbers, i.e. for minimum wave lengths. The minimum wave length that can be resolved is $2\Delta x$, which corresponds to a maximum wave number $k_{max} = \frac{\pi}{\Delta x}$. Therefore, by substituting c by $c_{max} = \sqrt{\gamma\pi/\rho\Delta x}$ in Equation (2.23), one obtains the following time-step constraint:

$$\Delta t < \sqrt{\frac{\rho(\Delta x)^3}{2\pi\gamma}} \quad \text{or} \quad \Delta t = \mathcal{O}\left(\Delta x^{\frac{3}{2}}\right).$$

Contact angle

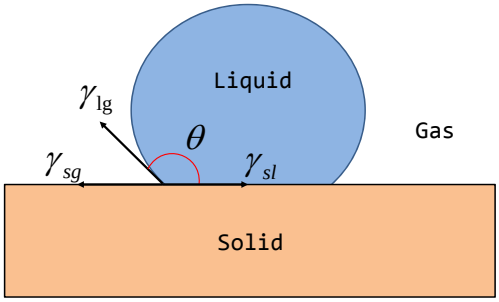

Figure 2.4: Solid-liquid-gas triple point and contact angle.

A contact angle is implemented in the Navier-Stokes solver in order to model the dynamics of the wetting of a surface. The model chosen involves another velocity boundary condition: at the triple point (the point where the wall, the bulk fluid and the external fluid, assumed to be at rest, meet), a velocity is imposed, equal to [57]:

$$\mathbf{u} = \frac{1}{\beta}(\cos(\theta_c) - \cos(\theta))\mathbf{t},$$

where β is the friction coefficient between the solid surface and the fluid (usually taken between 2 and 10), θ the angle formed by the fluid surface with the substrate, θ_c the contact angle (of about 45° for an interface between water and glass) and $\mathbf{t}$ is the tangent vector to the substrate.

2.5 Verification of the method

2.5.1 Verification in two spatial dimensions

Three types of tests are designed in order to validate separately the diffusive part of the governing equation for the interfacial concentration, the advective part of this same equation, and the diffusive part of the governing equation for the bulk concentration as well as the coupling terms between the bulk and the interface. Those tests are for the most part inspired by those of Muradoglu and Tryggvason in [12], some slightly modified in order to fully validate every term of the governing equations.

Verification of the surfactant diffusion

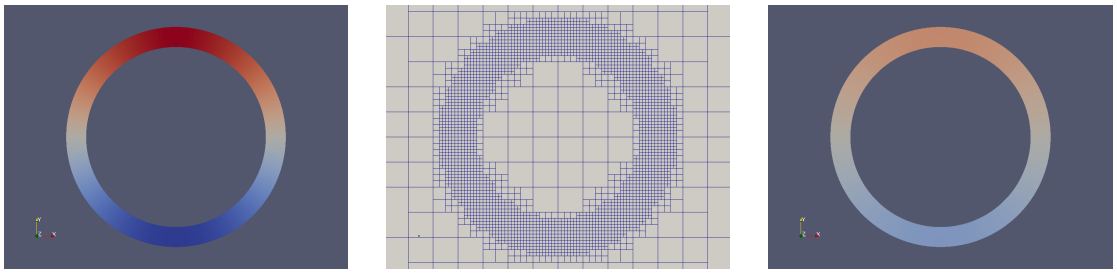

Figure 2.5: Representation of the geometry chosen for the interfacial diffusion test. From left to right: (a) the computational tube at initial time, colored by interfacial concentration; (b) the mesh used for the computation with minimum level/maximum level 0/8; and (c) the computational tube at final time, with the same coloration.

In order to validate the time-dependent evolution equation for Γ:

$$\frac{\partial \Gamma}{\partial t} = D_s \Delta_s \Gamma,$$

Muradoglu and Tryggvason [12] considered the diffusion of a surfactant around a circular bubble of radius one, on which an initial surfactant distribution has been imposed. The initial concentration is written in cylindrical coordinates as: $\Gamma(\theta, t = 0) = \frac{1}{2}(1 + \sin(\theta))$. Writing the surface Laplace operator on a circle of radius r in cylindrical coordinates, $\Delta_s = \frac{1}{r^2}\frac{\partial^2}{\partial \theta^2}$, one can

solve analytically the surface diffusion equation for Γ as:

$$\Gamma(\theta, t) = \frac{1}{2}\left(1 + e^{-D_s t/r^2}\sin(\theta)\right).$$

Figure 2.5 depicts the initial and final distribution for Γ as well as a typical adaptive grid. The results of the simulation with a mesh refinement of min/max-level equal to 0/8 are given in Figure 2.6.

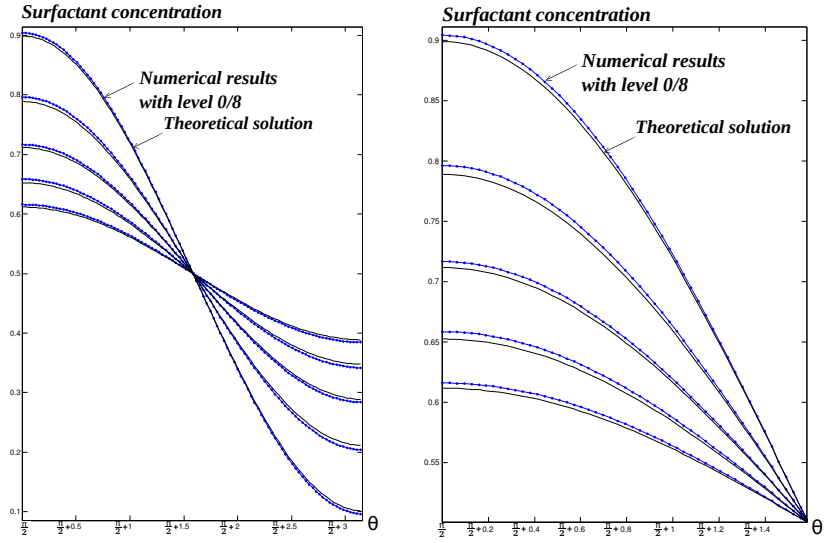

Figure 2.6: Representation of the interfacial concentration as a function of the angle θ for $\theta \in \left[\frac{\pi}{2}; \frac{3\pi}{2}\right]$ at different times. The blue dotted line represents the numerical results for a min/max-level of 0/8, whereas the black line represents the theoretical solution. A zoom of these curves is given in the right part of this figure. The time from the more stretched curves to the flatter ones are .25, .5, .75, 1 and 1.25.

We can also focus on the convergence of the algorithm, by starting with a simulation with a min/max-level of 0/6 and doing this simulation again after having split every cell (to obtain a min/max-level of 1/7). Afted having iterated this process up to a min/max-level of 3/9, we can compare the results, which are presented in Figure 2.7. We also computed the L^∞ error as a function of time for every min/max-level chosen. The result is represented in Figure 2.8. We observe that the L^∞ error increases fast during the first time steps, which is normal since the first time steps of our second-order-in-time discretization need to be initialized, and thus the

min/max-level	L^∞ error	order
0/6	1.32×10^{-2}	
1/7	6.97×10^{-3}	.921
2/8	3.60×10^{-3}	.953
3/9	1.83×10^{-3}	.976

Table 2.1: Order of accuracy for example 2.5.1.

first time steps are only of order one in time. We also observe that the error tends to decrease after some time, which can be explained by the fact that for every resolution chosen, the method converges asymptotically to a uniform distribution of surfactant around the bubble, with $\Gamma(\theta, t = +\infty) = \frac{1}{2}$. Table 2.1 indicates that the method is first-order accurate in the L^∞-norm.

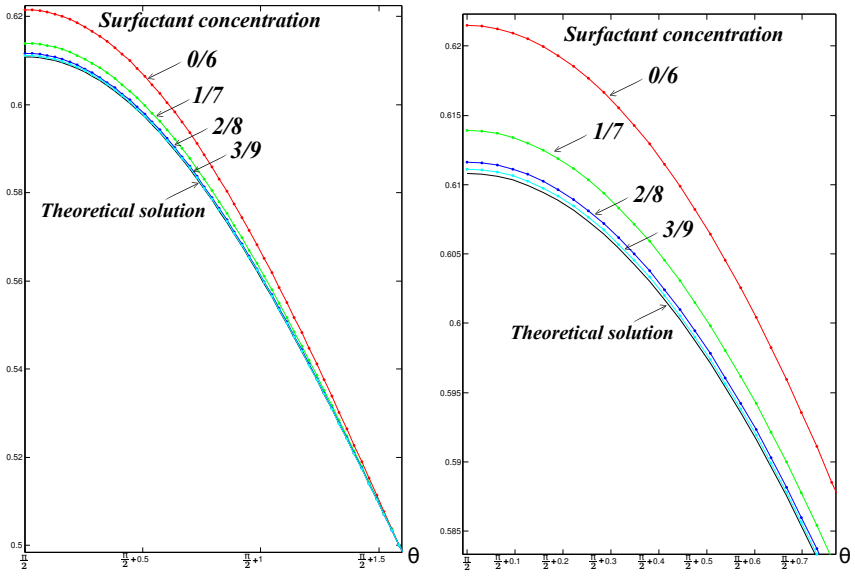

Figure 2.7: Representation of the interfacial concentration as a function of the angle θ for $\theta \in \left[\frac{\pi}{2}; \pi\right]$ at the same time for different min/max-level chosen for the simulation. A detail of these curves is given in the right part of this figure.

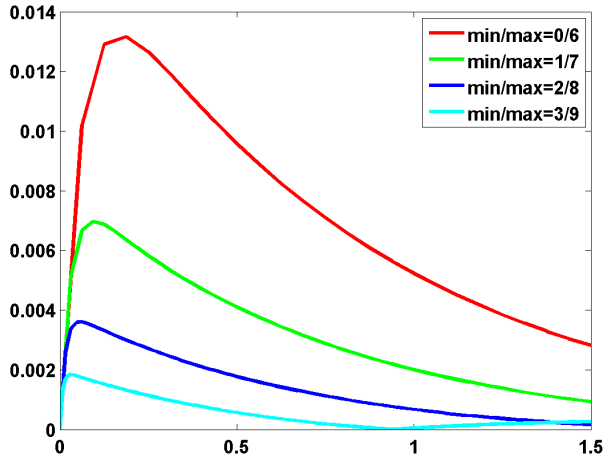

Figure 2.8: L^{∞} error for example 2.5.1 as a function of time for different min/max-level.

Verification of the surfactant advection

The test proposed by Muradoglu and Tryggvason in [12] consists of a spherical bubble with initial radius 1 that is laden with a uniform distribution of surfactant. This bubble is expanding under a radial unit velocity flow. Note that this velocity field is not divergence free, but has a divergence equal to: $\nabla \cdot \mathbf{u} = \frac{1}{r}$ in cylindrical coordinates; the advection equation that needs to be solved is therefore:

$$\frac{\partial \Gamma}{\partial t} + \mathbf{u} \cdot \nabla \Gamma + \Gamma \nabla \cdot \mathbf{u} - \Gamma\, \mathbf{n} \cdot [(\nabla\ \mathbf{u}) \cdot \mathbf{n}] = 0\ . \tag{2.25}$$

However, since we have chosen $\mathbf{u}$ confounded with the outward normal $\mathbf{n}$ ($\mathbf{u} = \frac{\mathbf{x}}{|\mathbf{x}|} = \mathbf{n}$), the relation $||\mathbf{n}|| = ||\mathbf{u}|| = 1$ implies that $(\nabla\ \mathbf{u}) \cdot \mathbf{n} = (\nabla\ \mathbf{n}) \cdot \mathbf{n} = 0$. Therefore, the last term on the left member of Equation (2.25) is always equal to zero. This test therefore does not fully test the interface advection and we modify it with a more complex geometry while keeping the radial velocity field $\mathbf{u} = \frac{\mathbf{x}}{|\mathbf{x}|}$. Specifically, we consider a star-like shape, with an equation in cylindrical coordinates given by:

$$r(\theta) = 0.75\,(1 - 0.2\sin(7\theta))\,.$$

Figure 2.9 represents the geometry chosen for those advection tests. In particular, it is obvious that the radial velocity field is now not confounded anymore with the normal so the term $-\Gamma \mathbf{n} \cdot [(\nabla\ \mathbf{u}) \cdot \mathbf{n}]$ in Equation (2.25) now has a value that depends on the location on the star-shaped bubble. Finally, taking the initial surfactant concentration to be $\Gamma(\theta, t = 0) = \frac{1}{2}$ and invoking the conservation principle of the interfacial surfactant, we get the following analytical description of the time-dependent evolution of the surfactant concentration on the star:

$$\Gamma(\theta, t) = \frac{1}{2} \frac{\sqrt{r^2(\theta) + (r')^2(\theta)}}{\sqrt{(t + r(\theta))^2 + (r')^2(\theta)}}.$$

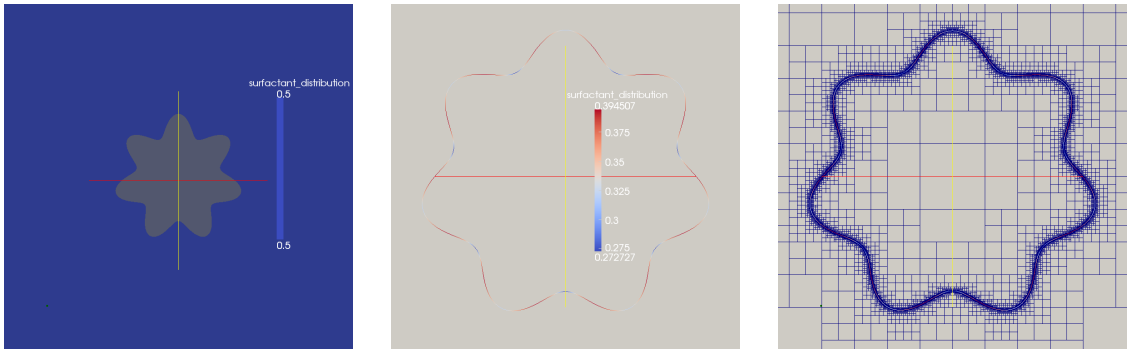

Figure 2.9: Representation of the geometry chosen for the interfacial advection test: (a) the star at initial time, colored according to the interfacial concentration; (b) the concentration distribution at final time, with the same color map; and (c) the mesh used for the computation with a min/max-level of 0/9.

The interfacial concentration as a function of the angle θ is given in Figure 2.10. The numerical results are in agreement with the analytical solution. As we could have expected the error is greater in the hollows between two branches of the star (which corresponds to where the concentration reaches its maximum), because it is where the interface is less resolved.

A more challenging test that we consider is the advection of a circular bubble in a vortex. In a computational domain with dimensions $[0, 1] \times [0, 1]$, we place a circular bubble of radius 0.15 and centered at $(0.5, 0.75)$. The bubble is initially laden with a uniform surfactant concentration

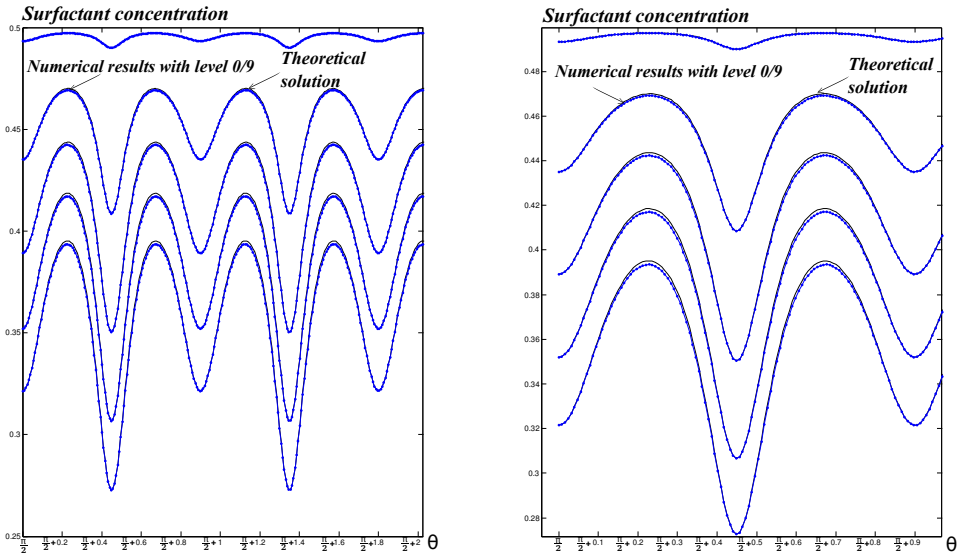

Figure 2.10: Representation of the interfacial concentration as a function of the angle θ for $\theta \in \left[\frac{\pi}{2}; \frac{8\pi}{7}\right]$ at different times for a min/max-level of 0/9. The blue dotted lines correspond to the numerical results whereas the black lines represent the analytical solution. A detail of these curves is given on the right part of this figure. Times from top curve to bottom curve are .025, .125, .25, .375 and .5.

$\Gamma(x, y, t = 0) = \frac{1}{2}$, and is advected by the following divergence-free velocity field $\mathbf{u} = (u, v)$:

$$u(x, y) = \quad \sin^2(\pi x)\sin(2\pi y), \tag{2.26a}$$

$$v(x, y) = -\sin^2(\pi y)\sin(2\pi x), \tag{2.26b}$$

3 for $t \in [0, \frac{1}{2}]$. At $t = \frac{1}{2}$ the velocity field is reverted so that at $t = 1$ the system should return to its initial configuration.

Figure 2.11 represents the global configuration for this test, at initial time and final time. It gives an idea of how challenging this test is, since the surface of the bubble is very stretched during this advection, and it develops a very sharp extremity that tends to be under-resolved for low grid resolutions. This test is therefore an indication of the typical accuracy that one may expect in the case where an interface undergoes large deformations, especially when fine features develop (here the thin tail of the interface). It also illustrates the advantage of an

adaptive grid.

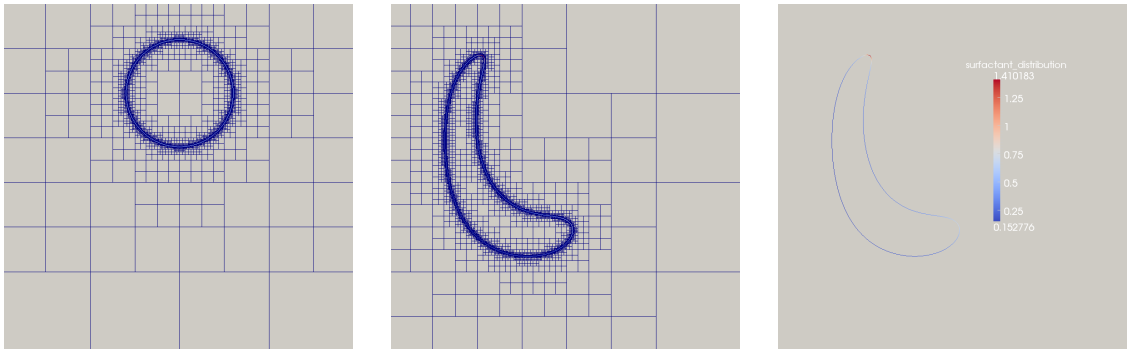

Figure 2.11: Representation of the geometry chosen for the vortex advection test. From left to right: (a) the grid (with min/max-level 0/9) at initial time; (b) the same grid at time $t = 0.5$; and (c) the interface at time $t = 0.5$, colored by interfacial concentration.

In Figure 2.12 we have represented the repartition of the concentration as a function of θ around the circle for different spatial resolutions ranging from 0/8 to 4/12 after having performed an advection with the velocity field $\mathbf{u}$ given by Equations 2.26 during a time 0.5 and having advected it back to its initial position with the velocity field $-\mathbf{u}$ during the same time interval 0.5.

We can also observe the time-evolution of the surfactant loss on the bubble by integrating the surface concentration around the interface, and observing how this amount evolves with time. The integration along the interface is performed using the integration method described in [47]. The results are given in Figure 2.13.

Figure 2.13 indicates that the sudden change of the velocity field from $\mathbf{u}$ to to $-\mathbf{u}$ at time 0.5 has no significant influence on the evolution of the total amount of surfactant. The surfactant loss at final time is about 6% for the lowest spatial resolution, which is a good result since the interface tends to be under-resolved around time 0.5 when the bubble is most distorted.

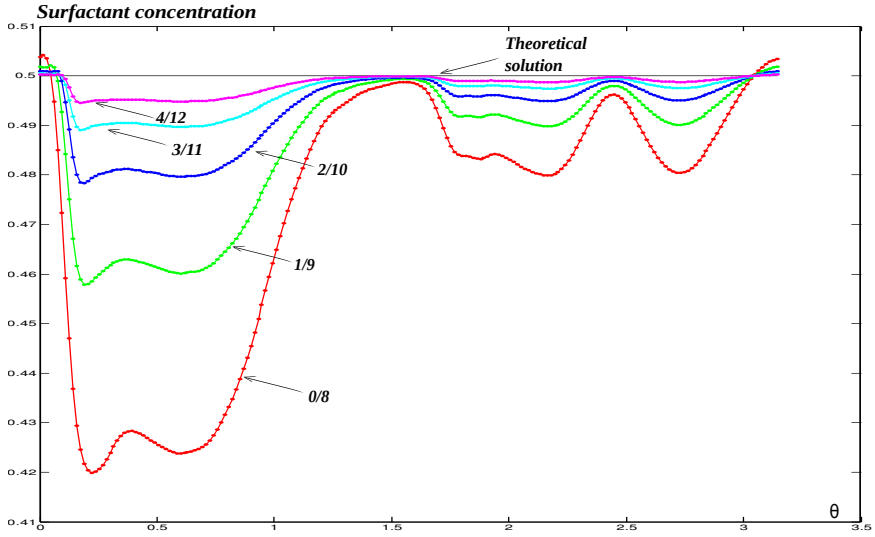

Figure 2.12: Representation of the interfacial concentration as a function of the angle θ for $\theta \in [0; \pi]$ at the final time ($t = 1$) for different min/max-level chosen for the simulation. The red dotted line corresponds to a min/max-level of 0/8, the green one to 1/9, the blue one to 2/10, the cyan one to 3/11 and the magenta one to 4/12. The black line represents the theoretical solution.

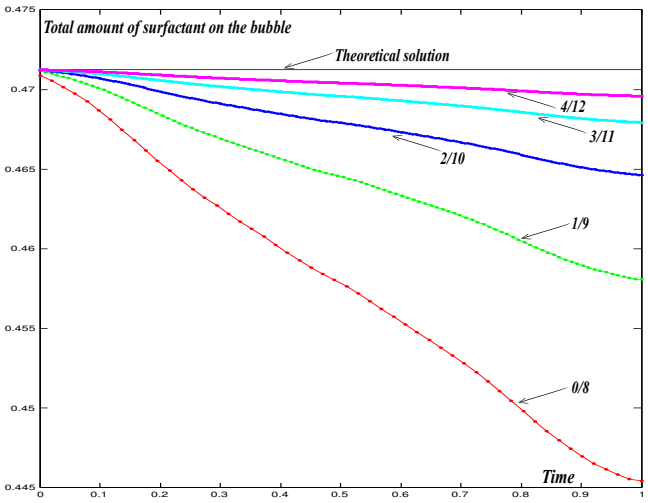

Figure 2.13: Representation of the total amount of surfactant as a function of time for different min/max-level chosen for the simulation. The red dotted line corresponds to a min/max-level of 0/8, the green one to 1/9, the blue one to 2/10, the cyan one to 3/11 and the magenta one to 4/12. The black line represents the theoretical solution.

Verification of the bulk concentration diffusion and of the coupling between the bulk and the interface

The first test is that proposed in [12]: a circular bubble of radius 1, initially clean, is placed in an infinite bulk charged with an initial constant concentration c_∞ of surfactant. The surfactant concentration c in the bulk diffuses with a diffusion constant D but is not advected, i.e. we take $\mathbf{u} = 0$ in Equation (2.13). A simplified coupling term S is chosen as $S = k_a c$. In this setting, [12] give an analytical solution, with the restriction that it is valid for short times only. Indeed, in an infinite domain and with a source term of the form given above, the concentration on the bubble will tend to $+\infty$, whereas for a finite computational domain the conservation of the total amount of surfactant (having implemented homogeneous Neumann boundary conditions for c at the boundary of the domain) prevents the concentration of surfactant in the bulk from diverging. In addition, it appears that even in an infinite domain this analytical solution remains an approximation, valid for short times only [58]. For these two reasons (the facts that we work with a finite domain, and that the analytical solution to which we compare our results is only an approximation, valid for short times only), we will restrict our investigations of the results of this test to short times after the beginning of the diffusion and coupling between the bulk and the interface.

Figure 2.14 provides the results for the time-dependent evolution of the total amount of surfactant on the interface, with min/max-level ranging from 6/8 to 10/12. We can observe that the numerical results obtained are consistent for short times with the analytical solution proposed in [12]. However, the time scale observed is so small compared to the characteristic time scale of diffusion that the analytical solution reduces to a line, which means that we only observe the dominant order of the source term, which is: $S = k_a c_\infty + \mathcal{O}(t)$.

For our second test, we consider a clean infinite wall that is placed in front of a semi-infinite bulk domain with initial concentration c_∞ that diffuses with a diffusion coefficient D. A simplified coupling term $S = k_a c$ ensures the surfactant transfer between the bulk and the interface. The analytical solution for the time-dependent evolution of the concentration c as a

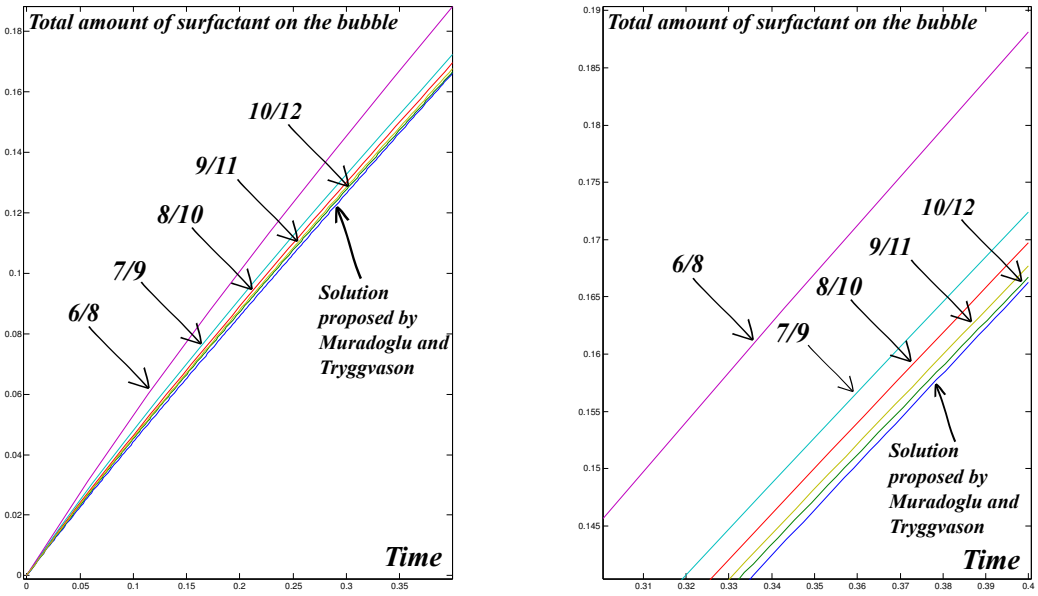

Figure 2.14: Representation of the total amount of surfactant on the bubble as a function of time for short times. The magenta line corresponds to a min/max-level of 6/8, the cyan one to 7/9, the red one to 8/10, the yellow one to 9/11 and the green one to 10/12. The black line represents the analytical solution proposed by [12]. A detail of these curves is given in the right part of this figure.

function of the time t and of the distance x to the interface is given by:

$$c(x,t) = c_\infty \left[\mathrm{erf}\left(\frac{x}{2\sqrt{Dt}} \right) + e^{k_a x + k_a^2 Dt} \mathrm{erfc}\left(\frac{x}{2\sqrt{Dt}} + k_a \sqrt{Dt} \right) \right], \tag{2.27}$$

where

$$\mathrm{erf}(x) = \frac{2}{\sqrt{\pi}} \int_0^x e^{-t^2} dt \ ,$$

and

$$\mathrm{erfc}(x) = 1 - \mathrm{erf}(x) = \frac{2}{\sqrt{\pi}} \int_x^{+\infty} e^{-t^2} dt \ .$$

The results presented in Figure 2.15 give the surfactant concentration c as a function of the distance to the wall for different times, and with different min/max-level ranging from 6/8 to 8/10. Figure 2.15 shows that even for long times, the diffusion of the bulk concentration c as

well as the surfactant transfer between the bulk and the interface occur as predicted by the analytical solution. As expected, though, the accuracy of the results tends to be deteriorate for long times. This can be attributed to the fact that the analytical solution was computed for an infinite domain, whereas the simulations were only performed on a finite computational domain. This explanation is consistent with the observation that the concentration in the bulk for long times tends to be lower than predicted by the analytical solution in infinite domain.

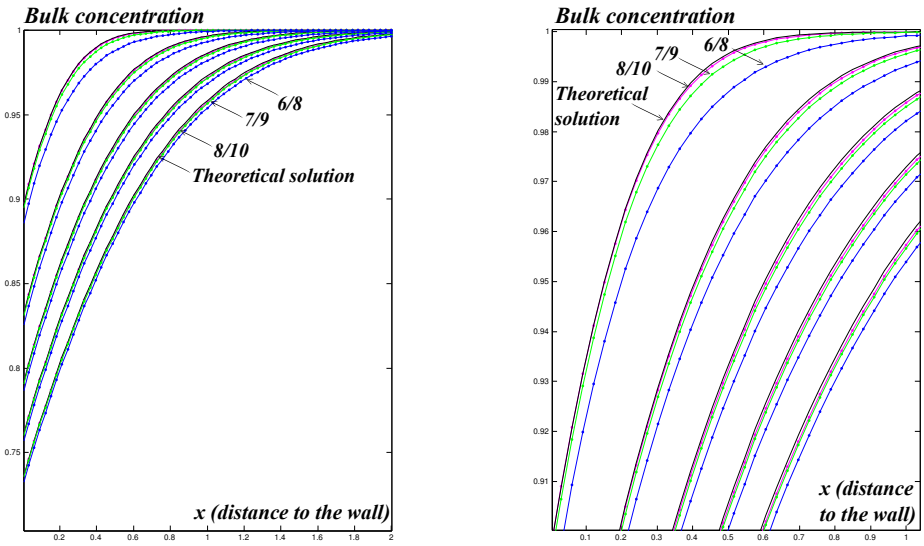

Figure 2.15: Bulk concentration c as a function of the distance x to the interface. The blue dotted line corresponds to a min/max-level of 6/8, the green one to 7/9 and the magenta one to 8/10. The black line represents the analytical solution. A detail of these curves is given in the right part of this figure. The time elapsed, from top to bottom curves, is .04, .12, .2, .28 and .36.

2.5.2 Verification in three spatial dimensions

Verification of the surfactant diffusion

We consider the diffusion of surfactant around a spherical bubble of radius 1, on which an initial distribution of the surfactant has been imposed. The initial concentration chosen, in spherical coordinates, is $\Gamma(\theta, t = 0) = \frac{1}{2}(1 + \sin(\theta))$. The surface Laplace operator on a sphere

of radius r can be written in spherical coordinates, yielding $\Delta_s = \frac{1}{r^2 \sin(\theta)} \frac{\partial}{\partial \theta} \left(\sin(\theta) \frac{\partial}{\partial \theta} \right)$. The solution of the time-dependent evolution equation for Γ,

$$\frac{\partial \Gamma}{\partial t} = D_s \Delta_s \Gamma,$$

is therefore

$$\Gamma(\theta, t) = \frac{1}{2} \left(1 + e^{-\frac{2tD_s}{r^2}} \sin(\theta) \right).$$

Figure 2.16 proposes different visualizations for the geometry of this problem. The results of the simulations with a mesh refinement of min/max-level of 0/7 are given in Figure 2.17. Figure 2.18 provides the results of the simulation under mesh refinement.

Verification of the surfactant advection

For the verification of the interface advection, we use the same idea as in the two-dimensional case, performing the expansion of a shape laden with surfactant under a radial velocity field. For the same reasons as in section 2.5.1, the shape should not be a sphere if the test is to be relevant. We thus consider a star-like shape given by the equation, in spherical coordinates,

$$r(\theta, \phi) = 0.75 + 0.2 \left(1 - 0.6 \cos(6\phi)\right) \left(1 - \cos(6\theta)\right).$$

Taking the initial surfactant concentration to be $\Gamma(\theta, t = 0) = \frac{1}{2}$, the conservation of the interfacial surfactant leads to the following analytical description of the time-dependent evolution of the surfactant concentration on the star:

$$\Gamma(\theta, \phi, t) = \frac{1}{2} \frac{\sqrt{r^2(\theta, \phi) + \left(\frac{\partial r}{\partial \theta}\right)^2 (\theta, \phi)} \sqrt{r^2(\theta, \phi) + \left(\frac{\partial r}{\partial \phi}\right)^2 (\theta, \phi)}}{\sqrt{(t + r(\theta, \phi))^2 + \left(\frac{\partial r}{\partial \theta}\right)^2 (\theta, \phi)} \sqrt{(t + r(\theta, \phi))^2 + \left(\frac{\partial r}{\partial \phi}\right)^2 (\theta, \phi)}}.$$

Figure 2.19 represents the geometry, while Figure 2.20 depicts the solution at different times.

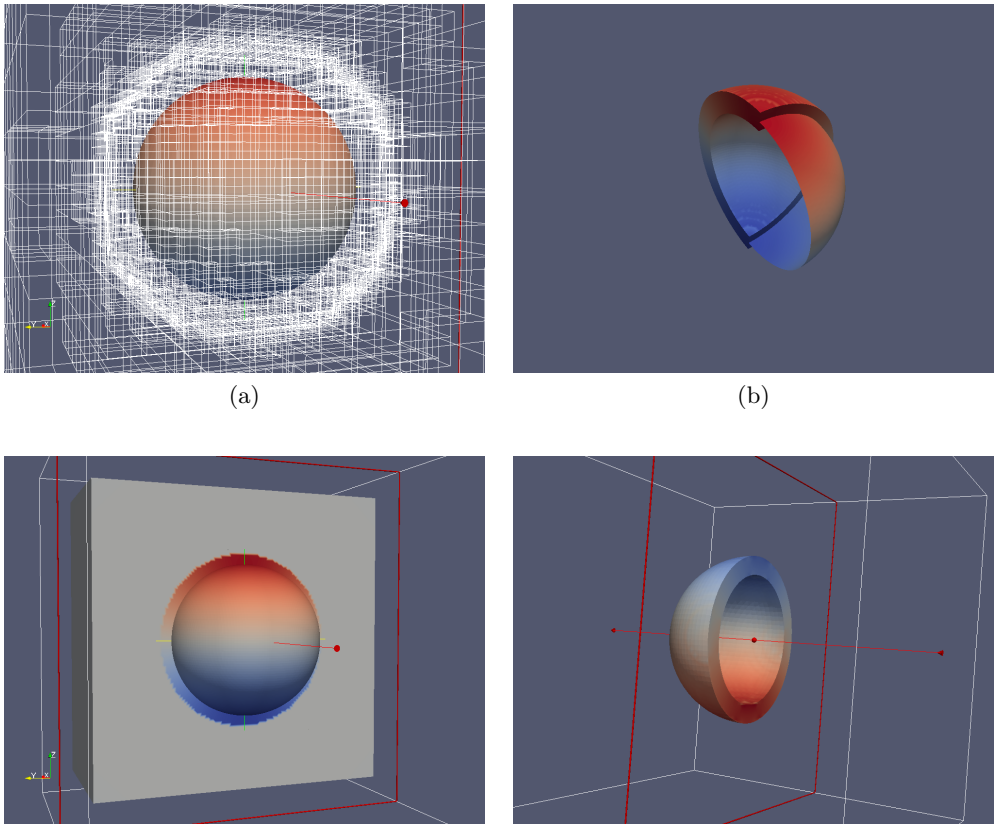

(a) (b)

(c) (d)

Figure 2.16: Setup for example 2.5.2: (a) the mesh used for this computation with a min/max-level of 0/6; (b) a visualization of the tube and the solution at initial time with a min/max-level of 0/7 (c) solid visualization of the computational tube and the solution at final time with min-level/max/level 0/7, colored by the interface concentration; (d) another visualization of the tube, with the same min/max-level.

Similarly to the two-dimensional case, we can study the interfacial concentration as a function of the angle θ at different times. We do that in two different ways: by clipping the star by a plane that crosses the apexes of the star, or by clipping it by a plane that passes through the hollow regions (see Figure 2.21). The numerical results for a clipping plane that passes through the hollow regions of the star are given in Figure 2.22 whereas the results for a clipping plane crossing the apexes of the star are given in Figure 2.23. The numerical results obtained are in good agreement with the analytical solution, and are convergent. As we could have expected, the errors are greater when clipping the interface by a plane that passes through the hollows between two branches of the star since the interface is less resolved in those regions. For the

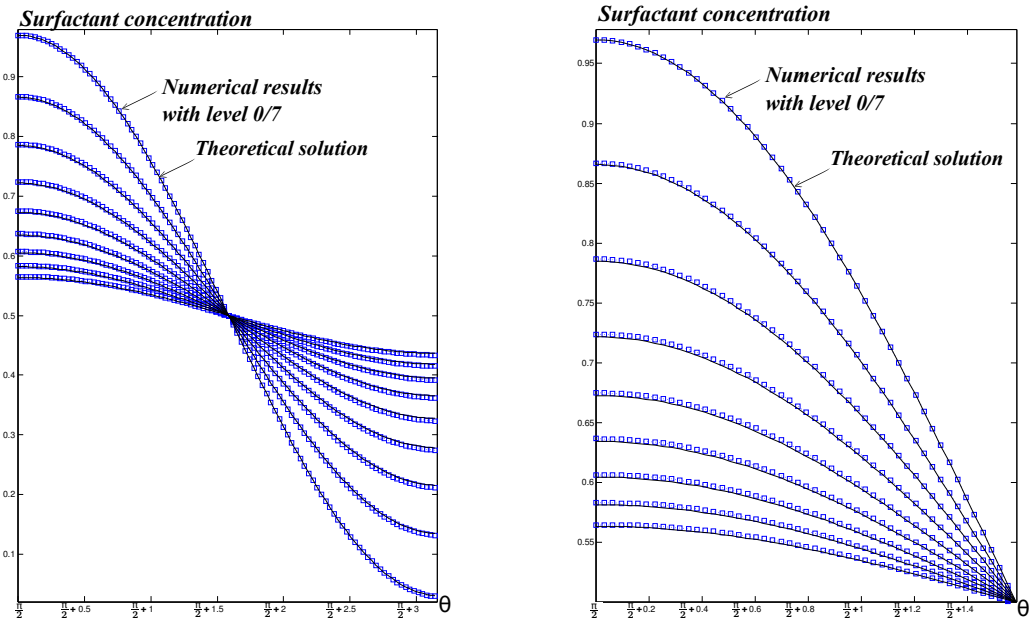

Figure 2.17: Representation of the interfacial concentration as a function of the angle θ for $\theta \in \left[\frac{\pi}{2}; \frac{3\pi}{2}\right]$ at different times. The blue dotted line with square markers represents the numerical results for a min/max-level of 0/7, whereas the black line represents the theoretical solution. A detail of these curves is given in the right part of this figure. The times from the top to bottom curves are .04, .16, .28, .4, .52, .64, .76, .88 and 1.

same reason, the results are less accurate for angles θ close to 0 or π.

2.6 Computational examples

In this section, we consider a few physically relevant problems that can be studied with our computational method.

2.6.1 Bubble in a shear flow

The problem of the deformation of bubbles or drops in a shear flow or a uniaxial extensional flow and in the presence of surfactant, has already been widely studied in the literature (see e.g.

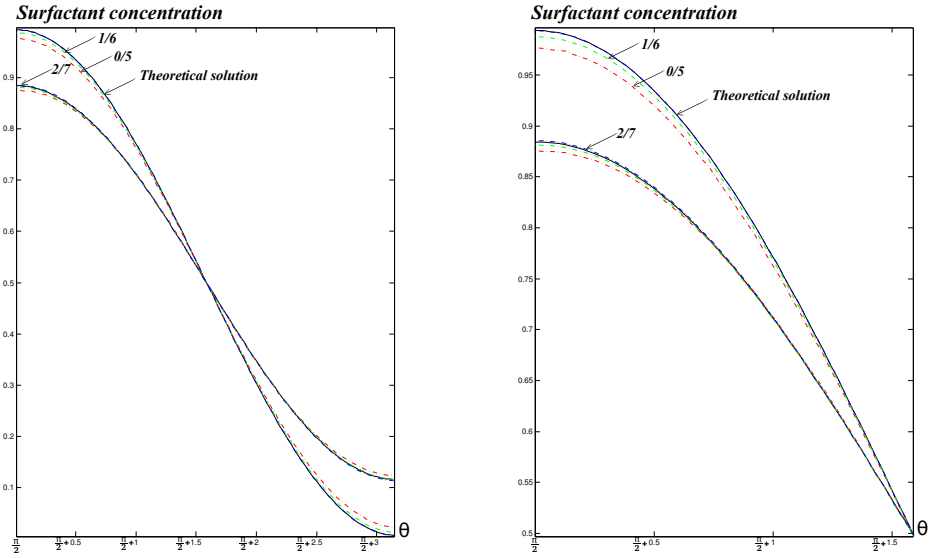

Figure 2.18: Representation of the interfacial concentration as a function of the angle θ for $\theta \in \left[\frac{\pi}{2}; \pi\right]$ at two different times (from top to bottom, .02 and .14) for various min/max-level. The red dotted lines correspond to a min/max-level of 0/5, the green lines correspond to a min/max-level of to 1/6 and the blue lines correspond to a min/max-level of to 2/7. The black lines represent the theoretical solution. A detail of these curves is given in the right part of this figure.

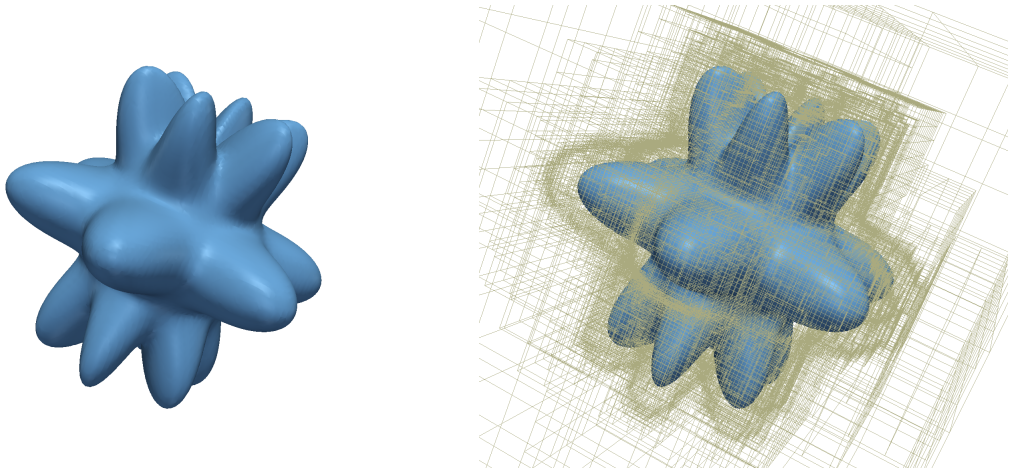

Figure 2.19: Representation of the geometry chosen for the interfacial advection test in 3D. From left to right: the star at initial time and the same star with the mesh used for the computation with a min/max-level of 0/7.

[4] and the references therein). The results of all those studies tend to prove that the presence of surfactant promotes the cleavage of drops and bubbles, which can be expected since the

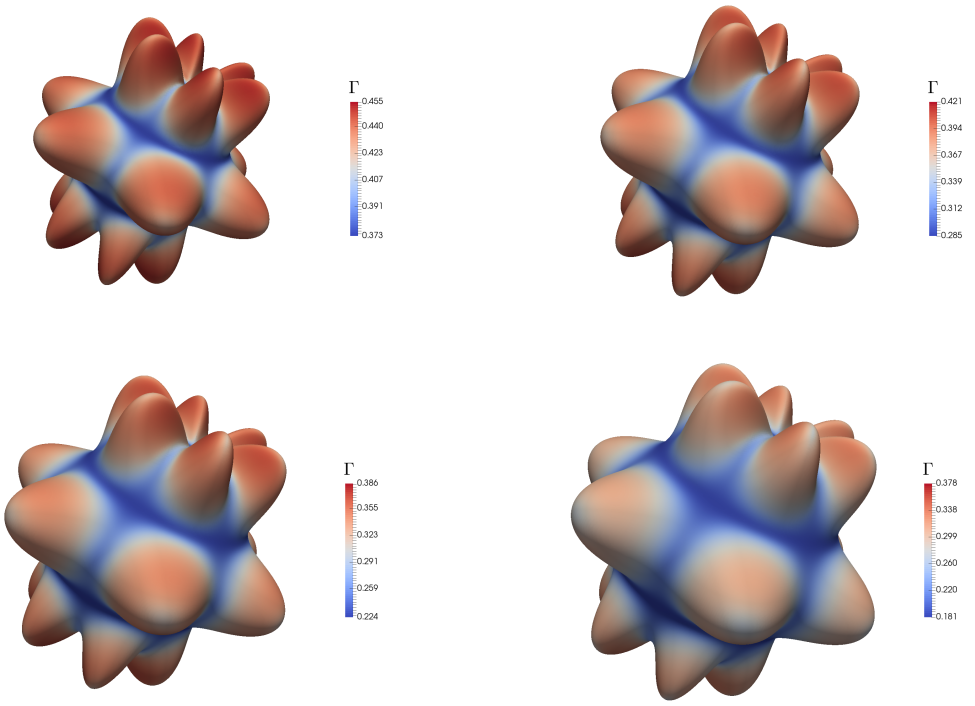

Figure 2.20: Visualization of the motion and surface concentration evolution on a star advected under a radial velocity field. The time elapsed is, from top left to bottom right: .125, .25, .375 and .5.

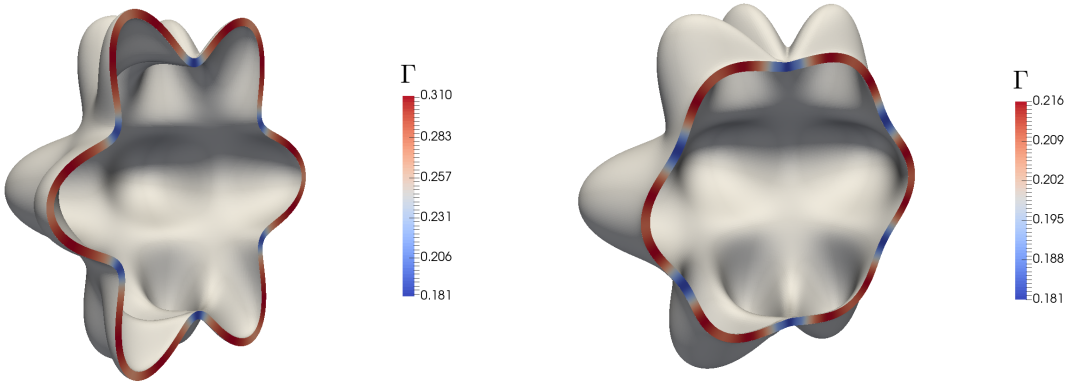

Figure 2.21: Representation of two different ways to clip the star with a plane containing the z axis: by a plane that crosses the apexes of the star (left) or by a plane that passes through the hollow regions (right). Both figures show the star at $t = 0.5$, with Γ represented in the tube in which the interface transport is solved.

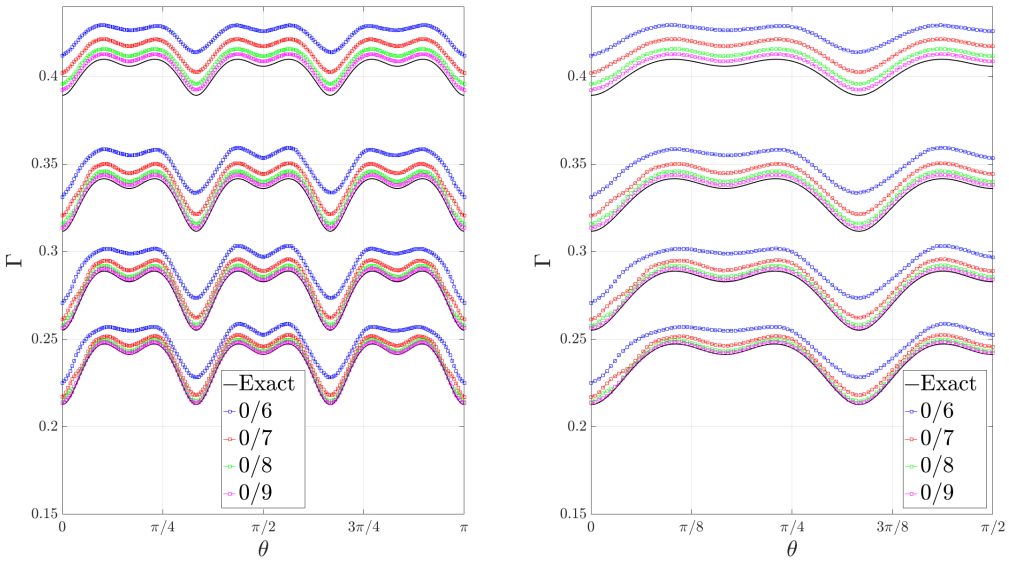

Figure 2.22: Representation of the interfacial concentration as a function of the angle θ for $\theta \in [0; \pi]$ at different times (from top to bottom .1, .2, .3 and .4), clipping the star by a plane that passes through the hollow regions between the apexes. The color of the lines with square markers indicates the resolution of the simulation. The black lines represent the exact solution. A detail of these curves is given in the right part of this figure.

presence of surfactant lowers the surface tension. Moreover, when the coupling term between the interfacial concentration and the bulk concentration is small, or when the surfactant is supposed to be insoluble, the flow tends to advect the surfactant towards the ends of the drop, where it accumulates, causing the drop to develop pointed ends as the surface tension becomes very small at its extremities. As expected, these effects become less visible as the surface Péclet number $Pe_s = \frac{LU}{D_s}$ increases. The surface Péclet number, which measures the ratio between the advective effects and the diffusive effects of the interfacial surfactant, considers length and velocity scales L and U, respectively.

In this section, we focus on the case when the surfactant is soluble and when the interfacial and the bulk concentrations are not initially balanced, with the interfacial concentration being significantly lower than the bulk's. Figure 2.24 shows the time evolution of a bubble placed in such conditions. For this simulation, we modeled the effect of the surfactant on the surface

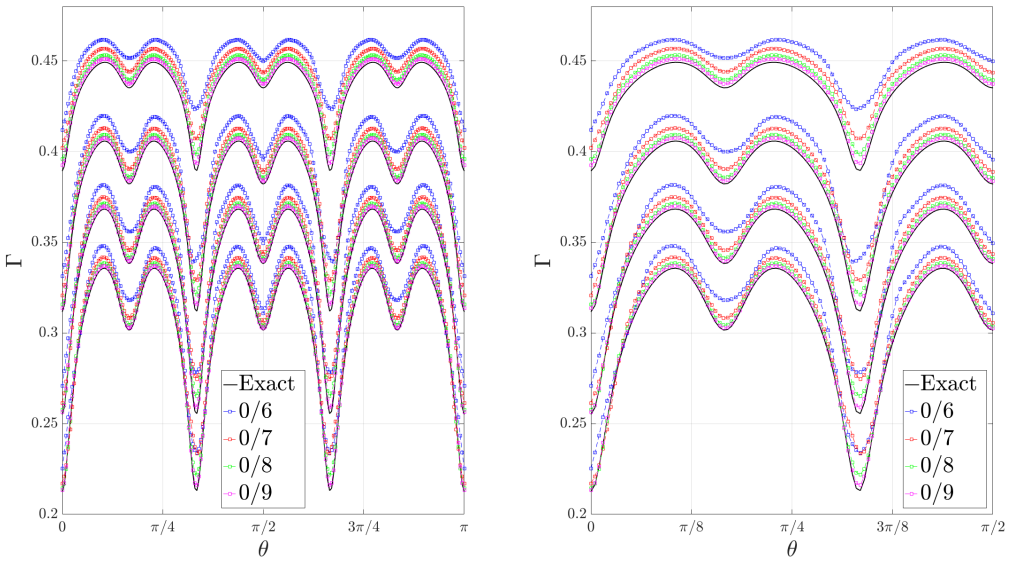

Figure 2.23: Representation of the interfacial concentration as a function of the angle θ for $\theta \in [0;\pi]$ at different times (from top to bottom .1, .2, .3 and .4), clipping the star by a plane that passes through the apexes of the star. The color of the lines with square markers indicates the resolution of the simulation. The black lines represent the exact solution. A detail of these curves is given in the right part of this figure.

tension through Frumkin kinetics (see Equations (2.6)), using the parameters of the 1-nonanol ($C_9H_{19}OH$) given by Lin *et al.* :

$$\begin{cases} n & = 1\ , \\ A & = 3.410\ , \\ \Gamma_\infty & = 5.915 \cdot 10^{-6}\ (\mathrm{mol/m^2}), \\ k_b/k_a & = 0.3137\ (\mathrm{mol/m^3}), \\ D_s & = 6.3 \cdot 10^{-10}\ (\mathrm{m^2/s})\ , \\ T & = 295.85\ (\mathrm{K}), \end{cases}$$

and noting that the surface tension for a clean interface is in this case the value for a water-air interface $\gamma_0 = 0.072$ (N/m).

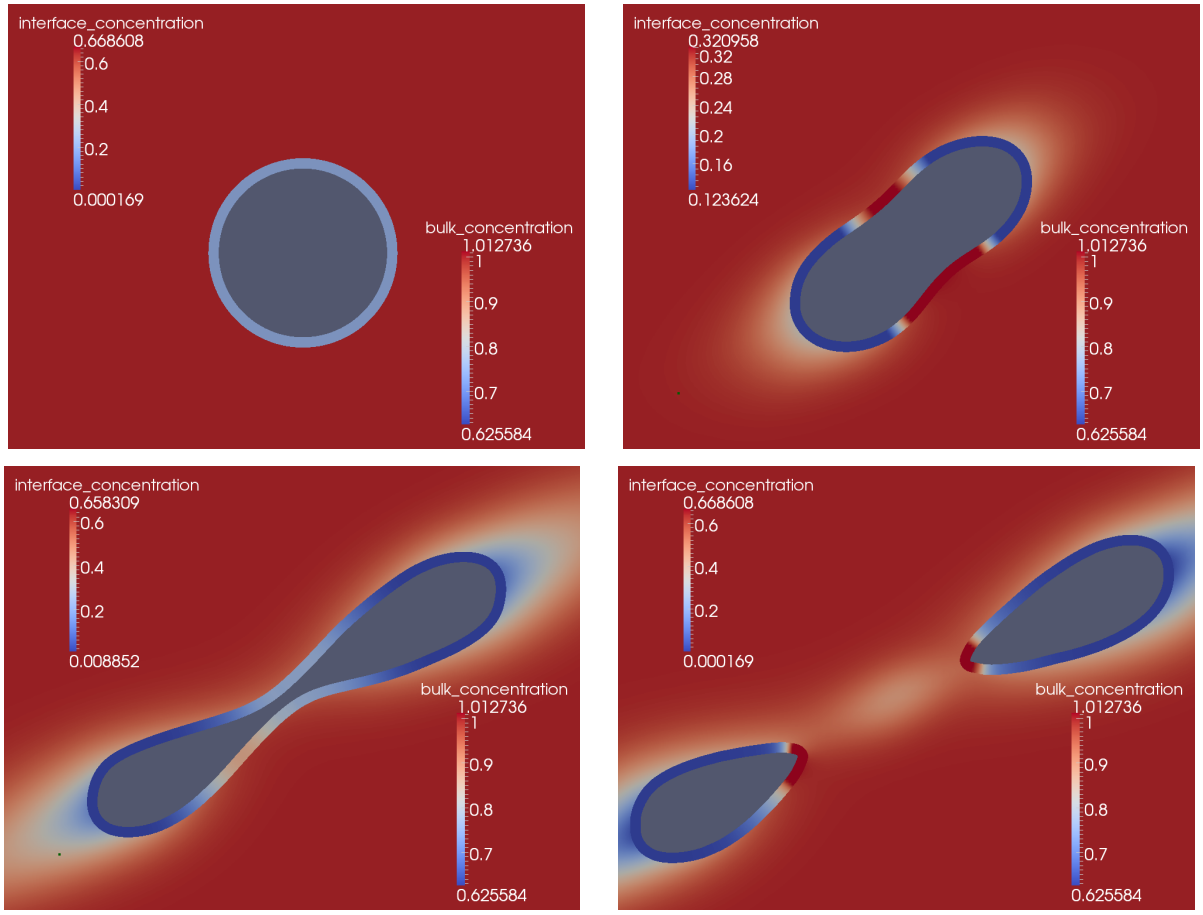

Figure 2.24: Drop breakup and evolution of the normalized concentrations in the bulk and on the interface for a bubble with a low initial concentration of surfactant placed in a contaminated bulk and under a shear flow. The time elapsed, from top left to bottom right, is 0, .25, .5 and .75.

Figure 2.24 reveals that the motion of the advected fluid around the bubble tends to enhance the adsorption of surfactant on the bubble's interface near the location of breakup, thus creating propitious conditions for the future breakup of the bubble. Moreover, as the surfactant accumulates near the future breakup point, driven by the flow, its presence not only weakens the surface tension around it, but also creates a gradient of surface tension from the regions of high surfactant concentration to the regions of low surfactant concentration thus generating Marangoni forces that drive the flow close to the interface from the equatorial plane of the bubble to its edges, which is another mechanism that can be held responsible for the breakup of the bubble.

After the breakup occurs, we can observe that the ends of the two daughter bubbles near the breakup point present a sharp pointed shape. This can be attributed to the fact that the high surfactant concentration near those two edges has weakened the surface tension thus allowing such shapes to exist. This is perfectly consistent with all the observations reported in the literature inventoried above, such sharp-ended shapes having already been reported in the case of bubbles in shear flows or extensional flows in the presence of surfactant.

2.6.2 Tears of wine

Figure 2.25: Illustration of the phenomenon of tears of wine along the wall of a glass containing ordinary table wine.

We consider the phenomenon of tears of wine (see Figure 2.25), which is an emblematic manifestation of the Marangoni forces. The reason for the formation of the so called tears of wine is that the evaporation of ethanol at the air-fluid interface of the thin layer of wine deposited on the wall of a glass causes a huge decrease of the alcohol concentration in the film; whereas on the surface of the rest of the wine inside the glass, evaporation is compensated by diffusion inside the glass, and the concentration of ethanol near the interface remains almost constant. As the ethanol surface tension is much lower than the one of water, this creates a gradient of surface tension in the fluid film from the bottom to the top of the glass. This gradient of surface tension causes the emergence of Marangoni forces directed upwards. As the width of the film layer is very small, the fluid is not sheared very much by the gravity (this

is why it tends to be static), and the Marangoni forces are strong enough to counterbalance those gravitational forces. This causes the fluid to climb along the wall of the glass, hence the formation of droplets that fall under their own weight once they have reached a critical size, evoking the shape of tears. This phenomenon has been reported for centuries but was first correctly explained by physicist James Thomson, the elder brother of Lord Kelvin, in 1855[1].

As ethanol is not a surfactant, it is of no use to define an interfacial concentration since the only variable of interest in order to compute the surface tension is the bulk concentration near the interface. However, the evaporation rate of alcohol can be modeled by a desorption term on the interface. We can use our computational framework to simulate the evaporation of ethanol. The value of k_b is set to zero, since we neglect the contribution of the vapors of alcohol to the concentration of ethanol in the wine; and the source term is taken equal to $S(c) = k_a c$, the value of the evaporation rate k_a being given by O'Hare *et al.* (fitting the data reported in [59] reveals that $k_a = 5.919 \cdot 10^{-4}$ (m/s)). Of course, since the interfacial surfactant concentration has no physical meaning (despite the fact that it allows one to keep track of the evaporated ethanol and check that the total amount of ethanol remains constant in time, even though it decreases in the bulk), the surface diffusion coefficient is set to zero. The surface tension of the fluid is taken to be equal to a function of the molar fraction of ethanol, following the law that has been identified by Ghahremani *et al.* [60], namely:

$$\gamma\left(x_m\right) = \left[11.53\left(\log\left(x_m\right)\right)^3 + 26.54\left(\log\left(x_m\right)\right)^2 - 10.08\log\left(x_m\right) + 22.48\right] \cdot 10^{-3} \quad \text{(N/m)},$$

where x_m is the molar fraction of bulk ethanol at the interface. Note also that the molar fraction

[1]Contrary to common beliefs, the number, width and thickness of the tears (or legs) and how slow they fall does not predict the quality of wine. Rather they are indicative of the degree of alcohol and quantity of glycerol (that increases the viscosity and thus makes the tears slower to fall).

can be obtained from c as follows:

$$x_m(c) = \frac{c}{c + \dfrac{\rho_{\mathrm{w}}}{\mathrm{MW}_{\mathrm{w}}}\left(1 - \dfrac{\mathrm{MW}_{\mathrm{e}} \cdot c}{\rho_{\mathrm{e}}}\right)},$$

where:

$$\begin{cases} \rho_{\mathrm{w}} & = 1000 \ (\mathrm{kg/m^3}), \\ \rho_{\mathrm{e}} & = 789 \ (\mathrm{kg/m^3}), \\ \mathrm{MW}_{\mathrm{w}} & = 0.018 \ (\mathrm{kg/mol}), \\ \mathrm{MW}_{\mathrm{e}} & = 0.046 \ (\mathrm{kg/mol}) \end{cases}$$

are the densities and molecular weights of water and ethanol, respectively.

Figure 2.26 depicts the motion of the wine in a thin layer deposited on the wall of a glass and connected to the rest of the wine in the glass. We can clearly see that as the mechanisms of evaporation and ethanol diffusion in water lower the ethanol concentration specifically in the thin layer, the gradient of surface tension thus created causes the wine to climb the side of the glass. The contact angle combined with the effects of gravity prevent the drop from climbing higher than a certain height. The wine thus accumulates at the upper extremity of the film, forming a droplet that eventually falls back under its own weight. Even though it seems difficult to define precise numerical parameters that could be measured in order to confirm the relevance of this simulation, the general behavior of the flow, the shape of the droplet that forms, and the mechanism responsible for its formation tend to show that this simulation is in good qualitative agreement with the phenomenon of tears of wine.

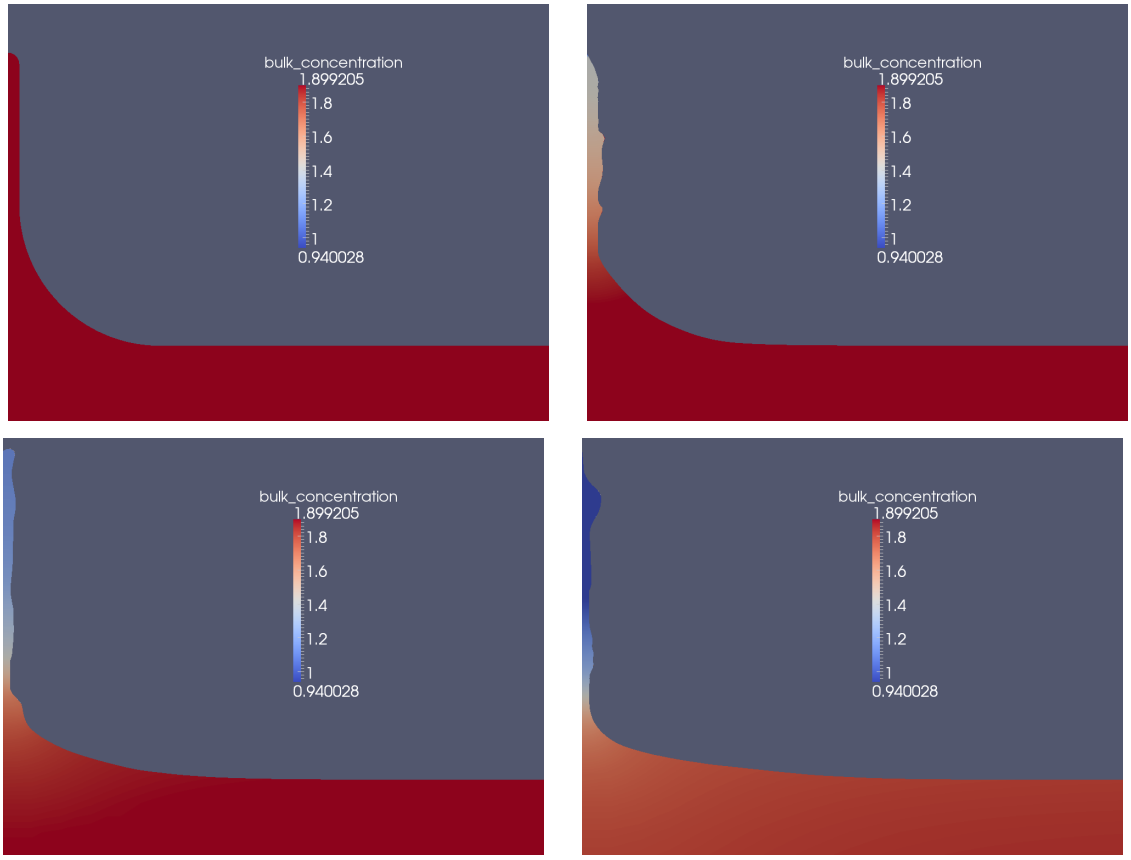

Figure 2.26: Visualization of the motion and evolution of the normalized bulk concentration of ethanol in a thin layer of wine deposited on the wall of a glass and connected to a reservoir (the content of the glass itself). Time elapses from top left to bottom right.

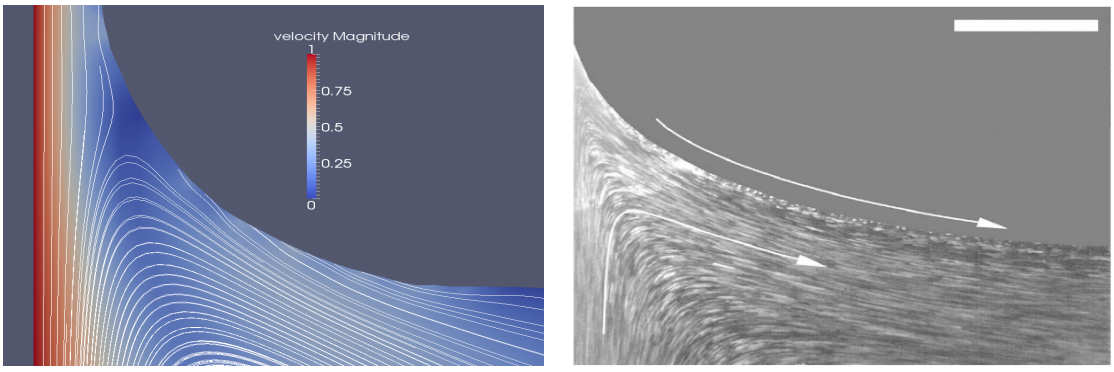

(a) (b)

Figure 2.27: Visualization of the streamlines occurring during dip coating without surfactant. (a) Numerical simulations with $Ca = 5 \times 10^{-2}$. (b) Flow visualization established by Mayer and Krechetnikov in [7] at $Ca = 1.8 \times 10^{-3}$. Both visualizations clearly reveal the presence of an interfacial stagnation point. The values of velocity displayed are normalized.

2.6.3 Coating

Dip coating, which consists in the deposition of a liquid on a solid substrate by simply withdrawing the substrate from a bath, is the simplest form of coating. Despite its numerous and important industrial applications, some of the phenomena involved are not fully understood. One of these phenomena is the film thickening due to the presence of surfactant. Landau and Levich were the first to determine the theoretical thickness h_∞ of the film deposited by the withdrawal of a flat wall of a fluid bath (with no surfactant). Under the hypothesis of low Reynolds number, this thickness is proportional to the capillary length l_c and depends on the capillary number Ca through:

$$h_\infty = 0.945\ l_c\ Ca^{\frac{2}{3}}, \tag{2.28}$$

where $l_c = \sqrt{\gamma/\rho g}$ and $Ca = \mu U/\gamma$.

However in the presence of surfactant, the thickness of the film given by Equation (2.28) proves too small. Despite numerous reports of this phenomenon of film thickening, it is only rather recently that the first experimental study of the flow field close to the coated substrate has been undertaken by Mayer and Krechetnikov in [7]. Their study features outstanding visualizations of the flow near the interface. This experimental work did not completely settle the controversy about the reasons of this film thickening, but it revealed that the flow field thus identified allows Marangoni stresses to be the mechanism responsible for the film thickening.

Few numerical studies of this phenomenon have been undertaken. In [61] Krechetnikov and Homsy have conducted a study of the effects of surfactant on the film thickness in the Landau-Levich problem as well as the Bretherton problem, with a numerical algorithm based on a boundary-integral formulation. However, their simulations led to a film thinning instead of the thickening observed experimentally. More recently, in [62], Campana, Ubal, Giavedoni and Saita have solved the full hydrodynamic problem using the finite elements method on a domain tessellated into quadrangular elements and have found values of film thickening in good agreement with the experiments reported by Krechetnikov and Homsy.

It appears that two different phenomena could account for the film thickening observed experimentally in the Landau-Levich problem in the presence of surfactant. Equation (2.28) combined with the expression given above for l_c and Ca shows that the thickness of the film is proportional to $\gamma^{-\frac{1}{6}}$. By weakening the surface tension, the presence of surfactant have therefore the immediate effect of thickening the film. But another effect that must be taken into account is the Marangoni effect. As the surface of the fluid is stretched by the withdrawal of the wall at constant velocity, the surfactant concentration on the film becomes smaller. Therefore the surface tension gets bigger on the film portion of the interface than on the rest of the horizontal interface. In turn, this generates Marangoni forces that tend to advect the fluid near the interface from the reservoir to the film, creating very characteristic flow patterns, depending on the parameters of the problem. The experimental study undertaken in [7] reveals these patterns.

We have used our computational framework to simulate dip coating (using the same parameters for the surfactant as in Section 2.6.1) and we find that similar patterns occur. We also studied the qualitative evolution as a function of the parameters of the problem. In particular, while solving the Landau-Levich problem without any surfactant leads to a flow with an interfacial stagnation point (see Figure 2.27), the presence of surfactant leads to more complex flow patterns, with the notable presence of an interior stagnation point. Figure 2.28 presents the flow topologies for the Landau-Levich problem in the presence of surfactant for increasing capillary numbers, and compares them with the experimental visualization of [7]. We note that we do not consider the same Ca as in [7], as such computations would take about half a year on our workstation and we leave this exercise for when we develop a parallel approach. Nevertheless, we can observe that the fluid near the interface is advected upwards by Marangoni forces, and that both the fluid advected by the wall and the fluid advected by Marangoni forces near the interface are flowing back to the reservoir inside the meniscus; a phenomenon named in [7] the Separating Streamline (SSL). Our numerical results are consistent with the experimental visualizations of [7]. In particular we can observe in both numerical and experimental

visualizations that as the capillary number increases, the SSL clearly approaches the shape of the interface and the upper recirculation region gets thinner and thinner, which could perhaps indicate a decrease of the significance of surface tension gradients for high capillary numbers.

2.7 Conclusion

We have introduced a numerical method for solving the governing equations of surfactant-driven flows in the case of both soluble and insoluble surfactant. Numerical examples in two and three spatial dimensions indicate that this approach can faithfully simulate the surface and bulk diffusion processes for the surfactant concentration. We then coupled these equations to a Navier-Stokes solver and showed that the method can enable the study of the effects of both soluble and insoluble surfactant on free surface flows. This methodology may be used to study the numerous interesting scientific questions, motivated by important industrial applications, that still have to be explored.

2.8 Acknowledgments

This research was supported by ONR N00014-11-1-0027 and ARO W911NF-16-1-0136.

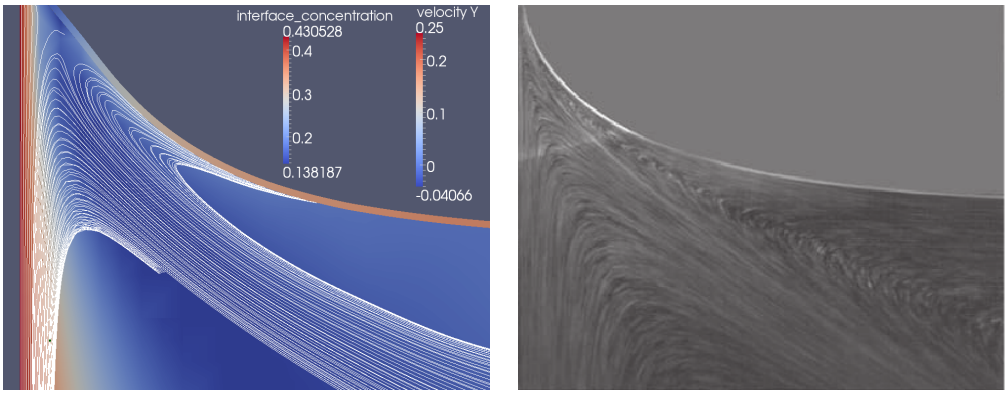

(a) (b)

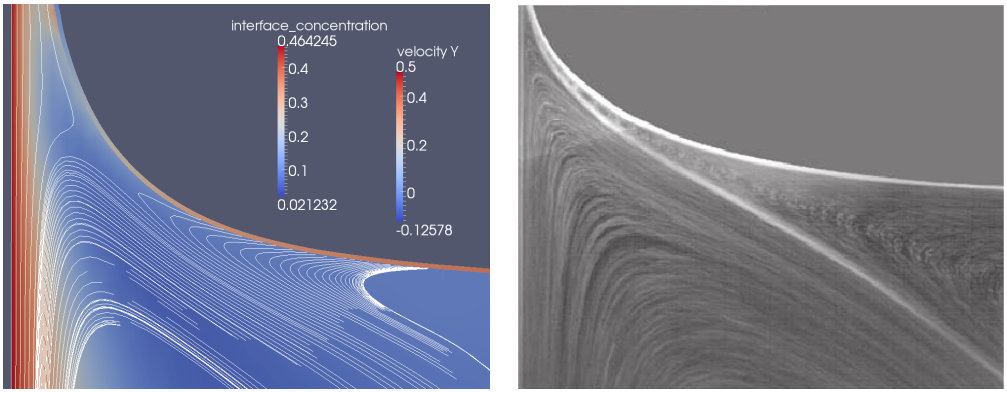

(c) (d)

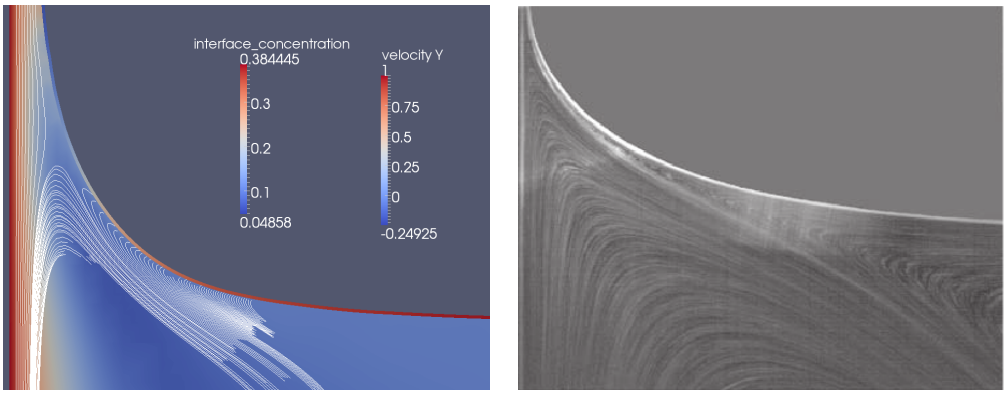

(e) (f)

Figure 2.28: Effect of increasing the capillary number on the shape of the streamlines in the context of dip coating. The first column presents the results of our simulations for different capillary numbers: (a) $Ca = 2.5 \times 10^{-2}$, (c) $Ca = 5 \times 10^{-2}$ and (e) $Ca = 10^{-1}$. The second column presents the visualizations obtained by Mayer and Krechetnikov in [7]: (b) $Ca = 5.9 \times 10^{-4}$, (d) $Ca = 1.2 \times 10^{-3}$ and (f) $Ca = 1.8 \times 10^{-3}$. The values of interface concentration and velocity displayed are normalized.

Chapter 3

A parallel numerical method for incompressible fluid flows

3.1 Abstract

We introduce an approach for solving the incompressible Navier-Stokes equations on a forest of Octree grids in a parallel environment. The methodology uses the `p4est` library of Burstedde *et al.*, *SIAM J. Sci. Comput.*, 33(3) (2011) [63] for the construction and the handling of forests of Octree meshes on massively parallel distributed machines and the framework of Mirzadeh *et al.*, *J. Comput. Phys.*, 322 (2016) [64] for the discretizations on Octree data structures. We introduce relevant additional parallel algorithms and provide performance analyses for individual building bricks and for the full solver. We demonstrate strong scaling for the solver up to 32,768 cores for a problem involving $\mathcal{O}\left(6.1 \cdot 10^8\right)$ computational cells. We illustrate the dynamic adaptive capabilities of our approach by simulating flows past a stationary sphere, flows due to an oscillatory sphere in a closed box and transport of a passive scalar. Without sacrificing accuracy nor spatial resolution in regions of interest, our approach successfully reduces the number of computational cells to (at most) a few percents of uniform grids with equivalent resolution. We also perform a numerical simulation of the turbulent flow in a superhydrophobic

channel with unparalleled wall grid resolution in the streamwise and spanwise directions.

3.2 Introduction

In the last decade, the democratization of the access to supercomputers has prompted the development of massively parallel simulation techniques. The previously existing serial codes are progressively being adapted to exploit the hundreds of thousands of cores available through the main computing clusters. We propose a parallel implementation of the solver for the incompressible Navier-Stokes equations introduced in [65], based on the parallel level-set framework presented in [64]. Additional novel algorithms, necessary to solving the Navier-Stokes equations in a forest of Quad-/Oc-trees, are presented.

Numerical simulations at the continuum scale are generally divided into two categories characterized by their meshing techniques. On the one hand, the finite elements community relies on body-fitted unstructured meshes to represent irregular domains. Given a high quality mesh, the resulting solvers are fast and very accurate. This approach has been successfully applied to the simulation of incompressible viscous flows [66, 67, 68]. However, the mesh generation is very costly and impractical when tracking moving interfaces and fluid features requiring high spatial resolution. On the other hand, methods based on structured Cartesian grids render the mesh geometry mainly trivial, but lead to a higher complexity for the implicit representation of irregular interfaces. We focus here on the latter class of methods.

A common approach to represent an irregular interface in a implicit framework is to use Peskin's immersed boundary method [69, 70, 71] or its level-set counterpart [72]. However, these methods introduce a smoothing of the interface through a delta formulation and therefore restrict the accuracy of the solution with $O(1)$ errors near fluid-fluid interfaces[1]. We therefore opt for the sharp interface representation provided by the level-set function [73]. We use the finite-volume/cut-cell approach of Ng *et al.* [74] to impose the boundary condition at the solid-

[1]Although we do not consider fluid-fluid interfaces, the present work is intended as a stepping stone toward that case.

fluid interface for its demonstrated convergence in the L^∞-norm.

Fluid flows are by nature multiscale, thus limiting the scope of uniform Cartesian grids. A range of strategies have been proposed to leverage the spatial locality of the fluid information such as stretched grids [75, 76], nested grids [77, 78, 79, 80, 81], chimera grids [82, 83] or unstructured meshes [84, 85, 86, 87, 88]. Another approach is to use a Quadtree [89] (in two spatial dimensions) or Octree [90] (in three spatial dimensions) data structure to store the mesh information [91, 92]. Popinet applied this idea combined with a non-compact finite volume discretization on the Marker-And-Cell (MAC) configuration [93] to the simulation of incompressible fluid flows [94]. Losasso *et al.* also proposed a compact finite volume solver on Octree for inviscid free surface flows [95], while Min *et al.* presented a node-based second-order accurate viscous solver [96]. The present work is based on the approach presented in Guittet *et al.* [65], which solves the viscous Navier-Stokes equations implicitly on the MAC configuration using a Voronoi partition and where the advection part of the momentum equation is discretized along the characteristic curves with a Backward Differentiation Formula (BDF), semi-Lagrangian scheme [97, 98]. The projection step is solved with the second-order discretization of Losasso *et al.* [99] for the Poisson equation.

The extension of [65] to parallel architectures relies on the existence of an efficient parallel Quad-/Oc-tree structure. Possible ways to implement parallel tree structures include the replication of the entire grid on each process. This approach, however, is not feasible when the grid size exceeds the memory of a single compute node, which must be considered a common scenario nowadays. Using graph partitioners such as `parMETIS` [100] on a tree structure would discard the mathematical relations between neighbor and child elements that are implicit in the tree, and thus result in additional overhead. Another option, which we find preferable, is to exploit the tree's logical structure using space-filling curves [101]. This approach has been shown to lead to load balanced configurations with good information locality for a selection of space-filling curves including the Morton (or Z-ordering) curve and the Hilbert curve [102].

Space-filling curves have been used in several ways, for example augmented by hashing

[103], tailored to PDE solvers [104], or focusing on optimized traversals [105]. `Octor` [106] and `Dendro` [107] are two examples of parallel Octree libraries making use of this strategy that have been scaled to 62,000 [108] and 32,000 [109] cores, operating on parent-child pointers and a linearized octant storage, respectively. Extending the linearized storage strategy to a forest of interconnected Octrees [110, 111], the `p4est` library [63] provides a publicly available implementation of the parallel algorithms required to handle the parallel mesh, including an efficient 2:1 balancing algorithm [112]. `p4est` has been shown to scale up to over 458,000 cores [113], with applications using it successfully on 1.57M cores [114] and 3.14M cores [115].

The algorithms pertaining to the second-order accurate level-set method on Quad-/Oc-tree presented in Min and Gibou [116] have been extended in Mirzadeh *et al.* [64] parallel architecture by leveraging the `p4est` library. Starting from this existing basis for the level-set function procedures, we present the implementation of the algorithms pertaining to the simulation of incompressible fluid flows detailed in [65]. The Voronoi tessellation that we construct over the adaptive tree mesh requires (at least) two layers of ghost cells, whose efficient parallel construction we describe in detail. We report on the scalability of the algorithms presented before illustrating the full capabilities of the resulting solver.

3.3 The computational method

In this section, we present mathematical and computational components pertaining to our numerical method for solving the incompressible Navier-Stokes equations on a forest of Octree grids. The first five subsections are mainly dedicated to the mathematical description of the discretization procedures (the interested reader may find more details in [65]). The implementation of these building bricks in a distributed computing framework reveals two grid-related requirements: access to second-degree (or third-degree) cell neighbors and unambiguous indexing of grid faces. The last two subsections present the computational strategies developed to address challenges related to these requirements. Throughout this section, schematics and illustrations are presented in two dimensions for the sake of clarity. Their extension to three

dimensions follows the exact same principles without any loss of generality.

3.3.1 Representation of the spatial information

The level-set method

A central desired feature of the proposed solver is to be able to handle complex, possibly moving interfaces in a sharp fashion[2]. The level-set framework, first introduced by [73] and extended to Quad-/Oc-trees in [116] is a highly suited tool for such a goal. The level-set representation of an arbitrary contour Γ, separating a domain Ω into two subdomains Ω^- and Ω^+, is achieved by defining a function ϕ, called the level-set function, such that $\Gamma = \{\boldsymbol{x} \in \mathbb{R}^n | \phi(\boldsymbol{x}) = 0\}$, $\Omega^- = \{\boldsymbol{x} \in \mathbb{R}^n | \phi(\boldsymbol{x}) < 0\}$ and $\Omega^+ = \{\boldsymbol{x} \in \mathbb{R}^n | \phi(\boldsymbol{x}) > 0\}$.

Among all the possible candidates that satisfy these criteria, a signed distance function (i.e., $|\nabla\phi| = 1$) is the most convenient one. In order to transform any function $\varphi(\boldsymbol{x})$ into a signed distance function $\phi(\boldsymbol{x})$ that shares the same zero contour, one can solve the reinitialization problem

$$\frac{\partial \phi}{\partial \tau} + \text{sign}(\varphi)\left(|\nabla\phi| - 1\right) = 0, \quad \phi(\boldsymbol{x})|_{\tau=0} = \varphi(\boldsymbol{x})$$

until a steady state in the fictitious time τ is found. The finite difference discretization and its corresponding parallel implementation employed to solve this equation are presented respectively in [116] and [64].

Forests of Quad-/Oc-trees and the `p4est` library

When dealing with physical problems that exhibit a wide range of length scales, uniform Cartesian meshes become impractical since capturing the smallest length scales requires a very high resolution. This is the case for high Reynolds number flows, for which the boundary layers and any wake vortices have a length scale significantly smaller than that of the far-field flow. This observation naturally leads to the use of adaptive Cartesian grids, including Octrees grids.

[2] We consider irregular solid objects in this work; multiphase interfaces are left for future work [117].

The `p4est` library [63] is a collection of parallel algorithms that handles a linearized tree data structure and its manipulation methods, which were shown to collectively scale up to 458,752 cores [113], as noted in the previous section. In `p4est` the domain is first divided by a coarse grid, which we will refer to as the "macromesh", common to all the processes. For our purpose we will consider solely uniform Cartesian macromeshes in a brick layout, although a general macromesh is not limited to such a configuration in `p4est`. This layout can be constructed at no cost using predefined and self-contained functions. A collection of trees rooted in each cell of the macromesh is then constructed and partitioned, and their associated (expanded) ghost layers are generated. The refinement and coarsening criteria necessary for the construction of the trees are provided to `p4est` by defining callback functions. We propose to use four criteria based on the physical characteristics at hand. Different combinations of these criteria are used depending on the specific problem considered.

The first criterion, presented in [116] and [64], captures the location of the interface: coarse cells are allowed locally, provided they are (at least) K cell diagonal(s) away from the interface, where $K \geq 1$ is defined by the user. Specifically, a cell $\mathcal{C}$ is marked for refinement if

$$\min_{v \in V(\mathcal{C})} |\phi(v)| \leq K \operatorname{Lip}(\phi) \operatorname{diag}(\mathcal{C}), \tag{3.1}$$

where $V(\mathcal{C})$ is the set of all the vertices of cell $\mathcal{C}$, $\operatorname{Lip}(\phi)$ is the Lipschitz constant of the level-set function ϕ, and $\operatorname{diag}(\mathcal{C})$ is the length of the diagonal of cell $\mathcal{C}$. Similarly, a cell is marked for coarsening if

$$\min_{v \in V(\mathcal{C})} |\phi(v)| > 2K \operatorname{Lip}(\phi) \operatorname{diag}(\mathcal{C}).$$

The second criterion, introduced for Quad-/Oc-trees in [94] and used in [96] and [65], is based on the vorticity of the fluid. High vorticity corresponds to small length scales and therefore necessitates a high mesh resolution. We mark a cell $\mathcal{C}$ for refinement if

$$h_{\max} \frac{\max_{v \in V(\mathcal{C})} \|\nabla \times \boldsymbol{u}(v)\|_2}{\max_{\Omega} \|\boldsymbol{u}\|_2} \geq \gamma, \tag{3.2}$$

where $h_{\max}$ is the largest edge length of cell $\mathcal{C}$ and γ is a parameter controlling the level of refinement. Analogously, a cell $\mathcal{C}$ is marked for coarsening if

$$2\, h_{\max} \frac{\max_{v \in V(\mathcal{C})} \|\nabla \times \boldsymbol{u}(v)\|_2}{\max_{\Omega} \|\boldsymbol{u}\|_2} < \gamma.$$

Another criterion enforces a band of b grid cells of highest desired resolution around the irregular interface. We mark for refinement every cell such that

$$\min_{v \in V(\mathcal{C})} \operatorname{dist}(v, \Gamma) < b \, \max\left(\Delta x_{\text{finest}}, \Delta y_{\text{finest}}, \Delta z_{\text{finest}}\right),$$

where Δx_{finest}, Δy_{finest} and Δz_{finest} are the cell sizes along cartesian directions for the finest cells to be found in the domain.

Finally, the solver was augmented with the optional capability of advecting a passive scalar for visualization purposes (this is illustrated in section 3.5.4). For enhanced graphical results, we propose to refine the mesh where the density of the marker exceeds a threshold. Given a density $\beta \in [0, 1]$ for the advected passive scalar, a cell $\mathcal{C}$ is marked for refinement (resp. coarsening) if

$$\max_{v \in V(\mathcal{C})} \beta(v) \geq \chi, \qquad (\text{resp. } \max_{v \in V(\mathcal{C})} \beta(v) < \chi), \tag{3.3}$$

where χ is a parameter controlling the level of refinement.

The Marker-And-Cell layout

The standard data layout used to simulate incompressible viscous flows on uniform grids is the Marker-And-Cell (MAC)[93] layout. The analogous layout for Quadtrees is presented in figure 3.1 and leads to complications in the discretizations compared to uniform grids. However, second order accuracy is achievable for the elliptic and advection-diffusion problems that appear in our discretization of the Navier-Stokes equations. Two possible corresponding discretizations are presented for the data located at the center of the cells (the leaves of the trees) and at their

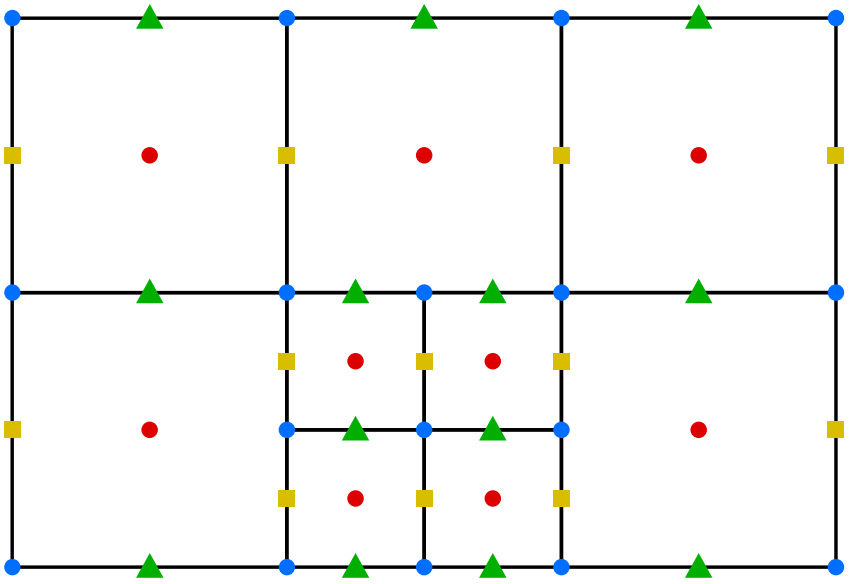

Figure 3.1: Representation of the Marker-And-Cell (MAC) data layout on a Quadtree structure with the location of the x-velocity (■), the y-velocity (▲), the Hodge variable (●) and the level-set values (●).

faces in sections 3.3.4 and 3.3.3 respectively.

3.3.2 The projection method

Consider the incompressible Navier-Stokes equations for a fluid with velocity $\boldsymbol{u}$, pressure p, density ρ and dynamic viscosity μ, with a force per unit mass $\boldsymbol{f}$

$$\rho\left(\frac{\partial^+ \boldsymbol{u}}{\partial t^+}\boldsymbol{u}\cdot\nabla\boldsymbol{u}\right) = -\nabla p + \rho\boldsymbol{f} + \mu\nabla^2\boldsymbol{u}, \tag{3.4}$$

$$\nabla\cdot\boldsymbol{u} = 0. \tag{3.5}$$

The standard approach to solve this system is the projection method introduced by Chorin [118]. We refer the reader to [119] for a review of the variations of the projection method. The system is decomposed into two distinct steps, identified as the viscosity step and the projection

step. The first step consists in solving the momentum equation (3.4) without the pressure term,

$$\rho\left(\frac{\partial^{+}\boldsymbol{u}}{\partial t^{+}}\boldsymbol{u}\cdot\nabla\boldsymbol{u}\right)=\rho\boldsymbol{f}+\mu\nabla^{2}\boldsymbol{u}, \tag{3.6}$$

to find an intermediate velocity field $\boldsymbol{u}^{*}$. Since this field does not satisfy the incompressibility condition (3.5), it is then projected on the divergence-free subspace to obtain $\boldsymbol{u}^{n+1}$, the solution at time t^{n+1}, via

$$\boldsymbol{u}^{n+1}=\boldsymbol{u}^{*}-\nabla\Phi \tag{3.7}$$

where Φ is referred to as the Hodge variable and satisfies

$$\nabla^{2}\Phi=\nabla\cdot\boldsymbol{u}^{*}. \tag{3.8}$$

The two following sections describe the discretization applied to solve steps (3.6) and (3.8) respectively.

3.3.3 Implicit discretization of the viscosity step

The viscosity step (3.6) contains two distinct terms besides the possible bulk force: the advection term on the left-hand side and the viscous term on the right-hand side. In order to prevent stringent time step restrictions due to the latter, we opt for a second order backward differentiation method to advance (3.6) in time. This integration scheme can address stiff problems without theoretical stability-related constraints on the time step.

Discretization of the advection term with a semi-Lagrangian approach

We discretize the advection part of the viscosity step using a semi-Lagrangian approach [120, 97]. This method relies on the fact that the solution $\boldsymbol{u}(\boldsymbol{x},t)$ of the advection equation

$$\frac{\partial^{+}\boldsymbol{u}}{\partial t^{+}}\boldsymbol{u}\cdot\nabla\boldsymbol{u}=0 \tag{3.9}$$

is constant along the characteristics of the equation, i.e., along material trajectories $(\boldsymbol{x}(s), t(s))$ such that $\dfrac{\mathrm{d}t}{\mathrm{d}s} = 1$ and $\dfrac{\mathrm{d}\boldsymbol{x}}{\mathrm{d}s} = \boldsymbol{u}(\boldsymbol{x}, t)$. Using this parameterization, equation (3.9) is equivalent to

$$\frac{\mathrm{d}\boldsymbol{u}}{\mathrm{d}s} = 0,$$

which we integrate with respect to s using a second-order BDF [98].

Given the location $\boldsymbol{x}^*$ where the solution $\boldsymbol{u}^*$ is sought at time t_{n+1}, the local material trajectory passing through $\boldsymbol{x}^*$ at time t^{n+1} is traced back in time to find the points $\boldsymbol{x}_d^n$ and $\boldsymbol{x}_d^{n-1}$ through which it passed at times t^n and t^{n-1} respectively. The values $\boldsymbol{u}_d^n = \boldsymbol{u}(\boldsymbol{x}_d^n, t_n)$ and $\boldsymbol{u}_d^{n-1} = \boldsymbol{u}\left(\boldsymbol{x}_d^{n-1}, t_{n-1}\right)$ are then calculated using quadratic interpolation and the application of the second order BDF (note that $\Delta s = \Delta t$) leads to

$$\frac{\partial^+ \boldsymbol{u}}{\partial t^+}\boldsymbol{u} \cdot \nabla \boldsymbol{u} \approx \frac{\alpha}{\Delta t_n}\boldsymbol{u}^* + \left(\frac{\beta}{\Delta t_{n-1}} - \frac{\alpha}{\Delta t_n}\right)\boldsymbol{u}_d^n - \frac{\beta}{\Delta t_{n-1}}\boldsymbol{u}_d^{n-1},$$

where

$$\Delta t_n = t_{n+1} - t_n, \qquad \Delta t_{n-1} = t_n - t_{n-1}, \qquad \alpha = \frac{2\Delta t_n + \Delta t_{n-1}}{\Delta t_n + \Delta t_{n-1}} \qquad \text{and} \qquad \beta = -\frac{\Delta t_n}{\Delta t_n + \Delta t_{n-1}}.$$

We refer the reader to [65] for further details.

Discretization of face-centered Laplace operators

Since we consider constant-viscosity incompressible flows of Newtonian fluids, the velocity components are effectively decoupled in the viscous terms. This allows us to solve for the individual components of $\boldsymbol{u}^*$ separately when advancing (3.6). In that context, we require appropriate discretizations for the Laplace operators associated with degrees of freedom sampled at faces of similar orientations, i.e., at faces where similar velocity components are sampled. We obtain these discretized operators by applying a finite volume approach to Voronoi tessellations. We present a summary of the approach and refer the reader to [65] for further details.

Given a set of points in space, called seeds, we define the Voronoi cell of a seed as the region

of space that is closer to that seed than to any other seed. The union of all the Voronoi cells forms a tessellation of the domain, i.e., a non-overlapping gap-free tiling of the domain. By placing these seeds at the centers of faces of the computational mesh sharing the same cartesian orientation, one obtains a new computational grid for the corresponding velocity component that is sampled at those faces. Two-dimensional examples of Voronoi tessellation are presented in figure 3.2 for Quadtree grids.

Considering a diffusion equation for the unknown u with constant diffusion coefficient μ

$$\mu \nabla^2 u = r,$$

it is discretized on the Voronoi tessellation with a finite volume approach where the control volume for each degree of freedom i is its Voronoi cell $\mathcal{C}_i$. This leads to

$$\int_{\mathcal{C}_i} \mu \nabla^2 u = \int_{\partial \mathcal{C}_i} \mu \ \nabla u \cdot \boldsymbol{n} \approx \sum_{j \in \text{ngbd}(i)} \mu \ s_{ij} \frac{u_j - u_i}{d_{ij}},$$

where ngbd(i) is the set of neighbors for the degree of freedom i, $\boldsymbol{n}$ is the vector normal to $\partial \mathcal{C}_i$ (pointing outwards), d_{ij} is the length between degrees of freedom i and j, and s_{ij} is the area — or the length, in 2D— of the face between them, as illustrated in figure 3.2. This discretization provides a second-order accurate solution [121].

General discretization for the viscosity step

Combining the discretizations presented in the two previous sections, we obtain the general discretization formula. Considering the x-component of the velocity field u, for the ith face with normal $\boldsymbol{e}_x$ and associated Voronoi cell $\mathcal{C}_i$, we have

$$\text{Vol}(\mathcal{C}_i)\rho \frac{\alpha}{\Delta t_n} u_i^* + \mu \sum_{j \in \text{ngbd}(i)} s_{ij} \frac{u_i^* - u_j^*}{d_{ij}} = \text{Vol}(\mathcal{C}_i)\rho \left[\left(\frac{\alpha}{\Delta t_n} - \frac{\beta}{\Delta t_{n-1}} \right) u_{i,d}^n + \frac{\beta}{\Delta t_{n-1}} u_{i,d}^{n-1} + \boldsymbol{e}_x \cdot \boldsymbol{f}_i \right],$$

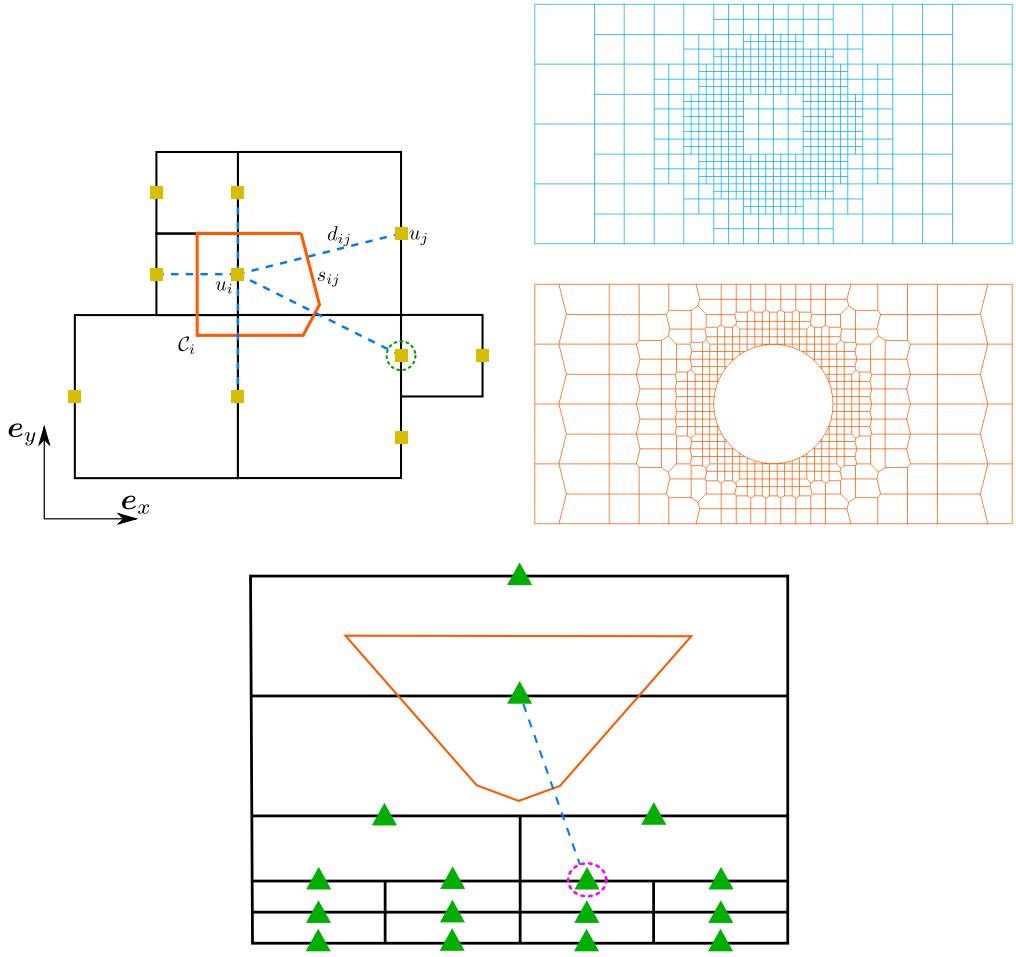

Figure 3.2: Top left: nomenclature for the discretization of the Laplace operator on a Voronoi diagram (illustrated for a vertical face). The degree of freedom circled in green can potentially belong to a second-degree neighbor cell, i.e., a cell that is not adjacent to the current cell but adjacent to one of the current cell's immediate neighbor. Top right: example of a Quadtree mesh (top) and its Voronoi tessellation for the vertical faces (bottom). Bottom: illustration of a two-dimensional Voronoi cell for a horizontal face which may require knowledge of a face associated with a third-degree neighbor cell, in case of stretched computational grids (aspect ratio much different from 1). The face circled in pink is indexed by a third-degree neighbor quadrant of the top quadrant indexing the center seed.

where $\mathrm{Vol}(\mathcal{C}_i)$ is the volume of $\mathcal{C}_i$. The very same approach is then used for the y- and z-components of the velocity, i.e., v and w.

This produces a symmetric positive definite linear system that we solve using the BiConjugate Gradient stabilized iterative solver and the successive over-relaxation preconditioner

provided by the PETSc library [122, 123, 124].

A note on the boundary conditions The boundary conditions to consider when solving the viscosity step are to be imposed on $\boldsymbol{u}^*$. As a consequence, the type of boundary condition that is desired for $\boldsymbol{u}$ is used for $\boldsymbol{u}^*$ as well, but the enforced boundary value is corrected in order to take into account the correction from the projection step (3.7), given the current best estimate of $\nabla\Phi$.

3.3.4 A stable projection

The projection step consists in solving the Poisson equation (3.8) with the data located at the center of the leaves of the tree. Stability and accuracy constraints result in the discretization presented in [99]. The method relies on a finite volume approach with a leaf being the control volume for the degree of freedom located at its center. Using the notations defined in figure 3.3, we now explain the discretization of the flux of the Hodge variable Φ on the right face of $\mathcal{C}_2$. For the sake of clarity, we assume that all other neighbor cells of $\mathcal{C}_2$ in Cartesian directions are of the same size as $\mathcal{C}_2$; if not, the reasoning presented here below needs to be applied for all variables sampled on faces shared between cells of different sizes.

The first step is to define the weighted average distance Δ between Φ_0 and its neighboring small leaves on the left side,

$$\Delta = \sum_{i \in \mathcal{N}} \frac{s_i}{s_0} \delta_i,$$

where $\mathcal{N}$ is the set of leaves whose right neighbor leaf is $\mathcal{C}_0$. We then define the partial derivative of Φ with respect to x on the right face of $\mathcal{C}_2$ as

$$\frac{\partial^{=}\Phi}{\partial x^{=}} \sum_{i \in \mathcal{N}} \frac{s_i}{s_0} \frac{\Phi_0 - \Phi_i}{\Delta}.$$

This discretization collapses to the standard central finite difference discretization in case of (locally) uniform grids. The other components of $\nabla\Phi$ are defined analogously and stored at the

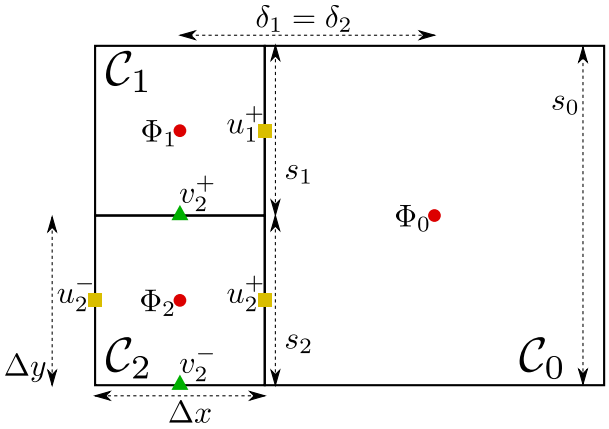

Figure 3.3: Nomenclature for the discretization of the flux of the Hodge variable at cell faces and the discretization of the divergence of the velocity field.

corresponding faces. We then define the divergence of $\boldsymbol{u}$ at the center of the leaf containing Φ_2 as

$$\nabla \cdot \boldsymbol{u} = \frac{1}{\Delta x}\left(\sum_{i \in \mathcal{N}} \frac{s_i}{s_0} u_i^+ - u_2^-\right) + \frac{1}{\Delta y}\left(v_2^+ - v_2^-\right).$$

Both the divergence and the gradient operators involve all small leaves having $\mathcal{C}_0$ as a right neighbor. The cell-centered Laplace operator in eq. (3.8) is obtained by chaining the above divergence and gradient operator, i.e., $\nabla^2\Phi = \nabla \cdot (\nabla\Phi)$. This produces a second-order accurate discretization for cell-centered Poisson equations. The correspondence between the two operators defined here above ensures that the gradient is the negative adjoint of the divergence in a well-defined face-weighted norm, ensuring the stability of the projection step [65]. The linear system resulting from this approach is symmetric positive definite, and it is solved using a (possibly preconditioned) conjugate gradient method.

3.3.5 Typical flowchart of the solver

As detailed in subsection 3.3.3, boundary conditions to be enforced on the intermediate velocity field $\boldsymbol{u}^*$ require the knowledge of $\nabla\Phi$. Yet, Φ itself is defined as the solution of an elliptic problem that requires $\nabla \cdot \boldsymbol{u}^*$ (see (3.8)).

In order to best enforce the desired boundary conditions on $\boldsymbol{u}$, the solver addresses this

circular dependency between $\boldsymbol{u}^*$ and $\nabla\Phi$ through a fixed-point iteration. The solver determines a sequence $\boldsymbol{u}^{*,k}$ and Φ^k, with $k \geq 1$: the intermediate velocity field $\boldsymbol{u}^{*,k}$ is the solution of the viscosity step (3.6) with boundary condition values defined using the known field Φ^{k-1} (see subsection 3.3.3 - note that Φ^0 is defined as the scalar field Φ obtained at the end of the previous time step, or as 0 for the very first time step). The scalar field Φ^k is determined in turn as the solution of the projection equation (3.8) using $\nabla\cdot\boldsymbol{u}^{*,k}$ as the right-hand side. Figure 3.4 illustrates this iterative procedure.

This process is repeated for increasing k until convergence is reached or until a user-defined maximum number of iterations $k_{\max}$ is reached. Note that the standard, approximate projection method corresponds to $k_{\max} = 1$ (the computational cost and the relevance of additional inner-loop iterations are estimated and discussed for some relevant applications within section 3.5). Two different convergence criteria may be used: the user may choose to enforce

- either $\left\|\Phi^k - \Phi^{k-1}\right\|_\infty < \varepsilon_\Phi$, where ε_Φ is a user-defined threshold (most relevant if the pressure is a primary variable of interest and is well-defined everywhere);
- or $\left\|\dfrac{\partial\Phi^k}{\partial\zeta} - \dfrac{\partial\Phi^{k-1}}{\partial\zeta}\right\|_\infty < \varepsilon_{\nabla\Phi}$, where $\varepsilon_{\nabla\Phi}$ is a user-defined threshold and ζ is any (or all) of x, y, z (most relevant to ensure strict wall and/or interface no-slip boundary boundary conditions).

The structure and internal logic of the solver is designed so as to minimize the cost of such extra iterations when $1 < k \leq k_{\max}$: relevant computation-intensive data pertaining to the construction of the discretized linear systems is kept in memory (to avoid re-computing), as well as discretization matrices, possible preconditioners, etc.

3.3.6 Expansion of the ghost layer

Several building bricks of the solver require second-degree (or even third-degree) neighbor cells to ensure robust behavior and properly defined operators. For instance, the construction

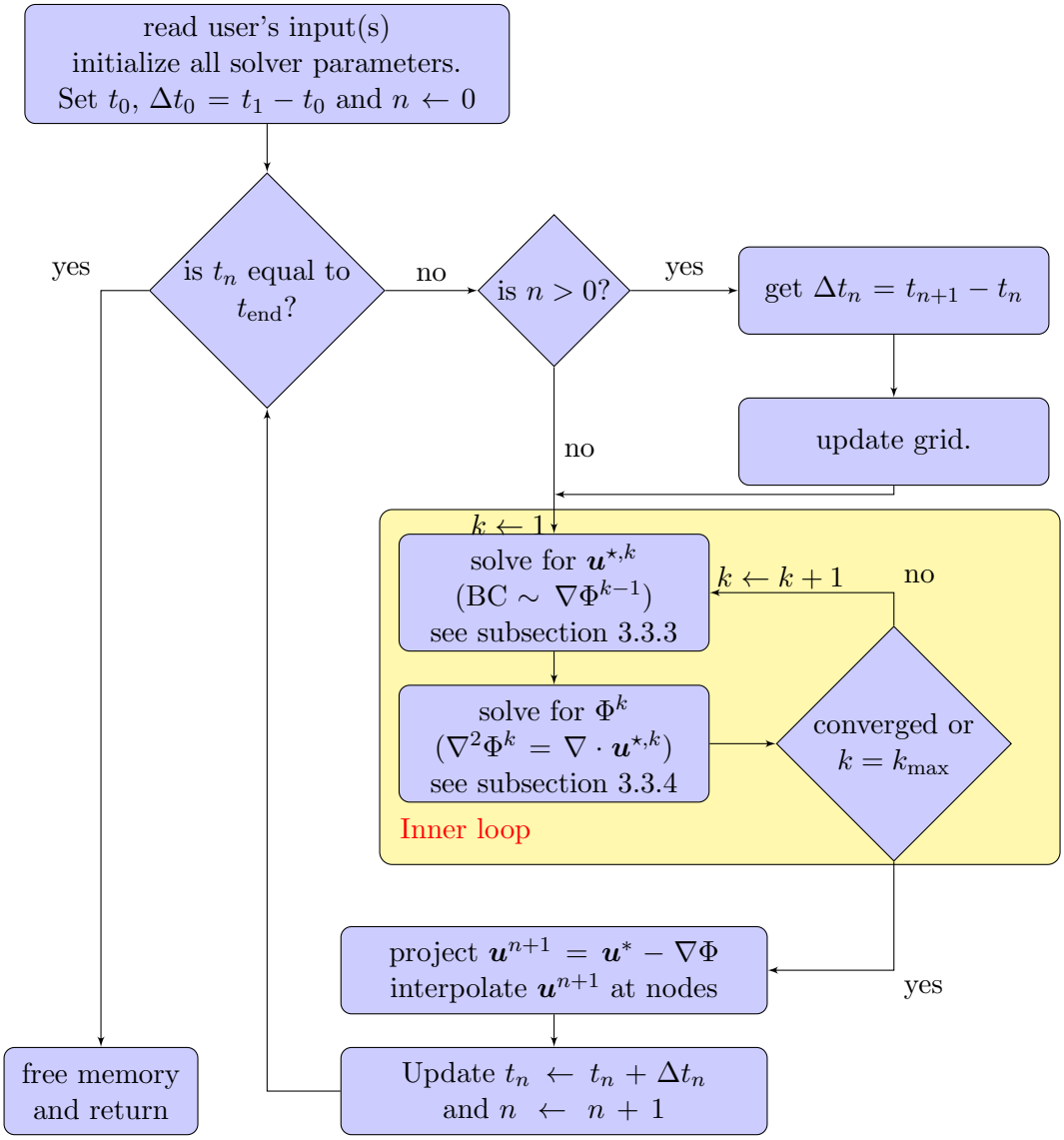

Figure 3.4: Typical flow chart for the presented incompressible Navier-Stokes solver.

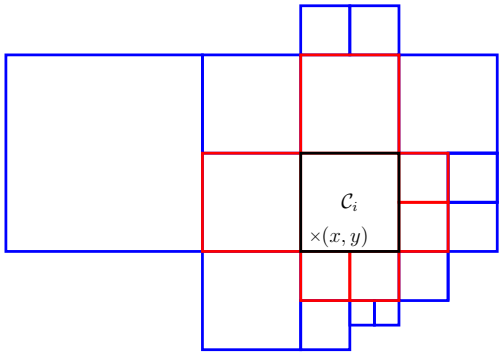

Figure 3.5: The stencil used to interpolate the velocity at (x, y) in cell $\mathcal{C}_i$ does not only require the data in $\text{ngbd}(\mathcal{C}_i)$ (red), but also in $\text{ngbd}^2(\mathcal{C}_i)$ (blue), a set of cells including second-degree (indirect) neighbors.

of Voronoi cells based on face-collocated seeds requires to connect neighboring face-sampled degrees of freedom. As illustrated in figure 3.2, such neighboring seeds may lie on a face that is shared between a (large) first-degree neighbor cell and a (small) second-degree neighbor cell. In such a case, only the (small) second-degree neighbor cell indexes the queried face. Therefore, second-degree neighbors need to be accessible from every locally owned face degree of freedom. Besides, when using stretched grids, more remote neighbors may be involved in the construction of a local Voronoi cell (see figure 3.2). Similarly, the cell-centered operators defined in section 3.3.4 require second-degree neighbors in case of non-graded grids. As depicted in figure 3.5, the ability to access second-degree neighbor cells is also desirable regarding the accuracy and the inter-processor smoothness of the moving least-square interpolation procedure used to define the node-sampled velocity fields based on the face-sampled components [65]. The ability to construct deep ghost layers is a recent extension to the `p4est` interface, which we briefly describe here.

The algorithm used by `p4est` to construct a single layer of ghosts ([63, Algorithm 19]) is able to maximize the overlap of computation and communication because each process can determine for itself which other processes are adjacent to it. This is because the "shape" of each process's subdomain (determined by the interval of the space-filling curve assigned to it) is known to every other process. As a consequence, the communication pattern is symmetric and no sender-receiver handshake is required.

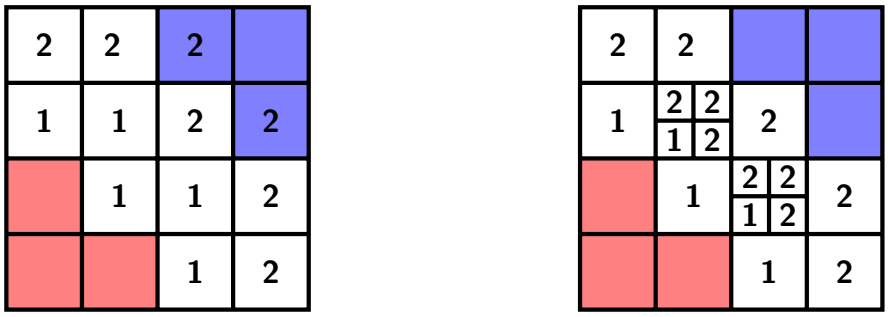

Figure 3.6: Two meshes with the same partition shapes, but with different two-deep ghost layers. For each mesh we show the first and second layers of the ghost layer of process p (red). In the first mesh, the second layer includes cells from process q (blue), but in the second it does not.

As a first extension, when creating the send buffers we remember their entries, since they identify the subset of local cells that are ghosts to one or more remote processes. We store these pre-image cells or "mirrors" in ascending order with respect to the space filling curve, and create one separate index list per remote processor into this array. This data is accommodated inside the ghost layer data structure and proves useful for many purposes, the most common being the local processor needing to iterate through the pre-image to define and fill send buffers with application-dependent numerical data.

The communication pattern of a deeper ghost layer, on the other hand, depends not just on the shapes of the subdomains, but the leaves within them, as illustrated in figure 3.6. Rather than complicating the existing ghost layer construction algorithm to accommodate deep ghost layers, a function that adds an additional layer to an existing ghost layer has been added to `p4est`. This function is called `p4est_ghost_expand`() and adds to both the ghosts and the pre-images. Thus, as a second extension to the data structure, we also identify those local leaves that are on the inward-facing front of each preimage, in other words the most recently added mirrors. This is illustrated in figure 3.7.

When process p expands its portion of process q, it loops over the leaves in the front of the pre-image for process q and adds any neighbors that are not already in the ghost layer. Sometimes this will include a leaf from a third process r: process p will also send such leaves

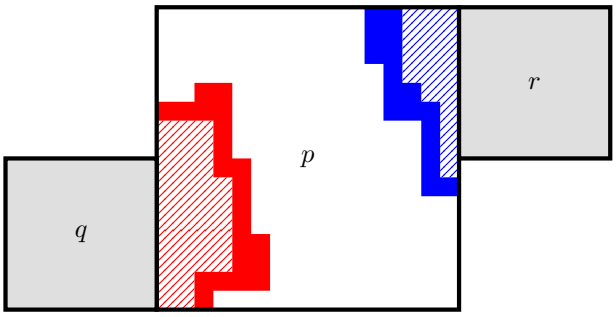

Figure 3.7: We show the preimages of process q's and process r's ghost layers in the leaves of process p. The solid red area represent the cells at the "front" of the preimage for q (`preimage_front`$[q]$ in algorithm 1), while the solid and dashed together form the whole preimage (`preimage`$[q]$).

to process q, because it may be that r is not yet represented in q's ghost layer, and so communication between q and r is not yet expected. The basic structure of this algorithm is outlined in algorithm 1.

3.3.7 Indexing the faces

Although the `p4est` library provides a global numbering for the faces of the leaves, its numbering differs from our needs because it does not number the small faces on a coarse-fine interface, where we have degrees of freedom in our MAC scheme. Therefore, we implement a procedure to distribute the faces of the leaves across the processes and to generate a unique global index for each face. Since some faces are shared between two processes, we chose to attribute a shared face to the process with the smaller index. With this rule, each face belongs to a unique process and after broadcasting the local number of faces a global index can be generated for all the local faces. The second step is to update the remote index of the faces located in the ghost layer so that their global index can be constructed easily by simply adding the offset of the process each face belongs to. We do so in two steps, represented in figure 3.8. First, the indices of the ghost faces of the local leaves are synchronized, then the indices of the faces of the ghost layer of leaves are updated. This has some similarities to the two-pass node numbering from [125], here extended to two layers of ghosts. Algorithm 2 details the steps

```
1: for q ∈ ghost_neighbors do                          ▷ processes that contribute to ghost layer
2:     initialize empty sets send_forward[q], send_back[q], and new_front[q]
3: end for
4: for q ∈ ghost_neighbors do
5:     for l ∈ preimage_front[q] do
6:         for each neighbor n of l in local_leaves do                    ▷ n found by search
7:             if n ∉ preimage[q] then
8:                 add n to send_forward[q], preimage[q], and new_front[q]
9:             end if
10:        end for
11:        for each neighbor n of l in ghost_layer do                     ▷ n found by search
12:            if n belongs to process r ≠ q then
13:                add n to send_forward[q] and (n, q) to send_back[r]
14:            end if
15:        end for
16:    end for
17:    replace preimage_front[q] with new_front[q]
18: end for
19: for q ∈ ghost_neighbors do
20:    send send_forward[q] and send_back[q] and receive recv_forward[q] and recv_back[q]
21:    add all of recv_forward[q] to ghost_layer
22:    for (l, r) ∈ recv_back[q] do
23:        if r ∉ ghost_neighbors or l ∉ preimage[r] then
24:            add l to preimage[r] and preimage_front[r]                 ▷ new lists if
   r ∉ ghost_neighbors
25:        end if
26:    end for
27: end for
28: recompute ghost_neighbors from leaves in ghost_layer
```

Algorithm 1: Process p's algorithm for expanding other processes' ghost layers, and receiving expansions to its own ghost layer. Note that finding a neighbor of a leaf l entails a fixed number of binary searches through the `local_leaves`, which are sorted by the space-filling curve induced total ordering.

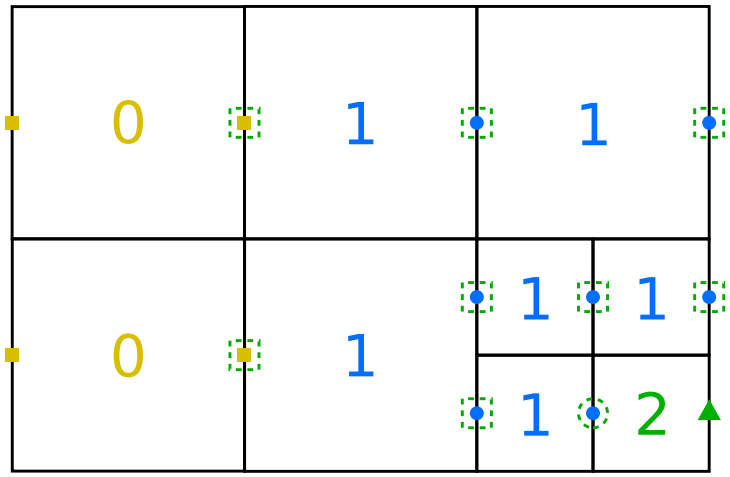

Figure 3.8: Illustration of the ghost layer of x-faces of depth 2 and of the global indexing procedure for process 2. The numbers in the leaves correspond to the indices of the processes owning them. After the first step, the remote index for the circled face is known to process 2, and after the second step the remote indices for the faces in a square are known to process 2. Note that a single step would not be sufficient for process 2 to gain knowledge of the remote index of the two faces belonging to process 0.

of our implementation and makes use of the `Notify` collective algorithm described in [112] to reverse the asymmetric communication pattern.

3.4 Scalability

In this section, we present an analysis of the scaling performance of our implementation. We define the parallel efficiency as $e = s\,(P_0/P)^\sigma$ where $s = t_0/t_p$ is the speed-up, σ is the optimal parallel scaling coefficient ($\sigma = 1$ for linear scaling), P_0 is the smallest considered number of processes with its associated runtime t_0 and P is the number of processes with its associated runtime t_p. All the results were obtained on the "Knights Landing" Intel Xeon Phi 7250 (KNL) compute nodes of the Stampede2 supercomputer at the Texas Advanced Computing Center (TACC), at The University of Texas at Austin, and on the Comet supercomputer at the San Diego Supercomputer Center, at the University of California at San Diego. Those resources are available through the Extreme Science and Engineering Discovery Environment (XSEDE)

```
1: for l ∈ (local|ghost) leaves do
2:     for f ∈ remote_faces(l) do
3:         add proc(f) to receivers
4:         add f to buffer[proc(f)]
5:     end for
6: end for
7: Notify(receivers,senders)                          ▷ reverse communication pattern
8: for p ∈ receivers do                                                  ▷ send requests
9:     MPI_Isend(buffer[p])                              ▷ send request to process p
10: end for
11: for p ∈ senders do                                          ▷ process remote requests
12:     MPI_Recv(req)                                  ▷ receive request from process p
13:     assemble answer with local indices requested
14:     MPI_Isend(ans)                                    ▷ send answer to process p
15: end for
16: for p ∈ receivers do                                                 ▷ process answers
17:     MPI_Recv(p)                                    ▷ receive answer from process p
18:     update faces information
19: end for
```

Algorithm 2: Communication algorithm to generate a global indexing of the faces. The `Notify` collective algorithm is used to reverse the communication pattern, described in more detail in [112].

[126]. The strong scaling performance was analyzed up to 32,768 cores on Stampede2.

3.4.1 Expansion of the ghost layer

We present both weak and strong scaling results for the algorithm used to expand the ghost layer of cells for each process in figure 3.9. The associated efficiency is presented in table 3.1. The strong scaling consists in choosing a problem and solving it with increasing number of processes. Ideally, for an algorithm with a workload increasing linearly with the problem size (i.e., with parallel scaling coefficient $\sigma = 1$), doubling the amount of resources spent on solving a problem should half the runtime. However, in the case of the ghost layer expansion, the amount of work depends on the size of the ghost layers, as explained in [113]. For a well behaved partition, we expect $O(N^{\frac{(d-1)}{d}})$ of the leaves to be in the ghost layer, where d is the number of spatial dimensions. We therefore consider a parallel scaling coefficient $\sigma = 2/3$ to be optimal for a three dimensional problem, i.e., $O((N/P)^{2/3})$ is the ideal scaling, with P the

number of processes and N the problem size. The results presented in figure 3.9 were obtained on Stampede2 for a mesh of level 9/13, corresponding to 588,548,472 leaves, and on Comet for a mesh of level 10/13, corresponding to 1,595,058,088 leaves. The computed parallel efficiency between the smallest and the largest run is 66% for Stampede2 and 59% for Comet.

The idea behind the weak scaling is to keep the problem size constant for each process while increasing the number of processes. The right graph of figure 3.9 presents the results obtained on Stampede2 for two problems of sizes 30,248 leaves per process and 473,768 leaves per process, and for a number of processes ranging from 27 to 4,096. The runtime increases by 16% between the smallest and the largest run for the small problem and by 6% for the large problem.

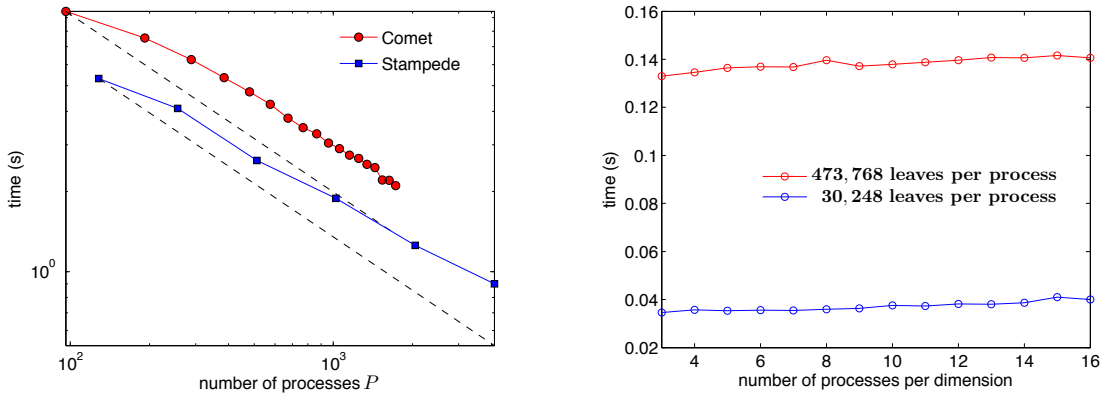

Figure 3.9: Scaling results for the expansion of the layer of ghost cells (see section 3.4.1). The strong scaling results are presented in the left figure together with the optimal reference scaling for a parallel scaling coefficient $\sigma = 2/3$ (dashed lines) while the weak scaling results are shown on the right figure. The increases in runtime observed for the weak scaling are of 16% for the small problem and 6% for the large problem.

3.4.2 Indexing the faces

The scaling procedure presented in the previous section is repeated for Algorithm 2 and the results are presented in figure 3.10. Even though the workload for this procedure increases slightly as the number of processes increases and the number of leaves in the ghost layers

Stampede2

Number of processes P	128	256	512	1024	2048	4096
Efficiency e	100%	79%	70%	69%	66%	66%

Comet

Number of processes P	96	192	384	672	1152	1728
Efficiency e	100%	82%	81%	71%	67%	59%

Table 3.1: Efficiency of the procedure for expanding the ghost layer of leaves.

increases, we compare our results to an ideal linear scaling $\sigma = 1$. The corresponding efficiency is computed in table 3.2. The parallel efficiency e computed between the smallest and the largest run from the strong scaling results is 44% for Stampede2 and 70% for Comet. The weak scaling results show an increase in runtime of 71% for the small problem and of 14% for the large problem.

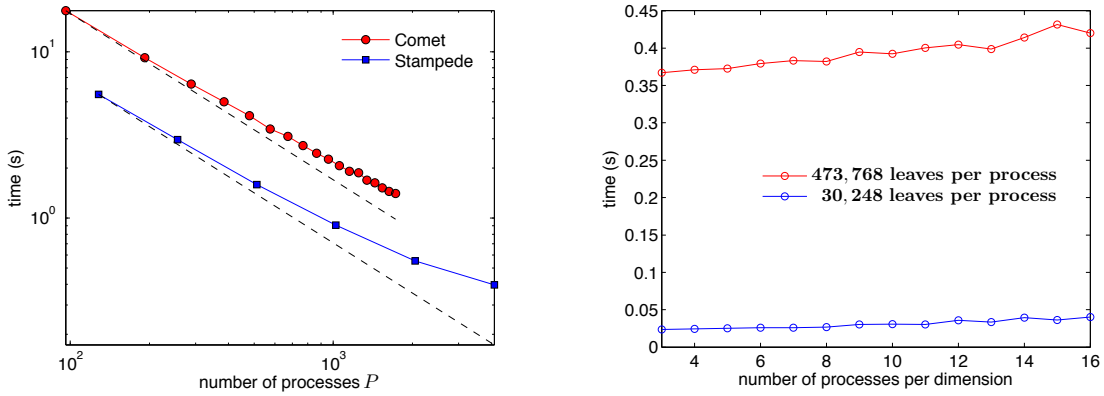

Figure 3.10: Scaling results for the indexing of the faces with Algorithm 2. The strong scaling results are presented in the left figure together with the reference ideal linear scaling (dash lines) while the weak scaling results are shown on the right figure. The strong scaling problem shown for Comet is three times larger than the one for Stampede2. The increases in runtime observed for the weak scaling are of 71% for the small problem and 14% for the large problem.

Stampede2

Number of processes P	128	256	512	1024	2048	4096
Efficiency e	100%	94%	87%	76%	63%	44%

Comet

Number of processes P	96	192	384	672	1152	1728
Efficiency e	100%	96%	88%	82%	77%	70%

Table 3.2: Efficiency of Algorithm 2 producing a global index for the faces.

3.4.3 Scalability of the full solver

We now analyze the scaling performance of the full incompressible Navier-Stokes solver, breaking its execution time down into its four main fundamental components: the viscosity step (see subsection 3.3.3), the projection step (see subsection 3.3.4), the moving least-square interpolation of the velocity components from cell faces to the grid nodes and the re-meshing step (denoted as grid update). We intend to show satisfactory strong scaling on large numbers of processors, so this scaling analysis was conducted on Stampede2 only since we do not have access to the same resources on other supercomputers.

For this purpose, the solver is restarted from a physically relevant and computationally challenging simulation state, defined as the inception of vortex shedding for the flow past a sphere at $Re = 500$, as illustrated in figure 3.11. A macromesh of size $8 \times 4 \times 4$ is used with two different refinement criteria. In the first case, the Octrees are refined with a minimum level 6 and a maximum level 11 with a vorticity threshold $\gamma = 0.02$ (see (3.2)), leading to a total of about $270 \cdot 10^6$ grid computational cells. In the second case, the Octrees are refined with a minimum level 7 and a maximum level 11 with a vorticity threshold $\gamma = 0.015$, leading to a total of about $610 \cdot 10^6$ grid cells. The grids for the initial states of the two scenarios are illustrated in figure 3.12. The three successive linear systems of the viscosity steps are solved using a BiConjugate Gradient Stabilized solver, while a Conjugate Gradient solver is used for the (symmetric positive definite) projection step.

In the first case, the wall-clock execution time is measured and averaged over 10 full time

steps, while only 5 time steps are considered for the second larger case (to limit the cost of these runs). A minimum of 64 (resp. 90) KNL nodes were required for the problem to fit in memory in the first (resp. second) case. Therefore, the first two data points in the left (resp. right) graph from figure 3.13 used less than 68 cores per node (maximum available). In either case, the solver performs two subiterations of the inner loop per time step (see figure 3.4): for each time step, $\left\|\Phi^k - \Phi^{k-1}\right\|_\infty$ drops by 4 orders of magnitude between $k = 1$ and $k = 2$.

The results are presented in figure 3.13 and table 3.3. As expected, the projection step is the most challenging part, thus determining the strong scalability limits of the solver: no significant speed-up is observed when the number of cells per process falls under $10,000$[3]. In comparison, the scaling behavior of the grid update procedure is not impeded yet around that limit, which shows the extremely good performance of all `p4est`'s grid management operations that are in play: grid refinement and/or grid coarsening, grid partitioning, ghost layer creation and ghost layer expansion.

Given that the global solver makes use of various separate routines having different (theoretical) ideal scaling coefficients σ, it is expected that the strong scaling performance of the solver is less than ideal. In fact, some of the operations at play cannot even be attributed such a theoretical scaling coefficients: when considering a very large number of processes, several of them will be associated with regions of the computational domain that are (very) far away from the interface and will end up stalling during the geometric extrapolation tasks of primary face- and cell-sampled fields, for instance. Though these extrapolations represent a small portion of the overall workload when using a small number of processes, they do contribute to less than ideal scaling on large numbers of processes in such an application. Therefore, regarding several aspects, this analysis may be considered a "worst case" scenario, which aims to produce insightful information when it comes to estimating a lower bound for the (effective) scaling coefficient σ to consider when estimating the computational cost of future large-scale simulations and/or when assessing the limits of accessible simulations for the solver. As illustrated in figure 3.13,

[3]This is consistent with PETSc scaling performance reported in their documentation.

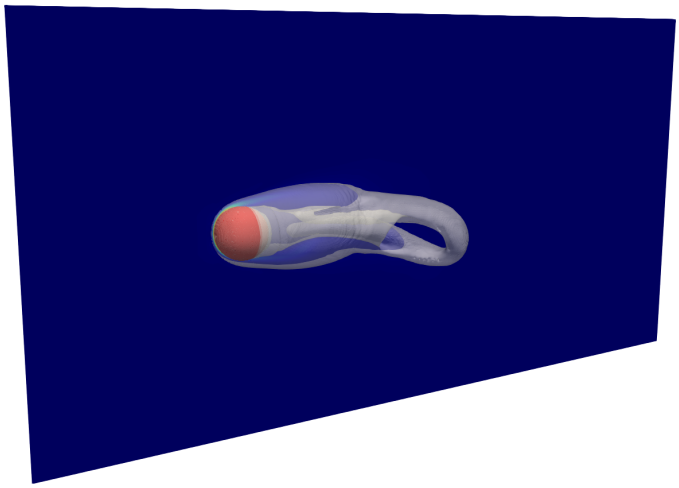

Figure 3.11: Physically relevant initial state considered for the scaling analysis on large number of cores. This figure illustrates the inception of vortex shedding for the flow past a sphere at $Re = 500$ (the full description of the computational set-up can be found in section 3.5.2). The vertical slice has equation $z = -0.5$ and it is colored by vorticity. The static sphere is colored in red and the translucent white surface represents the isocontour of vorticity $\|\nabla \times \boldsymbol{u}\| = 0.6\, u_0/r$.

the solver's scaling behavior seems to follow an asymptotic law of $\sigma \simeq 0.78$, in such a symptomatic case; Table 3.3 also indicates an efficiency above 80% (in the relevant range of P) when considering $\sigma \simeq 0.85$ (almost all calculated efficiencies are 100% or higher when considering $\sigma = 0.78$).

Stampede2 ($270 \cdot 10^6$ grid cells)

# of processes P	1,024	2,048	4,096	5,800	8,192	11,590	16,384	23,170	32,768
e ($\sigma = 1$)	100%	92.1%	77.9%	75.4%	65.9%	60.9%	56.9%	50.3%	39.6%
e ($\sigma = 0.85$)	100%	102.2%	95.8%	97.7%	90.0%	87.7%	86.2%	80.36%	66.6%

Stampede2 ($610 \cdot 10^6$ grid cells)

# of processes P	2,048	4,096	5,900	8,192	11,590	16,384	23,170	32,768
e ($\sigma = 1$)	100%	82.7 %	82.7 %	77 %	69.2 %	64.1 %	59.4 %	54.2 %
e ($\sigma = 0.85$)	100%	91.8 %	96.6 %	94.8 %	89.8 %	87.6 %	85.5 %	82.2 %

Table 3.3: Efficiencies e of the full solver proposed for the incompressible Navier-Stokes equations on Stampede2, when considering an ideal linear scaling (i.e., $\sigma = 1$) or a scaling coefficient of 85%.

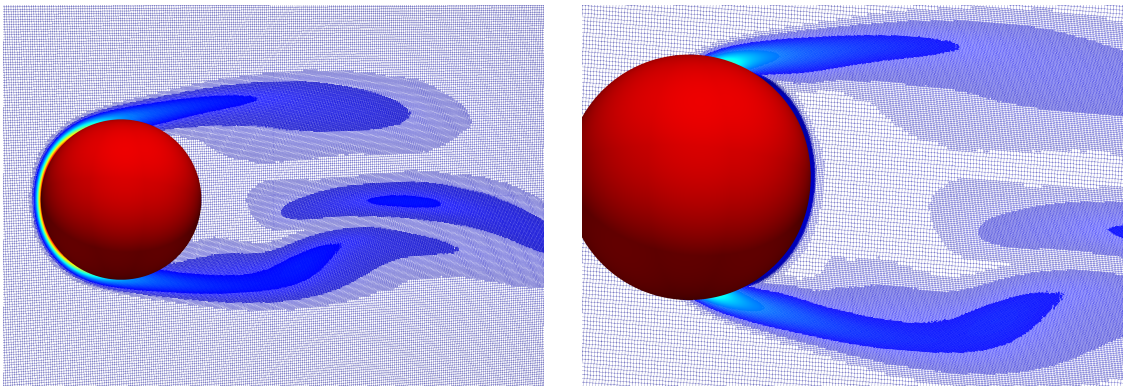

Figure 3.12: Grid illustrations for the scaling analyses from section 3.4.3. A grid slice in the computational domain is illustrated and its edges are colored by vorticity intensity. The Octrees are refined with a minimum level 7 and a maximum level 11 with a vorticity threshold $\gamma = 0.015$ (total of about $610 \cdot 10^6$ grid cells).

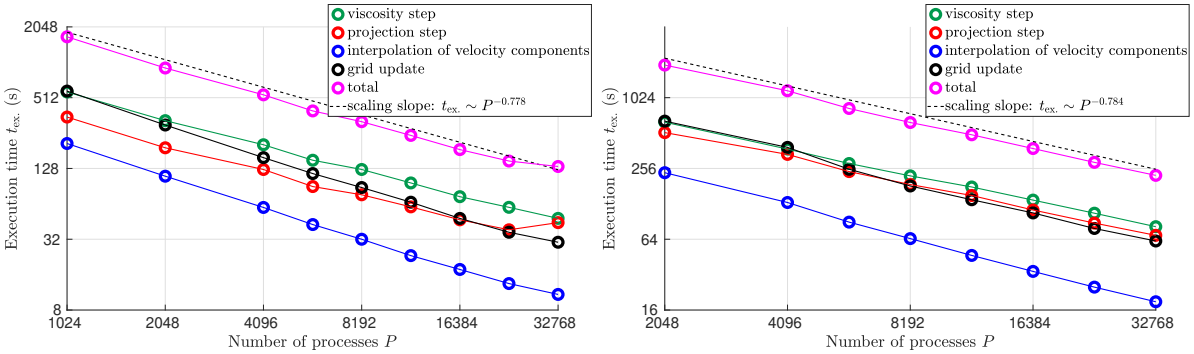

Figure 3.13: Scaling results on large number of cores on Stampede2 for the two grids considered. Left: scaling results for Octrees refined with a minimum level 6 and a maximum level 11 with a vorticity threshold $\gamma = 0.02$ (total of about $270 \cdot 10^6$ grid cells). Right: scaling results for Octrees refined with a minimum level 7 and a maximum level 11 with a vorticity threshold $\gamma = 0.015$ (total of about $610 \cdot 10^6$ grid cells).

3.5 Numerical validation and illustrations

In this section, we present a series of numerical examples to validate the implementation as well as to demonstrate the potential of the approach.

3.5.1 Validation with an analytical solution

The first application aims at validating the implementation by monitoring the convergence of the solver using the analytical solution presented in [74]. Consider the irregular domain $\Omega = \{(x, y, z)| - \cos(x)\cos(y)\cos(z) \geq 0.4 \text{ and } \frac{\pi}{2} \leq x, y, z \leq \frac{3\pi}{2}\}$ and the exact solution

$$\begin{aligned} u(x, y, z) &= \cos(x)\sin(y)\sin(z)\cos(t), \\ v(x, y, z) &= \sin(x)\cos(y)\sin(z)\cos(t), \\ w(x, y, z) &= -2\sin(x)\sin(y)\cos(z)\cos(t), \\ p(x, y, z) &= 0. \end{aligned}$$

The exact velocity is prescribed at the domain's boundary and homogeneous Neumann boundary conditions are enforced on the Hodge variable. The corresponding forcing term is applied to the viscosity step. We take a final time of $\frac{\pi}{3}$ and monitor the error on the velocity field and on the Hodge variable as the mesh resolution increases. The computational grid is not dynamically adapted for this accuracy analysis, so the grid-parameter γ (see (3.2)) is irrelevant in this case. The first computational grid is built to satisfy the distance-based criterion from section 3.3.1 using $\phi(x, y, z) = \cos(x)\cos(y)\cos(z) + .4$, $K = 1.2$ and $b = 5$. The successive resolutions are then obtained by splitting every cell from the previous resolution. The results are presented in table 3.4 and indicate first-order accuracy for the velocity field and second order accuracy for the Hodge variable in the L^∞ norm.

	u, v		w		Hodge variable	
level (min/max)	L^∞ error	order	L^∞ error	order	L^∞ error	order
4/6	$4.65 \cdot 10^{-3}$	-	$3.50 \cdot 10^{-3}$	-	$8.96 \cdot 10^{-4}$	-
5/7	$3.27 \cdot 10^{-3}$	0.50	$2.11 \cdot 10^{-3}$	0.73	$2.85 \cdot 10^{-4}$	1.65
6/8	$1.67 \cdot 10^{-3}$	0.97	$1.16 \cdot 10^{-3}$	0.86	$8.07 \cdot 10^{-5}$	1.82
7/9	$8.42 \cdot 10^{-4}$	0.99	$5.52 \cdot 10^{-4}$	1.07	$2.27 \cdot 10^{-5}$	1.83

Table 3.4: Convergence of the solver for the analytical solution presented in section 3.5.1. First-order accuracy is observed for the velocity field and second order accuracy for the Hodge variable.

3.5.2 Vortex shedding of a flow past a sphere

In order to further assess the performance of the solver, we also address the flow past a sphere. Related properties like drag and lift forces as well as vortex shedding frequency (if applicable) are calculated and compared to available data for this canonical problem.

We consider a static sphere of radius $r = 1$, located at $(8, 0, 0)$ in the domain $\Omega = [0, 32] \times [-8, 8] \times [-8, 8]$. An inflow velocity $\boldsymbol{u}_0 = u_0 \boldsymbol{e}_x$ is imposed on the $x = 0$ face of the domain as well as on the the side walls, homogeneous Neumann boundary conditions are imposed on the velocity field at the outlet $x = 32$ and no-slip conditions are imposed on the sphere. The pressure is set to zero at the outlet and is subject to homogeneous Neumann boundary conditions on the other walls as well as on the sphere. We set $u_0 = 1$, the density of the fluid to $\rho = 1$ and vary the viscosity μ to match the desired Reynolds number $Re = \dfrac{2\,\rho u_0 r}{\mu}$, set by the user. Eight Reynolds numbers ranging from 50 to 500 are considered.

The Octree mesh is refined around the sphere and according to the vorticity criterion (3.2) of section 3.3.1: we use $\phi(\boldsymbol{x}) = r - \sqrt{(x-8)^2 + y^2 + z^2}$, $K = 1.2$, $b = 16$, with a vorticity-based threshold of $\gamma = 0.01$. All the results were obtained with a macromesh $8 \times 4 \times 4$ and with trees of levels 4/7, leading to approximately 6 million leaves and corresponding to an equivalent uniform grid resolution of 268,435,456 cells. The time step Δt is set such that $\dfrac{\max_\Omega \|\boldsymbol{u}\|\,\Delta t}{\Delta x_{\min}} \leq 1$ at all times. Figure 3.14 shows a snapshot of the unsteady flow for $Re = 300$ at $t = 221\, r/u_0$.

The nondimensional force $\boldsymbol{F}$ applied onto the static sphere is monitored over time. The force is evaluated by geometric integration [127] of the stress vector (including viscous and

pressure contributions) on the surface of the sphere Γ, i.e.,

$$\boldsymbol{F} = \frac{1}{\frac{1}{2}\rho u_0^2 \pi r^2} \int_\Gamma \left(-p\underline{\underline{I}} + 2\mu\underline{\underline{D}}\right) \cdot \boldsymbol{n}\, \mathrm{d}\Gamma, \tag{3.10}$$

where $\underline{\underline{I}}$ is the identity tensor, $\underline{\underline{D}}$ is the symmetric strain-rate tensor and $\boldsymbol{n}$ is the outward normal to the sphere. Figure 3.16 shows the evolution of the streamwise force component. Figure 3.15 shows the evolution of the pressure and azimuthal vorticity on the sphere surface, at steady state for $Re = 100$. Figure 3.17 illustrates the transverse force components with respect to time for $Re \geq 250$. Time-averaged drag and lift coefficients C_D and C_L are then calculated as

$$C_D = \frac{1}{(t_{\text{end}} - t_{\text{start}})} \int_{t_{\text{start}}}^{t_{\text{end}}} \boldsymbol{F} \cdot \boldsymbol{e}_x \, \mathrm{d}t, \qquad C_L = \frac{1}{(t_{\text{end}} - t_{\text{start}})} \int_{t_{\text{start}}}^{t_{\text{end}}} \left((\boldsymbol{F} \cdot \boldsymbol{e}_y)^2 + (\boldsymbol{F} \cdot \boldsymbol{e}_z)^2\right)^{1/2} \mathrm{d}t, \tag{3.11}$$

where t_{start} is chosen to disregard the initial transient due to the chosen (uniform) initial condition and t_{end} is the final simulation time.

For $Re \geq 275 \pm 5$, the flow is unsteady and vortices shed from the static sphere [128, 129]. Similarly to [129], we evaluate the vortex shedding frequency f and the corresponding Strouhal number $St = \frac{2rf}{u_0}$ by calculating an averaged period between successive peak values in the transverse force components[4]. A main vortex shedding frequency cannot be reliably defined using this methodology for $Re = 500$: as it can be seen from figure 3.17, the time variations in the transverse force components do not reveal a well-defined periodic pattern for $Re = 500$. In fact, a Fourier decomposition of (pseudoperiodic portions of) the signals actually reveals a broad frequency spectrum with significant contributions up to $St \simeq 0.17$ in that case.

Our results are summarized and presented in tables 3.5 and 3.6 along with available data from various publications from the literature.

[4]Note that the analysis from [128] is different in that it is based on time variations of the pressure in the wake.

	$Re = 50$	$Re = 100$	$Re = 150$	$Re = 215$	$Re = 250$	
	C_D	C_D	C_D	C_D	C_D	C_L
Kim *et al.* [130]	-	1.09	-	-	0.70	0.059
Johnson *et al.* [131]	1.57	1.08	0.90	-	0.70	0.062
Constantinescu *et al.* [132]	-	-	-	-	0.70	0.062
Choi *et al.* [133]	-	1.09	-	-	0.70	0.052
Bagchi *et al.* [129]	1.57	1.09	-	-	0.70	-
Marella *et al.* [134]	1.56	1.06	0.85	0.70	-	-
Guittet *et al.* [65]	-	1.11	-	-	-	-
Present	1.61	1.11	0.91	0.76	0.72	0.062

Table 3.5: Drag coefficient (and lift coefficient, if relevant) for the steady flow past a sphere. The time averages were obtained with $t_{\text{start}} = 50\, r/u_0$ and $t_{\text{end}} = 200\, r/u_0$ for $Re \leq 215$ and with $t_{\text{start}} = 275\, r/u_0$ and $t_{\text{end}} = 400\, r/u_0$ for $Re = 250$ (see (3.11)).

	$Re = 300$			$Re = 350$		$Re = 500$
	C_D	C_L	St	C_D	St	C_D
Kim *et al.* [135]	0.657	0.067	0.134	-	-	-
Johnson *et al.* [131]	0.656	0.069	0.137	-	-	-
Constantinescu *et al.* [132]	0.655	0.065	0.136	-	-	-
Choi *et al.* [133]	0.658	0.068	0.134	-	-	-
Marella *et al.* [134]	0.621	-	0.133	-	-	-
Bagchi *et al.* [129]	-	-	-	0.62	0.135	0.555
Mittal *et al.* [128]	0.64	-	0.135	0.625	0.142	-
Guittet *et al.* [65]	0.659	-	0.137	0.627	0.141	-
Present	0.673	0.068	0.134	0.633	0.132±0.002	0.558

Table 3.6: Drag coefficients for the unsteady flow past a sphere. If relevant, the lift coefficient and the Strouhal number are presented as well. The time averages were obtained with $t_{\text{start}} = 200\, r/u_0$ and $t_{\text{end}} = 400\, r/u_0$ (see (3.11)).

For all the simulations from this section, we have used the inner-loop convergence criterion $\left\|\nabla\Phi^k - \nabla\Phi^{k-1}\right\| < 10^{-4}\, u_0$ (see section 3.3.5) in order to ensure a proper and accurate enforcement of the no-slip boundary condition on the surface of the sphere and to investigate the relevance of such a procedure in this specific case. Figure 3.18 shows relevant information pertaining to that analysis. As illustrated in that figure, the solver converges most of the time in two iterations and the correction brought by the second iteration is 3 to 4 orders of magnitude smaller than for the approximate projection step, in this case. Although the added computational cost is limited (around 30%), the accuracy of the results would most likely not have suffered from using an approximate projection in this context.

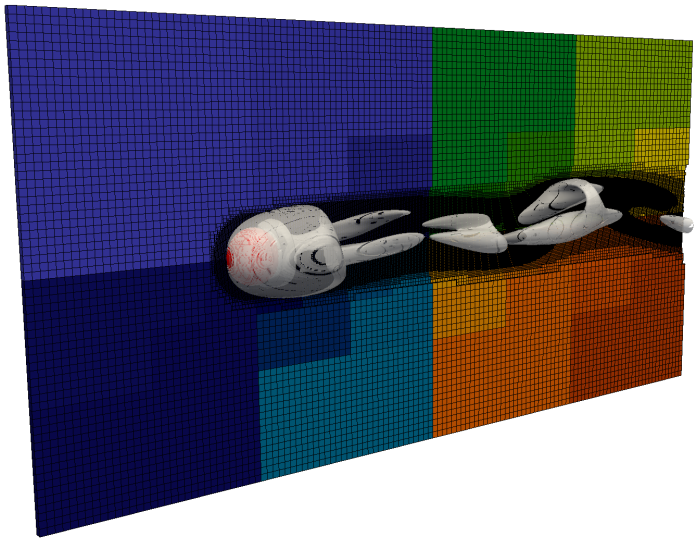

Figure 3.14: Visualization of the unsteady flow past a sphere for $Re = 300$. The trees are level 4/7 rooted in a $8 \times 4 \times 4$ macromesh, leading to approximately 6 million leaves. The snapshot is taken at time $t = 221\, r/u_0$. The colors correspond to the process ranks and the surface is an isocontour of the Q-criterion [136] for $Q = 0.006$. This simulation was run on the Stampede2 supercomputer with 1024 processes.

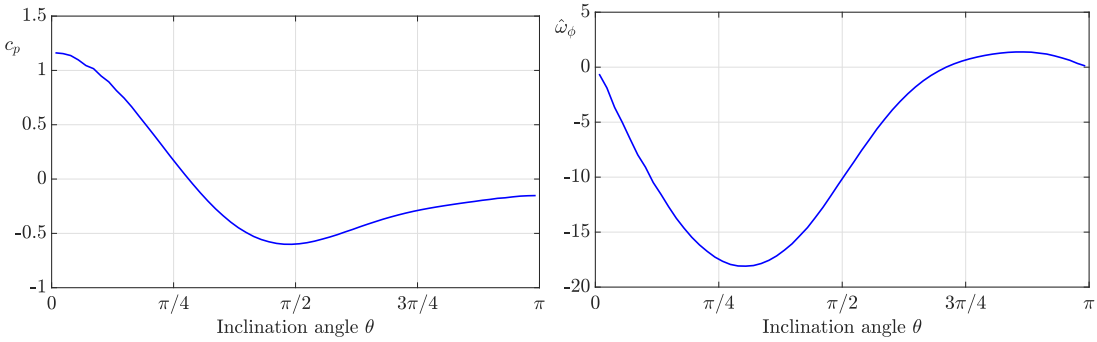

Figure 3.15: Evolution of relevant surface quantities on the surface of the static sphere for $Re = 100$, as a function of the inclination angle θ measured from the front point $(-r, 0, 0)$. Left: non-dimensional local pressure $c_p = p/\left(\frac{1}{2}\rho u_0^2\right)$ as a function of the inclination angle. Right: non-dimensional azimuthal vorticity $\hat{\omega}_\phi = \dfrac{-2r}{u_0}\boldsymbol{e}_\phi \cdot (\nabla \times \boldsymbol{u})$, where $\boldsymbol{e}_\phi = \boldsymbol{e}_r \times \boldsymbol{e}_\theta$, using spherical coordinates centered at the sphere's center along with the defintion of θ given here above. These results are in good agreement with [135].

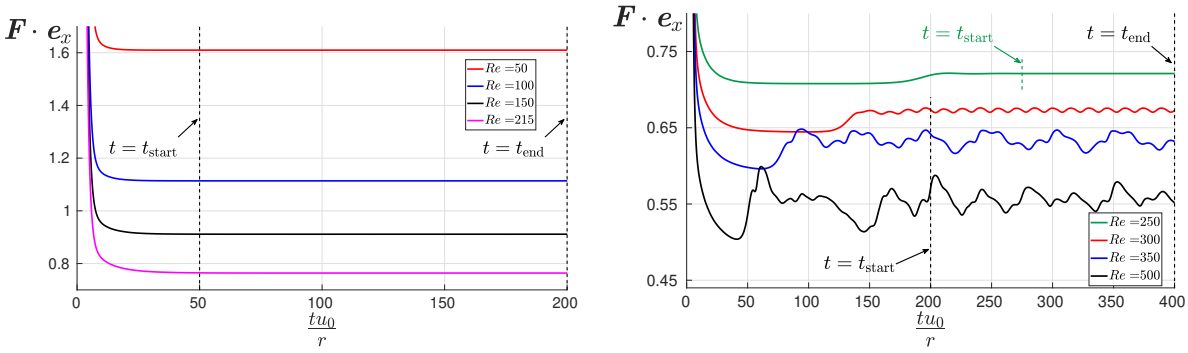

Figure 3.16: Drag coefficient on a sphere for axisymmetric steady flows (left) and for non-axisymmetric or unsteady flows (right), corresponding to Reynolds numbers ranging from 50 to 500.

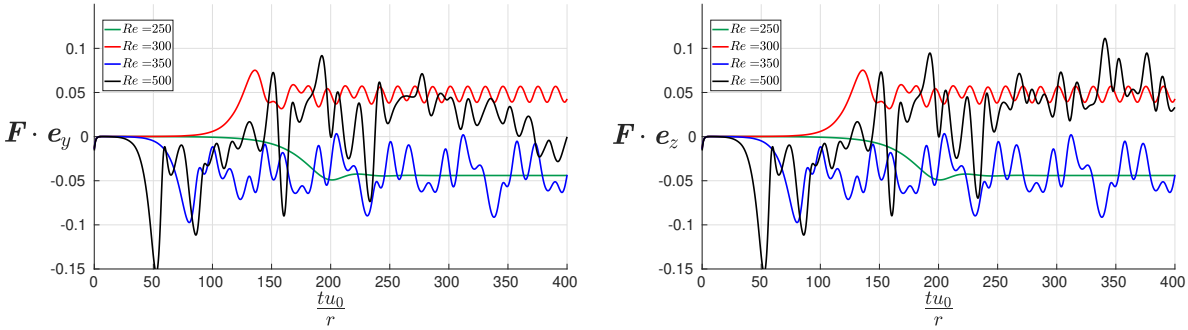

Figure 3.17: Nondimensional transverse force components for non-axisymmetric and/or unsteady flows.

3.5.3 Oscillating sphere in a viscous fluid

The solver presented in this article is able to handle moving geometries. We illustrate this capacity by computing the drag force developed by the flow of a viscous fluid due to the oscillatory motion of a rigid sphere in a closed box.

We consider a sphere of radius $r = 0.1$ in a domain $\Omega = [-1, 1]^3$. The kinematics of the center of the sphere $\boldsymbol{c}(t)$ is dictated by

$$\boldsymbol{c}(t) = -X_0 \cos(2\pi f_0 t)\, \boldsymbol{e}_x, \tag{3.12}$$

and we use the (time-varying) levelset function $\phi(\boldsymbol{x}, t) = r - \|\boldsymbol{x} - \boldsymbol{c}(t)\|$ with the corresponding

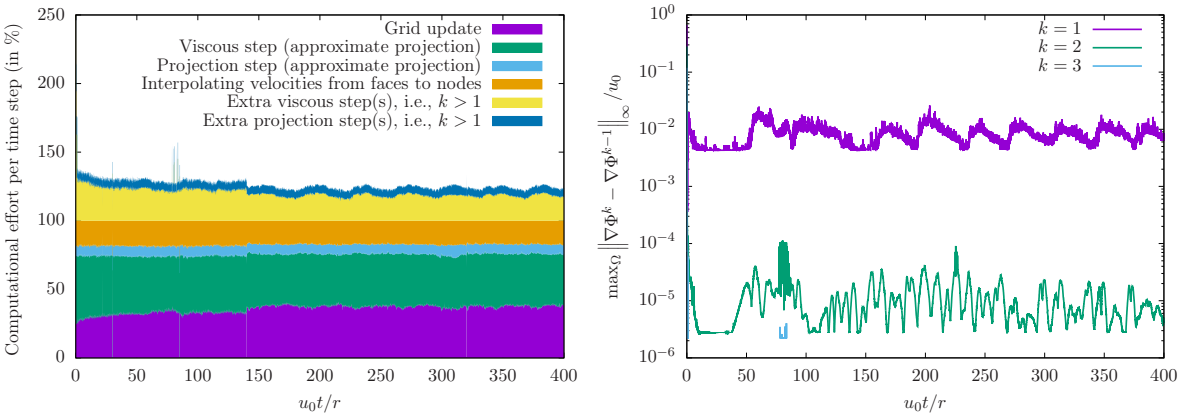

Figure 3.18: Illustration of the computational cost and convergence rate associated with the fixed point iteration from section 3.3.5, when ensuring a stringent user-defined control on $\boldsymbol{u}$ at all time steps, for the simulation of the flow past a sphere with $Re = 500$. Left: ratio(s) of the computational costs per time step for the main tasks at play, normalized to the raw computational cost of an approximate projection method (which would correspond to $k_{\max} = 1$). Right: measures of interest considered by the inner loop criterion (only a few time steps required 3 inner iterations hence the partial blue curve).

grid-construction parameters $K = 1.2$, $b = 4$ and $\gamma = 0.1$. The motion of the sphere is set to be purely translational (no rotation) so that its kinematics is fully described by (3.12). The dynamics of the surrounding fluid is dictated by no-slip boundary conditions enforced onto the surface of the oscillatory sphere, i.e.,

$$\boldsymbol{u}\left(\boldsymbol{x}, t\right) = 2\pi f_0 X_0 \sin\left(2\pi f_0 t\right) \boldsymbol{e}_x, \quad \forall \boldsymbol{x} \in \Omega : \left\| \boldsymbol{x} - \boldsymbol{c}\left(t\right) \right\| = r. \tag{3.13}$$

No-slip boundary conditions are also enforced on the (static) borders of the computational domain.

This setup naturally defines a characteristic velocity scale $u_0 = 2\pi f_0 X_0$, a characteristic frequency f_0 and a characteristic length scale r leading to two nondimensional numbers

$$\frac{r}{X_0} \quad \text{and} \quad Re = \frac{\rho\, 2\pi f_0 X_0\, 2r}{\mu}. \tag{3.14}$$

We set the first nondimensional number to 4 by assigning $X_0 = r/4$. The density is set to 1 and the dynamic viscosity μ is determined to match the desired Reynolds number set by the

user based on (3.14).

For this example, we choose the fixed time step $\Delta t = \dfrac{1}{200 f_0}$ and the simulations are run for three full oscillation cycles for 7 different Reynolds numbers ranging from 10 to 300. The iterative procedure explained in section 3.3.5 is necessary in this case of moving boundary in order to correctly enforce the desired no-slip condition (3.13). Since we are interested in the overall forces applied onto the sphere as a result of its motion, the inner iterative technique is carried on until $\left\|\Phi^k - \Phi^{k-1}\right\|_\infty < \varepsilon_\Phi = 2\,\varepsilon\,(\pi f_0 X_0)^2\,\Delta t$ where $\varepsilon = 0.1$ for all time steps. This corresponds to limiting the difference in pressure between successive iterates to 10% at most of the maximum dynamic pressure resulting from the motion of the sphere. The fixed point method seems more relevant in this context compared to what was observed in section 3.5.2: the number of iterations required to ensure this convergence condition grows with Re: for every time step, the solver performs 3 to 4 inner iterations to enforce the desired boundary conditions correctly , as illustrated in figure 3.21 for $Re = 300$. A mesh of resolution 5/10 rooted in a single macromesh cell is used, resulting in about 500,000 leaves. A uniform grid with similar finest resolution would have $2^{30} \simeq 10^9$ computational cells. Every simulation completed in about 8 hours using 40 MPI tasks on a local workstation running a Dual Intel Xeon Gold 6148 processor with 64 GB of RAM.

As for the flow past a sphere, the nondimensional force applied onto the oscillating sphere is monitored over time, according to equation (3.10). The results are presented in figure 3.19. As expected, we observe that the amplitude of the drag coefficient increases as the Reynolds number decreases. Furthermore, we observe a lag in the response as the Reynolds number decreases. Indeed, as the viscous forces become more important, the information takes longer to propagate in the fluid. In contrast, the forces in a system dominated by inertia come mainly from the pressure term and the incompressibility condition enforces instantaneous propagation of the information. Figure 3.20 shows some visual representations of the computational grid for $Re = 50$ at $t = 2.4/f_0$.

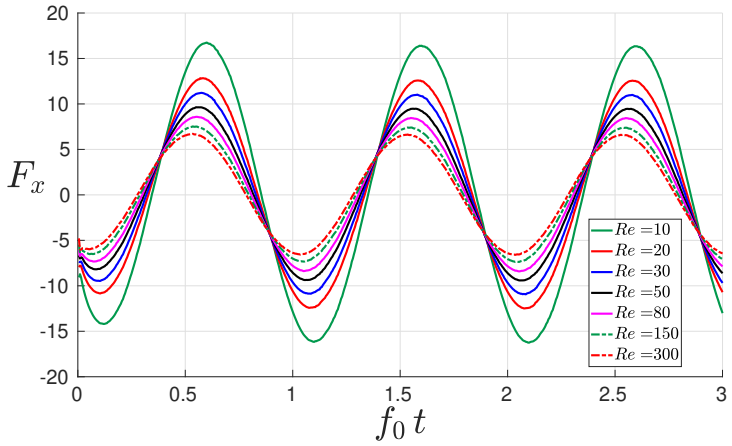

Figure 3.19: Evolution of the $x-$component of the nondimensional force applied onto the periodically oscillating sphere in a closed box for a range of Reynolds numbers. The magnitude of the force increases and the peaks appear at later times as the Reynolds number decreases and the viscous forces become dominant.

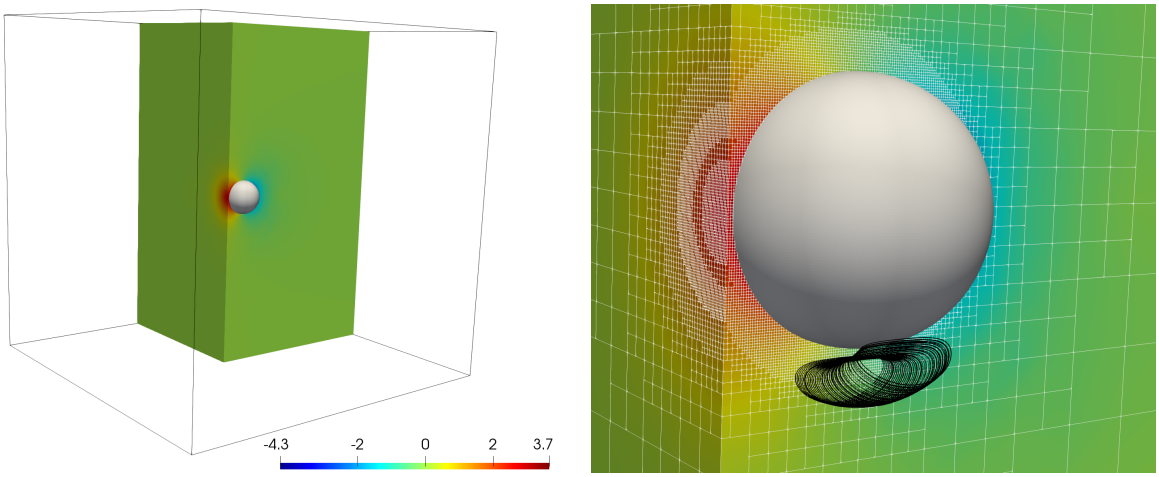

Figure 3.20: Left: illustration of one fourth of the computational domain colored with the pressure (nondimensionalized by $\frac{1}{2}\rho\pi r^2 f_0^2$), along with the solid sphere ($Re = 50$, $t = 2.4/f_0$). Right: zoom-in on the sphere, illustration of the local adaptivity of the computational grid and representation of some streamlines near the moving interface.

3.5.4 Transport of a scalar quantity in a flow

In this section, we provide two examples to qualitatively illustrate the ability of the solver to track scalar fields advected by the flow and to capture the resulting complex structures using high spatial resolution in the required regions. The (non-dimensional) node-sampled scalar

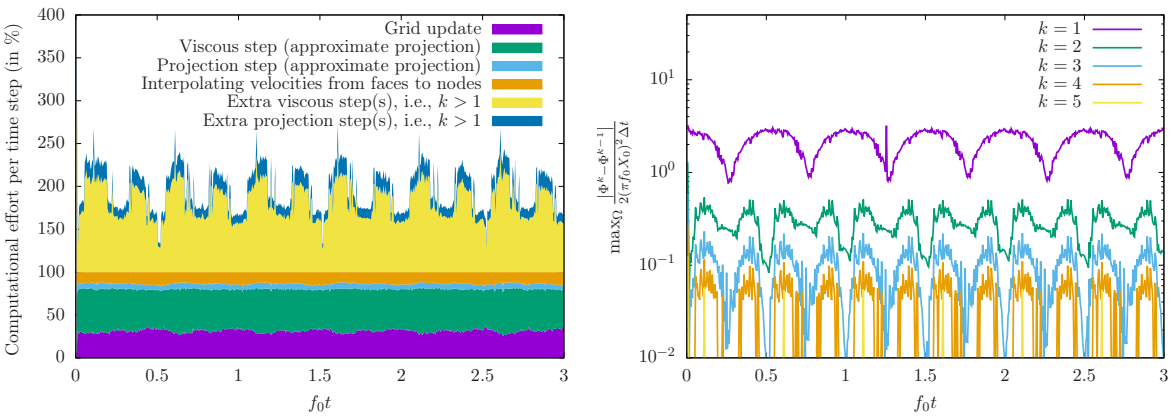

Figure 3.21: Illustration of the computational cost and convergence rate associated with the fixed point iteration from section 3.3.5, when ensuring point-wise convergence on the Hodge variable within bounds corresponding to a pressure threshold of 10% of the maximum dynamic pressure resulting from the kinematics of the oscillating sphere, as considered in section 3.5.3, for $Re = 300$. Left: ratio(s) of the computational costs per time step for the main tasks at play, normalized to the raw computational cost of an approximate projection method (which would correspond to $k_{\max} = 1$). Right: measures of interest considered by the inner loop criterion.

concentration $\beta(\boldsymbol{x}, t) \in [0, 1]$ is determined by solving the governing equation

$$\frac{\partial^+ \beta}{\partial t^+} \boldsymbol{u} \cdot \nabla \beta = 0 \tag{3.15}$$

using a semi-Lagrangian approach, as described in 3.3.3. Since this numerical example is intended to only illustrate an additional refinement capability of our adaptive-grid strategy, the diffusion terms were discarded in the above equation in order to make the simulation cheaper. In fact, numerical diffusion comes into play through the approximation errors of the semi-Lagrangian approach and the successive interpolation steps, so that $\beta(\boldsymbol{x}, t)$ is numerically smoothened over time.

In this section, the refinement criterion (3.3) is activated using a refinement threshold set to $\chi = 0.05$ in the mesh construction, along with criteria (3.1) and (3.2). We illustrate this capability with the flow past a sphere. The simulation setup is the same as in section 3.5.2 and the solver's parameters were set to match a Reynolds number of $Re = 5,000$ using an $8 \times 4 \times 4$ macromesh with trees of level 2/8, leading to around $34 \cdot 10^6$ leaves for a fully developed flow.

Figure 3.22 presents a visualization after $48\dfrac{r}{u_0}$ where r and u_0 are defined as in section 3.5.2, which corresponds to 857 time steps. The entire simulation took 20 hours on 1,024 cores of the Stampede2 supercomputer.

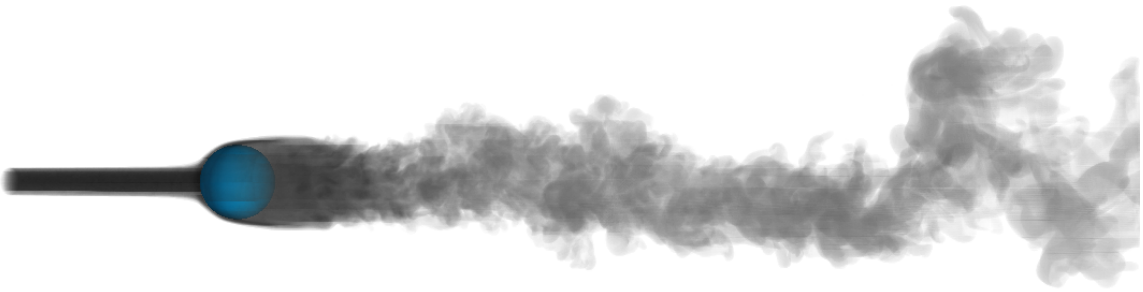

Figure 3.22: Visualization of a passively advected smoke marker in a flow past a sphere for a Reynolds number $Re = 5,000$.

As a second illustration, we consider a buoyancy-driven flow. In a cubic box of side length L, we consider the motion of a fluid of dynamic viscosity μ due to buoyancy with gravity acceleration $\boldsymbol{g} = -g\boldsymbol{e}_z$. A relative scalar concentration $\beta \in [0, 1]$ is passively advected by the flow according to (3.15) and the local fluid density depends linearly on β as $\rho_0 + \beta\Delta\rho$ with $\dfrac{\Delta\rho}{\rho_0} \ll 1$. Using Boussinesq approximation, the momentum equation reads

$$\rho_0 \left(\frac{\partial^+ \boldsymbol{u}}{\partial t^+} \boldsymbol{u} \cdot \nabla \boldsymbol{u} \right) = -\nabla p - \Delta\rho g \beta \boldsymbol{e}_z + \mu \nabla^2 \boldsymbol{u}. \tag{3.16}$$

The simulation is initialized with a flow at rest, $\beta = 1$ in a ball of radius $r = 0.1L$ centered at $(L/2, L/2, 3L/4)$ and $\beta = 0$ outside that ball. Using L as a characteristic length scale and $\dfrac{gr^2\Delta\rho}{\mu}$ as a characteristic velocity scale, (3.16) takes the non-dimensional form

$$\frac{\partial^+ \boldsymbol{u}}{\partial t^+} \boldsymbol{u} \cdot \nabla \boldsymbol{u} = -\nabla p - \frac{L^2}{r^2 Ar} \beta \boldsymbol{e}_z + \frac{1}{Ar} \nabla^2 \boldsymbol{u} \tag{3.17}$$

where the Archimedes number is defined as $Ar = \dfrac{\rho_0 g r^2 \Delta\rho L}{\mu^2}$. In figure 3.23, we show three snapshots of a simulation obtained with $Ar = 2.4525 \cdot 10^6$, using a $2 \times 2 \times 2$ macromesh with

trees of resolution 4/8, leading to about 20 million leaves. Here again, this simulation intends to show the capabilities of our parallel adaptive refinement approach, accurate results would require much finer and much more computationally intensive runs. The simulation took 20 hours on 256 cores of the Stampede2 supercomputer for 603 time steps.

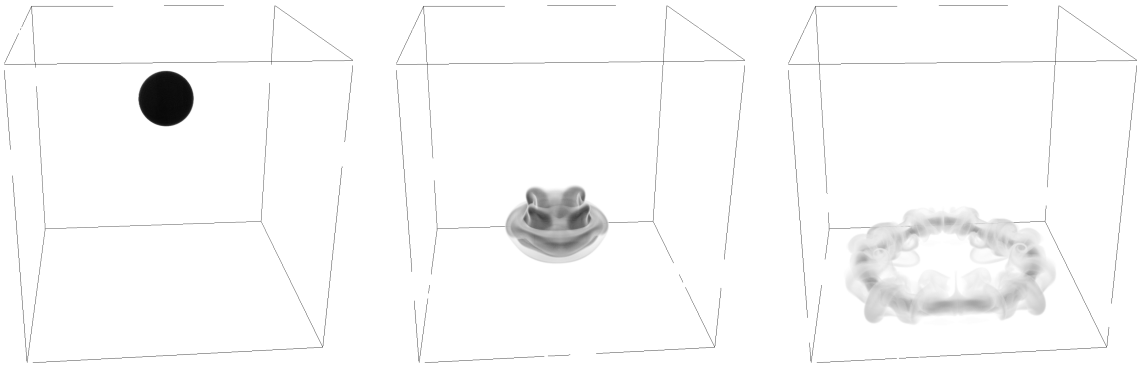

Figure 3.23: Visualization of a drop of high density smoke falling under gravity at the initial state (left), after nondimensional times of 367.88 (center) and 760.28 (right), where the nondimensional time is defined as $\frac{gr^2\Delta\rho t}{\mu L}$.

3.5.5 Turbulent superhydrophobic channel

As detailed and illustrated above, the solver is designed to allow dynamic grid adaptation over time. This feature is especially relevant and appealing when the complex flow dynamics to be captured are bounded to a (small) evolving portion of the computational domain, as it dramatically reduces the global number of computational cells compared to a regular uniform grid. Indeed, in such cases, the computational overhead associated with dynamically adapting the computational grid, with setting new operators and new linear solvers is small compared to the prohibitive computational cost of using a uniform grid of equivalent finest resolution throughout the domain.

However, while local mesh refinement remains valuable, dynamic re-meshing may not be most desirable in applications requiring (almost) static, dense regions of fine grid cells, as extra

operations associated with dynamic grid adaptation would significantly increase the overall computational cost, without any significant reduction of the overall number of computational cells to consider. We have alleviated this issue by allowing the solver to store all possible data structures[5] (linear solvers, possible preconditioners, interpolation operators, etc.) in memory and use them as long as they are valid, i.e., as long as the grid is not modified.

Statistically steady physical problems align perfectly with the above solver features, since they require fixed regions of specified spatial resolution by nature, and the results need to be accumulated over a (very) large number of time steps to ensure their statistical convergence. In order to illustrate the capability of the solver to address such problems, we consider the fully developed turbulent flow in a superhydrophobic channel as previously simulated in [137, 138]. We use a computational domain of dimensions $6\delta \times 2\delta \times 3\delta$, where δ is half of the channel height, with periodic boundary conditions along the streamwise and spanwise directions, as illustrated in figure 3.24. The coordinates are chosen such that x points downstream, y is normal to the walls and z is in the spanwise direction. The flow is driven in the positive streamwise direction by a spatially uniform and constant force per unit mass $\boldsymbol{f} = f_x \boldsymbol{e}_x$. By analogy with canonical channel flows, we define the friction velocity $u_\tau = \sqrt{f_x \delta}$.

We consider gratings oriented parallel to the flow on both walls $y = \pm\delta$. The superhydrophobic nature of these surfaces enables them to entrap pockets of air, such that parts of he walls are replaced by a liquid-air interface, which is assumed to be shear-free. We assume the liquid-air interface to be and remain flat at all times (deflections of the interface are neglected). We therefore model the air-liquid interface regions using no-penetration, free-slip boundary conditions[6]

$$v|_{y=\pm\delta} = 0, \qquad \left.\frac{\partial u}{\partial y}\right|_{y=\pm\delta} = 0 \quad \text{and} \quad \left.\frac{\partial w}{\partial y}\right|_{y=\pm\delta} = 0, \tag{3.18}$$

[5] For the linear solvers associated with the viscosity step, only diagonal terms are affected by a new value of Δt (see subsection 3.3.3). Therefore, only diagonal terms are updated when the computational grid is not modified.

[6] Note that $\left.\frac{\partial v}{\partial x}\right|_{y=\pm\delta} = \left.\frac{\partial v}{\partial z}\right|_{y=\pm\delta} = 0$ since $v|_{y=\pm\delta} = 0$ on the entire wall surfaces.

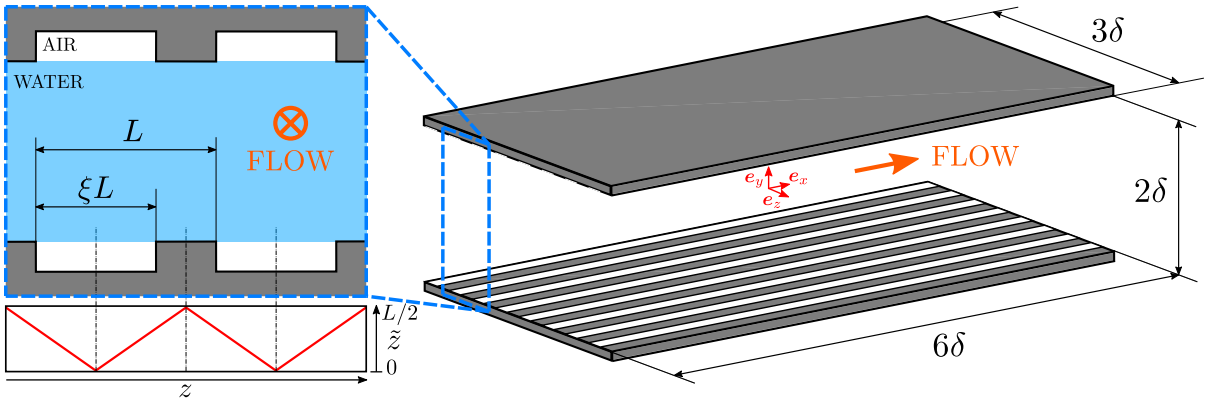

Figure 3.24: Schematic of the superhydrophobic surface and corresponding notations considered in section 3.5.5: we denote the pitch by L and the gas fraction by ξ. The variable $\tilde{z}$ is used to average over corresponding spanwise locations.

while the rest of wall surfaces use no-slip boundary conditions,

$$\boldsymbol{u}|_{y=\pm\delta} = \mathbf{0}.$$

Eight longitudinal grates giving a gas fraction of 50% are used, i.e., the pitch length L is set to $3\delta/8$ and the gas fraction ξ is set to 0.5 (see figure 3.24). The fluid properties and other control parameters are set such that the canonical friction Reynolds number $Re_\tau = \dfrac{\rho u_\tau \delta}{\mu}$ is equal to 143. The computational domain is meshed with one single Octree of minimum level 7 and maximum level 9. This choice of macromesh results in computational cells with an aspect ratio so different from 1 that third-degree neighbor cells are required for the reliable construction of face-seeded Voronoi cells (see figure 3.2 for a two-dimensional illustration). Therefore, this simulation setup makes an extensive use of the capability to fetch third-degree ghost neighbor cells, which is enabled by the algorithms from section 3.3.6. The capability of the solver to address such problems even with stretched computational cells is discussed in 3.7 using a known analytical solution in the laminar case.

In order to ensure sufficient grid resolution for regions close to the no-slip parts of the walls,

we define the level-set function[7]

$$\phi(\boldsymbol{x}) = -\text{dist}(\boldsymbol{x}, \text{no-slip region of the wall})$$

to be used with the refinement criterion (3.1) setting $K = 10$. This choice of K and maximum refinement level ensures that the walls are entirely covered by the finest computational cells over a thickness of 0.1δ. Except for the thickness of four grid cells layering the walls, the local grid resolution is equivalent to, or finer than, the resolution from [137, 138] everywhere. In [137, 138], a stretched grid was used with constant mesh size in the streamwise and spanwise directions while the cell thickness was distributed using a hyperbolic tangent profile in the wall-normal direction. The main difference between such a stretched grid and our Octree approach lies in the fact that the aspect ratio of our computational cells is constant. As cells get thinner when approaching the wall regions, they also get shorter and narrower: the spatial resolution close to the walls for the Octree grid is four times finer than for the stretched grid in the spanwise and streamwise directions, hence producing more accurate results in those directions than stretched grids do. This however significantly increases the total number of computational cells to be used in our approach, since we need more than $21.8 \cdot 10^6$ cells, as opposed to about $2.1 \cdot 10^6$ in the case of a stretched grid. Dynamic grid adaptation based on local vorticity is less useful in this example, since the background grid already captures enough details (γ is thus irrelevant in this case), which enables us to reduce time execution. The conjugate gradient method is used for solving the projection step along with an algebraic multigrid preconditioner (from the HYPRE distribution).

A thorough analysis of the analytical solution known in the laminar cases shows that the viscous stress is singular at the edges of the walls transitioning between free-slip and no-slip boundary conditions (see 3.7 and references therein for more details). Early numerical tests revealed that setting the inner loop convergence criterion (see section 3.3.5) to ensure $\left\|\Phi^k - \Phi^{k-1}\right\|_\infty < \varepsilon_\Phi$ would fail because the (floating-value) Hodge variable Φ would grow

[7] Note that ϕ is negative everywhere so no interface is defined within the domain.

unbounded in the cells layering these transition edges. However, the velocity field must be bounded everywhere, and therefore, so must be $\|\nabla\Phi\|_\infty$. As a matter of fact, setting the inner loop convergence criterion (see section 3.3.5) to ensure $\max_\Omega \left\|\nabla\Phi^k - \nabla\Phi^{k-1}\right\|_\infty < 10^{-6}U_\mathrm{b}$, wherein U_b is the mean, bulk velocity in the streamwise direction through the channel, resulted in fully controlled simulations. For most time steps, the solver required three inner iterations to converge (the value of the convergence measure for the first iterate, i.e., $\max_\Omega \|\nabla\Phi^1 - \nabla\Phi^0\|_\infty$, was observed to be of the order of $10^{-4}U_\mathrm{b}$).

The simulation is initialized to the known laminar solution and executes until flow instabilities amplify and a fully-developed turbulent state is eventually reached. The bulk Reynolds number

$$Re_\mathrm{b} = \frac{\rho U_\mathrm{b}\delta}{\mu}, \text{ where } U_\mathrm{b} = \frac{1}{6\delta^2}\int_{-\delta}^{\delta}\int_{-1.5\delta}^{1.5\delta} \boldsymbol{u}\cdot\boldsymbol{e}_x \,\mathrm{d}z\,\mathrm{d}y$$

and the nondimensional viscous forces from the no-slip regions of the walls

$$\boldsymbol{F}_{\text{wall, visc.}} = \frac{1}{\rho f_x\, 36\delta^3}\sum_{k_y=\{-1,1\}}\sum_{k_z=-4}^{3}\int_{-3\delta}^{3\delta}\int_{(k_z+\xi)L}^{(k_z+1)L} -k_y\left[\mu\left(\nabla\boldsymbol{u}+(\nabla\boldsymbol{u})^\mathrm{T}\right)\cdot\boldsymbol{e}_y\right]\Big|_{y=k_y\delta}\mathrm{d}z\,\mathrm{d}x$$

are monitored over time. Their evolution is illustrated in figure 3.25.

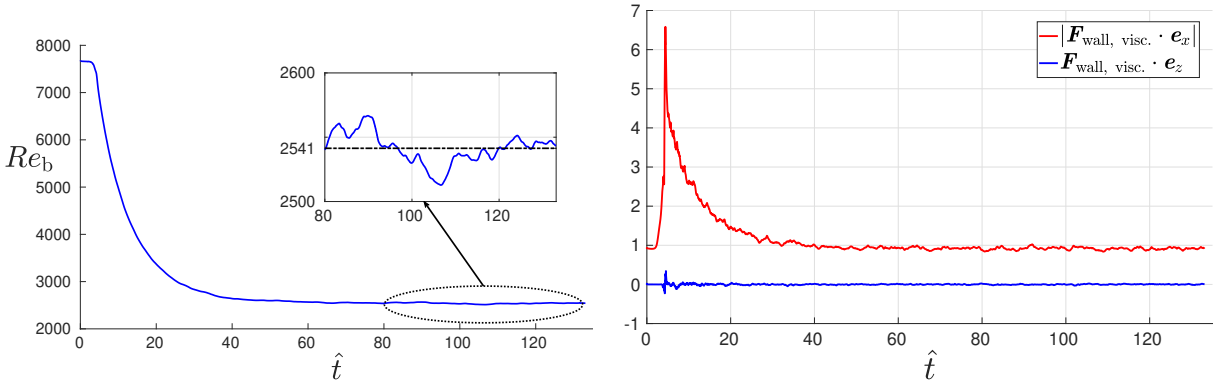

Figure 3.25: Macroscopic variables monitored over the course of the simulation of a turbulent flow through a superhydrophobic channel. Left: evolution of $Re_\mathrm{b} = \rho U_\mathrm{b}\delta/\mu$; right: evolution of the nondimensional viscous forces from the no-slip regions of the walls. In these graphs, the nondimensional time $\hat{t}$ is defined as $\hat{t} = \dfrac{u_\tau t}{\delta}$.

From the evolution of the monitored macroscopic quantities of interest illustrated in figure 3.25, we consider the time window from $\hat{t}_{\text{start}} = \dfrac{u_\tau t}{\delta} = 80$ until the end of the simulation, $\hat{t}_{\text{end}} = 133.1$, which we use for time-averaging results associated with the fully-developed regime (which corresponds to about 300,000 time steps). An illustrative snapshot of the simulation in this time window is presented in figure 3.27.

We obtain an average bulk Reynolds number of 2541; we also consider the time-and-slice-averaged velocity profile, i.e.,

$$\left\langle \frac{u}{u_\tau} \right\rangle_{x,z,t} = \frac{1}{18\delta^2 \left(\hat{t}_{\text{end}} - \hat{t}_{\text{start}}\right)} \int_{\hat{t}_{\text{start}}}^{\hat{t}_{\text{end}}} \int_{-3\delta}^{3\delta} \int_{-1.5\delta}^{1.5\delta} \frac{u}{u_\tau} \, \mathrm{d}z \, \mathrm{d}x \, \mathrm{d}\hat{t}$$

as a function of y/δ, as well as the time-and-line-averaged velocity profile, i.e.,

$$\left\langle \frac{u}{u_\tau} \right\rangle_{x,t} = \frac{1}{6\delta \left(\hat{t}_{\text{end}} - \hat{t}_{\text{start}}\right)} \int_{\hat{t}_{\text{start}}}^{\hat{t}_{\text{end}}} \int_{-3\delta}^{3\delta} \frac{u}{u_\tau} \, \mathrm{d}x \, \mathrm{d}\hat{t},$$

which is built by also averaging corresponding locations over the air-interface and over the ridges in the spanwise direction. Formally, this results in a function of y/δ and of the grate-normalized spanwise coordinate $\tilde{z}$ defined as

$$\tilde{z} = \begin{cases} \left| (z \pmod L) - \dfrac{L\xi}{2} \right| & \text{if } z \pmod L \leq L\xi, \\ \dfrac{L}{2} - \left| (z \pmod L) - \dfrac{L\,(1+\xi)}{2} \right| & \text{otherwise,} \end{cases} \tag{3.19}$$

(see illustration in figure 3.24). These time-averaged velocity profiles are illustrated in figure 3.26.

As illustrated in figure 3.26, the mean fluid velocity at the air interface can reach up to 50% of the maximum mean velocity (found at the center of the channel). This figure also illustrates how sharp the change is: 74% of the variation from the no-slip ridge to the maximum air interface velocity (found above the center line of the interface) occurs over a distance of $3\delta/128$ in the spanwise direction, which corresponds to 4 computational cells in our setup (versus 1 cell

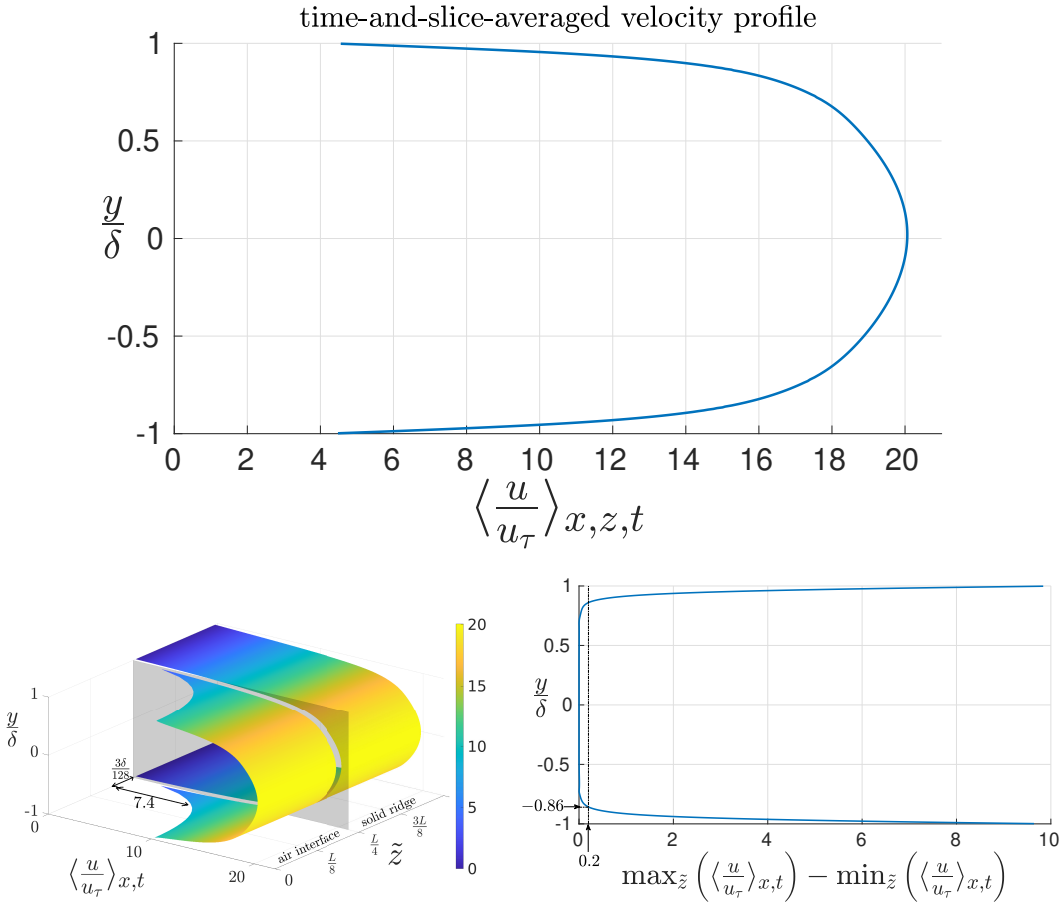

Figure 3.26: Top: time-and-slice-averaged velocity profile. Bottom left: time-and-line-averaged velocity profiles. Notice the sharpness of the transition between no-slip and free-slip line-averaged profiles. A significant portion of the transition (74%) takes place over a distance of $\frac{3\delta}{128}$ in the spanwise direction. While this distance corresponds to the width of one single computational cell in the stretched grid approach of [138], our octree grid uses 4 narrower computational cells over that region. Bottom right: illustration of how the time-and-line-averaged profiles become $\tilde{z}$-independent far enough from the walls; in this case, time-and-line-averaged velocity profiles are essentially all equivalent (within 1% of the mean velocity to be found in the center of the channel) farther than 0.14δ from the walls.

in [138]).

When averaging velocity profiles across entire planar sections of the channel, the existence of such free-slip regions results in a nonzero slip velocity U_s at the wall. This slip velocity is a quantity of primary relevance in the context of Navier's slip model, along with the slip length b which relates the slip velocity to the mean wall shear via $U_s = \pm b \frac{\partial}{\partial y} \langle u \rangle_{x,z,t} \Big|_{y=\mp\delta}$. The slip

parameters U_s and b were evaluated by least-square fitting the linear profiles $\frac{U_s}{u_\tau}\left(1+\frac{\delta \pm y}{b}\right)$ ($+$ and $-$ correspond to bottom and top walls, respectively) to our results for $\left\langle \frac{u}{u_\tau} \right\rangle_{x,z,t}$ over the 5 finest grid cells layering the walls, which corresponds to a thickness of about $2.8\delta_\tau$, where $\delta_\tau = \frac{\mu}{\rho u_\tau}$ is the viscous lengthscale. The two sets of fitting parameters yield $b = (0.0302 \pm 0.0002)\,\delta = (4.320 \pm 0.025)\,\delta_\tau$ and $U_s = (4.255 \pm 0.040)\,u_\tau$.

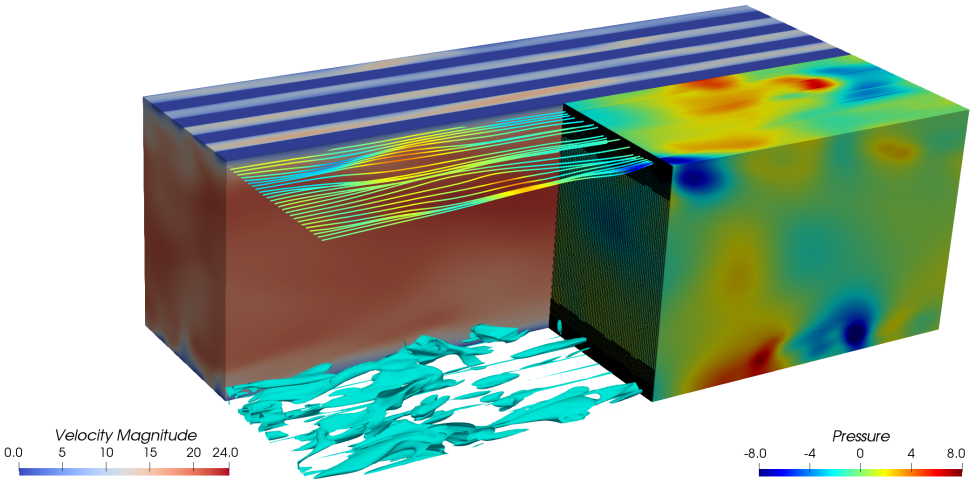

Figure 3.27: Visualization of a snapshot for the simulation of the turbulent superhydrophobic channel flow. The half of the domain corresponding to $z < 0$ is colored by $\frac{\|\boldsymbol{u}\|}{u_\tau}$; the quarter of the domain corresponding to $z > 0$ and $x > 0$ is colored by $\frac{p}{\rho u_\tau^2}$. A slice of the computational grid, streamlines and isocontours of $\lambda_2 = -0.3\left(\frac{U_b}{\delta}\right)^2$ (using the λ_2-criterion from [139]) are also shown.

Our setup value of Re_τ was chosen for comparison purposes with one of the simulations from [138, 137], which reports a (mean) value of $Re_\tau = 143$ using a simulation setup enforcing a (constant) mass flow corresponding to $Re_b = 2,800$ for the same channel geometry. Under these conditions, [138, 137] reports $b = 0.0366\,\delta = 5.17\,\delta_\tau$ and $U_s = 5.26\,u_\tau$. Therefore, when compared to those results, our simulation leads to a reduced flow rate for a comparable driving force (about 10% less) and to a smaller slip velocity as well as a smaller slip length. Besides the difference in simulation setup (constant driving force as opposed to constant mass flow rate), such deviations may also originate from numerical and/or modeling differences to be found

between the two approaches. To assess this, we also compare our results to the simulations of [140], who used a lattice-Boltzmann method. We select their simulation whose value of L/δ_τ is closest to ours, since [138] established that L/δ_τ is the single most important parameter that determines slip length (at fixed gas fraction). We therefore compare our simulation, which has $L/\delta_\tau = 53.6$, to the $L/\delta_\tau = 56.2$ case of [140], who found $b/\delta_\tau = 4.23$. This value is appreciably smaller than the result of 5.17 of [138], but matches closely our $b/\delta_\tau = 4.32$.

In terms of modeling, [138, 137] opted for a simplified wall-treatment for the spanwise velocity component w, by setting $w|_{y=\pm\delta} = 0$ instead of the stress-free condition (3.18) above the free-slip wall regions. Enforcing $w|_{y=\pm\delta} = 0$ above the air pockets does not rely on physical grounds, and may result in simplified near-wall flow structures that artificially promote streamwise velocity. Indeed, this simplified condition results in $\dfrac{\partial w}{\partial z} = 0$, which in turn simplifies the incompressibility condition, at the walls, into $\dfrac{\partial u}{\partial x} + \dfrac{\partial v}{\partial y} = 0$. At the wall-located air interfaces, this latter equation stands as an artificial constraint, within z-orthogonal planes, enabling transfer of kinetic energy only between wall-normal and streamwise velocity components. This constraint could lead, in turn, to an overestimation of the slip velocity and/or of the total mass flow across the channel, which could help explain the difference between the results of [138] and those of subsequent simulations.

In terms of numerical methods, we emphasize that the use of a semi-Lagrangian scheme for the advection terms comes with a significant amount of numerical dissipation, which may in turn lead to overestimated viscous dissipation. While this cannot be excluded, we also want to point out that our simulation setup makes use of a spatial resolution that is 4 times finer than the resolution from [138], in both the streamwise and spanwise directions. Firstly, such a fine resolution in the streamwise direction is expected to alleviate the numerical dissipation associated with our advection scheme. Secondly, such a resolution in the spanwise direction may actually stand as a requirement in order to capture the sharp variation in velocity profiles between free-slip and no-slip wall regions. Indeed, figure 3.26 illustrates that $\dfrac{\partial}{\partial z}\langle u\rangle_{x,t}\Big|_{y=\pm\delta}$ is the largest near the boundaries transitioning from free-slip to no-slip regions; therefore, using

a coarse spanwise resolution in that area may lead to an underestimation of the overall viscous dissipation.

In order to quantify the relative importance of this term, we estimate its contribution to the viscous dissipation taking place in near-wall layers and compare it to the contribution of the mean, slice-averaged streamwise shear term (i.e., as if we were dealing with a regular channel). Assuming that $\frac{\partial}{\partial z}\langle u\rangle_{x,t}\Big|_{y=\pm\delta}$ is not negligible within bands of $3\delta/128$ around solid ridges only (in our case, we have 16 such bands on either wall), our comparative estimate is

$$\frac{6\delta\,\frac{16\times 3\delta}{128}\mu\left(\frac{\partial}{\partial z}\langle u\rangle_{x,t}\Big|_{y=-\delta}\right)^2}{6\delta\,3\delta\,\mu\left(\frac{\partial}{\partial y}\langle u\rangle_{x,z,t}\Big|_{y=-\delta}\right)^2}\approx\frac{16}{128}\frac{\left(\frac{7.4u_\tau}{3\delta/128}\right)^2}{\left(\frac{U_s}{b}\right)^2}=62.8\%,$$

where we estimated $\frac{\partial}{\partial z}\langle u\rangle_{x,t}\Big|_{y=-\delta}=\frac{7.4u_\tau}{3\delta/128}$ based on the results illustrated in figure 3.26 to produce a fair measure in comparison with the grid resolution from [138], although $\frac{\partial}{\partial z}\langle u\rangle_{x,t}\Big|_{y=-\delta}$ becomes almost twice as large as we approach the edge in our computational setting. Although wall viscous shear dissipation may be smaller than the overall (bulk) turbulent dissipation, we expect it to be non-negligible nonetheless, in particular when considering a relatively low friction Reynolds number as it is the case here[8]; in this context, the above comparative estimation indicates that spanwise wall shear, though not evenly distributed on the walls, is not a negligible factor to the overall viscous dissipation.

[8]In fact, if we consider an equivalent canonical channel with a mean, streamwise wall shear of U_s/b that we assume constant over layers of at least $3\frac{\mu}{\rho u_\tau}$, the viscous dissipation in these layers amounts for

$$2\times 3\frac{\mu}{\rho u_\tau}\times 6\delta\times 3\delta\times\mu\left(\frac{U_s}{b}\right)^2\simeq 105\,\rho u_\tau^3\delta^2$$

which represents about 1/6 of the energy injection rate $36\delta^3\rho f_x U_\mathrm{b}$ in our simulation setup.

3.6 Conclusion

We have described a Navier-Stokes solver for simulating incompressible flows in irregular domains on a forest of Octrees in a distributed computing framework. The parallel implementation of the solver requires the ability to access second- (or third-)degree cell neighbors, which led to the need for an expanded ghost layer of cells. We have introduced an algorithm to address that computational challenge on distributed forest of octree grids. We also have introduced parallel algorithms for the unambiguous definition and synchronization of global faces indices as required in a standard MAC arrangement. The performance of these individual algorithms has been assessed in terms of strong and weak scaling analyses. The strong scaling behavior of the entire solver has been verified up to more than 32,000 cores using a problem on a grid of $6.1 \cdot 10^8$ grid cells. The performance of the solver has been assessed on several large-scale three-dimensional problems: accurate results for the flow past sphere at various Reynolds numbers have been shown, several illustrations of the capabilities of our adaptive refinement approach have been provided and a simulation of the turbulent flow through a superhydrophobic channel has been performed with unparalleled spanwise (and streamwise) spatial resolution over regions of interest. When flow structures have a limited lifetime and/or are bounded to relatively small regions in the computational domain, our adaptive grid refinement approach was shown to successfully simulate the problems of interest using only a few percent of the number of grid cells that a uniform grid of equivalent finest resolution would require. The encapsulation of such a feature in a distributed computing framework allows for very-large scale simulations to be considered tractable from a computational standpoint and, therefore, to address increasingly complex multiscale and/or multiphysics problems.

3.7 Appendix:Validation test in laminar cases superhydrophobic channel flows

Given the numerical difficulties typically associated with this kind of mixed boundary-value problems [141], we assess the performance of the solver for the simpler *laminar* steady case, in which the flow is unidirectional and exact solutions exist (see [142, 143]). In this context, we consider longitudinal gratings, i.e., aligned with the flow direction, on both the upper and lower walls. The analytical solution can be expressed as the following series

$$\boldsymbol{u}_{\text{exact}}(y,\tilde{z}) = \frac{\mu Re_\tau^2}{\rho\delta}\left\{\frac{1}{2}\left[1-\left(\frac{y}{\delta}\right)^2\right] + c_0 + \sum_{n=1}^{\infty} c_n \frac{\cosh(2\pi n y/L)}{\cosh(2\pi n\delta/L)}\cos\left(\frac{2\pi n\tilde{z}}{L}\right)\right\}\boldsymbol{e}_x,$$

where $Re_\tau = \dfrac{\rho\delta\sqrt{f_x\delta}}{\mu}$ is the canonical friction Reynolds number, L is the pitch (that is the distance between consecutive gratings), and $\tilde{z}\in[0,L/2]$ is the normalized spanwise coordinate that parametrizes each periodic unit as defined in (3.19) (see figure 3.24 for a detailed illustration of all parameters).

Due to the mixed boundary conditions, the coefficients c_n must be determined numerically by enforcing the dual cosine series conditions [143]

$$\begin{aligned}
g_{\text{no slip}}\left(\tilde{z};c_0,c_1,\ldots\right) &= c_0 + \sum_{n=1}^{\infty} c_n \cos\Big(\frac{2\pi n\tilde{z}}{L}\Big) = 0, && \forall\tilde{z}\in\Big[\frac{\xi L}{2},\ \frac{L}{2}\Big]\\
g_{\text{free slip}}\left(\tilde{z};c_0,c_1,\ldots\right) &= \sum_{n=1}^{\infty} c_n n\tanh\Big(\frac{2\pi n\delta}{L}\Big)\cos\Big(\frac{2\pi n\tilde{z}}{L}\Big) - \frac{L}{2\pi\delta} = 0, && \forall\tilde{z}\in\Big[0,\ \frac{\xi L}{2}\Big[.
\end{aligned}$$

where $0<\xi<1$ is the gas fraction. We truncate the above series up to N terms and solve the (dense) $N\times N$ linear system derived from the resulting algebraic conditions

$$\begin{aligned}
&\int_0^{\frac{\xi L}{2}} g_{\text{free slip}}\left(\tilde{z};c_0,c_1,\ldots,c_{N-1}\right)\cos\Big(\frac{2\pi k\tilde{z}}{L}\Big)\,\mathrm{d}\tilde{z}\\
&\qquad + \int_{\frac{\xi L}{2}}^{\frac{L}{2}} g_{\text{no slip}}\left(\tilde{z};c_0,c_1,\ldots,c_{N-1}\right)\cos\Big(\frac{2\pi k\tilde{z}}{L}\Big)\,\mathrm{d}\tilde{z} = 0, \qquad \forall k\in\{0,1,\ldots,N-1\}.
\end{aligned}$$

Even in this simplified laminar case, the velocity gradient components $\frac{\partial u}{\partial y}$ and $\frac{\partial u}{\partial z}$ display singularities at the edges between the no-slip and free-slip wall regions that may compromise the point-wise convergence of the numerical solution. We thus explore the performance of the solver, setting simulations of increasing spatial resolution for $Re_\tau = 10$, using 2 grates with pitch $L = \delta$ and gas fraction $\xi = 0.875$. We use $N = 2500$ terms in the above series, which ensures that all the coefficients in the exact solution are computed to machine precision for this particular setup.

In order to assess the validity of the face-seeded Voronoi diagrams associated with stretched computational cells, we also investigate how the accuracy is affected by the aspect ratio of the computational cells by replicating the same simulation runs in two macromeshes of different aspect ratios. This is especially relevant to anticipate the validity of our results in the turbulent simulations, since in those cases the cells must be stretched in the streamwise direction to result in a feasible computational cost. The solver is then executed until a steady state is reached, and the resulting numerical errors for the streamwise velocity component are measured. We present them in Table 3.7.

	u/u_τ							
	Domain dimensions: $\delta \times 2\delta \times 2\delta$ Macromesh: $1 \times 2 \times 2$ root trees Cubic cells ($\Delta x/\Delta y = \Delta x/\Delta z = 1$)				Domain dimensions: $6\delta \times 2\delta \times 2\delta$ Macromesh: $1 \times 1 \times 1$ root tree Stretched cells ($\Delta x/\Delta y = \Delta x/\Delta z = 3$)			
levels	L^1 error	order	L^∞ error	order	L^1 error	order	L^∞ error	order
4/6	$9.63 \cdot 10^{-2}$	-	$3.09 \cdot 10^{-1}$	-	$2.02 \cdot 10^{-1}$	-	$4.67 \cdot 10^{-1}$	-
5/7	$2.67 \cdot 10^{-2}$	1.85	$1.69 \cdot 10^{-1}$	0.87	$9.75 \cdot 10^{-2}$	1.05	$2.99 \cdot 10^{-1}$	0.64
6/8	$6.20 \cdot 10^{-3}$	2.11	$1.39 \cdot 10^{-1}$	0.29	$3.84 \cdot 10^{-2}$	1.34	$1.67 \cdot 10^{-1}$	0.84

Table 3.7: Convergence of the solver for the case of laminar flow over a superhydrophobic surface, with $Re_\tau = 10$. The pitch is $L = \delta$ and the gas fraction is $\xi = 0.875$.

As expected from Section 3.5.1, the accuracy is close to, or even exceeds, first order in the L^1 norm[9] for all cases. Moreover, the errors are comparable for similar Δy and Δz between cubic cells and stretched cells: we set $\Delta y = \Delta z$ in both cases, but we use twice as many root

[9]Here, the L^1 error is already normalized with the domain volume for a straightforward comparison with the L^∞ error. Specifically, we define the L^1 error as the discrete equivalent of $\int_\Omega |u_{\text{num.}} - u_{\text{exact}}| \, \mathrm{d}\Omega \,/\, \mathrm{vol}(\Omega)$.

trees along y and z in the case of cubic cells, which effectively doubles the wall-normal and spanwise resolutions compared to stretched cells.

On the other hand, the L^∞ error does not display a clean first-order convergence. Indeed, a closer analysis of the spatial distribution of the error reveals that, unsurprisingly, its maximum is located at the transitions between no-slip and free-slip regions at the walls, and that the convergence in these areas is slower than in the rest of the domain. This drop in the convergence rate is expected in mixed boundary-value problems [141], although we still observe that in all cases the maximum error is monotonically decreasing with refinement.

3.8 Acknowledgments

This research was funded by ONR N00014-11-1-0027. In addition, F. Temprano-Coleto and P. Luzzatto-Fegiz were partially supported by ARO MURI W911NF-17-1-0306. F. J. Peaudecerf acknowledges funding from the European Union's Horizon 2020 research and innovation programme under the Marie Skłodowska-Curie grant agreement No 798411. This work was also partially supported by the California NanoSystems Institute at UC Santa Barbara through a Challenge Grant. This work used the Extreme Science and Engineering Discovery Environment (XSEDE), which is supported by National Science Foundation grant number ACI-1053575. The authors acknowledge the Texas Advanced Computing Center (TACC) at The University of Texas at Austin for providing HPC and visualization resources that have contributed to the research results reported within this paper. URL: http://www.tacc.utexas.edu. In addition, use was made of computational facilities purchased with funds from the National Science Foundation (CNS-1725797) and administered by the Center for Scientific Computing (CSC). The CSC is supported by the California NanoSystems Institute and the Materials Research Science and Engineering Center (MRSEC; NSF DMR 1720256) at UC Santa Barbara.

Chapter 4

A striking experiment: Maze-solving behavior of Marangoni flows

4.1 Abstract

We present here the experimental observation of maze-solving by surfactants. After introducing soap at the entrance of a maze formed by open channels filled with liquid, the resulting Marangoni flow reaches the outlet with minimal incursions in dead-end branches. This behavior is unexpected, since normally the flow would progress into every channel with a lower surfactant concentration. We postulate that the higher resistance to spreading in dead-end channels stems from the presence of *endogenous surfactants* at the fluid surface. This visually striking phenomenon exemplifies the crucial role of geometry in Marangoni flows.

4.2 Introduction

The ancient Greek myth of Theseus and the Minotaur is perhaps the most famous example of the fascination that maze-solving has historically triggered in humankind. Maze-solving strategies also have important practical applications, including path finding in robotics [144], urban transportation [145], and cognitive neuroscience [146]. Since the digital computation of

the shortest path across a maze is efficient for simple cases only [147, 148], numerous more unconventional, analog methods have been suggested in the last few decades. For instance, amoeboid organisms are able to solve mazes when a suitable gradient of nutrients is present [149], and chemical waves have been reported to find optimal pathways in complex labyrinths [150]. Other examples among these analog maze-solving techniques rely on fluid-mechanical effects, such as exploiting a pressure gradient between the inlet and outlet of a complex microfluidic network in order to drive a dyed fluid between the two [151].

We demonstrate here that the Marangoni effect produced by a surfactant is a fast and highly efficient mechanism of maze solving. We present the experimental observation of a small amount of dilute soap, which successfully solves a maze filled with milk with minimal penetration into side branches. While maze solving using thermal [152], pH-induced [153, 154], and surfactant-generated [155] Marangoni flows have previously been reported, in those cases the motion is established in the maze by introducing an alteration at the outlet, with the tracer particles being drawn from the inlet by the resulting flow, such that a tracer anywhere in the maze is also transported towards the exit. However, in the present work the decrease in surface tension originates at the inlet, and the tracer follows the correct path to the outlet without any pre-existing gradient of surface tension ahead of its path.

4.3 Results and discussion

The experiment consists of a square plate of acrylic (127 $\times$ 127 mm) with a series of open channels of approximately 3 mm of depth and forming a small maze. First, the maze is filled with milk [1], and a drop of red dye is added at the inlet reservoir, acting as a passive tracer. Subsequently, a brush previously immersed in a soap solution (0.2% volume, 'Seventh Generation' brand) is briefly introduced in the milk at the inlet, for a time not exceeding one second (Figs. 4.1(a) and 4.2(a)). Immediately after the brush is introduced, a Marangoni flow

[1]The choice of milk is for visualization purposes due to the high contrast with the red dye. The same maze-solving effect is observed if water is used as the base fluid.

away from it is triggered, due to the locally lower surface tension of the milk-air interface in the area with soap, which overlaps with the dye.

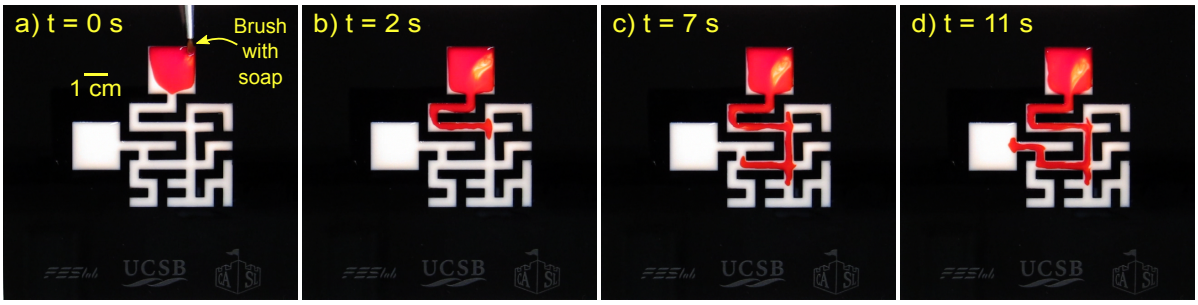

Figure 4.1: Snapshots of a 0.2% solution of soap solving a small maze filled with milk, from time $t = 0$ s until $t = 11$ s, when the red dye reaches the exit. The width of the channels is 4 mm.

The dyed milk, entrained by the soap, barely penetrates into side channels with dead ends, opting for the right path towards the outlet at every bifurcation until it solves the maze (Figs. 4.1(b-d) and 4.2(b-f)). This fact may appear surprising since, as mentioned above, the front of red dye does not advance following a gradient of surface tension originated from the outlet. However, it could potentially be explained by the presence of *endogenous surfactants*, trace amounts of other surface-active substances that are naturally unavoidable in the fluid. These small quantities of surfactant are usually insufficient to produce a noticeable decrease of surface tension in the initial fluid, but can have a marked effect on the dynamics, described as follows. As the front of dye spreads across the maze, it compresses the interface ahead, thus increasing the concentration of endogenous surfactant and creating a Marangoni force opposing the motion, eventually stopping the flow. This effect has been reported to occur in the spreading of surfactants in a thin film of liquid [156], and could explain the maze-solving effect here. Indeed, when reaching a bifurcation the dye would naturally choose the path of least resistance, which is the one with the largest surface area ahead, since it would minimize the downstream concentration of endogenous surfactants. According to this hypothesis, the relatively large surface area of the outlet reservoir of the maze offers the lowest resistance at

every bifurcation, thus enabling the soap to solve the maze correctly.

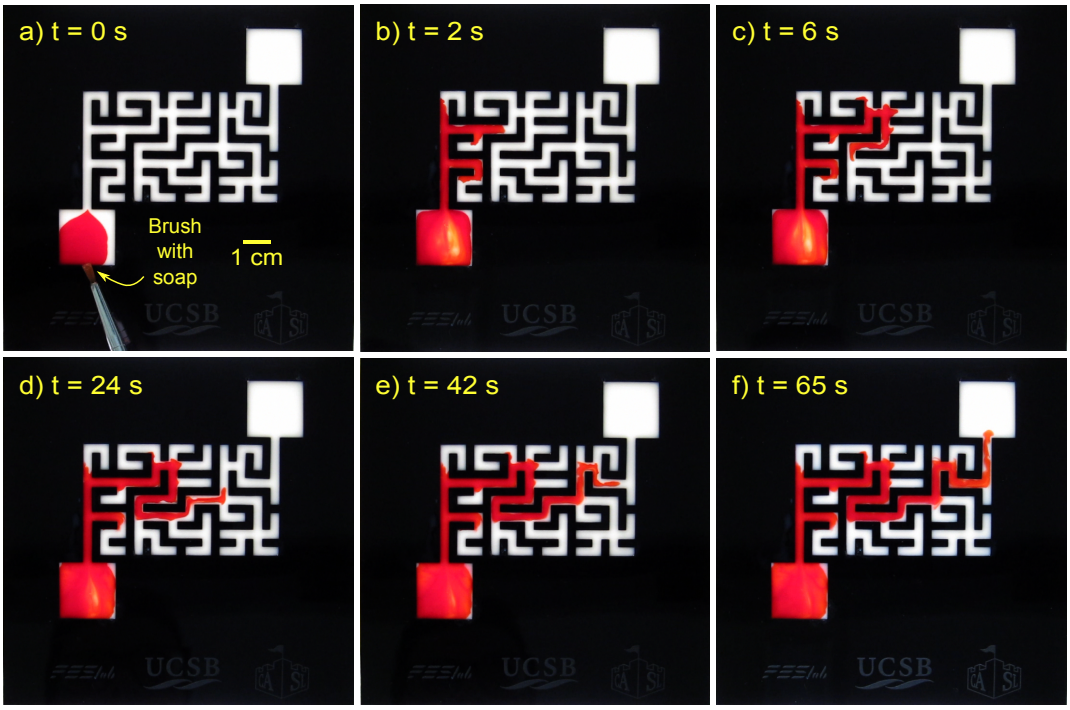

Figure 4.2: Snapshots of a 0.2% solution of soap solving a larger and more complex maze, also filled with milk. The red dye used as tracer reaches the exit at time $t = 60$ s. The width of the channels is 3 mm.

This result is a striking example of the dramatic consequences of surface-active impurities in fluid flows. Their role in slowing down the rising motion of bubbles in a liquid [157] has been known for decades [1]. Very recently, it has been shown experimentally that trace amounts of surfactants can also critically hinder the drag reduction ability of superhydrophobic surfaces [19]. Taking these effects into account can therefore be essential in the study and prediction of flows involving fluid interfaces.

4.4 Acknowledgements

This work has been supported by the University of California Santa Barbara Academic Senate and California NanoSystems Institute Challenge Grant, as well as by ONR MURI N00014-17-1-2676. We gratefully acknowledge conversations with Oliver Jensen, who pointed us to

works on endogenous surfactant.

Chapter 5

Theory for laminar flows with surfactant over two-dimensional superhydrophobic gratings

5.1 Abstract

Superhydrophobic surfaces (SHSs) have the potential to reduce drag at solid boundaries. However, multiple independent studies have recently shown that small amounts of surfactant, naturally present in the environment, can induce Marangoni forces that increase drag, at least in the laminar regime. To obtain accurate drag predictions, one must solve the mass, momentum, bulk surfactant and interfacial surfactant conservation equations. This requires expensive simulations, thus preventing surfactant from being widely considered in SHS studies. To address this issue, we propose a theory for steady, pressure-driven, laminar, two-dimensional flow in a periodic SHS channel with soluble surfactant. We linearise the coupling between flow and surfactant, under the assumption of small concentration, finding a scaling prediction for the local slip length. To obtain the drag reduction and interfacial shear, we find a series solution for the velocity field by assuming Stokes flow in the bulk and uniform interfacial shear. We

find how the slip and drag depend on the nine dimensionless groups that together characterize the surfactant transport near SHSs, the gas fraction and the normalized interface length. Our model agrees with numerical simulations spanning orders of magnitude in each dimensionless group. The simulations also provide the constants in the scaling theory. Our model significantly improves predictions relative to a surfactant-free one, which can otherwise overestimate slip and underestimate drag by several orders of magnitude. Our slip length model can provide the boundary condition in other simulations, thereby accounting for surfactant effects without having to solve the full problem.

5.2 Introduction

Superhydrophobic surfaces (SHSs) consist of hydrophobic coatings equipped with micro- or nano-scale textures, such that a layer of air (known as a "plastron"; see *e.g.* [158]) is retained when the surface is submerged in water (see e.g. the reviews of [159, 160, 161, 162, 163]). The air layer is held in place by the texture, with the upper edges of the micro- or nano-structures making contact with the water. Since air is approximately 50 times less viscous than water, the plastron has often been approximated as a shear-free surface in analytical models [164, 165, 166, 167, 168, 169, 170, 171, 172], leading to the expectation that SHSs could achieve very large drag reduction. Potential applications include high-Reynolds-number, turbulent flows e.g. [173, 174, 175, 176, 177, 178], as well as low-Reynolds-number, internal flows, which are the focus of the present paper (e.g. [166, 14, 15, 168, 16, 17, 18, 179, 20]). At low Reynolds numbers, the use of SHSs has been proposed to reduce what are otherwise very large pressure differences across microchannels, as is the case in microfluidic devices or in micro-cooling applications [180, 181, 182], as well as to minimize Taylor dispersion in the chemical or biological analysis of species [167].

However, laminar-flow experimental results have been mixed. While early works reported large drag reduction (e.g. [14, 183, 184]), several more recent studies found no benefits, even though a plastron was clearly retained on the surface [16, 17, 185]. [162] reviewed possible

sources of experimental errors that might have affected some of the early measurements.

A key step towards solving this puzzle has come with the realization that surfactants could induce Marangoni stresses that impair drag reduction. More specifically, [16] experimentally examined flow over an SHS consisting of gratings perpendicular to the flow, for which they found no measurable slip at the surface. [17] also found negligible slip for an SHS consisting of gratings aligned with the flow, in contradiction with traditional theoretical and numerical results. [17] hypothesized that surfactant effects could be to blame. Following this hypothesis, surfactants naturally present in water would adsorb onto the air–water interface, as sketched in figure 5.1(a). They would then be advected by the flow and accumulate at downstream stagnation points, where the interface terminates in a three-phase contact line. The resulting surfactant gradient would therefore produce a Marangoni stress opposing the fluid motion, thereby decreasing slip and increasing drag (figure 5.1b). Since traditional models of SHSs are surfactant-free, they cannot account for this additional surfactant-induced Marangoni drag.

Motivated by this hypothesis, [18] performed detailed measurements of the interface slip on an SHS comprising posts. They reported slip velocities far smaller than predicted by surfactant-free simulations. The slip pattern also exhibited strong anisotropy, consistently with what may be expected from surfactant-induced Marangoni stresses in their geometry. Deliberately adding surfactant resulted in a further small decrease in slip, although the magnitude of this change was within experimental uncertainty. [179] performed unsteady microchannel experiments over SHS consisting of gratings aligned with the flow. By introducing unsteady forcing, they uncovered complex interfacial responses that could only be explained by surfactant effects. They found that, if the driving pressure difference across the microchannel is suddenly removed, the plastron starts flowing backwards relative to the initial flow due to a surfactant-induced Marangoni force. The reverse flow decays as the inverse power of time, consistently with a similarity solution that assumes advection-dominated surfactant transport at the interface.

Since numerous works [16, 17, 18, 179, 20] observed drastically reduced slip even in nominally clean conditions, [179] performed steady simulations inclusive of surfactants, where they

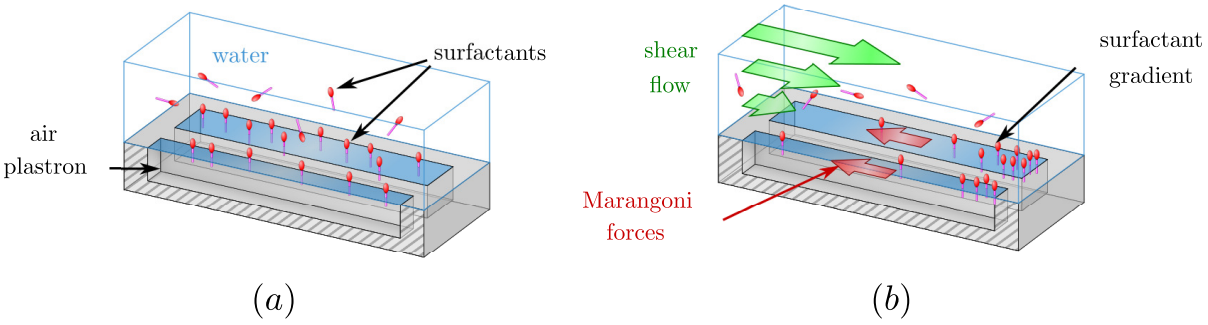

Figure 5.1: Schematic illustrating the impact of surfactants above a superhydrophobic surface (SHS) made of longitudinal rectangular grating. (a) Surfactants present in water adsorb at the air–water interface of the gratings. (b) In the presence of an external flow, surfactants distribute in gradients between stagnation points, yielding a Marangoni stress opposing the flow.

could precisely control surfactant concentrations. They found that surfactant effects can impair drag reduction even at extremely low surfactant concentrations, well below values naturally occurring in the laboratory or the environment. They also found that increasing the streamwise distance between stagnation points on the SHS helped to reduce the surfactant gradient and to increase slip. This explained the large slip achieved in the previous experiments of [183], who used a circular rheometer with annular gratings. Annular gratings are effectively infinitely long, without any stagnation point for surfactants to accumulate, thus avoiding Marangoni stresses. To illustrate this sensitivity of surfactant-induced Marangoni stresses with respect to the interface geometry, [186] devised an experiment whereby a complex maze is solved by a small amount of surfactant, which is introduced at the maze entrance.

More recently, [20] performed detailed experiments on an SHS consisting of a rectangular cavity with small streamwise length. They found that the rectangular gas–liquid interface exhibits recirculation, with reverse flow developing either along the middle or the sides of the plastron, depending on whether the gas–liquid interface is deformed towards the liquid phase (convex) or towards the gas phase (concave), respectively. They performed simulations where a uniform stress was applied to the interface (to approximate a Marangoni stress), showing that the experimentally-observed recirculation pattern could be induced by surfactants.

While the importance of surfactants is an emerging topic in the context of superhydrophobic surfaces, it should be noted that the importance of surfactant effects has been well-established in many other interfacial flows, often after protracted scientific debates that sought explanations for surprising phenomena. Well-known examples can be found for small bubbles rising in water, where the increased drag due to surfactant adsorption has been studied extensively (see *e.g.* [187, 188, 189, 190] and references therein), as well as in dip-coating problems, where accounting for Marangoni stresses is important to predict the coating thickness [191]. In the ocean, the impact of naturally-occurring surfactants is well-established, as they have important effects on wave breaking and gas fluxes [192]. Furthermore, steady motions in the bulk (such as internal waves or Langmuir circulations) can cause accumulation of surfactants at the surface. The resulting change in the amplitude of capillary waves affects light scattering, as revealed by satellite photographs [193]. In laboratory models of oceanic flows, surfactant accumulation can be disproportionately important, driving stresses that qualitatively change the interior flow [194]. Traces of surfactant have also been shown to modify drastically the behavior of the air–water interface of small bubbles probed with atomic force microscopy (see [195, 196]). While a free-slip boundary condition would have been expected, force measurements demonstrated a cross-over between free-slip and no slip depending on the approaching speed of the cantilever or its probing frequency. These modified hydrodynamic boundary conditions are well-modelled by theories that include traces of surfactant, at levels undetectable through traditional surface tension measurements [195, 196]. These findings further support the notion that surfactant traces can qualitatively alter the hydrodynamics.

Predicting surfactant effects is also important since surface-active molecules are inevitably present in both natural end engineered applications. Indeed, biological or environmental samples have been found to contain large amounts of surface-active compounds, including water from seas, rivers, estuaries and fog [193, 197, 198]. For engineered systems, recently [199] used experiments involving insoluble liquid drops in water to demonstrate that uncrosslinked chains of polydimethylsiloxane (PDMS) can act as a surfactant. Since PDMS is one of the most com-

mon materials for microchannel fabrication, their results imply that surfactants are commonly present in microfluidic systems.

While this mounting evidence shows the importance of surfactant effects to superhydrophobic surfaces (at least in the laminar regime), there are presently no theoretical models that can predict slip as a function of surfactant properties and flow geometry.

In this paper, we build a scaling theory that describes slip length, and the associated Marangoni shear stress, in surfactant-laden laminar flows over SHS. As noted earlier, these surfactant effects are induced by accumulation of surfactant at stagnation points on the plastron, which are unavoidable in real applications (except in annular gratings in a rotating flow). As a fundamental model of such a flow, we consider a two-dimensional SHS consisting of transverse grooves, such as those considered by [16], [17] and [172]. This case also serves as an upper bound for the slip and drag reduction that will be obtained in a three-dimensional flow over finite rectangular gratings. Furthermore, the model developed here constitutes a stepping stone towards a more complex theory for three-dimensional flow over SHSs with surfactant.

The problem definition and governing equations are described in § 5.3. In § 5.4, we present the key assumptions which allow us to develop a low-order scaling model for the local slip length at the plastron, as a function of the relevant dimensionless numbers. In § 5.5, a model for the interior flow in a microchannel with a superhydrophobic side is developed, and coupled to the slip-length model to obtain the effective slip length and drag reduction for the overall channel flow. The overall theory is tested against numerical simulations of the full governing equations. The computational setup is described in § 5.6, and results are reported in § 5.7. Each parameter is varied over several orders of magnitude, confirming each aspect of the theory. The performance, key assumptions and potential uses of the theory are discussed in § 5.8, with conclusions presented in § 5.9. To ease adoption and testing of our model, MATLAB codes that automate the theoretical calculations are included as online supplementary material (https://doi.org/10.1017/jfm.2019.857).

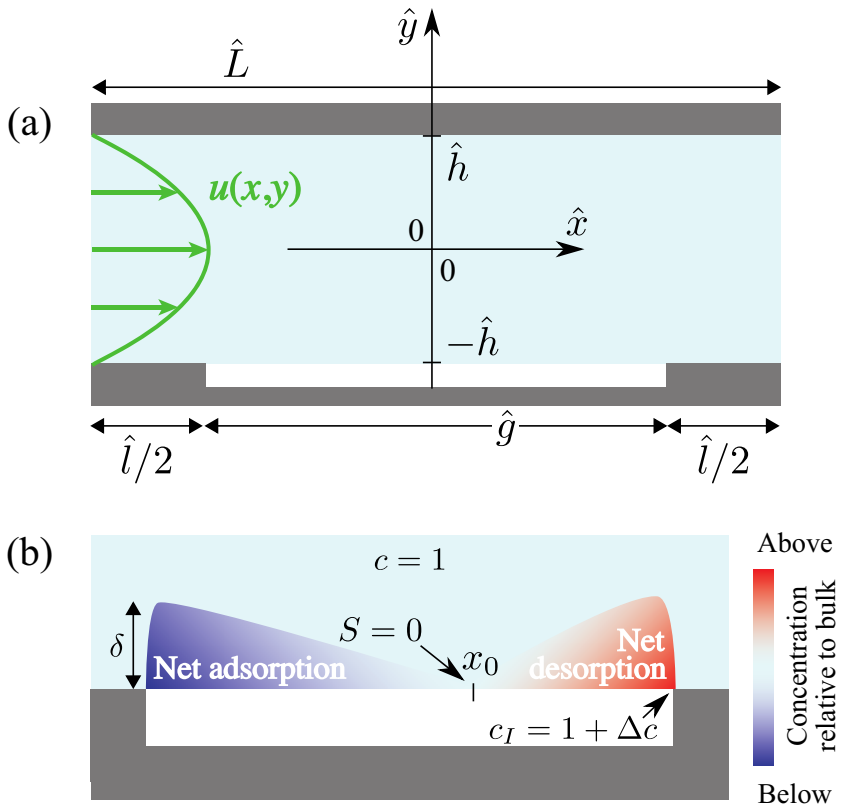

Figure 5.2: (a) Schematic of the geometry of the problem studied. (b) Schematic illustrating the bulk concentration profile near the interface.

5.3 Problem description and governing equations

We study a steady, laminar, two-dimensional liquid flow with a small concentration of surfactant in a channel with a periodic array of flat gas–liquid interfaces on one side, as illustrated in figure 5.2(a). This geometry is typical of microchannel experiments, where the smooth side of the channel is made transparent to ensure optical access (see *e.g.* [15, 17, 18, 179, 20]). We use hats to denote dimensional quantities throughout the paper, whilst dimensionless quantities are without hats. The dimensional velocity field is $\hat{\boldsymbol{u}}(\hat{x},\hat{y}) = (\hat{u}(\hat{x},\hat{y}),\hat{v}(\hat{x},\hat{y}))$. The surfactant bulk and interfacial concentration fields are $\hat{c}(\hat{x},\hat{y})$ and $\hat{\Gamma}(\hat{x})$, respectively. Owing to the periodicity of the geometry, we can restrict our study to a single periodic cell of total length $\hat{L}$ and height $2\hat{h}$, as shown in figure 5.2(a). This cell has a centred gas–liquid interface (hereafter designated as "the interface") of length $\hat{g}$ at $\hat{y} = -\hat{h}$, with solid surfaces on either side of the interface. The solid surfaces have overall combined length $\hat{l} = \hat{L} - \hat{g}$. Opposite to the interface is a solid surface, located at $\hat{y} = \hat{h}$. The flow is driven in the positive $\hat{x}$ direction by a constant streamwise mean pressure drop, per unit length, $\hat{G} = -\Delta\hat{p}/\hat{L} > 0$.

We deliberately choose to study the transverse flow over SHS gratings of arbitrary but finite length $\hat{g}$, instead of the longitudinal flow over infinitely long gratings as has been done in many previous theoretical and numerical studies [164, 165, 166, 169, 170, 173, 180, 172, 178]. Indeed, as mentioned in § 1, the establishment of adverse surfactant-induced Marangoni stresses requires stagnation points, as is necessarily found at the end of real SHS gratings, except in the special case of annular gratings [183]. One of the aim of our model is to predict the effect of $\hat{g}$ on the effective slip length, following the observations made by [179] that increasing $\hat{g}$ reduces surfactant-induced Marangoni stresses. As also noted earlier, the two-dimensional flow studied here will yield an upper bound for the slip and drag reduction that can be expected in a three-dimensional flow over finite rectangular gratings.

The governing steady conservation equations for mass, momentum, bulk surfactant, and interfacial surfactant can be found in dimensional form in [179]. We non-dimensionalize them using the channel half-height $\hat{h}$ as the length scale, the mean pressure drop per unit length $\hat{G}$

as the scale for pressure gradients, the corresponding velocity $\hat{U} = \hat{G}\hat{h}^2/\hat{\mu}$ as the velocity scale (with $\hat{\mu}$ the dynamic viscosity), the background bulk surfactant concentration $\hat{c}_0$ as the bulk concentration scale, and the maximum packing concentration of the surfactant at the interface $\hat{\Gamma}_m$ [200] as the interfacial concentration scale, such that

$$x = \frac{\hat{x}}{\hat{h}},\ y = \frac{\hat{y}}{\hat{h}},\ \boldsymbol{u} = \frac{\hat{\boldsymbol{u}}}{\hat{U}},\ \nabla p = \frac{\hat{\nabla}\hat{p}}{\hat{G}},\ c = \frac{\hat{c}}{\hat{c}_0},\ \Gamma = \frac{\hat{\Gamma}}{\hat{\Gamma}_m}. \tag{5.1}$$

The governing equations are, in dimensionless form,

$$\nabla \cdot \boldsymbol{u} = 0, \tag{5.2}$$

$$Re\nabla \cdot (\boldsymbol{u}\boldsymbol{u}) = -\nabla p + \nabla^2 \boldsymbol{u}, \tag{5.3}$$

$$\nabla \cdot (\boldsymbol{u}c) = \frac{1}{Pe}\nabla^2 c, \tag{5.4}$$

$$\frac{\mathrm{d}}{\mathrm{d}x}(u_I\Gamma) = \frac{1}{Pe_I}\frac{\mathrm{d}^2\Gamma}{\mathrm{d}x^2} + S(c_I,\Gamma) \quad \text{on the interface}, \tag{5.5}$$

where bold symbols are used for vectors, $u_I(x)$ designates the velocity at the interface, and $p(x,y)$ is the bulk pressure. The subscript I designates the limit of the bulk quantity considered, as it approaches the interface. In general, this limit is equal to the value taken by the quantity at the interface, except where mentioned explicitly. For instance, we have $u_I(x) = \lim_{y\to -1^+} u(x,y) = u(x,y=-1)$ for $|x| < g/2$. The Reynolds number Re, and bulk and interfacial Péclet numbers Pe, Pe_I are defined below after (5.17), together with all other dimensionless groups in the problem. A summary is also provided in table 5.1.

We assume that the source–sink term modelling the flux of surfactants between the bulk and the interface follows kinetics consistent with the Frumkin isotherm, which has been found to model accurately single-component surfactant systems [201, 200],

$$S(c_I,\Gamma) = Bi\left(kc_I(1-\Gamma) - \mathrm{e}^{A\Gamma}\Gamma\right). \tag{5.6}$$

with $c_I(x) = \lim_{y\to -1^+} c(x,y)$ for $|x| < g/2$. Here A is the Frumkin interaction parameter,

which takes negative values $A < 0$ for surfactants with attractive intermolecular interactions and positive values $A > 0$ in the case of repulsive interactions. This sign convention for A coincides with the one adopted by [200], but the opposite convention can also be found elsewhere in the literature (e.g. in [201]). In (5.6), we note that the bulk concentration near the interface c_I is different from the interfacial concentration Γ. This follows the subsurface layer model, where adsorption and desorption kinetics occur between a bulk subsurface layer and the interface [201]. We note that $S > 0$ corresponds to an adsorption flux and $S < 0$ to a desorption flux, see figure 5.2(b). By definition, $\boldsymbol{u}$ and c are periodic (with period L), while the pressure p has a normalized mean drop per unit of length of -1, which is enforced by imposing a net pressure drop of value L across each periodic unit of length L, so that

$$\boldsymbol{u}(x,y) = \boldsymbol{u} \quad (x+L,\, y), \tag{5.7}$$

$$c(x,y) = c \quad (x+L,\, y), \tag{5.8}$$

$$\text{and } p(x,y) = p \quad (x+L,\, y) + L. \tag{5.9}$$

The boundary conditions include

$$\boldsymbol{u} = \boldsymbol{0} \quad \text{on all solid surfaces (no slip)}, \tag{5.10}$$

$$v = 0 \quad \text{on the interface (no penetration)}, \tag{5.11}$$

$$\frac{\partial c}{\partial y} = 0 \quad \text{on all solid surfaces (no flux)}, \tag{5.12}$$

$$\frac{\mathrm{d}\Gamma}{\mathrm{d}x} = 0 \quad \text{at } (x = \pm\frac{g}{2},\, y = -1) \text{ (no flux)}. \tag{5.13}$$

Additionally, the continuity of the surfactant fluxes between the bulk and the interface is given by

$$\frac{\chi k}{Pe}\left.\frac{\partial c}{\partial y}\right|_I = S(c_I, \Gamma) \quad \text{on the interface}. \tag{5.14}$$

The last piece of the model is the balance of forces between the viscous drag from the bulk flow and the surfactant Marangoni force at the interface. The decrease in surface tension σ induced

by the surfactant is given by an equation of state consistent with the Frumkin isotherm [200], that is

$$\sigma = 1 + Ma\ Ca \left[\ln\left(1-\Gamma\right) - \frac{A\Gamma^2}{2} \right], \tag{5.15}$$

and the Marangoni shear stress at the interface is given by the gradient of surface tension, yielding the last boundary condition

$$\left.\frac{\partial u}{\partial y}\right|_I = -\frac{1}{Ca}\,\frac{\mathrm{d}\sigma}{\mathrm{d}x}\,, \tag{5.16}$$

$$\text{that is} \quad \left.\frac{\partial u}{\partial y}\right|_I = Ma\left(\frac{1}{1-\Gamma} + A\Gamma\right)\frac{\mathrm{d}\Gamma}{\mathrm{d}x} \quad \text{on the interface.} \tag{5.17}$$

The chosen characteristic scales imply the following definitions for the dimensionless groups. The Reynolds number is $Re = \hat{\rho}\hat{h}\hat{U}/\hat{\mu}$, with $\hat{\rho}$ the liquid density. The bulk and interface Péclet numbers are $Pe = \hat{h}\hat{U}/\hat{D}$ and $Pe_I = \hat{h}\hat{U}/\hat{D}_I$, where $\hat{D}$ and $\hat{D}_I$ are the bulk and interface surfactant diffusivities, respectively. The Biot number is $Bi = \hat{\kappa}_d\hat{h}/\hat{U}$. The effective bulk concentration is $k = \hat{\kappa}_a\hat{c}_0/\hat{\kappa}_d$, where $\hat{\kappa}_a$ and $\hat{\kappa}_d$ are the adsorption and desorption coefficients, respectively. Note that, consistently with the canonical definition of Frumkin kinetics, the adsorption and desorption coefficients $\hat{\kappa}_a$ and $\hat{\kappa}_d$ have different units, so that k is non-dimensional. The surfactant adsorption–desorption kinetics are parameterized by $\chi = \hat{\kappa}_d\hat{h}/(\hat{\kappa}_a\hat{\Gamma}_m)$. We note that $\chi k = \hat{c}_0\hat{h}/\hat{\Gamma}_m$ in (5.14) is effectively the non-dimensional ratio between the characteristic bulk and interfacial concentration scales. The Marangoni number is $Ma = n_\sigma\hat{R}\hat{T}\hat{\Gamma}_m/(\hat{\mu}\hat{U})$, where n_σ is a parameter associated with the Frumkin isotherm [201], $\hat{R}$ is the universal gas constant, and $\hat{T}$ is the absolute temperature. Temperature-driven Marangoni effects are not considered in this study and we assume that temperature is uniform in the domain. Note also that the capillary number $Ca = \hat{\mu}\hat{U}/\hat{\sigma}_0$ (where $\hat{\sigma}_0$ is the surface tension of a clean interface) has no effect in our model, since it does not appear in the final form of the Marangoni boundary condition (5.17) and we do not consider any other physical mechanism, such as interface curvature, in which it could play a role (§ 5.8.5 provides a discussion of this assumption).

The governing equations (5.2–5.5) with the periodicity and boundary conditions (5.7–5.14 and 5.17) define a complex nonlinear coupled problem where the unknowns are the two-dimensional velocity field $\boldsymbol{u}$, the pressure p, the bulk concentration c and the interfacial concentration Γ. This transport problem depends on nine non-dimensional numbers, which collectively depend on a combination of flow, liquid and surfactant properties, as well as geometry, namely Re, Pe, Pe_I, Bi, k, χ, Ma, $g = \hat{g}/\hat{h}$ and $\phi = g/L = \hat{g}/\hat{L}$. Here g is the normalized interface length, whereas ϕ is the gas fraction. According to (5.17), a surfactant-induced Marangoni shear can develop at the interface when a gradient of interfacial surfactant concentration forms.

The main goal of this study is to determine a low-order model for the interfacial Marangoni shear rate $\partial u/\partial y|_I \geq 0$ and the interfacial velocity $u_I \geq 0$ as a function of the nine non-dimensional numbers above, considering realistic parameter regimes. Such model could be used, for instance, to parameterise a slip-length condition in direct numerical simulations of flow over SHS, without having to solve the full complex coupled problem above.

5.4 Scaling theory for slip length with surfactant traces

5.4.1 Introducing the Marangoni concentration $k^* \equiv k\,Ma$ for small concentrations

The key assumption we propose is that the normalised interfacial surfactant concentration Γ is sufficiently small, such that (5.6) and (5.17) can be linearised. The same assumption was made by [202] for the study of air bubbles rising in contaminated water. Hence, we obtain kinetics congruent with the Henry isotherm [201], namely

$$S(c_I, \Gamma) \approx Bi\,(kc_I - \Gamma)\,, \tag{5.18}$$

$$\left.\frac{\partial u}{\partial y}\right|_I \approx Ma \frac{\mathrm{d}\Gamma}{\mathrm{d}x} \quad \text{on the interface.} \tag{5.19}$$

In many realistic situations where surfactants are not artificially added, we indeed expect to have low effective bulk concentrations, i.e. $k \ll 1$, which generally lead to small interfacial

concentrations Γ. The interfacial concentration is usually away from saturation, i.e. $\Gamma \ll 1$, because the maximum packing concentration $\hat{\Gamma}_m$ used in surfactant models is in fact based on geometrical arguments [203] or on achieving good fit of experimental data based on a specific kinetic model [201]. Hence, $\hat{\Gamma}_m$ is usually not attained even when the bulk concentration is at the critical micellar concentration. We also have $A \lesssim 1$ for common surfactants (see [200]). We discuss further the relevance of our assumption $\Gamma \ll 1$ in the context of applications in § 5.8.

We take advantage of the linearisation of (5.6) and (5.17) to propose a parameter reduction in our problem, by introducing the following rescaled effective Marangoni concentration and surface concentration

$$k^* \equiv Ma\, k, \qquad \Gamma^* \equiv Ma\, \Gamma. \tag{5.20a,b}$$

Substituting $k = k^*/Ma$ and $\Gamma = \Gamma^*/Ma$ into (5.5), (5.14) and (5.13), with the Henry kinetics (5.18) and (5.19), we obtain a set of equations where k and Ma have been combined to form k^*, thereby reducing by one the number of dimensionless groups. This can be verified by examining the updated version of the complete set of equations (5.2)-(5.13), which becomes

$$\nabla \cdot \boldsymbol{u} = 0, \tag{5.21}$$

$$Re \nabla \cdot (\boldsymbol{u}\boldsymbol{u}) = -\nabla p + \nabla^2 \boldsymbol{u}, \tag{5.22}$$

$$\nabla \cdot (\boldsymbol{u} c) = \frac{1}{Pe} \nabla^2 c, \tag{5.23}$$

$$\frac{\mathrm{d}}{\mathrm{d}x}(u_I \Gamma^*) = \frac{1}{Pe_I} \frac{\mathrm{d}^2 \Gamma^*}{\mathrm{d}x^2} + Bi(k^* c_I - \Gamma^*) \quad \text{on the interface,} \tag{5.24}$$

with boundary conditions

$$\begin{aligned}
\boldsymbol{u} &= \mathbf{0} \quad \text{on all solid surfaces,} && (5.25)\\
v &= 0 \quad \text{on the interface,} && (5.26)\\
\frac{\partial c}{\partial y} &= 0 \quad \text{on all solid surfaces,} && (5.27)\\
\frac{\mathrm{d}\Gamma^*}{\mathrm{d}x} &= 0 \quad \text{at } (x = \pm\frac{g}{2}, y = -1), && (5.28)\\
\frac{\chi k^*}{Pe}\left.\frac{\partial c}{\partial y}\right|_I &= Bi(k^* c_I - \Gamma^*) \quad \text{on the interface,} && (5.29)\\
\left.\frac{\partial u}{\partial y}\right|_I &= \frac{\mathrm{d}\Gamma^*}{\mathrm{d}x} \quad \text{on the interface,} && (5.30)
\end{aligned}$$

such that the three quantities k, Γ and Ma have been replaced by the dimensionless number k^* and the variable Γ^*.

5.4.2 Scaling theory for surfactant dynamics

To make further progress in modelling the shear rate $\partial u/\partial y|_I$ and velocity u_I, we perform a scale analysis on the equations in our problem, starting with rearranging (5.29), which expresses continuity of surfactant fluxes between the bulk and the interface

$$\left.\frac{\partial c}{\partial y}\right|_I = \frac{Bi\,Pe}{\chi k^*}\left(k^* c_I - \Gamma^*\right). \tag{5.31}$$

For steady flows, adsorption and desorption fluxes between the bulk and the interface are in balance overall, implying

$$\int_{-g/2}^{g/2} \left.\frac{\partial c}{\partial y}\right|_I \mathrm{d}x = \frac{Bi\,Pe}{\chi k^*}\int_{-g/2}^{g/2}\left(k^* c_I - \Gamma^*\right)\mathrm{d}x = 0, \tag{5.32}$$

such that, by the mean value theorem, there is a point on the interface where $\partial c/\partial y|_I = 0$ and $k^* c_I = \Gamma^*$. With a flow in the positive x-direction, interfacial surfactant Γ^* is advected downstream, such that the beginning of the interface has a lower surfactant concentration,

implying that $\Gamma^* < k^* c_I$, and that an adsorption flux exists from the bulk onto the beginning of the interface, such that $\partial c/\partial y|_I > 0$ there, as illustrated in figure 5.2(b). By the same argument, near the end of the interface, a higher surfactant concentration $\Gamma^* > k^* c_I$ leads to desorption from the interface into the bulk, implying $\partial c/\partial y|_I < 0$. Therefore, somewhere along the interface, we must have $\partial c/\partial y|_I = 0$. We designate by x_0 this location where the kinetics flux $S = 0$, as depicted in figure 5.2(b).

In addition, at the beginning of the interface, c_I is less than the bulk concentration, i.e. $c_I < 1$ with our nondimensionalization, whereas towards the end of the interface, where surfactants accumulate, $c_I > 1$. This means that, at a specific location along the interface, the concentration near the interface is equal to the background bulk concentration, that is $c_I = 1$. Taking $c_I \sim 1$ along the interface, we then find that (5.31) implies that the interfacial concentration scales as $\Gamma^* \sim k^*$.

Next, assuming that the variations of c_I and Γ scale in the same way for the adsorption region, $-g/2 < x < x_0$, and the desorption region, $x_0 < x < g/2$, we have

$$\Gamma^* \sim k^* \mp \Delta\Gamma^*, \quad c_I \sim 1 \mp \Delta c_I, \tag{5.33}$$

for the adsorption ($-$) and desorption ($+$) regions, respectively (see figure 5.2b). The quantities $\Delta\Gamma^*$ and Δc_I are the characteristic variations of Γ^* and c_I, respectively. We must have $\Delta\Gamma^* > k^* \Delta c_I > 0$ to satisfy the direction of the kinetics flux, as described above.

From the relation between Marangoni stress and surfactant gradient (5.19), we also have

$$\Delta\Gamma^* \sim g\gamma_{Ma}, \tag{5.34}$$

where

$$\gamma_{Ma} = \frac{1}{g}\int_{-g/2}^{g/2} \left.\frac{\partial u}{\partial y}\right|_I \mathrm{d}x \tag{5.35}$$

is the average shear rate induced by Marangoni stresses along the interface, such that $\gamma_{Ma} = 0$ corresponds to free-slip at the interface and $\gamma_{Ma} = 1$ corresponds to a no-slip interface. Then,

a scale analysis of (5.31) gives

$$\left.\frac{\partial c}{\partial y}\right|_I \sim \frac{\Delta c_I}{\delta} \sim \frac{Bi\, Pe}{\chi k^*}\left(g\gamma_{Ma} - k^*\Delta c_I\right), \tag{5.36}$$

where δ is the typical thickness of the diffusive layer of bulk surfactant. To estimate δ, we can use the bulk advection–diffusion equation (5.4). At high Péclet numbers, $Pe \gg 1$, the diffusive layer of surfactant forms a thin boundary layer. As explained in detail in appendix 5.11, there are two main asymptotic regimes depending on whether there is slip or not at the interface. For large slip and small interfacial shear rate, $\gamma_{Ma} \ll 1$, we can show that the boundary layer thickness scales as (see appendix 5.11)

$$\frac{\delta}{g} = \delta_{0,1}\left(1 + \delta_{1,1} g^2 Pe\right)^{-1/2} \quad \text{for } g \lesssim 1, \tag{5.37}$$

$$\frac{\delta}{g} = \delta_{0,2}\left(1 + \delta_{1,2} g Pe\right)^{-1/2} \quad \text{for } g \gtrsim 1, \tag{5.38}$$

where $\delta_{0,1}$, $\delta_{1,1}$, $\delta_{0,2}$, $\delta_{1,2}$ are empirical parameters which need to be determined. We note that the scaling $\delta \sim Pe^{-1/2}$ at large Péclet numbers corresponds to having a uniform velocity in the diffusive boundary layer, consistently with the case $\gamma_{Ma} \ll 1$.

For negligible slip at the interface and $\gamma_{Ma} \sim 1$, we obtain

$$\frac{\delta}{g} = \delta_{0,3}\left(1 + \delta_{1,3} g^2 Pe\right)^{-1/3}, \tag{5.39}$$

for any $g > 0$, and with $\delta_{0,3}$ and $\delta_{1,3}$ two empirical parameters which need to be determined. This corresponds to the Lévêque regime [204, 205], giving a power law $\delta \sim Pe^{-1/3}$ at large Péclet numbers owing to a linear shear rate profile in the diffusive boundary layer. The scalings (5.37)–(5.39) assume that: (i) the variation of the bulk concentration along the interface is sufficiently smooth; (ii) the boundary layer is not confined vertically, i.e. $\delta \lesssim 1$; and (iii) the diffusive boundary layers between consecutive interfaces are independent. As we will discuss in § 5.7, our scaling prediction remains accurate even for confined diffusive boundary layers $\delta \sim 1$.

With δ assumed known in terms of g and Pe, we rearrange (5.36) to solve for Δc_I

$$\Delta c_I \sim \gamma_{Ma} \frac{\frac{Bi\,Pe}{\chi k^*}\, g\, \delta}{1 + \frac{Bi\,Pe}{\chi}\delta}, \tag{5.40}$$

such that, dividing by δ, we obtain a scaling that relates the kinetics flux to the shear

$$\left.\frac{\partial c}{\partial y}\right|_I \sim \frac{\Delta c_I}{\delta} \sim \gamma_{Ma} \frac{\frac{Bi\,Pe}{\chi k^*} g}{1 + \frac{Bi\,Pe}{\chi}\delta}. \tag{5.41}$$

5.4.3 Scaling for the interfacial velocity and for the slip length

We now seek a scaling expression for u_I. We integrate the interfacial advection–diffusion equation (5.24) from the upstream stagnation point $x = -g/2$ to x_0. We find

$$(u_I \Gamma^*)|_{x_0} = \frac{1}{Pe_I} \left.\frac{\mathrm{d}\Gamma^*}{\mathrm{d}x}\right|_{x_0} + \frac{k^* \chi}{Pe} \int_{-g/2}^{x_0} \left.\frac{\partial c}{\partial y}\right|_I \mathrm{d}x, \tag{5.42}$$

where we used the no-slip boundary condition (5.25) at $x = -g/2$ for the left hand side, the no flux boundary condition (5.28) at $x = -g/2$ for the first term on the right hand side, as well as the continuity of flux condition (5.29) for the last term. To write the right-hand side in terms of γ_{Ma}, note that $\Gamma^*|_{x_0} \sim k^*$ and $\mathrm{d}\Gamma^*/\mathrm{d}x|_{x_0} \sim \gamma_{Ma}$. For the last term, we use (5.41) to scale the integral

$$\int_{-g/2}^{x_0} \left.\frac{\partial c}{\partial y}\right|_I \mathrm{d}x \sim g \frac{\Delta c_I}{\delta} \sim \gamma_{Ma} \frac{\frac{Bi\,Pe}{\chi k^*} g^2}{1 + \frac{Bi\,Pe}{\chi}\delta}. \tag{5.43}$$

Substituting into (5.42) we obtain a scaling relation between interfacial velocity and shear. Introducing empirical prefactors (to be determined) ahead of each term, we write

$$u_I|_{x_0} = \frac{2}{a_1} \frac{1}{k^*} \left(\frac{1}{Pe_I} + a_2 \frac{g^2 Bi}{1 + \frac{BiPe}{\chi}\delta} \right) \gamma_{Ma}, \tag{5.44}$$

where a_1, a_2 are empirical parameters; the choice of writing $2/a_1$ for the overall prefactor leads to a more convenient expression for the results later in § 5.7.1.

As also noted in the previous section, scaling expressions for the boundary layer thickness

δ are given by (5.37), (5.38) or (5.39), which depend on g, ϕ and γ_{Ma}. Therefore, our scaling is a nonlinear function of the Marangoni shear rate. However, in the comparison of our model with numerical simulations (see § 5.7), we find that the nonlinear dependence of γ_{Ma} with δ is actually weak. Consequently, we adopt only (5.39) in our model. This proves to be a good approximation and allows us to regard δ as independent from γ_{Ma}.

Furthermore, we note that a first-order linear expansion of the concentrations c and Γ near x_0 predicts $a_2 = 1/8$ since $x_0 = 0$ (that is, x_0 is at the mid-gap location) due to the balance of desorption and adsorption fluxes along the interface.

A characteristic scale for the slip length near x_0, which corresponds to the mid-gap of the interface under our assumptions, is therefore simply

$$\lambda_{x_0} = \frac{u_I|_{x_0}}{\gamma_{Ma}} = \frac{2}{a_1}\frac{1}{k^*}\left(\frac{1}{Pe_I} + a_2\frac{g^2 Bi}{1+\frac{BiPe}{\chi}\delta}\right). \tag{5.45}$$

This scaling prediction shows that the local slip length λ_{x_0} depends strongly on the Marangoni concentration $k^* = k\,Ma$ and the normalised gap length g. It is intuitive that increasing the gap length tends to increase the slip length, since it would reduce the concentration gradient at the interface and thus the opposing Marangoni stress. In contrast, increasing the effective bulk surfactant concentration k or the Marangoni number tends to reduce the slip length, as expected. We also find increasing the bulk or interfacial Péclet numbers, Pe or Pe_I, reduces λ_{x_0}. Increasing the Biot or χ numbers has a positive effect on the slip length.

However, we note that (5.45) is only a local measure of the characteristic slip length near the middle of the interface, where $S(x_0) = 0$. In order to have an effective or global slip length over the entire SHS which takes into account all interfaces and solid ridges, we also need to model the channel flow over the SHS. In the next section, we analyse the remaining governing equations for the flow, i.e. the continuity and Navier–Stokes equations (5.21) and (5.22), to study how the flow is affected by a SHS with a surfactant-induced Marangoni stress over the interfaces.

5.5 Complete model for effective slip in channel flows with one-sided periodic transverse ridges

5.5.1 Stokes flow model for SHS channels with surfactant contamination

According to equation (5.19), interfacial surfactant concentration gradients can generate a Marangoni shear rate at the interface $\partial u/\partial y|_I \approx \mathrm{d}\Gamma^*/\mathrm{d}x \geq 0$. In this section, we derive an expression for how interfacial stresses with arbitrary profile can affect the flow over a periodic SHS. The geometry follows the same schematic presented in figure 5.2. Such a periodic SHS arrangement was studied in detail by [166] and [170] for a shear-free interface, i.e. with $\partial u/\partial y|_I = 0$ along the interface, at low Reynolds number. Here we generalize their approach to also study the case where $\partial u/\partial y|_I \geq 0$. We also assume $Re \ll 1$, such that (5.22) simplifies to the Stokes flow equation

$$\nabla p = \nabla^2 \boldsymbol{u}. \tag{5.46}$$

Taking the curl of (5.46) and using the continuity equation (5.21), we find that the pressure field p and the vorticity field, $\boldsymbol{\omega} = \nabla \times \boldsymbol{u}$ are both solutions of Laplace's equation. Using the superposition principle to solve Laplace's equation for the vorticity, we decompose it as the sum of the two-dimensional Poiseuille flow component, which is a pressure driven flow in a channel with full solid walls on both sides (denoted by a subscript p), and a deviating component (denoted by a subscript d), such that

$$\omega = \omega_p + \omega_d, \tag{5.47}$$

where $\omega_p = y$. As the flow is incompressible, we can also use the streamfunction $\boldsymbol{\Psi}$, defined such that $\boldsymbol{u} = \nabla \times \boldsymbol{\Psi}$, and which is the solution of the biharmonic equation $\nabla^4 \boldsymbol{\Psi} = \boldsymbol{0}$. Note that $\boldsymbol{\Psi} = (0, 0, \Psi)$ for two-dimensional flows. The solution for the deviating component of the vorticity is obtained using separation of variables considering the periodicity of the flow with wavelength L. Integrating twice, we then obtain the deviation streamfunction [166, 170].

Noting that the mean pressure gradient imposed by the deviating field is zero, neglecting the constant of integration, and using the no-flow boundary condition $v = 0$ in (5.25) and (5.26), the deviating component of the streamfunction is

$$\begin{aligned}\Psi_d =& B\frac{y^2}{2} + Ey + \sum_{n=1}^{\infty}\Big\{e_n\big[\cosh(k_n y) - \coth(k_n) y \sinh(k_n y)\big] \\ &+ d_n\big[\sinh(k_n y) - \tanh(k_n) y \cosh(k_n y)\big]\Big\}\cos(k_n x),\end{aligned} \tag{5.48}$$

where $k_n = 2\pi n/L$, and B, E, e_n and d_n are unknowns to be determined using the other boundary conditions. The streamfunction for the Poiseuille component is

$$\Psi_p = \frac{1}{6}(3y - y^3). \tag{5.49}$$

Up to this point, (5.48) and (5.49) are general solutions for any arrangement and geometry of SHS in a two-dimensional Stokes flow channel: i.e. they are not limited to one-sided SHS, symmetric patterns, or a particular shear rate profile at the interface.

With our geometry, using the no-slip boundary condition on the solid wall side at $y = 1$ for all x, we find $B = -E$ and

$$g_n = \frac{e_n}{d_n} = -\frac{\sinh(k_n) - k_n\cosh(k_n) + k_n\tanh(k_n)\sinh(k_n)}{\cosh(k_n) - k_n\sinh(k_n) + k_n\coth(k_n)\cosh(k_n)}. \tag{5.50}$$

Hence, the deviating streamfunction simplifies to

$$\begin{aligned}\Psi_d =& \left(-\frac{y^2}{2} + y\right)E + \sum_{n=1}^{\infty} d_n\Big\{g_n\big[\cosh(k_n y) - \coth(k_n) y \sinh(k_n y)\big] \\ &+ \sinh(k_n y) - \tanh(k_n) y \cosh(k_n y)\Big\}\cos(k_n x).\end{aligned} \tag{5.51}$$

To determine the unknowns E and d_n for $n \geq 1$, we can use the no-slip boundary condition

on the SHS side. At $y = -1$ for $g/2 < |x| < L/2$, we have the condition

$$0 = 2E + \sum_{n=1}^{\infty} d_n \alpha_n \cos(k_n x), \tag{5.52}$$

where

$$\alpha_n = 2k_n \Big[\cosh(k_n) - \tanh(k_n) \sinh(k_n) \Big] - 2 \sinh(k_n). \tag{5.53}$$

We then apply the last boundary condition on the interface, where we assume that there is an arbitrary shear rate profile $\partial u/\partial y|_I (x) \geq 0$. Hence, we obtain the general condition

$$0 = \frac{\partial u}{\partial y}\Big|_I - 1 + E + \sum_{n=1}^{\infty} d_n \beta_n \cos(k_n x) \tag{5.54}$$

for $|x| < g/2$, $y = -1$, and with

$$\beta_n = 2k_n \Big[g_n \coth(k_n) \cosh(k_n) - \tanh(k_n) \sinh(k_n) \Big]. \tag{5.55}$$

To make further progress and obtain a relationship between the interfacial shear rate and the interfacial velocity, we now assume that the interfacial shear rate is uniform along the interface: $\partial u/\partial y|_I = \gamma_{Ma}$, where $0 \leq \gamma_{Ma} \leq 1$ corresponds to the interface-averaged surfactant-induced Marangoni shear rate, as introduced previously in (5.34). This assumption is consistent with having a uniform concentration gradient, following the linearised coupling condition (5.19). In the context of air bubbles rising in surfactant-contaminated water, this assumption is also consistent with the 'uniformly retarded' regime described for instance by [190]. In the context of SHS, a similar assumption was made by [206] to model viscous effects from a gas phase trapped inside the cavities of the SHS. This allowed them to decouple the flow above the interface from the flow in the cavity of the SHS. We discuss further the relevance of this assumption in applications in § 5.8. Hence, (5.54) becomes

$$0 = \gamma_{Ma} - 1 + E + \sum_{n=1}^{\infty} d_n \beta_n \cos(k_n x). \tag{5.56}$$

If $\gamma_{Ma} = 0$ in the equation above, the interface is stress free and the surfactant concentration gradient at the interface vanishes. The surface is completely immobilized if $\gamma_{Ma} = 1$, and the flow follows a channel Poiseuille flow.

Following [166], we can compute an approximation of the solution by truncating the series in equations (5.52) and (5.56) at $n = N - 1$, multiplying (5.52) and (5.56) by $\cos(2\pi m r)$ for $m \in [0, N-1]$ (with $r = x/L$) and integrating them for $r \in (\phi/2, 1/2)$ and $r \in (0, \phi/2)$, respectively, where ϕ is the gas fraction. Summing together the results for each m in one single equation, we finally obtain a linear system of N equations for the N unknown coefficients E and d_n for $n \in [1, N-1]$, which we can solve numerically. The linear system in matrix form is, for $m \in [0, N-1]$ and $n \in [0, N-1]$,

$$\boldsymbol{A}_{m,n}\boldsymbol{U}_n = \boldsymbol{B}_m, \tag{5.57}$$

with $U_0 = E$ and $U_n = d_n$. The square matrix $\boldsymbol{A}_{m,n}$ has coefficients

$$A_{0,0} = 1 - \frac{\phi}{2}, \tag{5.58}$$

$$A_{0,n} = (\beta_n - \alpha_n)\frac{\sin(\pi n\phi)}{2\pi n},\ n > 0 \tag{5.59}$$

$$A_{m,0} = -\frac{\sin(\pi m\phi)}{2\pi m},\ m > 0 \tag{5.60}$$

$$A_{n,n} = \frac{\alpha_n}{4} + (\beta_n - \alpha_n)\left(\frac{\phi}{4} + \frac{\sin(2\pi n\phi)}{8\pi n}\right),\ n > 0 \tag{5.61}$$

$$A_{m,n} = (\beta_n - \alpha_n)\frac{1}{4\pi}\left(\frac{\sin(\pi(m+n)\phi)}{m+n} + \frac{\sin(\pi(m-n)\phi)}{m-n}\right),\ m \neq n > 0 \tag{5.62}$$

and the vector $\boldsymbol{B}_m$ has coefficients

$$B_0 = (1 - \gamma_{Ma})\frac{\phi}{2}, \tag{5.63}$$

$$B_m = (1 - \gamma_{Ma})\frac{\sin(\pi m\phi)}{2\pi m},\ m > 0. \tag{5.64}$$

Care must be taken at large n, where the system is not well conditioned, as pointed out by

[170]. We provide, as supplementary material (see https://doi.org/10.1017/jfm.2019.857), MATLAB routines solving the linear system (5.57).

5.5.2 Interfacial slip velocity

Once all the coefficients E and d_n are computed, the non-dimensional slip velocity at the interface u_I can be determined to machine precision, depending on the size N of the matrix $\boldsymbol{A}$, such that

$$u_I = 2E + \sum_{n=1}^{\infty} d_n \alpha_n \cos(k_n x). \tag{5.65}$$

Through its coefficients E and d_n, (5.65) is a function of the uniform Marangoni interfacial shear rate γ_{Ma} and of the two non-dimensional geometrical parameters g and ϕ. Hence, we have

$$u_I = \mathcal{G}(\gamma_{Ma}, g, \phi, x). \tag{5.66}$$

The function $\mathcal{G}$ is only known implicitly through the solution of the linear system (5.57). In practice, it would be useful to obtain an explicit analytical solution, or at least a scaling expression for $\mathcal{G}$ which can give an approximate solution to the coupled surfactant–flow transport problem in combination with (5.44). In the linear system (5.57), we can factorize all the coefficients of $\boldsymbol{B}_m$ by $(1 - \gamma_{Ma})$. This means that E and d_n are proportional to $(1 - \gamma_{Ma})$ for all $n \geq 1$. Thus, the velocity at the interface is such that

$$u_I = 2(1 - \gamma_{Ma})\mathcal{F}(g, \phi, x), \tag{5.67}$$

where, again, $\mathcal{F}$ is an implicit function. Now, $\mathcal{F}$ is decoupled from the surfactant transport problem since it does not depend on γ_{Ma}. It can thus be computed to arbitrary numerical precision for each couple of geometrical non-dimensional parameters (g, ϕ) and for all x by solving the linear system (5.57) in the surfactant-free case, i.e. setting $\gamma_{Ma} = 0$ in (5.63) and (5.64).

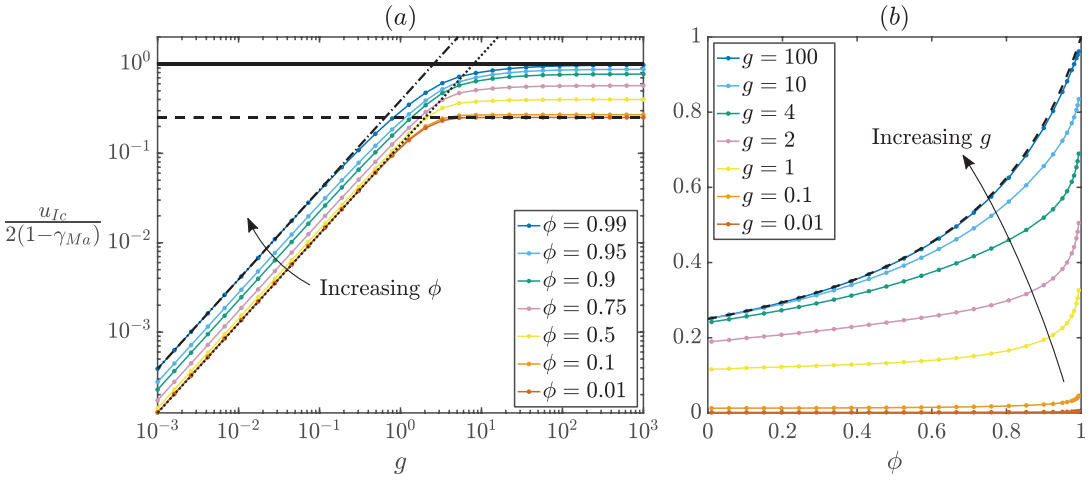

Figure 5.3: Variation of the normalised mid-gap interfacial velocity, $u_{Ic}/(2(1-\gamma_{Ma})) = \mathcal{F}(g,\phi,x=0) = \mathcal{F}_0(g,\phi)$ (see (5.67) and text), as a function of: (a) the non-dimensional interfacial length g, for different non-dimensional gas fraction from $\phi = 0.01$ to 0.99 (shown with different colors, see legend); (b) the gas fraction ϕ, for various interfacial lengths g (shown with different colors, see legend). The implicit function $\mathcal{F}_0(g,\phi)$ has been computed by solving the linear system (5.57) with $N = 500$, except in the more demanding cases of $0.01 < \phi \leq 0.1$ ($N = 2{,}500$), $0.99 \leq \phi \leq 1$ ($N = 2{,}500$) and $0 \leq \phi \leq 0.01$ ($N = 15{,}000$). In (a) the black dotted line is plotted using (5.69) for $\phi \ll 1$ and $g \lesssim 1$, the black dot-dashed line is plotted using (5.120) for $g \lesssim 1$ and $\phi = 0.99$, and the black dashed line is plotted using (5.70) for $\phi \ll 1$ and $g \gtrsim 1$. The black solid line corresponds to the maximum asymptotic value for $\phi \to 1$: $u_{I,c} \to u_u(y=-1) = 2(1-\gamma_{Ma})$ (see (5.72)). In (b), the black dashed line has been plotted using the asymptotic trend (5.73) for $g \gg 1$ (see also appendix 5.12).

Based on this observation, $\mathcal{F}(g,\phi,x) = u_I(x)/(2(1-\gamma_{Ma}))$ is a normalised interfacial velocity. In figure 5.3(a), we plot on a log–log scale this normalised interfacial velocity at the middle of the gap, $x = 0$:

$$\frac{u_{Ic}}{2(1-\gamma_{Ma})} = \mathcal{F}(g,\phi,x=0) = \mathcal{F}_0(g,\phi), \tag{5.68}$$

as a function of g and for different ϕ (shown with different colors, see legend). For $\phi \ll 1$ and $g \lesssim 1$, the normalised interfacial velocity follows a linear asymptotic trend

$$\frac{u_{Ic}}{2(1-\gamma_{Ma})} \simeq \frac{g}{8}, \tag{5.69}$$

plotted with a black dotted line in figure 5.3(a). We can see that for $\phi = 0.99$ the interfacial velocity still follows a linear scaling, although with a higher slope than in the asymptotic limit (5.69), as shown by the black dot-dashed line in figure 5.3(a), which was computed using (5.120). At large gap length, $g \gg 1$, and for low gas fraction, $\phi \ll 1$, the interfacial velocity collapses on the asymptotic plateau

$$\frac{u_{Ic}}{2(1-\gamma_{Ma})} \to \frac{1}{4}, \tag{5.70}$$

plotted with a black dashed line in figure 5.3(a). More details about the behaviour of the interfacial velocity u_{Ic} with ϕ and g and the two asymptotic limits (5.69) and (5.70) can be found in appendix 5.12. The transition observed at $g \sim 1$ from a linear trend towards a plateau is due to the importance of the opposite wall at $y = 1$ through viscous effects.

We note that the behaviour of $u_{I,c}/(2(1-\gamma_{Ma}))$ is similar across all g and for any ϕ. This function goes from a linear behaviour for $g \lesssim 1$ to a plateau for $g \gtrsim 1$, and with simple asymptotics in the case $\phi \ll 1$. Most of the data in figure 5.3(a) follows these limiting regimes, suggesting that asymptotic results are sufficiently accurate in many applications.

This common behavior of the interfacial velocity might also suggest that the velocity field follows a closed analytical form. However, we have not been able to demonstrate this theoretically from the biharmonic equation. As far as we are aware, the case of Stokes flow in a

transverse channel with mixed boundary conditions changing twice (on one or both channel sides), which is reminiscent of the longitudinal-channel work of [164], has not been shown to have a closed analytical form in the literature. It would be valuable to re-examine the present problem with conformal mapping tools similar to those used by [172, 207].

Figure 5.3(b) plots curves of $u_{I,c}/(2(1-\gamma_{Ma}))$ versus gas fraction ϕ, with g as a parameter. As the gas fraction ϕ increases towards 1, the normalised interfacial velocity increases rapidly at any fixed g. In the limit $\phi \to 1$ we have

$$\frac{u_{Ic}}{2(1-\gamma_{Ma})} \to 1, \tag{5.71}$$

which can be predicted from the velocity field with uniform boundary conditions at the top and bottom sides, that is $u(y=1)=0$ and $\mathrm{d}u_u/\mathrm{d}y(y=-1)=\gamma_{Ma}$, respectively. The solution to the Stokes problem (5.46) with these uniform boundary conditions is independent of x:

$$u_u = \frac{1}{2}\left(1-y^2\right) + (1-\gamma_{Ma})(1-y), \tag{5.72}$$

and can be used to yield the limit of $u_{Ic} \to u_u(y=-1)$ for $\phi \to 1$. At $g \lesssim 1$, it is also clear from figure 5.3(b) that $u_{Ic}/(2(1-\gamma_{Ma})) \to 1$ only for gas fraction very close to 1, i.e. in the limit $\phi \to 1$, as already observed in figure 5.3(a). This result confirms the range of validity of the first scaling (5.37) for the diffusive boundary layer thickness δ. Then, we can show (see appendix 5.12) that in the limit of large gap length, $g \gg 1$, the normalised interfacial velocity follows the asymptotic hyperbolic trend

$$\frac{u_{Ic}}{2(1-\gamma_{Ma})} \simeq \frac{1}{4-3\phi}, \tag{5.73}$$

plotted with a black dashed line in figure 5.3(b). The asymptotic result (5.73) is valid for any ϕ. This result is consistent with (5.70) and (5.71).

5.5.3 Predictions of the interfacial shear rate, effective slip length and drag reduction

We now have two independent expressions relating the interfacial velocity u_I and the Marangoni shear γ_{Ma}. The scaling (5.44) was found based on near-interface surfactant dynamics, whereas (5.67) was derived from a Stokes flow solution. Eliminating the interface velocity, we deduce a scaling expression for the average Marangoni shear rate,

$$\gamma_{Ma} = a_1 k^* \mathcal{F}_0(g,\phi) \left(\frac{1}{Pe_I} + a_2 \frac{g^2 Bi}{1 + \frac{Bi\,Pe}{\chi}\delta} + a_1 k^* \mathcal{F}_0(g,\phi) \right)^{-1}, \tag{5.74}$$

where a_1 and a_2 are the empirical parameters that were introduced in § 5.4.2. This predictive scaling depends only on the properties of the flow, fluid and surfactant through the non-dimensional numbers $k^* = k\,Ma$, Pe_I, Bi, Pe and χ, and on the two geometrical parameters g and ϕ. As noted earlier, it assumes a sufficiently small concentration of surfactant and a small Reynolds number in the flow, and the diffusive boundary layer thickness δ depends only weakly on γ_{Ma} following (5.37), (5.38) or (5.39). The parameters a_1, a_2, as well as $\delta_{0,i}$ and $\delta_{1,i}$ (with $i = 1$, 2 or 3 for the scaling predictions (5.37), (5.38) or (5.39), respectively) for δ, are determined empirically by fitting to our numerical simulations in § 5.7.

We can also compute a global effective slip length λ_e as defined by [166], which corresponds to the value λ_e such that an equivalent channel flow under the same pressure gradient, but with a uniform Navier slip boundary condition $u(y=-1) = \lambda_e\, \partial u/\partial y|_{y=-1}$ replaces the mixed conditions of the SHS at the bottom boundary. We can show that the contribution of the effective slip length λ_e is such that the total volume flux in the channel is the sum of the background Poiseuille volume flux, $Q_p = 2/3$, and the volume flux of the deviating flow,

$$Q = Q_p + Q_d = \frac{2}{3} + \frac{2\lambda_e}{\lambda_e + 2}, \tag{5.75}$$

where the maximum value for the deviating flux is $Q_d \to 2$, as $\lambda_e \to \infty$. The effective slip

length as a function of the deviating flux is

$$\lambda_e = \frac{2Q_d}{2 - Q_d}. \tag{5.76}$$

From equation (5.51), the deviating streamfunction is

$$Q_d = \Psi_d(y = 1) - \Psi_d(y = -1) = \frac{E}{2} - \left(-\frac{3E}{2}\right) = 2E, \tag{5.77}$$

and substituting into (5.76) yields

$$\lambda_e = \frac{2E}{1 - E}. \tag{5.78}$$

Following from the linearity of the governing equations, and of the boundary conditions, E also scales linearly with $(1 - \gamma_{Ma})$. Accordingly, we can find the explicit dependence of λ_e with the Marangoni shear rate γ_{Ma},

$$\lambda_e = \frac{2(1 - \gamma_{Ma})E_0}{1 - (1 - \gamma_{Ma})E_0}, \tag{5.79}$$

where E_0 is the first coefficient of the vector $\boldsymbol{U}_n$ (see (5.57)) in the surfactant-free case, i.e. $E_0 = E$ for $\gamma_{Ma} = 0$, and γ_{Ma} is expressed by (5.74). As expected, $0 \leq \lambda_e < \infty$, since $0 \leq \gamma_{Ma} \leq 1$ and $0 \leq E_0 \leq 1$.

The corresponding drag reduction due to the presence of the SHS in our pressure-driven channel flows, inclusive of surfactant, can be computed as

$$DR = 1 - \frac{C_f}{C_{f,p}} = 1 - \frac{\dfrac{\langle \hat{\tau}_s \rangle}{\hat{\rho}(\hat{Q}/2)^2}}{\dfrac{\langle \hat{\tau}_s \rangle_p}{\hat{\rho}(\hat{Q}_p/2)^2}} \tag{5.80}$$

where $C_f = \langle \hat{\tau}_s \rangle / (\hat{\rho}(\hat{Q}/2)^2)$ is the laminar friction coefficient for a pressure-driven flow through a SHS channel with surfactants and $C_{f,p} = \langle \hat{\tau}_s \rangle_p / (\hat{\rho}(\hat{Q}_p/2)^2)$ is the laminar friction coefficient for the equivalent Poiseuille channel flow driven with the same pressure gradient and for the same channel height. The quantities $\langle \tau_s \rangle$ and $\langle \tau_s \rangle_p$ are the surface stresses averaged along both

top and bottom surfaces for an SHS channel flow and a Poiseuille channel flow with the same geometry, respectively. Since, by construction, the pressure gradient is the same for the flow in the SHS channel and the Poiseuille channel flow, we have $\langle \hat{\tau}_s \rangle = \langle \hat{\tau}_s \rangle_p$. Then, using (5.75) and (5.76) into (5.80) we find

$$DR = 1 - \left(1 + \frac{3Q_d}{2}\right)^{-2} = 1 - \left(1 + \frac{3\lambda_e}{\lambda_e + 2}\right)^{-2}. \tag{5.81}$$

The maximum possible drag reduction is $DR \to 15/16$ as $\lambda_e \to \infty$. We can compute λ_e in (5.81) using (5.79) and (5.74). We also provide, as supplementary materials, MATLAB routines computing λ_e, DR and γ_{Ma} for any specified flow-related, surfactant or geometrical parameters (see https://doi.org/10.1017/jfm.2019.857).

5.6 Surfactant-laden numerical simulations

To test the validity of our theoretical model and its predictions for the surfactant-induced Marangoni shear γ_{Ma} in (5.74) and for the effective slip length λ_e in (5.79), we performed 137 surfactant-laden numerical simulations of the full governing equations (5.2)–(5.13).

We varied the nine dimensionless numbers independently over several orders of magnitude to comprehensively explore the parameter space. As introduced in § 5.3, these dimensionless groups are the Reynolds number $Re = \hat{\rho}\hat{h}\hat{U}/\hat{\mu}$, the bulk and interface Péclet numbers $Pe = \hat{h}\hat{U}/\hat{D}$ and $Pe_I = \hat{h}\hat{U}/\hat{D}_I$, the Biot number $Bi = \hat{\kappa}_d\hat{h}/\hat{U}$, the non-dimensional bulk concentration $k = \hat{\kappa}_a\hat{c}_0/\hat{\kappa}_d$, the surfactant adsorption–desorption kinetics number $\chi = \hat{\kappa}_d\hat{h}/(\hat{\kappa}_a\hat{\Gamma}_m)$, the Marangoni number $Ma = n_\sigma\hat{R}\hat{T}\hat{\Gamma}_m/(\hat{\mu}\hat{U})$, the gas fraction $\phi = \hat{g}/\hat{L}$ and the non-dimensional interfacial length $g = \hat{g}/\hat{h}$. The Frumkin interaction parameter, used in equation (5.6), is kept constant at $A = -1$ for all our simulations. Since this parameter has a weak influence on the surfactant-induced Marangoni shear rate, we chose a value for A corresponding to moderate attractive interactions between the adsorbed surfactant molecules. This value is close to the measured value for the common surfactant sodium dodecyl sulfate in de-ionised water:

$A = -2.4$ [201, 200]. The aim is also to obtain values for the empirical parameters a_1, a_2 in (5.74) and $\delta_{0,i}$ and $\delta_{1,i}$ (with $i = 1$, 2 or 3) in the uniform shear regime.

The model described by the dimensional form of equations (5.2) to (5.13) was implemented in COMSOL Multiphysics 5.2® in two-dimensional finite-element numerical simulations. The SHS channel geometry shown in figure 5.2(a) was used for the simulation domain, where the range of values for the gap length $\hat{g}$, the ridge length $\hat{l}$, the channel half-height $\hat{h}$ and the streamwise mean pressure drop per unit length $\hat{G}$ are presented in Supplementary Table S1 (https://doi.org/10.1017/jfm.2019.857).

When designing the mesh of the domain, we were particularly careful to ensure we could capture strong possible variations of some variables near the stagnation points at the beginning and end of the interface ($x = \pm g/2$), and in the vicinity of the interface. For each simulation, the maximum size of the mesh elements at the stagnation points, on the interface, and in the bulk, is detailed in Supplementary Table S1 (https://doi.org/10.1017/jfm.2019.857). Across all the simulations, the maximum density of elements close to the two stagnation points of the interface is 200 per micron, while the lowest density of elements at the middle of the interface is 20 per micron.

To implement the model in COMSOL, we combine the Laminar Flow module with a Dilute Species Transport module for the transport equations in the bulk (5.2–5.4). The equation for the transport of surfactant on the interface (5.5) is implemented through a General Form Boundary PDE, with a source term corresponding to the Frumkin kinetics flux S (5.6). This flux also serves to implement the condition for the continuity of the diffusive flux and the kinetics flux (5.14) at the interface for the Dilute Species Transport module. The non-uniform distribution of surfactants at the interface yield Marangoni forces, which modify the Laminar Flow module, as stated in (5.17), through a weak contribution at the interface coupled to a free-slip boundary condition, resulting in the required partial slip at the interface.

The flow is forced by a mean pressure drop per unit length, which is implemented through a Periodic Flow Condition between inlet and outlet following (5.9), also enforcing velocity

field periodicity between inlet and outlet. A gauge for the pressure is imposed through a pressure point constraint at a corner of the domain. The initial guess for the velocity, for the stationary solver, is set to the reference Poiseuille profile $u_p = (1-y^2)/2$ in the entire chamber, corresponding to the stream-function (5.49). Periodic boundary conditions between inlet and outlet following (5.8) are also imposed in the Dilute Species Transport module for the bulk surfactant concentration c.

To ensure the accuracy and stability of the numerical simulations, we discretize the fluid flow with quadratic elements for the velocity field and linear elements for the pressure field (Taylor-Hood elements), as well as quadratic elements for the concentration fields in the bulk and on the interface. We use the MUMPS solver of COMSOL to solve for the steady state of the system, with a relative tolerance of 10^{-5}. All our 137 COMSOL numerical simulations were fully converged, satisfying this strict relative tolerance.

The surfactant properties correspond to the well-characterized surfactant sodium dodecyl sulfate (SDS), which are well described by Frumkin kinetics [200]. The physical parameters were chosen in order to explore a large range of the key non-dimensional numbers. Variations by four to six orders of magnitude were explored, as summarized in table 5.1 in this section, as well as in figure 5.8 in appendix 5.10. In five simulations, we explored the limit of high Reynolds number with $Re \geq 1,000$, for which the flow should physically be at or above the transition to a turbulent regime. However, we imposed the flow to remain laminar in these simulations, since we are not interested in the effect of inertial instabilities or turbulence in this study. We will return to this point in § 5.7, when discussing results at large Reynolds numbers under laminar conditions. All other relevant physical and kinetics parameters of the 137 performed simulations are presented in Supplementary Table S1 at https://doi.org/10.1017/jfm.2019.857.

Parameter	Symbol	Minimum	Maximum
Gas fraction	$\phi = \hat{g}/\hat{L}$	$1 \cdot 10^{-3}$	$9.5 \cdot 10^{-1}$
Length of the air–water interface	$g = \hat{g}/\hat{h}$	$1 \cdot 10^{-3}$	$1 \cdot 10^{2}$
Reynolds number	$Re = \hat{\rho}\hat{h}\hat{U}/\hat{\mu}$	$4 \cdot 10^{-4}$	$1 \cdot 10^{5}$
Bulk concentration	$k = \hat{\kappa}_a\hat{c}_0/\hat{\kappa}_d$	$1 \cdot 10^{-7}$	$1 \cdot 10^{2}$
Bulk Péclet number	$Pe = \hat{h}\hat{U}/\hat{D}$	$5 \cdot 10^{-6}$	$2.5 \cdot 10^{7}$
Bulk Péclet number (with $\hat{g}$)	$Pe_g = \hat{g}\hat{U}/\hat{D}$	$1 \cdot 10^{-6}$	$1 \cdot 10^{6}$
Interface Péclet number	$Pe_I = \hat{h}\hat{U}/\hat{D}_I$	4	$2 \cdot 10^{8}$
Interface Péclet number (with $\hat{g}$)	$\mathcal{F}_0 Pe_{I,g} = \mathcal{F}_0\hat{g}\hat{U}/\hat{D}_I$	$3.1 \cdot 10^{-4}$	$2.5 \cdot 10^{5}$
Biot number	$Bi = \hat{\kappa}_d\hat{h}/\hat{U}$	$1.2 \cdot 10^{-4}$	$5 \cdot 10^{2}$
Biot number (with $\hat{g}$)	$Bi_g = \hat{\kappa}_d\hat{g}/\hat{U}$	$1.2 \cdot 10^{-5}$	2.5
Kinetics number	$\chi = \hat{\kappa}_d\hat{h}/(\hat{\kappa}_a\hat{\Gamma}_m)$	$5 \cdot 10^{-3}$	$5 \cdot 10^{3}$
Kinetics number (with $\hat{g}$)	$\chi_g = \hat{\kappa}_d\hat{g}/(\hat{\kappa}_a\hat{\Gamma}_m)$	$2 \cdot 10^{-3}$	$2 \cdot 10^{2}$
Marangoni number	$Ma = n_\sigma\hat{R}\hat{T}\hat{\Gamma}_m/(\hat{\mu}\hat{U})$	3	$1.2 \cdot 10^{12}$
Marangoni concentration	$k^* = kMa$	$3 \cdot 10^{-7}$	$1.2 \cdot 10^{14}$
Ratio of kinetics flux to advective flux at the interface	$\mathcal{K}_{I,g} = Bi_g(1+k)/\mathcal{F}_0$	$9.9 \cdot 10^{-4}$	$3.2 \cdot 10^{3}$
Ratio of diffusive flux to advective flux at the interface	$\mathcal{D}_{I,g} = \chi_g(1+k)/(\mathcal{F}_0 Pe_g)^{\frac{1}{2}}$	$4 \cdot 10^{-5}$	$4.4 \cdot 10^{3}$

Table 5.1: Range of values for all the non-dimensional parameters varied in the 137 finite element numerical simulations. Hatted quantities are dimensional. See also Supplementary Table S1 (https://doi.org/10.1017/jfm.2019.857) for the value of each parameter in each numerical simulation.

5.7 Results and model performance

5.7.1 Effective slip length

In figure 5.4, we compare our scaling predictions for the effective slip length $\lambda_e^{\text{theory}}$ with the numerical results λ_e^{data}. We compute $\lambda_e^{\text{theory}}$ using (5.79), where γ_{Ma} follows (5.74) and the coefficients E_0 are computed by solving the linear problem (5.57) in the surfactant-free case for each couple of geometrical parameters (g, ϕ). The empirical parameters a_1, a_2 in (5.74) and $\delta_{0,i}$, $\delta_{1,i}$, with $i = 1$, 2 or 3 for δ (see equations (5.37)–(5.39)) can be determined using a least-squares fitting approach and the Trust Region Reflective algorithm, as implemented in the package `optimize.least_squares` of Scipy [208].

First, we determine $\delta_{1,3}$ in δ by fitting a measure of the characteristic diffusive boundary layer thickness in our numerical simulations, calculated using (5.41), with the scaling model given in (5.39). We have only used the Lévêque scaling (5.39) for δ in (5.74). In our numerical simulations, the diffusive boundary layer mostly follows the Lévêque regime, which assumes a background linear shear flow, since the slip velocity u_I is small. Moreover, as also noted earlier, the scaling model (5.74) for γ_{Ma} depends weakly on δ. Hence, the choice of scaling for δ, which can vary between (5.37), (5.38) or (5.39) depending on the geometry and the slip, does not appear to be critical. The fit gives

$$\delta_{1,3} = 0.0528, \tag{5.82}$$

from the minimization of the sum of the squares of the relative distance of theory from data, i.e. $(\delta^{\text{theory}} - \delta^{\text{data}})^2/(\delta^{\text{data}})^2$. This prior independent determination of $\delta_{1,3}$ reduces the number of fitting parameters to three in (5.74): a_1, a_2 and $\delta_{0,3}$. This ensures a more accurate and robust fit for $\lambda_e^{\text{theory}}$, less sensitive on the actual fitting technique used.

Then, using $\delta_{1,3} = 0.0528$ in (5.74), we fit the effective slip length $\lambda_e^{\text{theory}}$ given by (5.79) to λ_e^{data} computed via the deviating flux Q_d using (5.76). Incidentally, computing λ_e^{data} using (5.76) gives an accurate and robust estimation of the effective slip length in our numerical simulations, as it relies solely on the integral quantity $Q_d = Q - Q_p$ (see 5.75). Minimising the

sum of the squares of the absolute distance between $\lambda_e^{\text{theory}}$ and λ_e^{data}, we obtain

$$a_1 = 2.30,\ a_2 = 0.319 \ \text{ and } \ \delta_{0,3} = 1.68. \tag{5.83}$$

As we can see in figure 5.4(a,b), the scaling predictions for $\lambda_e^{\text{theory}}$, using the values for a_1, a_2, $\delta_{0,3}$ and $\delta_{1,3}$ stated in the previous paragraph, show an excellent agreement with λ_e^{data} over a very large range: $10^{-12} \lesssim \lambda_e \lesssim 1$.

The nine data points at non-negligible Reynolds numbers, $1 \leq Re \leq 10^5$ (identified with blue circles in figure 5.4(a,b)), also exhibit good agreement despite violating the low Reynolds number assumption made in our flow model (see § 5.5.1). As explained previously in § 5.6, although the full steady nonlinear Navier–Stokes equation (5.3) was used in the simulations, the flow remained in the laminar regime for all Reynolds numbers tested.

At large non-dimensional background concentrations, $1 \leq k \leq 100$ (identified with green triangles in figure 5.4(b)), the scaling predictions underestimate slightly the slip length. This is due to the fact that the model assumes a low concentration of surfactant. However, the model still provides a practically useful prediction of the boundary condition at the interface, which can be effectively considered as no-slip for all our simulations with $k \geq 1$. We also find that the maximum boundary layer thickness is $\delta = 1.20$, which suggests that our scaling prediction is accurate even if the diffusive boundary layer is vertically confined.

We indicate in figure 5.4 (as well as in figures 5.5 and 5.6) data where the interface properties are strongly nonuniform, which are labeled by vermilion squares and orange diamonds. Qualitatively similar interface non-uniformities have been studied extensively in the context of air bubbles rising in surfactant-contaminated water (*e.g.* [187, 188, 189, 209]), where they correspond to the 'stagnant cap regime'. In this regime, an upstream part of the interface has a negligible surfactant gradient and can be considered as shear-free ($\gamma_{Ma} \to 0$), whilst the rest of the interface downstream has a large Marangoni shear ($\gamma_{Ma} \to 1$), leading to a no-slip condition over a portion of the bubble known as the 'stagnant cap' (hereafter designated as SC). In the

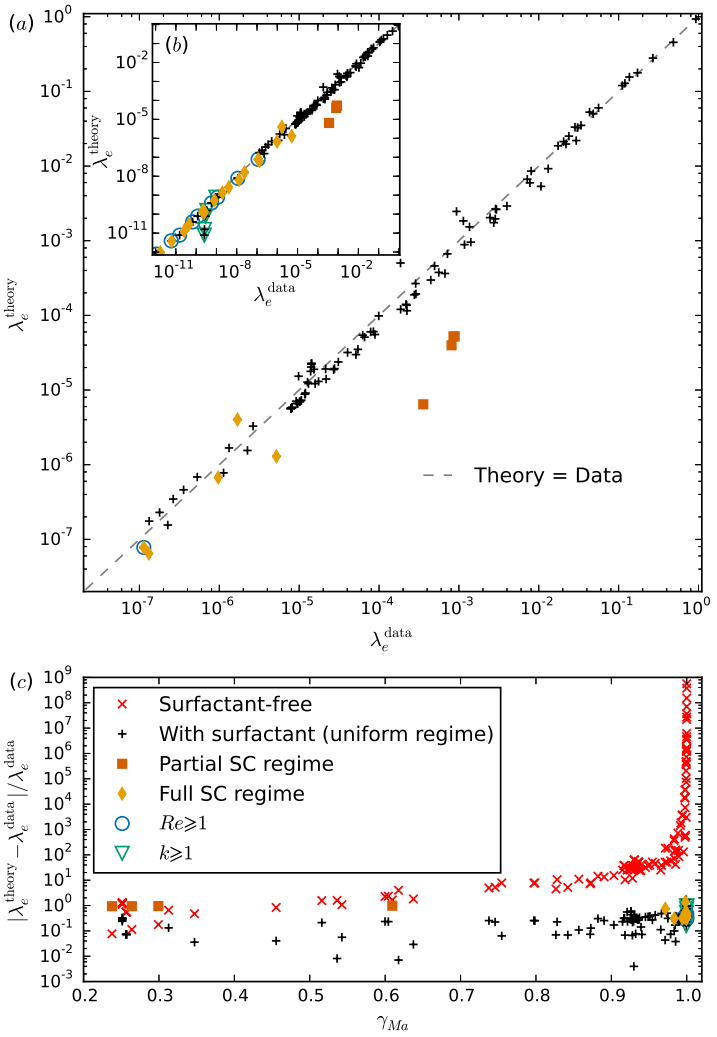

Figure 5.4: (a) Comparison of the scaling predictions for the effective slip length $\lambda_e^{\text{theory}}$, computed using (5.79) and (5.74), with fitting parameters $a_1 = 2.30$, $a_2 = 0.319$, $\delta_{0,3} = 1.68$ and $\delta_{1,3} = 0.0528$, with the numerical results from our simulations λ_e^{data}, calculated from (5.76). Results are plotted on a log–log scale, with the grey dashed line showing equality between predictions and simulations. The predictions for the four data points in the partial stagnant cap (SC) regime, plotted with vermilion squares, underestimate the data owing to the strong non-uniformity of the interfacial shear rate profile. Nevertheless, the theory remains practically useful also for these cases, as it correctly predicts $\lambda_e \ll 1$. In the inset (b), we plot an extended range of λ_e^{data}. In (c), a linear–log plot shows the relative error between the data and the scaling predictions, as a function of the average interfacial shear rate. Red crosses show the error in the effective slip length when surfactants are neglected, such that λ_e is calculated using (5.79) with $\gamma_{Ma} = 0$.

SC regime, advection of surfactant along the interface dominates relative to surfactant transport between the interface and the bulk. This makes possible highly non-uniform interfacial concentrations. Since transport between the interface and the bulk is mediated by both the diffusive boundary layer flux and the surfactant kinetics, the SC regime requires that advection along the interface must be large compared to either diffusive or kinetic fluxes (or both).

We briefly summarize here the bubble-flow analysis of [190], and translate it to SHS flow. For a bubble, the SC regime is found when the characteristic interfacial Péclet number is large, and either the adsorption–desorption kinetics flux S is small, or the diffusive flux through the boundary layer is small compared with the interfacial advective flux. Denoting with a superscript 'bubble' the results of [190], they showed that this implies $Pe_I^{\text{bubble}} \gg 1$, and $\mathcal{K}_I = Bi^{\text{bubble}}(1+k) \ll 1$ or $\mathcal{D}_I = \chi^{\text{bubble}}(1+k)/(Pe^{\text{bubble}})^{1/2} \ll 1$. For a bubble, the characteristic length and velocity scales are the bubble radius and interfacial velocity in the surfactant-free case. In order to translate these canonical bubble results to SHSs, note that the bubble radius is analogous to the grating length $\hat{g}$. For the SHS, the characteristic velocity scale for these non-dimensional numbers is the mid-gap interfacial velocity in the surfactant-free case, namely $\hat{u}_{Ic}(\gamma_{Ma}=0)$, which differs from the bulk characteristic velocity, such that $\hat{u}_{Ic}(\gamma_{Ma}=0) = 2\mathcal{F}_0\hat{U}$, according to (5.67). This contrasts slightly with contaminated air bubbles in water, where the characteristic interfacial velocity in the surfactant-free case scales as the far-field bulk velocity, owing to the absence of rigid no-slip walls. As shown in figure 5.3 and explained in detail in appendix 5.12, we have $\mathcal{F}_0 \sim 1$ for $g \gtrsim 1$ (as for bubbles) and $\mathcal{F}_0 \sim g$ for $g \lesssim 1$.

Therefore, using our dimensionless group definitions of § 5.3, and using a 'g' subscript to characterize dimensionless groups where we use the lengthscale $\hat{g}$, rather than $\hat{h}$, we have $Pe_I^{\text{bubble}} \mapsto \mathcal{F}_0 g Pe_I = \mathcal{F}_0 Pe_{I,g}$ and $\mathcal{K}_I = Bi^{\text{bubble}}(1+k) \mapsto \mathcal{K}_{I,g} = Bi_g(1+k)/\mathcal{F}_0$, as well as $\mathcal{D}_I = \chi^{\text{bubble}}(1+k)/(Pe^{\text{bubble}})^{1/2} \mapsto \mathcal{D}_{I,g} = \chi_g(1+k)/(\mathcal{F}_0 Pe_g)^{1/2}$. The ranges spanned by the quantities $\mathcal{F}_0 Pe_{I,g}$, $\mathcal{K}_{I,g}$ and $\mathcal{D}_{I,g}$ are reported in table 5.1.

The distinction between the partial SC regime, where the SC fills only part of the interface,

and the full SC regime, where the SC fills all the interface, is revealed by an inspection of the shear rate profiles along the interface (not shown here). In the partial SC regime, the shear rate increases abruptly from negligible values to $\gamma_{Ma} \sim 1$ at a particular location along the interface. In the partial SC regime, the non-dimensional numbers in our simulations range approximately: $2.5 \cdot 10^3 \leq \mathcal{F}_0 Pe_{I,g} \leq 2.5 \cdot 10^5$, $9.9 \cdot 10^{-4} \leq \mathcal{K}_{I,g} \leq 0.4$ and $0.04 \leq \mathcal{D}_{I,g} \leq 0.4$ (see also figure 5.8, appendix 5.10, for the variations of these numbers across all our numerical simulations and for the different regimes, as well as Supplementary Table S1 for the value of each parameter for each simulation). In the full SC regime, the non-dimensional numbers range approximately: $52 \leq \mathcal{F}_0 Pe_{I,g} \leq 2.5 \cdot 10^4$, $2 \cdot 10^{-2} \leq \mathcal{K}_{I,g} \leq 50$ and $4.0 \cdot 10^{-5} \leq \mathcal{D}_{I,g} \leq 1.3$. The interfacial Péclet number is mostly higher in the partial SC regime than in the full SC regime, which is intuitively expected. We can see in figure 5.4(a) that the four data points in the partial SC regime (plotted with vermilion squares) are the only data points where the scaling predictions significantly underestimates the effective slip length with $\lambda_e^{\text{theory}} \leq 5.2 \cdot 10^{-5}$, whereas $\lambda_e^{\text{data}} \geq 3.5 \cdot 10^{-4}$. This discrepancy is due to the strong non-uniformity of the shear rate profile in the SC regime, not taken into account by our scaling model which is based on the assumption that the shear rate is approximately uniform along the interface (see (5.34)). The predictions $\lambda_e^{\text{theory}}$ in the full SC regime, plotted with orange diamonds, are in reasonable agreement with the data λ_e^{data}. We can see that $\lambda_e^{\text{theory}}$ underestimates slightly the data, although by less than one order of magnitude for all our results in the full SC regime, with $0.25 \leq \lambda_e^{\text{theory}}/\lambda_e^{\text{data}} \leq 2.4$.

The data plotted with black pluses in figure 5.4, i.e. not in the SC regime, are in a state analogous to the 'uniformly retarded regime' described by [190] in their study of air bubbles rising in contaminated water, where they make the case that this regime exists for $\mathcal{K}_{I,g} \sim 1$ and $\mathcal{D}_{I,g} \sim 1$. However, in our simulations we find that the interfacial shear rate is in the 'uniform' regime, and thus satisfies our modelling assumption, over a range of $\mathcal{K}_{I,g}$ and $\mathcal{D}_{I,g}$ that spans several orders of magnitude, implying that the vast majority of the simulations satisfy our modelling assumptions. More specifically, we find that simulations in the 'uniformly

retarded regime' have parameters that satisfy approximately $2.8 \cdot 10^{-3} \leq \mathcal{D}_{I,g} \leq 4.4 \cdot 10^{3}$ and $1.9 \cdot 10^{-2} \leq \mathcal{K}_{I,g} \leq 3.2 \cdot 10^{3}$. This is most likely due to the fact that some of our simulations are in an intermediate or transition regime between the SC regime and the uniformly retarded regime, and for which λ_e still follows our scaling prediction, though perhaps with slightly more scatter, as shown by some of the black pluses in figure 5.4.

In figure 5.4(c), we show the relative error between the scaling predictions $\lambda_e^{\text{theory}}$ and the numerical results λ_e^{data} for the effective slip length. The error remains relatively small across all values of the average interfacial shear rate γ_{Ma}. It is less than approximately 33% for $\gamma_{Ma} \leq 0.7$, except for the four simulations in the partial SC regime plotted with vermilion squares. The relative error is less than 1.7 for $0.7 \leq \gamma_{Ma} \leq 1$.

For comparison, we also show with red crosses in figure 5.4(c) the prediction from a surfactant-free model, which is obtained using (5.79) with $\gamma_{Ma} = 0$. Our model provides consistently better predictions than the one that neglects surfactant effect. In particular, the error made by neglecting surfactant effects becomes very large when the interfacial shear rate increases towards the Poiseuille value $\gamma_p = 1$. At low shear rate, $\gamma_{Ma} \leq 0.3$ we can see that the two models have comparable (small) relative errors.

Overall, we find that our scaling model for λ_e provides excellent quantitative predictions across a large range of non-dimensional numbers, beyond the strict range of validity based on our modelling assumptions. Although our model predictions can underestimate the slip length in some cases (at large concentrations, and in the stagnant cap regime), our model remains practically useful as both theory and simulation yield negligible slip in those instances.

5.7.2 Drag reduction

We compare the drag reduction predicted by our theory (DR^{theory}) with the numerical results from our simulations (DR^{data}), as shown in figure 5.5. The value of DR^{theory} is obtained from (5.81), where the corresponding values of $\lambda_e^{\text{theory}}$ are shown earlier in figure 5.4. Similarly, DR^{data}, is calculated using λ_e^{data}, whose values are also shown in figure 5.4. Using a log–log

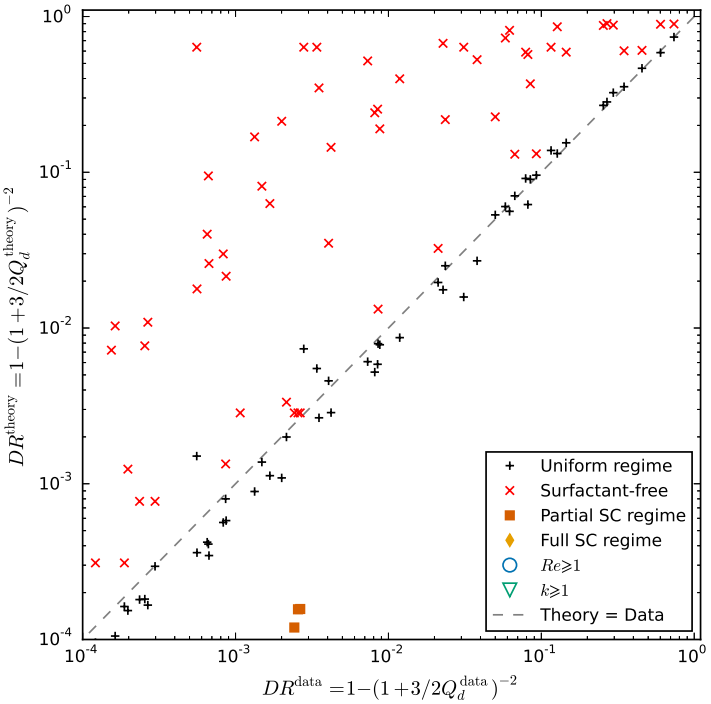

Figure 5.5: Comparison of the scaling predictions for the drag reduction DR^{theory}, computed using (5.81), with the numerical results from our simulations DR^{data}. We also show with red crosses the drag reduction DR^{theory} estimated using a model neglecting surfactant effect. Note that we plot in this graph only data for $DR \geq 10^{-4}$, to show more clearly our results in a range useful to applications. Equality between data and theory falls on the grey dashed line.

scale, we only plot data for $DR \geq 10^{-4}$, which correspond to the more meaningful range for practical applications. The predictions from our scaling model are in very good agreement with the numerical results. Data at even lower drag reductions (not shown here) still exhibit a very good agreement with our theoretical prediction.

In figure 5.5, we also plot, using red crosses, the drag reduction computed using a surfactant-free model. This is obtained by substituting the values for the surfactant-free $\lambda_e^{\text{theory}}$ (plotted with red crosses in figure 5.4*c*) into (5.81). As may be expected, the surfactant-free theory almost always incorrectly predicts a larger drag reduction, with values often more than an order of magnitude larger that the actual ones. This clearly shows that the drag reduction potential of SHSs can be significantly overestimated in conditions where surfactants are important. This is consistent with the findings of [179], who showed that, for SHSs with rectangular longitudinal gratings, surfactant effects become important at very low concentrations, similar to background levels found in the environment. As may be expected, the few surfactant-free predictions in figure 5.5 that show better agreement with the numerical simulations correspond to lower values of γ_{Ma}, when the surfactant-free predictions converge towards our model predictions (see figure 5.4*c*).

5.7.3 Interfacial shear rate

We compare in figure 5.6 the numerical results for the average interfacial shear rate $\gamma_{Ma}^{\text{data}}$ with the theoretical predictions, $\gamma_{Ma}^{\text{theory}}$ computed using (5.74) using the four empirical parameters optimized for λ_e in § 5.7.1: $a_1 = 2.30$ and $a_2 = 0.319$ for γ_{Ma}, and $\delta_{0,3} = 1.68$ and $\delta_{1,3} = 0.0528$ for δ based on (5.39). The numerical results for $\gamma_{Ma}^{\text{data}}$ have been computed by taking the spatial average of the interfacial shear rate in the interior of the interface $-g/2 \leq x \leq g/2$.

In figure 5.6(*a*), we show $(1 - \gamma_{Ma})$ in a log–log plot to focus on the no-slip limit $\gamma_{Ma} \to 1$. Over the limited range shown on this graph, we find good agreement between our scaling predictions and the data for all our numerical simulations where the interfacial shear rate is

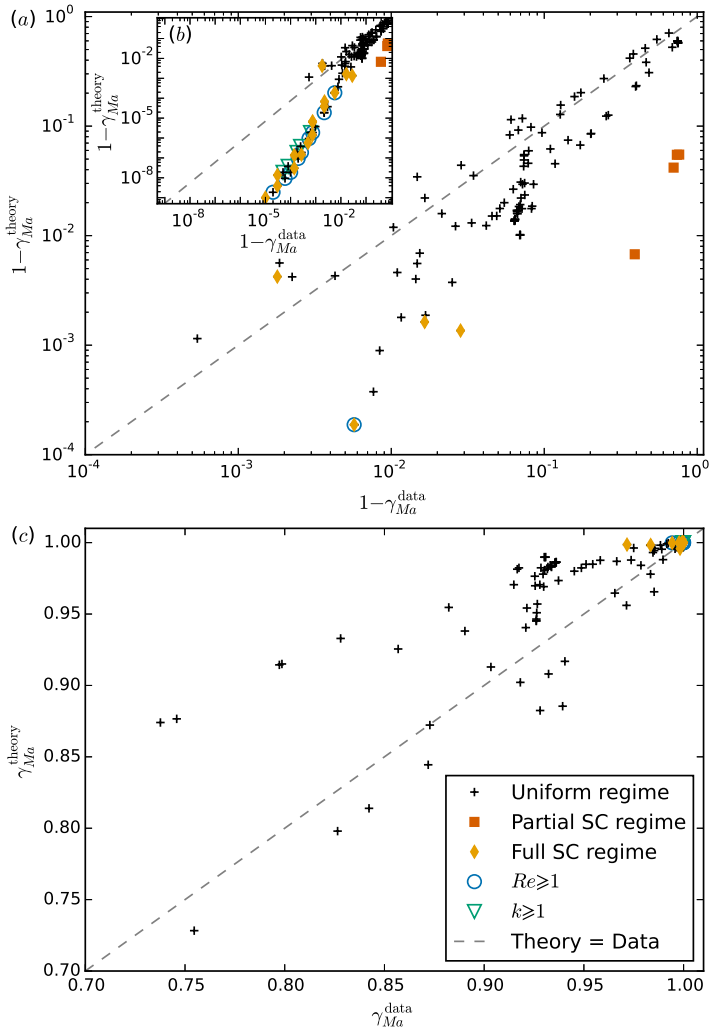

Figure 5.6: Comparison of the scaling predictions for the average interfacial shear rate $\gamma_{Ma}^{\text{theory}}$, computed using (5.74), with the numerical results from our simulations $\gamma_{Ma}^{\text{data}}$, calculated by averaging the shear rate along the interface. The scaling prediction use empirical parameters: $a_1 = 2.30$ and $a_2 = 0.319$ for γ_{Ma}, and $\delta_{0,3} = 1.68$ and $\delta_{1,3} = 0.0528$ for δ (see (5.39)), computed from the fit of λ_e (see § 5.7.1). In (a), we plot using a log–log scale $(1-\gamma_{Ma})$ to reveal the behaviour at large shear rate, when $\gamma_{Ma}^{\text{data}} \to \gamma_p = 1$. The predictions $\gamma_{Ma}^{\text{theory}}$ for the four data points in the partial stagnant cap (SC) regime, plotted with vermilion squares, overestimate the data owing to the strong non-uniformity of the interfacial shear rate profile. In (b), we plot $(1-\gamma_{Ma})$ over a larger range revealing the error related to the singularity at the stagnation points. In (c), we plot γ_{Ma} to show more clearly the behaviour at intermediate shear rate, $0.7 \leq \gamma_{Ma} \leq 1$. In all plots, equality between data and theory would fall on the grey dashed line.

found approximately uniform along the interface (see the uniform regime, plotted with black plusses). Similar to λ_e shown in figure 5.4, we can see that the four data points in the partial SC regime (vermilion squares) with $(1-\gamma_{Ma}^{\text{data}}) \geq 0.4$ are the only ones where the predictions underestimate the data. As discussed earlier, this is due to the strong non-uniformity of the shear rate profile in the SC regime, in contradiction with the uniform assumption made in our model (see (5.34)). Nevertheless, the theory remains practically useful, as both model and simulation yield shear that is essentially indistinguishable from that of a no-slip boundary.

In figure 5.6(b) (which is the inset of figure 5.6a), we plot $(1-\gamma_{Ma}^{\text{data}})$ over the full range of values tested. As the average shear rate tends to the maximum Poiseuille value, $\gamma_{Ma}^{\text{data}} \to \gamma_p = 1$ or equivalently $(1-\gamma_{Ma}^{\text{data}}) \to 0$, $(1-\gamma_{Ma}^{\text{theory}})$ underestimates the data. The difference becomes significant for $(1-\gamma_{Ma}^{\text{theory}}) \lesssim 10^{-3}$. This is due to the singularity at the two stagnation points and the difficulty associated with resolving it numerically. The shear rate exhibits extreme variations very close to the stagnation points, whilst the shear rate remains flat in the interior of the interface with values very close to the Poiseuille shear rate. We note however that the effect of the singularity appears only in the limit $\gamma_{Ma}^{\text{data}} \to \gamma_p = 1$, at values practically equivalent to a no-slip boundary condition at the interface.

This can also be seen in figure 5.6(c), where we plot γ_{Ma} directly, for $\gamma_{Ma} \geq 0.7$. The scaling predictions consistently predict a no-slip boundary condition $\gamma_{Ma}^{\text{theory}} \to 1$, as $\gamma_{Ma}^{\text{data}} \to 1$. This shows that the actual error between $\gamma_{Ma}^{\text{theory}}$ and $\gamma_{Ma}^{\text{data}}$ is actually very small in this limit, where we find the simulations at large Reynolds numbers $Re \geq 1$ (blue circles), large non-dimensional concentrations $k \geq 1$ (green triangles) and in the full SC regime (orange diamonds). Predictions at intermediate values (shown by plusses in figure 5.6c), for $0.7 \leq \gamma_{Ma}^{\text{theory}} \leq 1$, show a good agreement with $\gamma_{Ma}^{\text{data}}$ although with a slight overestimation.

Therefore, our scaling model also provides reasonable predictions across the whole range of interfacial shear rate values, even though the model has been fitted for λ_e and not for γ_{Ma}. An agreement is found from intermediate to large values, provided the interface is not in a partial SC regime. Our scaling model remains accurate across a broad range of non-dimensional numbers

(see table 5.1 and figure 5.8, appendix 5.10) and in the full SC regime.

5.8 Discussion

5.8.1 Verifying the validity of our main assumptions

The first key assumption in our scaling model is that the non-dimensional interfacial surfactant concentration Γ is sufficiently small so that the adsorption–desorption kinetics flux S in (5.6) and the coupling condition (5.17) between the viscous stress and the surfactant-induced Marangoni stress can be linearised (see § 5.4.1). To test the validity of the assumption $\Gamma \ll 1$, at least a posteriori, we can note that it implies $\Gamma \sim k \ll 1$, which results from applying (5.18) at $S = 0$ along the interface. As mentioned before, we expect that k should remain low in many applications where surfactants are not artificially added. [179] estimated typical ranges of k, depending on whether one considers 'weak' or 'strong' surfactant. [179] calculated that, for 'weak' types of surfactants, the non-dimensional concentration range is $10^{-9} \lesssim k \lesssim 10^{-2}$, which supports our hypothesis. Note that the upper bound of this range is given at the critical micellar concentration for the bulk concentration $\hat{c}_0$, implying that the worst-case scenario corresponds to water that is saturated with surfactant. Only for 'strong' types of surfactant they indicated that the $k \ll 1$ assumption could potentially be invalid, since $10^{-6} \lesssim k \lesssim 10^{3}$. Strong surfactants are likely to be found only in applications where they have been artificially added. Nevertheless, the model presented here performed well even at large k, as seen for example in figure 5.4.

The second key assumption made in our scaling model is that the surfactant-induced Marangoni shear rate along the interface is approximately uniform. This is related to having a uniform concentration gradient, following the linearised coupling condition (5.19). From the broad range of parameters tested, see table 5.1 and figure 5.8, appendix 5.10, we find that this assumption is invalid only in the partial stagnant cap (SC) regime, where the concentration gradient presents an abrupt increase at some point along the interface, separating the no-shear

and no-slip regions. As we saw in figure 5.4, in the partial SC regime (see vermilion squares) our model underestimates the slip length. However, it is noteworthy that our scaling model provides reasonably accurate predictions for the full SC regime, where the no-slip region spans the whole interface. Furthermore, our scaling model remains practically useful in both the partial and full SC regimes, since it correctly predicts an essentially negligible effective slip length.

If wishing to strictly determine whether our model applies, we must therefore distinguish the parameter ranges between the full and partial SC regimes. As explained in § 5.7.1, the SC regime exists when the Péclet number at the interface, $\mathcal{F}_0 Pe_{I,g}$, is large and either $\mathcal{D}_{I,g}$ or $\mathcal{K}_{I,g}$ are small. From our simulations, we cannot find any clear distinction between the partial and full SC regimes based only on $\mathcal{D}_{I,g}$ or $\mathcal{K}_{I,g}$. However, we noted already that the partial SC regime was generally found at larger Péclet numbers, for $\mathcal{F}_0 Pe_{I,g} \gtrsim 10^3$, whilst the full SC regime was found for $1 \ll \mathcal{F}_0 Pe_{I,g} \lesssim 10^4$. This is physically intuitive as increasing the external flow velocity would eventually overcome the Marangoni stress at the interface. This would lead to a compression of the finite amount of surfactant adsorbed onto the interface towards the downstream end, thereby freeing the upstream part of the interface from any shear.

Since $\mathcal{F}_0 Pe_{I,g} \propto \mathcal{F}_0 \hat{U}$, $\mathcal{K}_{I,g} \propto 1/(\mathcal{F}_0 \hat{U})$ and $\mathcal{D}_{I,g} \propto 1/(\mathcal{F}_0 \hat{U})^{1/2}$, we expect to find the partial SC regime in applications where the characteristic velocity near the interface $\mathcal{F}_0 \hat{U}$ is large. We emphasize again that the characteristic velocity in these dimensionless numbers is the local characteristic velocity near the interface, $\mathcal{F}_0 \hat{U}$, where the bulk velocity $\hat{U}$ is modulated by the geometrical function $0 \leq \mathcal{F}_0 \leq 1$, which scales as $\mathcal{F}_0 \sim g$ for $g \lesssim 1$, otherwise $\mathcal{F}_0 \sim 1$. Hence, our model is valid for applications at sufficiently low $\hat{U}$ or if g is sufficiently small such that the SHS is away from the partial SC regime. Microfluidic applications, such as lab-on-a-chip systems or micro-cooling, where $\hat{U}$ is small would be typical applications for our model. For instance, we can consider a typical micro-fluidic channel with $\hat{h} = 50$ microns, a flow of water with characteristic speed ranging 0.1 to 10 mm/s, and SHS gratings of length $\hat{g} = 1$ mm with gas fraction $\phi \approx 0.95$. If surfactants similar to sodium dodecyl sulfate are present at a concentration

of approximately 10^{-3} mM (equivalent to traces naturally present in the water), then we obtain: $800 \leq \mathcal{F}_0 Pe_{I,g} \leq 8 \cdot 10^4$, $12 \leq \mathcal{K}_{I,g} \leq 120$, $0.7 \leq \mathcal{D}_{I,g} \leq 7$, and $k = 10^{-3}$. This shows that for this geometry with this range of flow speeds, the SHS would be in the uniform regime, far from the stagnant cap regime, such that our model would predict accurate estimates of the impact of surfactant on the slip length, drag reduction and average Marangoni shear rate.

5.8.2 Comparison to experimental studies of surfactant effects

Another application of our model is to analyze experimental studies reporting degradation of the performance of SHSs where surfactant contamination could be the cause. For example, two recent studies by [179] and [20] identified surfactant as the cause for the reduced or negligible slip measured near SHSs in laminar channel flows. As we discuss in detail in appendix 5.13, the main difficulty in applying our model to predict the reduction in slip in their experiments is the absence of information regarding the surfactant properties and concentration. This is due to the fact that the surfactants were not introduced artificially, but were present as unwanted and unknown contaminants in their experiments.

Nevertheless, we can use our model to analyze a posteriori the impact of surfactant in the studies of [179] and [20]. Assuming different possible surfactant types, we find that our theoretical model can predict physically sensible concentrations $\hat{c}_0$, which would lead to the reduced slip measured in their experiments. As detailed in appendix 5.13, our model predicts that for instance a 'strong' surfactant (see [179]) would only require minute traces, far below typical environmental concentrations, to reduce the slip velocity u_I as measured by [179] and [20]. A weak surfactant, e.g. SDS, would require large $\hat{c}_0$ close to the critical micellar concentration, whilst an intermediate surfactant (see appendix 5.13) would require small $\hat{c}_0$ at or below typical environmental conditions. Hence, our model predictions are consistent with the experimental results of [179] and [20] attributing their reduced performance to surfactant contaminant traces. Our model can also provide a rational a posteriori explanation for other experimental and field measurements that have reported poor SHS drag reduction performance, in contradiction with

surfactant-free theoretical or numerical predictions. Therefore, our model could help design future SHSs to mitigate or avoid surfactant effect a priori, for instance by identifying the optimal geometry and flow conditions for a given surfactant contaminant.

5.8.3 Analytical limits for slip and drag

It can be instructive and useful to examine practically relevant limits where our results simplify. We discuss effects of key dimensionless groups, and derive expressions in the limits of insoluble surfactant, and of very long gratings. In the latter case, it is possible to immediately predict the drag reduction without the need for solving the full Stokes flow problem. In any other case, we recommend using the MATLAB codes provided as supplementary materials.

To model insoluble surfactant, consider the interfacial advection–diffusion equation (5.24), setting the kinetics term on the right-hand side to zero. Integrating from the upstream stagnation point $x = -g/2$ to x_0, and dividing through by $\Gamma^*|_{x_0}$, we obtain

$$u_I|_{x_0,\mathrm{ins}} = \frac{\gamma_{Ma}}{\Gamma^*|_{x_0}\, Pe_I} \,. \tag{5.84}$$

Dividing by γ_{Ma} we find the plastron slip length, in the insoluble limit

$$\lambda_{x_0}|_{\mathrm{ins}} = \frac{1}{\Gamma^*|_{x_0}\, Pe_I} \simeq \frac{1}{Ma_{\mathrm{ins}}}, \tag{5.85}$$

Where we assume that $\Gamma|_{x_0} \simeq \Gamma_s$, where Γ_s is the (uniform) interfacial concentration found in static conditions, and Ma_{ins} is a Marangoni number for insoluble surfactant, namely

$$Ma_{\mathrm{ins}} = \Gamma_s^* Pe_I = \Gamma_s Ma\, Pe_I = \frac{\hat{\Gamma}_s}{\hat{\Gamma}_m} \frac{n_\sigma \hat{R}\hat{T}\hat{\Gamma}_m}{\hat{\mu}\hat{U}} \frac{\hat{U}\hat{h}}{\hat{D}_I} = \frac{\hat{\Gamma}_s n_\sigma \hat{R}\hat{T}\hat{h}}{\hat{\mu}\hat{D}_I}. \tag{5.86}$$

Therefore, in the insoluble case, the plastron slip length is simply inversely proportional to Ma_{ins}, such that $Ma_{\mathrm{ins}} \to \infty$ yields zero slip ($\lambda_{x_0} \to 0$), whereas $Ma_{\mathrm{ins}} \to 0$ allows the plastron to be free-slip ($\lambda_{x_0} \to \infty$), analogously to the soluble case.

In general, computing the effective slip length (or equivalently the drag) requires going thorugh the Stokes flow calculation described in § 5.5. However, in the $g \gg 1$ limit, it is also possible to evaluate analytically the effective slip length λ_e, and therefore the drag reduction. We start from (5.79), which expresses λ_e as a function of γ_{Ma} and E_0. Note that, based on (5.105),

$$E_0|_{g\gg1} = \frac{E^{(0)}\big|_{g\gg1}}{(1-\gamma_{Ma})} \simeq \frac{\phi}{(4-3\phi)}, \tag{5.87}$$

yielding λ_e in terms of (γ_{Ma}, ϕ)

$$\lambda_e|_{g\gg1} \simeq \frac{2\phi(1-\gamma_{Ma})}{(4-3\phi)-\phi(1-\gamma_{Ma})}. \tag{5.88}$$

To calculate γ_{Ma} in the insoluble limit, use (5.84) to eliminate u_I in (5.67), and obtain

$$\gamma_{Ma}|_{\text{ins}} \simeq \frac{Ma_{\text{ins}}\mathcal{F}_0}{1+Ma_{\text{ins}}\mathcal{F}_0}. \tag{5.89}$$

For $\mathcal{F}_0 = u_{Ic}/[2(1-\gamma_{Ma})]$, use the large-$g$ approximation (5.73), that is $\mathcal{F}_0 \simeq 1/(4-3\phi)$. Substituting into (5.89) and then into (5.90), the effective slip length for insoluble surfactant over a long grating is found explicitly as

$$\lambda_e|_{\text{ins},g\gg1} \simeq \frac{2\phi}{Ma_{\text{ins}}+4(1-\phi)}. \tag{5.90}$$

For long gratings, analytical expressions for λ_{x_0} and λ_e are also possible in the case of soluble surfactant. If $g \gg 1$, we expect the diffusive boundary layer to be limited by the channel height, and therefore δ will approach a constant. From our simulations, we find $\delta \simeq 1.20$ in this limit. For the plastron slip length, if g is sufficiently large, we expect the second term in (5.45) to be dominant, yielding

$$\lambda_{x_0}|_{g\gg1} \simeq \frac{2a_2}{a_1\,k^*}\frac{g^2\,Bi\,\chi}{\chi+1.20\,Bi\,Pe}. \tag{5.91}$$

To find λ_e, we calculate γ_{Ma} using (5.74), where we again set $\delta \simeq 1.20$ and $\mathcal{F}_0 \simeq 1/(4-3\phi)$. Without further approximation we obtain

$$\gamma_{Ma}\big|_{g\gg 1} \simeq \frac{a_1 k^* Pe_I(\chi + Bi\, Pe)}{(\chi + Bi\, Pe)\left[(4-3\phi) + a_1 k^* Pe_I\right] + 1.20\, a_2(4-3\phi) g^2 Bi\, \chi Pe_I}. \tag{5.92}$$

Recalling that $a_1 = 2.30$ and $a_2 = 0.319$, equations (5.92) and (5.88) together provide explicitly the effective slip length as a function of surfactant properties and geometry, without the need to solve the full Stokes flow problem. The drag reduction is then found from (5.81), as before.

5.8.4 Tentative deductions for turbulent regimes

Applications of our model in turbulent regimes might be possible if a sufficiently thick viscous sublayer exists. If the surfactant transport occurs within the viscous sublayer, where the flow is laminar, the viscous sublayer height would be the appropriate length scale instead of $\hat{h}$, and the flow velocity at the edge of the viscous sublayer would be the relevant velocity scale $\hat{U}$. In that case, the local characteristic velocity $\mathcal{F}_0\hat{U}$ at the interface may be sufficiently small to avoid the partial SC regime. While the resulting predictions based on our model would be at best qualitative, it is of great practical interest to explore this tentative application to turbulent flows. Here we restrict ourselves to examining the plastron slip length $\hat{\lambda}_{x_0}$, defined in (5.45) and which does not depend on whether the flow is internal (e.g. channel flow) or external (e.g. a boundary layer).

In a turbulent boundary layer, with dimensional wall shear stress $\hat{\tau}_w$, the canonical scales are the shear velocity $\hat{u}_\nu = \sqrt{\hat{\tau}_w/\hat{\rho}}$ and the viscous length scale $\hat{\delta}_\nu = \hat{\nu}/\hat{u}_\nu$ [210]. The height of the viscous sublayer is of order $10\,\hat{\delta}_\nu$. At this distance from a smooth wall, the flow velocity is of order $10\,\hat{u}_\nu$ [210]. We replace $\hat{h}$ and $\hat{U}$ in our analysis with these turbulent scales and set a representative wall shear stress $\hat{\tau}_w = 50\,\mathrm{N/m^2}$.

In practical applications, detection of a specific surfactant type is challenging. However,

dimensional surface tension $\hat{\sigma}$ has been measured for both clean 'synthetic' seawater (labelled '$\hat{\sigma}_0$' below), as well as for seawater samples collected through cruises ([211] and references therein). For the purpose of estimating the order of magnitude of k in this example, we use the Langmuir isotherm. While this is less accurate than the Frumkin isotherm, it does not require $k \ll 1$, yet it provides a relation between surfactant and surface tension that can be analytically inverted. In a liquid at equilibrium [201]

$$\hat{\sigma}_0 - \hat{\sigma} = n_\sigma \hat{R}\hat{T}\hat{\Gamma}_m \ln(1+k). \tag{5.93}$$

[212] find that seawater that is away from major surfactant sources (such as seasonal blooms of phytoplankton, oil seeps or wastewater treatment facilities) has $\hat{\sigma}_0 - \hat{\sigma} \sim 10^{-4}\,\mathrm{N/m}$ (see also [213]). Setting $n_\sigma \approx 2$, $\hat{R} = 8.314\,\mathrm{kg\,m^2/(s^2\,K\,mol)}$, $\hat{T} \approx 300\,\mathrm{K}$, $\hat{\Gamma}_m \approx 3.9 \times 10^{-6}\,\mathrm{mol/m^2}$ and rearranging (5.93) for k, we obtain, for low-surfactant oceanic conditions

$$k = \exp\left(\frac{\hat{\sigma}_0 - \hat{\sigma}}{n_\sigma \hat{R}\hat{T}\hat{\Gamma}_m}\right) - 1 \approx 0.005. \tag{5.94}$$

Incidentally, this example yields $k \ll 1$, consistently with our set of assumptions. Note that substantially higher k values can occur in oceans and lakes. In order to set up a well-defined calculation, we consider SDS with concentrations $\hat{c}_0 = (0.01, 0.1, 1)\,\mathrm{mM}$, corresponding to $k = 1.79 \times (10^{-3}, 10^{-2}, 10^{-1})$, which bracket the value of k found in (5.94). We change the length of the grating $\hat{g}$ from 1 µm to 2.5 cm, the latter being the grating length in [174]. We use (5.45) to calculate $\hat{\lambda}_{x_0}$, as shown in figure 5.7.

To interpret figure 5.7, we note that one needs the effective slip length to be comparable to the thickness of the viscous sublayer in order to achieve meaningful drag reduction in turbulent flow [160]. For this substantial effective slip to be possible, one needs the plastron to have an even larger slip length, since of course the solid walls will have no-slip. (For context, recall that, in canonical surfactant-free theories and simulations, the plastron is assumed to have infinite slip length.) Since the viscous sublayer thickness is $10\,\hat{\delta_\nu}$, we propose that a plastron slip length

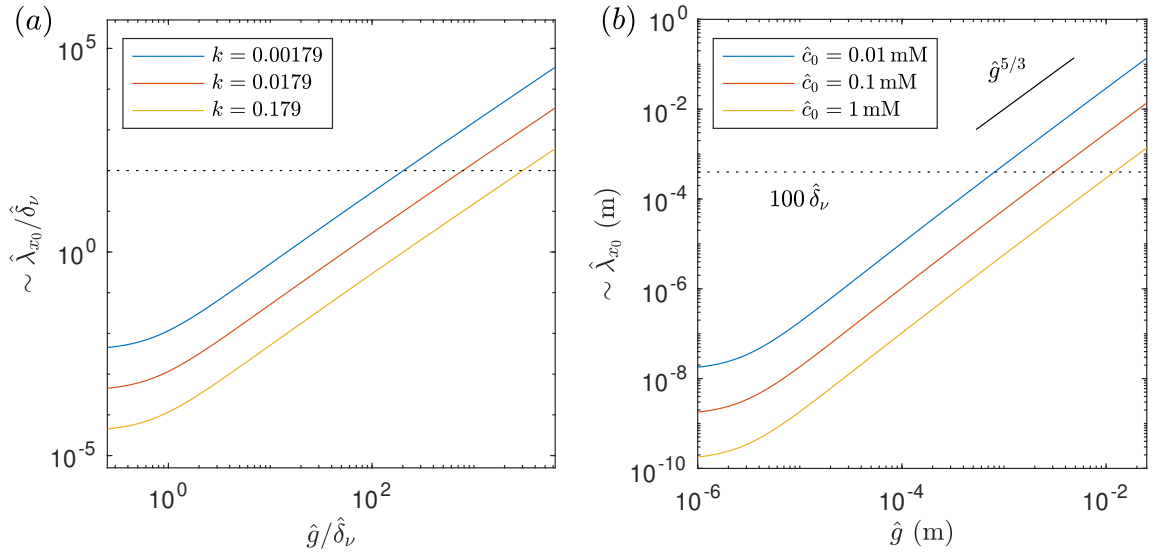

Figure 5.7: Order-of magnitude scaling for the slip length over the plastron of turbulent superhydrophobic gratings, such as those considered by [174], as a function of the grating length $\hat{g}$. A prescribed shear stress of $50\,\mathrm{N/m^2}$ is used in the calculation. (a) shows the mid-plastron slip length normalized by the viscous lengthscale $\hat{\delta}_\nu$, whereas (b) shows the corresponding dimensional results.

of around $100\,\hat{\delta_\nu}$ is a tentative relevant threshold for useful drag reduction. This value is marked by a dashed line in figure 5.7.

Note that, at small grating lengths $\hat{g}$, the first term in the right-hand side of (5.45) dominates. This is independent of $\hat{g}$. At larger $\hat{g}$, the second term in (5.45) dominates, eventually following a scaling of $\hat{g}^{5/3}$, as shown in figure 5.7(b). The slip length also increases with the inverse of $\hat{c}_0$. These results suggest that useful drag reduction may be possible provided the surfactant concentration is not too strong and the plastron is sufficiently long in the streamwise direction. Our conclusions are consistent with the experimental results of [174], who found strong drag reduction for gratings in laboratory experiments, indicating that traces of surfactant were not sufficient to negate drag reduction. However, our theory also indicates that a large drag increase may occur for a ship equipped with SHS, when it navigates through surfactant-rich waters, which are common in the coastal ocean, rivers, and lakes. Finally, we emphasize, once again, that these are tentative deductions, and that our model will require additional work to provide quantitative drag predictions in turbulent flow.

5.8.5 Relative importance of effects neglected in the present model

Surface rheology

It is also worth discussing some physical effects not considered in our model. For example, surface rheology could play a role in the boundary condition (5.17) if viscous surface stresses at the interface were comparable to viscous stresses in the bulk. The relevant dimensionless groups accounting for this balance are the Boussinesq numbers $Bo_\mu = \hat{\mu}_s/\hat{\mu}\hat{g}$ and $Bo_\kappa = \hat{\kappa}_s/\hat{\mu}\hat{g}$, with $\hat{\mu}_s$ and $\hat{\kappa}_s$ the surface shear and the surface dilatational viscosities of the surfactant-laden interface, respectively. The precise measurement of $\hat{\mu}_s$ and $\hat{\kappa}_s$ is itself a challenging problem with many open questions [214].

A recent experimental study by [215], who employed a technique of unprecedented precision, concludes that soluble surfactants can be regarded as surface shear inviscid, with values of $\hat{\mu}_s$ below their experimental sensitivity of $10^{-8}\,\mathrm{kg\,s^{-1}}$. In our problem, we can expect a negligible effect from surface shear viscous stresses, even at the smallest practical SHS length $\hat{g}$. Indeed, assuming a worst-case scenario with $\hat{\mu}_s = 10^{-8}\,\mathrm{kg\,s^{-1}}$ in water ($\hat{\mu} \approx 10^{-3}\,\mathrm{kg\,m^{-1}\,s^{-1}}$) we find $Bo_\mu \ll 1$ for $\hat{g} \gg \hat{\mu}_s/\hat{\mu} = 10^{-5}\,\mathrm{m}$, which is the case in practical applications.

Surface dilatational viscosities are even more challenging to measure, since dilatational rheology and Marangoni stresses are necessarily coupled, and therefore hard to distinguish, at an interface subject to compression or expansion [216, 217]. However, a natural (although unverified) assumption for soluble surfactant is to assume $\hat{\kappa}_s \sim \hat{\mu}_s$ [218], leading to $Bo_\kappa \sim Bo_\mu$. Thus, surface dilatational viscous stresses can also be considered negligible for SHS geometries with practical gap lengths $\hat{g} \gg 10^{-5}\,\mathrm{m}$. Note also that it is common to find an effective surface dilatational viscosity in the literature which can be much larger than $\hat{\mu}_s$. However, unlike the true intrinsic viscosity $\hat{\kappa}_s$, the effective surface dilatational viscosity actually accounts for dissipation from other non-rheological effects such as adsorption–desorption fluxes, which are already accounted for explicitly in our study.

Viscous stresses in the gas phase

In this model, we have neglected viscous stresses from a gas phase inside the grating compared with the other stresses, namely the driving viscous stress from the liquid phase and the surfactant-induced Marangoni stress at the interface. To assess the validity of this assumption, we compare an order-of-magnitude estimate of the characteristic gas viscous stress with order-of-magnitude estimates of the other two stresses.

Let us consider the condition of continuity of stress at a surfactant-free interface of a SHS, where a viscous gas phase fills two-dimensional rectangular gratings of depth $\hat{H}_g$ (see e.g. [206, 219]). The gas viscous stress at the interface, normalised by the characteristic driving stress from the liquid phase, is at most of the order of $\epsilon u_{Ic}/H_g$, where $u_{Ic} = \hat{u}_{Ic}/\hat{U} = 2\mathcal{F}_0(g, \phi)$ is the maximum shear-free interfacial velocity computed using (5.68) at $x = 0$ and with $\gamma_{Ma} = 0$, $\epsilon = \hat{\mu}_g/\hat{\mu}$ is the dynamic viscosity ratio between the gas and liquid phases, and $H_g = \hat{H}_g/\hat{h}$ is the normalised depth of the grating. From all our simulations presented in figures 5.4–5.6, we estimate that the gas viscous stress is negligible compared with the driving stress from the liquid phase, $\epsilon u_{Ic}/H_g \ll 1$, for all $\hat{H}_g \gtrsim 10^{-5}\,\mathrm{m}$, except at high viscosity ratio $\epsilon \gtrsim 1$. To calculate ϵ we have assumed that the gas in the grating is air, $\hat{\mu}_g = 1.81 \cdot 10^{-5}\,\mathrm{kgm^{-1}s^{-1}}$, whilst the liquid viscosity varies over a broad range such that $1.81 \cdot 10^{-4} \leq \epsilon \leq 1.81 \cdot 10^{5}$.

Compared with the Marangoni stress measured in our simulations, which can be estimated as k^*/g when normalised with the driving viscous stress from the liquid phase (see (5.19) and (5.33)), the gas viscous stress is also negligible in all our simulations, $(\epsilon u_{Ic}/H_g)/(k^*/g) \ll 1$ for all $\hat{H}_g \gtrsim 10^{-5}\,\mathrm{m}$ and all ϵ. If we assume $\hat{H}_g \sim 10^{-6}\,\mathrm{m}$, we find that the gas viscous stress is of the same order of magnitude as the Marangoni stress in a small number of simulations only.

We have also studied the effect of air viscosity in the experiments of [179] and [20], who measured the velocity profile near the air–water interface of SHSs made of longitudinal rectangular gratings in laminar channel flows. We find that the normalised air viscous stress at the interface is approximately $\epsilon u_{Ic}/H_g \approx 0.05$ in the experiments of [179] and of the order of 0.001 to 0.01 in the experiments of [20]. This ratio falls by at least an order of magnitude when

using their measured (reduced) slip velocity u_I, instead of our theoretical shear-free prediction (5.68). Since air viscous stresses are typically several orders of magnitude smaller than the characteristic driving force from the water phase, air viscous effects alone cannot explain the negligible or reduced slip velocity measured in their experiments. As we have shown above, the presence of surfactants, as modelled in this study, provides a consistent explanation for the reduced or negligible slip they measured.

The experimental and numerical study of [18] also provides compelling evidence that viscous effects from a gas phase are generally negligible or second order effects. They report experimental local and effective slip lengths in microfluidic channel flows over a SHS made of pillars. Since their geometry differs from the rectangular gratings considered in our model, the effect of Marangoni stresses due to the presence of surfactant is more difficult to estimate. Any surfactants in their experiments are transported over a complex two-dimensional interface with multiple local stagnation points, rather than a one-dimensional interface with two clear stagnation points. Nevertheless, their comparison between experimentally measured slip lengths and the slip lengths obtained from numerical simulations is revealing. Using their notation, the local experimental slip lengths, named $b_{local,exp}$ (see their figure 2b), is approximately 7% to 93% lower (depending on the location at the interface) than the slip lengths obtained numerically, which already account for viscous effect from the gas phase (named b_{cp}, see their figure 4b). Moreover, they find that if viscous effects from the gas phase are neglected in the numerical simulations, the effective (global) slip length increases only slightly, from $b_{eff,th} = 4.0\,\mu\text{m}$ to $4.3\,\mu\text{m}$, compared with $b_{eff} = 1.7\,\mu\text{m}$ as measured experimentally. They attribute the 58% reduction in the experimental effective slip length to 'interface contamination', i.e. surfactant, explaining that viscous effects from the gas phase cannot explain the discrepancy with their numerical simulations.

Based on our own simulations and the studies of [18], [179], and [20], we find that viscous effects from a gas phase inside SHS gratings can generally be neglected for most practical applications, as intuitively expected and commonly assumed in the SHS literature. Indeed, in

many applications or experimental studies on SHS, the liquid and gas phases are often water and air, respectively, such that $\epsilon \approx 0.02$ is very small. Moreover, the grating depth $\hat{H}_g$ can often be made sufficiently large so as to minimize viscous effects from the gas phase. The criterion found based on our simulations is $\hat{H}_g \gtrsim 10^{-5}\,\mathrm{m}$, which is technically feasible in many applications and often necessary in experiments to prevent collapse of the plastron during the filling of the chamber. We note that in general this criterion depends on the geometry, such as the ratios H_g and H_g/g, and whether the flow is confined in a channel or unbounded in a semi-infinite domain. For further detail about viscous effects from the gas phase in surfactant-free SHS flow, we refer the reader to the theoretical and numerical studies of [206], [220] and [219]. These studies also show that gas viscous effects are mainly important at large ϵ or small H_g, consistently with our findings. In these particular regimes, both viscous effects from the gas phase and surfactant Marangoni stresses would need to be modelled in order to assess their respective contribution on the drag reduction of the SHS.

Interface deformation

Another physical mechanism not considered in the present study is the effect of interface deformation. Many studies have investigated the effect of lateral or longitudinal curvature of the air–water interface of SHSs (see e.g. [219, 182, 221] and references therein). They have found positive or negative impact depending on the curvature sign (whether it points towards the liquid phase or the gas phase), geometry (transverse or longitudinal SHSs), whether the flow is bounded or unbounded [182], or the Reynolds number [221].

The deformation of the interface could be due to the gravity force, viscous forces or a pressure difference across the interface. These forces must be compared with the surface tension, which resists deformations associated with an increase in surface area of the interface, i.e. flattening the plastron in this specific problem. In general, gravity can be neglected since the smallest length scale in microfluidic applications is much smaller than the capillary length, which in this case has a typical value of $\hat{l}_c = \sqrt{\hat{\sigma}_0/(\Delta\hat{\rho}\,\hat{a}_g)} \approx 2.7 \cdot 10^{-3}\,\mathrm{m}$. For this estimate we have

chosen the representative values of $\hat{\sigma}_0 \approx 7.2 \cdot 10^{-2}\,\mathrm{N\,m^{-1}}$ for the surface tension, $\hat{a}_g = 9.81\,\mathrm{m/s^2}$ for the gravitational acceleration, and $\Delta\hat{\rho} \approx 1000\,\mathrm{kg/m^3}$ for the air-water density difference. Similarly, viscous forces are neglected in most applications due to small capillary numbers near the interface $Ca_I = u_I Ca = \hat{\mu}\hat{u}_I/\hat{\sigma}$. We typically find $Ca_I \lesssim 10^{-3}$ for a surfactant-free air–water interface across our range of parameters. We note the effect of surfactant would on the one hand tend to reduce σ, thus enhancing interfacial deformation. On the other, as we have shown in this study, surfactant would reduce u_I, thus limiting interfacial deformation. The reduction of u_I can occur at concentrations much smaller than concentrations necessary to change the surface tension noticeably [201]. Hence, we intuitively expect that viscous forces would have negligible effect, even when combined with surfactant, in regimes where surfactants affect u_I. The capillary length and the capillary number depend on the properties of the fluids on either side of the interface. Although air–water systems, as assumed above, are the most common across real applications, laboratory and field experiments, these characteristic numbers would need to be examined carefully in more specialised applications (e.g. liquid metals for micro-cooling [181]).

The effect of pressure difference is one of the most common cause of interfacial deformation (e.g. [221]). Interfacial curvature typically depends on the ratio of the pressure difference and the surface tension, $\Delta p/\sigma$, following the Young–Laplace law. Thus, surfactant could enhance curvature by reducing σ, thereby affecting the performance of the SHS. Similar to what we noted for viscous effect, we expect the negative impact of surfactant on u_I via Marangoni effects to be generally more important than via interface deformation. If the pressure difference is large enough, there can exist some regimes where both interface deformation and Marangoni stresses are important. The combined effects on SHS performance of negative Marangoni effects and positive or negative interfacial deformation effects would be an important topic for future research.

Three-dimensional effects

Although the geometry used in our model is two-dimensional, we expect the model to give a reasonable estimate of the impact of surfactants for flows above three-dimensional rectangular longitudinal SHS gratings, similar to those used by [179] and many other studies. For three-dimensional gratings with small aspect ratio $w/g = 1/15$, [20] observed three-dimensional flows with recirculations along the side boundaries or via the interior, depending on whether the interface was convex or concave. Overall, they found significant reduction of the slip velocity at the interface due to surfactant contamination, which shows that these three-dimensional recirculation flows are secondary effects compared to the mean two-dimensional effects due to the surfactant-induced Marangoni forces. For cases without this recirculation pattern, we expect surfactants to be advected along the grating, forming a longitudinal surfactant gradient which is approximately uniform in the spanwise direction (i.e. across the grating width). Owing to spanwise viscous friction, we can also note that our model would give a lower bound prediction on the surfactant-induced Marangoni shear, or conversely, an upper bound for the effective slip length and maximum drag reduction.

5.9 Conclusions

In this study, we present a reduced-order scaling model to account for the impact of soluble surfactants in channel flows with superhydrophobic surfaces. The drag reduction potential of superhydrophobic surfaces can be severely reduced if surfactants adsorbed onto the plastron induce Marangoni forces opposed to the flow. These Marangoni forces develop when a gradient of surfactant establishes along the interface.

To simplify the governing equations of this problem, we first linearised the kinetics source terms for the surfactant flux between the bulk and the interface, as well as the coupling condition balancing the viscous force and the surfactant-induced Marangoni force. This linearisation holds for small surfactant concentration $\Gamma \ll 1$, which is a reasonable assumption for most

applications where surfactants are not artificially added. Then, integrating the transport equations in the bulk and at the interface, we find a linear relationship between the interfacial slip velocity at mid-gap and the interface-averaged surfactant-induced Marangoni shear, given by (5.45). This relationship depends explicitly on the non-dimensional numbers $k^* = kMa$, which combines both the non-dimensional bulk background surfactant concentration k and the Marangoni number Ma, as well as Pe, Pe_I, g, Bi and χ.

To obtain a global effective slip length and predict how surfactant transport can affect the flow rate and the drag reduction potential of the SHS, we solve the continuity and momentum conservation equations for low Reynolds number flow. Using a technique based on the work of [166] for surfactant-free SHS flow, we solve Stokes' equation with mixed boundary conditions and a prescribed shear profile at the interface. In the case of a uniform interfacial shear γ_{Ma}, the interfacial velocity relates linearly to $1 - \gamma_{Ma}$, where the coefficient of proportionality depends on the geometric non-dimensional parameters of the SHS, namely the grating length g and the gas fraction ϕ. We close the problem and eliminate the interface velocity by using our earlier result, based on the surfactant problem, that also related interface velocity to shear. Hence, we find that the average Marangoni shear γ_{Ma} depends on seven non-dimensional parameters: k^*, Pe, Pe_I, Bi, χ, g and ϕ, following (5.74). The dependence on the geometry is implicit through the function $\mathcal{F}_0(g, \phi)$, which can be solved from the linear problem (5.57) assuming a surfactant-free Stokes' flow in the same geometry. We find that the effective slip length is $\lambda_e = 2(1-\gamma_{Ma})E_0/(1-(1-\gamma_{Ma})E_0)$, see (5.79), where $E_0 = Q_{d,0}/2$ with $Q_{d,0}$ the added volume flow rate in an SHS channel flow without any surfactant. The corresponding added flow rate Q_d and drag reduction DR due to the SHS, in the general case of a surfactant-contaminated flow, can be determined from the effective slip length following (5.76) and (5.81), respectively. These equations show how the slip length, the added flow rate and the drag reduction are affected by the surfactant-induced Marangoni shear rate at the interface.

In order to test the regime of validity and the accuracy of our model, we performed 137 finite-element numerical simulations of the full governing equations in steady, pressure-driven,

laminar channel flows, inclusive of soluble surfactants following (5.2)–(5.13). We varied the governing non-dimensional groups across a broad range of values to explore the vast parameter space of this problem (see figure 5.8, appendix 5.10, table 5.1 and the Supplementary Table S1). The model predictions for λ_e, DR and γ_{Ma} follow well the numerical results across almost all the parameter space explored. The model coefficients are determined through a least-squares fit for λ_e, yielding $a_1 = 2.30$, $a_2 = 0.319$, $\delta_{0,3} = 1.68$ and $\delta_{1,3} = 0.0528$. The flows that are least well captured by our model corresponds to the 'partial stagnant cap regime', which is also found in air bubbles rising in surfactant-contaminated water. This regime occurs at very large $\mathcal{F}_0 Pe_{I,g}$, and low $\mathcal{D}_{I,g}$ or low $\mathcal{K}_{I,g}$. The partial SC regime exhibits a sharp increase in the shear rate at the transition between a shear-free upstream part and a no-slip downstream part of the interface, which differs from our assumption of a uniform Marangoni shear along the interface. Nevertheless, at least for the simulations performed here, our model predictions are sufficiently accurate for practical purposes. It will be important to test the accuracy of our model also in more complex flows.

Canonical SHS models, which completely neglect surfactant effects, can yield a large error in the prediction of the slip length and of the drag reduction, as shown in figures 5.4 and 5.5. In particular, the error is very large, by several orders of magnitude, at large Marangoni stresses. Hence, models neglecting surfactant can significantly overestimate the drag reduction potential of the SHS. This is particularly important in applications where small background environmental surfactant traces are sufficient to induce strong Marangoni forces, as previously found by [179].

Overall, the model we present provides a useful quantitative estimate of the effect of surfactants on the drag reduction potential of SHSs, across a vast part of the parameter space except in the partial stagnant cap regime. Our scaling predictions can be used directly in numerical simulations of flow over SHS in realistic conditions where surfactants cannot be neglected. The effective slip length λ_e can be used in a Navier-slip boundary condition on the SHS side, without having to solve the full coupled nonlinear surfactant transport problem. This will reduce

considerably the computational burden associated with realistic simulations of SHS flows. We also note that our model can be easily adapted for a two-sided SHS channel, via changes in the boundary conditions in the Stokes' flow problem (see § 5.5.1). This change in boundary conditions will modify the geometric function $\mathcal{F}_0$.

Future work will investigate how the model can be modified for more complex three-dimensional flows over SHSs, such as pillars or disordered SHSs. Apart from annular flows [183, 20] or very long air–water interfaces [179], accumulation of surfactant at stagnation points in these three-dimensional problems can also lead to surfactant-induced Marangoni stresses. Predicting the magnitude of these forces and the overall effect on the effective slip length or the drag reduction is a complex problem. Many applications operate at larger Reynolds numbers, where the effect of turbulence on the surfactant Marangoni stresses may be important. At intermediate Reynolds numbers, where the viscous sub-layer forming at the SHS is sufficiently thick compared with the surfactant diffusive boundary layer thickness, our scaling model may still be applicable, though the empirical parameters may differ from those found here. At very large Reynolds numbers, turbulence is likely to enhance the diffusion of surfactant in the bulk and at the interface, which could change the concentration gradients and result in intermittent localised Marangoni forces at the interface. These problems have a direct impact on the performance of SHSs in many applications, and constitute important topics for future studies.

5.10 Appendix: Key dimensionless numbers across all numerical simulations

To help provide a visual overview of the simulations performed, figure 5.8 plots the value of each dimensionless group on the vertical axis, with the horizontal axis indicating different simulations. Ranges for each parameters are also reported earlier in table 5.1. Detailed values are included in table S1 of the Supplementary Materials.

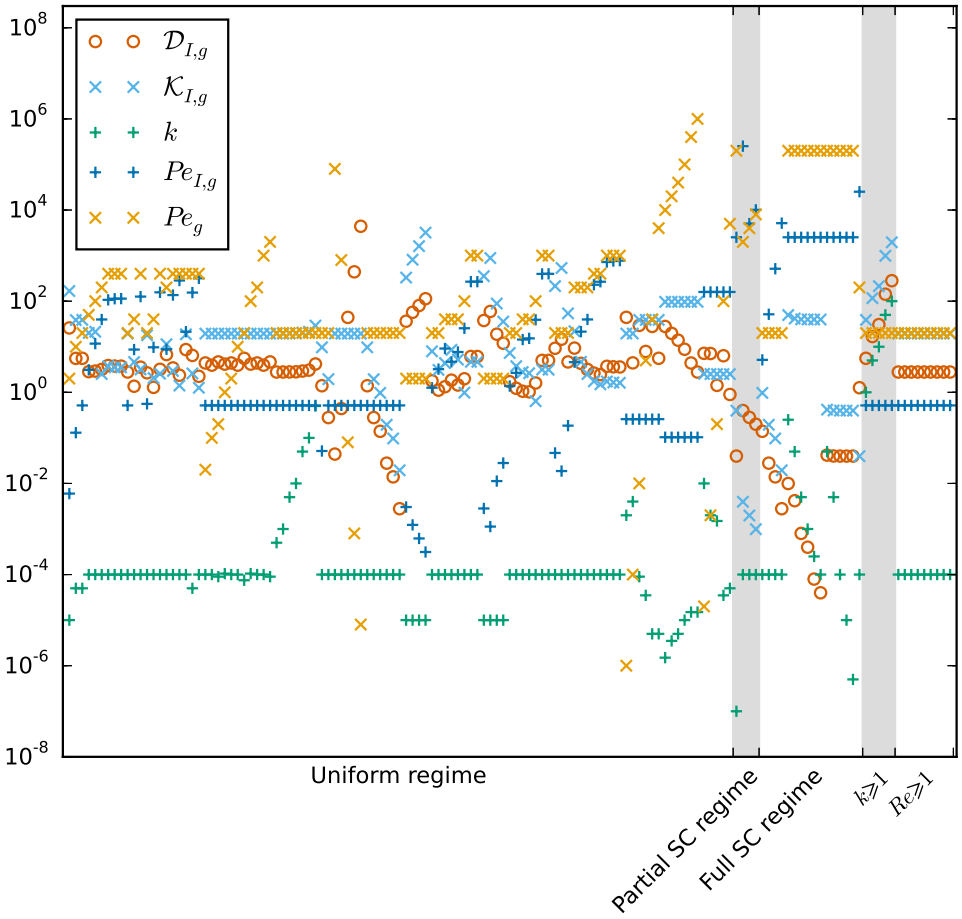

Figure 5.8: Variation of some of the characteristic non-dimensional numbers used in our 137 numerical simulations depending on the regime. The non-dimensional number $\mathcal{K}_{I,g} = Bi_g(1+k)/\mathcal{F}_0$ the ratio of the adsorption–desorption kinetics flux to the advective flux at the interface. The parameter $\mathcal{D}_{I,g} = \chi_g(1+k)/(\mathcal{F}_0 Pe_g)^{1/2}$ is the ratio of the transverse diffusive flux through the diffusive boundary layer to the advective flux at the interface. The function $\mathcal{F}_0 = \mathcal{F}(g, \phi, x = 0)$ is related to the interfacial slip velocity following (5.67).

5.11 Appendix: Diffusive boundary layer thickness

To determine an estimate of the boundary layer thickness δ for the surfactant concentration, we builds on the result in § 5.4.2 and perform a scale analysis of the bulk advection–diffusion equation (5.23), which is expanded below as

$$u\frac{\partial c}{\partial x} + v\frac{\partial c}{\partial y} = \frac{1}{Pe}\left(\frac{\partial^2 c}{\partial x^2} + \frac{\partial^2 c}{\partial y^2}\right). \tag{5.95}$$

In the surfactant adsorption (resp. desorption) boundary layer forming above the interface, we denote the characteristic variation of the bulk concentration as Δc. In the streamwise direction, we expect the change Δc to take place between between $x = -g/2$ and $x = x_0$ (resp. x_0 and $g/2$), as sketched in figure 5.2. As explained in § 5.4.2, x_0 is defined as the interface location where the kinetics flux S vanishes. Under the assumption of low interfacial concentration (see (5.33) and text above), we previously found that the adsorption and desorption diffusive boundary layers are approximately anti-symmetric and of characteristic streamwise length scale $\sim g$, as depicted in figure 5.2(b).

If we focus on the adsorption region of the interface, c at the interface is denoted as c_I, which varies by a scale Δc_I between $x = -g/2$ and $x = x_0$, where $S = 0$ implies $c_I \sim 1$. In addition, the characteristic cross-stream variation, across the boundary layer, is from c_I to 1, implying that this variation in c also scales as Δc_I. Therefore, in both the $x-$ and $y-$ directions, $\Delta c = \Delta c_I$ over characteristic distances g and δ, respectively.

We denote the characteristic streamwise and cross-stream velocities in the diffusive boundary layer as U_δ and V_δ, respectively. Hence, a scale analysis of equation (5.95) gives

$$U_\delta\frac{\Delta c_I}{g} + V_\delta\frac{\Delta c_I}{\delta} \sim \frac{1}{Pe}\left(\frac{\Delta c_I}{g^2} + \frac{\Delta c_I}{\delta^2}\right), \tag{5.96}$$

where we can divide throughout by Δc_I. Thus, δ is a function of the Péclet number Pe, the interface length g, as well as U_δ and V_δ. These velocity scales are expected to depend on the geometrical parameters g and ϕ, as well as on the interfacial velocity u_I and the characteristic

shear rate profile γ_{Ma}. We now seek an explicit dependence of U_δ and V_δ on these parameters.

We assume that the diffusive boundary layer thickness is not affected by the channel height, such that $\delta < 1$. We also assume that a diffusive boundary layer above a particular interface is independent from the other interfaces, and thus independent of the gas fraction ϕ. We retain the dependence on the interface length g. We can distinguish two main limits influencing U_δ and V_δ, depending on the boundary condition at the interface. This can either consist of a finite slip and negligible shear ($u_I > 0$ and $\gamma_{Ma} \ll 1$), or of no-slip and finite shear ($u_I = 0$ and $\gamma_{Ma} \sim 1$). Hence, in general, $U_\delta \sim u_I + \gamma_{Ma}\delta$. The two cases are analyzed further below.

- First, for $u_I > 0$ and $\gamma_{Ma} \ll 1$, according to the analysis in appendix 5.12, we have $U_\delta \sim u_I \sim g$ for $g \lesssim 1$, and $U_\delta \sim u_I \sim 1$ for $g \gtrsim 1$. We determine the scale for V_δ using the continuity equation (5.21), which gives $V_\delta \sim U_\delta \delta/g$. Replacing these velocity scales into (5.96), we find

$$\frac{\delta}{g} = \delta_{0,1}\left(1 + \delta_{1,1} g^2 Pe\right)^{-1/2} \quad \text{for } g \lesssim 1 \tag{5.97}$$

  and

$$\frac{\delta}{g} = \delta_{0,2}\left(1 + \delta_{1,2} g Pe\right)^{-1/2} \quad \text{for } g \gtrsim 1, \tag{5.98}$$

  where $\delta_{0,1}$, $\delta_{1,1}$, $\delta_{0,2}$, $\delta_{1,2}$ are empirical parameters.

- Second, for u_I negligible and $\gamma_{Ma} \sim 1$, U_δ depends only on the ratio of the thickness of the diffusive boundary layer and the channel height: $U_\delta \sim \delta\gamma_{Ma} = \delta$ for $\delta < 1$. This regime is also known as the Lévêque regime [204, 205]. Note that $V_\delta \sim 0$ in this case. Replacing these velocity scales into (5.96), we find the asymptotic behaviour

$$\frac{\delta}{g} = \delta_{0,3}\left(1 + \delta_{1,3} g^2 Pe\right)^{-1/3}, \tag{5.99}$$

  for any $g > 0$, and with $\delta_{0,3}$ and $\delta_{1,3}$ two empirical parameters.

As noted before, the results (5.97)–(5.99) are valid provided $\delta < 1$, which is satisfied for large enough Péclet numbers or small enough gap length. For an intermediate regime with

partial slip and partial shear, i.e. $U_\delta \sim u_I + \gamma_{Ma}\delta$, we expect that the boundary layer thickness has an exponent between $-1/2$ and $-1/3$. The transition between the slip dominated regime, with scaling (5.97) or (5.98), and the shear dominated regime, with scaling (5.99), should be smooth at low Reynolds numbers.

5.12 Appendix: Asymptotic limits for the slip velocity

The computation of the slip velocity yields distinctive simplified behaviours in the limits of large and small gap length g, as evidenced in figure 5.3. In this section, we analytically derive asymptotic limits for the slip velocity profile $u_I(x)$, and confirm their agreement with the numerically computed values at mid-gap from figure 5.3.

We start by considering the so-called dual series comprised of equations (5.52) and (5.56)

$$2E + \sum_{n=1}^{\infty} d_n \alpha_n \cos(k_n x) = 0 \qquad \text{for } g/2 < |x| \leq L/2, \tag{5.100a}$$

$$E + \sum_{n=1}^{\infty} d_n \beta_n \cos(k_n x) = 1 - \gamma_{Ma} \qquad \text{for } |x| < g/2, \tag{5.100b}$$

with α_n and β_n defined in equations (5.53) and (5.55), respectively. From this set of expressions, it is possible to obtain a closed form of the asymptotic behavior of the slip velocity by considering only the leading order of α_n and β_n in the relevant limits. This is done in a similar fashion to [166] and [170], who derived expressions for the effective slip length from the asymptotic behavior of the first coefficient E. However, the slip velocity depends on the whole set of coefficients, and in this case it is not enough to derive an expression for the first coefficient only. Indeed, recall the form of $u_I(x)$ from (5.65)

$$u_I(x) = 2E + \sum_{n=1}^{\infty} d_n \alpha_n \cos(k_n x). \tag{5.101}$$

The derivations of $u_I(x)$ and its value at mid-gap $u_{Ic} = u_I(x = 0)$ in the limits of large and small g are presented in the next two subsections.

5.12.1 Limit of large gap length

Consider the limit $g \to \infty$, with the gas fraction ϕ fixed. Since $L = g/\phi$, note that this case necessarily implies $L \to \infty$ as well. Note that, due to our choice of the channel height $\hat{h}$ as the length scale for the nondimensionalization, this limit corresponds to a "narrow" channel with the top wall close to the plastron. Consequently, we have

$$k_n = \frac{2\pi n}{L} \to 0,$$

and in this limit α_n and β_n can be expanded as

$$\alpha_n = -\frac{4k_n^3}{3} + O(k_n^5), \tag{5.102a}$$

$$\beta_n = -\frac{8k_n^3}{3} + O(k_n^5). \tag{5.102b}$$

Taking into account that $k_n \sim L^{-1}$, the expressions (5.100) and (5.102) lead to the following expansions of the unknown Fourier coefficients

$$E = E^{(0)} \quad + O(L^{-1}), \tag{5.103a}$$

$$d_n = d_n^{(0)} L^3 + O(L^2). \tag{5.103b}$$

Substituting (5.102) and (5.103) into (5.100) we arrive at the leading-order dual series for $E^{(0)}$ and $d_n^{(0)}$. After introducing the changes of variable $\widehat{d}_n^{(0)} = (2\pi n)^3 \, d_n^{(0)}$ and $z = 2\pi x/L$, this dual series yields

$$\frac{3}{2}E^{(0)} - \sum_{n=1}^{\infty} \widehat{d}_n^{(0)} \cos(nz) = 0 \qquad \text{for } \phi\pi < |z| \leq \pi, \tag{5.104a}$$

$$\frac{3}{8}E^{(0)} - \sum_{n=1}^{\infty} \widehat{d}_n^{(0)} \cos(nz) = \frac{3}{8}\left(1 - \gamma_{Ma}\right) \qquad \text{for } |z| < \phi\pi, \tag{5.104b}$$

and its coefficients can be obtained exactly. Indeed, after integrating (5.104a) from $\phi\pi$ to π and (5.104b) from 0 to $\phi\pi$, one can then sum the two expressions and obtain

$$E^{(0)} = \frac{\phi(1-\gamma_{Ma})}{(4-3\phi)}. \tag{5.105}$$

The rest of the coefficients $\widehat{d}_n^{(0)}$ can be retrieved multiplying (5.104) by harmonics of the form $\cos(mz)$ with $m \in \mathbb{N}$ and $m \geq 1$. Then, applying the same procedure of integration and summation and invoking orthogonality between the functions, we arrive at

$$\widehat{d}_n^{(0)} = -\frac{3(1-\gamma_{Ma})}{(4-3\phi)}\frac{\sin(n\pi\phi)}{n\pi}. \tag{5.106}$$

Using the obtained set of coefficients, one can now evaluate the slip velocity. Substituting (5.102a) and (5.103) in (5.101), we have

$$u_I(z) = 2E^{(0)} - \frac{4}{3}\sum_{n=1}^{\infty}\widehat{d}_n^{(0)}\cos(nz) + O(L^{-1}).$$

Applying (5.105) and (5.106), one subsequently obtains

$$u_I(z) = \frac{2(1-\gamma_{Ma})}{(4-3\phi)}\left[\phi + 2\sum_{n=1}^{\infty}\frac{\sin(n\pi\phi)}{n\pi}\cos(nz)\right] + O(L^{-1}). \tag{5.107}$$

First, note that for $\phi = 0$ the above expression (5.107) yields $u_I(x) = 0$ at leading order, as one would expect. We then observe that the expression in brackets in (5.107) is the Fourier cosine series of a square wave with value 1 for $|z - 2j\pi| < \phi\pi$ and 0 for $\phi\pi < |z - 2j\pi| \leq \pi$, where $j \in \mathbb{N}$. Consequently, by virtue of the uniqueness of a Fourier series one has, after undoing the change of variables

$$u_I(x) = \begin{cases} \dfrac{2(1-\gamma_{Ma})}{(4-3\phi)} + O(L^{-1}) & \text{for } |x| < g/2, \\ 0 & \text{for } g/2 < |x| \leq L/2. \end{cases} \tag{5.108}$$

The fact that the slip velocity tends to a constant value as $g \to \infty$ is expected, due to the confinement effect of the top wall. Indeed, the disparity of horizontal and vertical length scales ($g \gg 1$) leads to a lubrication regime in which the slip velocity asymptotically tends to a constant along the plastron. In such a regime, the velocity field can be approximated as unidirectional in the central "core region" following the thin-gap approximation (see for instance the examples in [222]). From (5.108), the value of the slip velocity at mid-gap $u_{Ic} = u_I(x = 0)$ would then yield at leading order

$$\frac{u_{Ic}}{2(1-\gamma_{Ma})} \simeq \frac{1}{4-3\phi}, \tag{5.109}$$

where u_{Ic} has been normalized with $2(1-\gamma_{Ma})$ following Section 5.5. Notice that this normalization implicitly assumes $0 \leq \gamma_{Ma} < 1$, however in the case $\gamma_{Ma} = 1$ it is straightforward from (5.108) that $u_{Ic} = 0$ at leading order.

The expression (5.109) is plotted in figure 5.3(b), confirming the trend of the values u_{Ic} computed numerically. Moreover, note that within this asymptotic regime $g \to \infty$, the expression (5.109) leads to the two following limits

$$\frac{u_{Ic}}{2(1-\gamma_{Ma})} \sim 1 \qquad \text{for } \phi \to 1, \tag{5.110a}$$

$$\frac{u_{Ic}}{2(1-\gamma_{Ma})} \sim \frac{1}{4} \qquad \text{for } \phi \to 0, \tag{5.110b}$$

which are corroborated as well by the asymptotic behavior in figure 5.3(a).

5.12.2 Limit of small gap length

Consider now the limit $g \to 0$, with the gas fraction ϕ fixed. Then, like in the previous case, $g \to 0$ necessarily implies $L \to 0$ as well. This case corresponds to a "tall" channel with distant top walls. We have

$$k_n = \frac{2\pi n}{L} \to \infty,$$

and therefore α_n and β_n can be expanded as

$$\alpha_n = -e^{k_n} \qquad + O(e^{-k_n}), \tag{5.111a}$$

$$\beta_n = -2k_n e^{k_n} + O(e^{-k_n}). \tag{5.111b}$$

Given the functional form of the leading order terms in (5.111), we introduce the change of variable $\widehat{d}_n = e^{k_n}\, d_n$ and seek the expansions

$$E = E^{(0)} + E^{(1)} L + O(L^2), \tag{5.112a}$$

$$\widehat{d}_n = \widehat{d}_n^{(0)} + \widehat{d}_n^{(1)} L + O(L^2). \tag{5.112b}$$

After re-scaling the spatial variable $z = 2\pi x/L$, we insert (5.111) and (5.112) into (5.100) and group the $O(1)$ terms to arrive at the leading-order dual series for $E^{(0)}$ and $\widehat{d}_n^{(0)}$

$$-2E^{(0)} + \sum_{n=1}^{\infty} \widehat{d}_n^{(0)} \cos(nz) = 0 \qquad \text{for } \phi\,\pi < |z| \leq \pi, \tag{5.113a}$$

$$\sum_{n=1}^{\infty} n\, \widehat{d}_n^{(0)} \cos(nz) = 0 \qquad \text{for } |z| < \phi\,\pi, \tag{5.113b}$$

which leads to $E^{(0)} = 0$ and $\widehat{d}_n^{(0)} = 0$. The terms of order $O(L)$ can then be grouped into the following dual series for $E^{(1)}$ and $\widehat{d}_n^{(1)}$

$$-2E^{(1)} + \sum_{n=1}^{\infty} \widehat{d}_n^{(1)} \cos(nz) = 0 \qquad \text{for } \phi\,\pi < |z| \leq \pi, \tag{5.114a}$$

$$\sum_{n=1}^{\infty} n\, \widehat{d}_n^{(1)} \cos(nz) = -\frac{1}{4\pi}\,(1 - \gamma_{Ma}) \qquad \text{for } |z| < \phi\,\pi. \tag{5.114b}$$

The coefficients in (5.114) can be obtained exactly following the procedure of [223]. However, in this case it is not necessary to explicitly obtain $E^{(1)}$ and $\widehat{d}_n^{(1)}$ in order to obtain the slip velocity, since the left-hand side of equation (5.114a) can be determined exactly for $|z| < \phi\pi$

(see page 161 of [223])

$$-2E^{(1)}+\sum_{n=1}^{\infty}\widehat{d}_n^{(1)}\cos(nz)=\cos\left(\frac{z}{2}\right)\int_z^{\phi\pi}\frac{h(t)}{\sqrt{\cos(z)-\cos(t)}}\,dt \qquad \text{for } |z|<\phi\pi. \tag{5.115}$$

Here $h(t)$ can be retrieved from equation (5.4.60) in page 162 of [223], which in our case simplifies to

$$\begin{aligned} h(t) &= \frac{2}{\pi}\frac{d}{dt}\int_0^t \frac{\sin(z/2)}{\sqrt{\cos(z)-\cos(t)}}\left(\int_0^z\left[-\frac{1}{4\pi}(1-\gamma_{Ma})\right]du\right)dz \\ &= -\frac{\sqrt{2}}{4\pi}(1-\gamma_{Ma})\tan\left(\frac{t}{2}\right), \end{aligned} \tag{5.116}$$

where it is worth noting that the closed form of the integral

$$\int_0^t \frac{z\sin(z/2)}{\sqrt{\cos(z)-\cos(t)}}\,dz=\sqrt{2}\,\pi\ln(\sec(t/2)) \tag{5.117}$$

has been used in the derivation above, obtained from [169].

The desired slip velocity for $0\le z<\phi\pi$ can now be retrieved at leading order introducing the expansions (5.111) and (5.112) into (5.101) and using equation (5.115)

$$\begin{aligned} u_I(z) &= L\left(2E^{(1)}-\sum_{n=1}^{\infty}\widehat{d}_n^{(1)}\cos(nz)\right) &&+O(L^2) \\ &= -L\cos\left(\frac{z}{2}\right)\int_z^{\phi\pi}\frac{h(t)}{\sqrt{\cos(z)-\cos(t)}}\,dt &&+O(L^2). \end{aligned} \tag{5.118}$$

Making use of (5.116), integrating and undoing the change of variable we obtain the velocity profile

$$u_I(x)=\begin{cases}(1-\gamma_{Ma})\dfrac{L}{2\pi}\operatorname{arccosh}\left(\dfrac{\cos(\pi x/L)}{\cos(\pi\phi/2)}\right)+O(L^2) & \text{for } |x|\le g/2, \\ 0 & \text{for } g/2\le|x|\le L/2. \end{cases} \tag{5.119}$$

The above formula (5.119), after setting $\gamma_{Ma} = 0$ and a change in the variables normalization, is at leading order exactly half of the slip velocity obtained by [169] for a configuration with longitudinal no-shear infinite gaps in a semi-infinite domain. This result is consistent with the analysis of [224], who conclude that the slip velocity profile in such a configuration should be larger than that of the equivalent transverse case by exactly a factor of two.

From (5.119), we can finally obtain the normalized slip velocity at mid-gap at leading order

$$\frac{u_{Ic}}{2(1-\gamma_{Ma})} \simeq \frac{g}{4\pi\phi}\operatorname{arccosh}\left(\sec\left(\frac{\pi\phi}{2}\right)\right), \tag{5.120}$$

where we have substituted $L = g/\phi$.

From (5.120) we can corroborate the validity of the linear scaling $u_I \sim g$ for $g \lesssim 1$. Indeed, the asymptote (5.120) is plotted for $\phi = 0.99$ in figure 5.3(a), showing good agreement with the numerically computed slip velocity.

Consider now the limit $\phi \to 0$ within the regime of small gap length $g \to 0$ investigated in this subsection. Then (5.120) yields, to leading order in g,

$$\frac{u_{Ic}}{2(1-\gamma_{Ma})} \sim \frac{g}{8} \qquad \text{for } \phi \to 0. \tag{5.121}$$

This is congruent with the linear asymptote for small g followed by the values calculated numerically, which is also shown in figure 5.3(a).

The coefficient E, which appears in the expressions for the effective slip length (5.79) and drag reduction (5.81), can also be obtained in this limit from (5.114) following [223]. We make use of (5.116) to arrive at

$$E = E^{(1)}L + O(L^2) = -\frac{\sqrt{2}\,L}{4}\int_0^{\pi\phi} h(t)dt + O(L^2)$$
$$= (1-\gamma_{Ma})\frac{L}{4\pi}\ln\left(\sec\left(\frac{\pi\phi}{2}\right)\right) + O(L^2) \tag{5.122}$$

5.13 Appendix: Application of our model to experimental studies in the literature showing reduced slip

We study the experimental results of [179] and [20] to analyse with our theoretical model how surfactant affected their SHS performance. The slip velocities extrapolated from the measurements of [179] on the interface ($z = 0$) at mid-gap ($y = 0$) are: $u_I \approx 4 \cdot 10^{-3} \pm 4 \cdot 10^{-3}$ for 2 mm long lanes (see their figure 3D), which is practically negligible; and $u_I \approx 5 \cdot 10^{-2} \pm 9 \cdot 10^{-3}$ for 30 mm long lanes (figure 3E), which is significantly reduced compared with the theoretical (surfactant-free) prediction. (Note that we have non-dimensionalised these velocities using the characteristic velocity U, following the convention used in the present study.) Similarly, [20] report: $u_I \approx 8 \cdot 10^{-2}$ for 5 mm long lanes (see their figure 3*b*), which is significantly reduced compared with the theoretical (surfactant-free) prediction; and $u_I \approx 8 \cdot 10^{-3}$ for 15 mm long lanes (figure 5), which is practically negligible.

The main difficulty in applying our theoretical model, for instance to predict the reduced slip velocities measured experimentally by [179] and [20], is that the surfactant properties and their concentrations are completely unknown in their experiments. Instead, we use our model to predict the concentration of surfactant, for three different possible surfactant types, which could lead to the measured u_I reported in [179] and [20]. The three surfactants we choose are: a 'strong' poorly soluble surfactant with properties described in [179], a 'weak' highly soluble surfactant, namely Sodium Dodecyl Sulfate (SDS), and an 'intermediate' type with similar weak properties as SDS but rendered almost insoluble in water by reducing its

desorption coefficient to $\hat{\kappa}_d = 1\,\mathrm{s}^{-1}$ (instead of $\hat{\kappa}_d = 500\,\mathrm{s}^{-1}$ for SDS in water). Surfactants have a large number of parameters ($\hat{\kappa}_d$, $\hat{\kappa}_a$, $\hat{D}$, $\hat{D}_I$, $\hat{\Gamma}_m$, A, n_σ), in addition to their bulk background concentration $\hat{c}_0$, which are almost all used in our theoretical model (see (5.44) and (5.74), which we use to compute u_I. Thus, by choosing only three different types of surfactants from the vast parameter space, the analysis in this section is primarily qualitative. The aim is to show that our theoretical model provides physically meaningful explanations regarding the impact of surfactant in experimental studies showing reduced SHS performance such as those of [179] and [20].

Assuming a strong surfactant, our model predicts that a bulk surfactant concentration $\hat{c}_0 \sim 10^{-13}\,\mathrm{mM}$ can reduce u_I in the same extent and under the same conditions as reported by [179] for both short and long lanes; and $\hat{c}_0 \sim 10^{-15}$ to $10^{-14}\,\mathrm{mM}$ for the experiments reported by [20]. Assuming the weak SDS surfactant, our model predicts $\hat{c}_0 \sim 1$ to $10\,\mathrm{mM}$ (i.e. near the critical micellar concentration) to obtain the results of [179] and $\hat{c}_0 \sim 0.1$ to $3\,\mathrm{mM}$ for the experimental results of [20]. Assuming an intermediate surfactant, $\hat{c}_0 \sim 10^{-5}$ to $10^{-4}\,\mathrm{mM}$ would lead to the results of [179], and $\hat{c}_0 \sim 4 \cdot 10^{-7}$ to $10^{-5}\,\mathrm{mM}$ for the results of [20]. These theoretical predictions show that: (i) a very strong surfactant would require only minute traces, unavoidable in normal environmental conditions, to strongly affect slip; (ii) whilst at the other extreme, a weak surfactant such as SDS would require a concentration of the order of the critical micellar concentration to lead to a no-slip or reduced slip condition. Then, an intermediate surfactant would require small concentration at or below typical environmental background concentration to lead to no-slip or reduced slip condition.

Therefore, our theoretical model provides physically sensible predictions with regard to surfactant types and concentrations that may have contaminated the experiments of [179] and [20]. This is consistent with their conclusions. We note that our theoretical model assumes a two-dimensional channel geometry with one-dimensional interfaces, whereas the experiments are three-dimensional with two-dimensional (flat) or three-dimensional (curved) interfaces bounded laterally by no-slip walls. Hence, we expect our model to over-predict the interfacial slip veloc-

ity (for a given surfactant type and concentration) or over-predict the background surfactant concentration (for a given surfactant type and interfacial slip velocity). This means that even lower surfactant concentrations could have affected the experimental results of [179] and [20].

5.14 Acknowledgments

We gratefully acknowledge financial support from the Raymond and Beverly Sackler Foundation, the Engineering and Physical Sciences Research Council, the European Research Council Grant 247333, Mines ParisTech, the Schlumberger Chair Fund, the California NanoSystems Institute through a Challenge Grant, ARO MURI W911NF-17-1-0306 and ONR MURI N00014-17-1-2676.

Chapter 6

Flows with surfactant over realistic, three-dimensional gratings

6.1 Abstract

Trace amounts of surfactants have been shown to critically prevent the drag reduction of superhydrophobic surfaces (SHSs), yet predictive models including their effects in realistic pattern geometries are still lacking. We present a theory accounting for the three-dimensional nature of laminar fluid flows over contaminated SHS gratings, which for the first time allows for a direct comparison with experiments in realistic SHS geometries. We find that the trend in the local slip velocity is in agreement with both numerical simulations and experimental measurements in microfluidic channels, which we obtain via confocal microscopy and micro-particle image velocimetry.

6.2 Letter

Superhydrophobic surfaces (SHSs) have the potential to yield enormous technological benefits in fields such as naval transportation or pipeline hydraulics, primarily due to their ability to reduce fluid drag [160]. Through a combination of hydrophobic chemistry and microscopic sur-

face patterning, these substrates are able to retain a superficial layer of air, thereby producing an apparent slip when in contact with a liquid flow [225]. Early theoretical work [164, 165, 166] modeled the air pockets trapped within these textures as flat boundaries with no shear, predicting large drag reductions in the laminar regime. Initial studies reported measured values of the drag in good agreement with these results [14, 15, 184, 183]. However, subsequent experiments found a reduced or even nonexistent slip [16, 17, 18], pointing at the interfacial stresses induced by surface-active contaminants as one possible cause of this discrepancy.

In recent years, independent experimental studies have unequivocally demonstrated the pivotal role of surfactants deteriorating the performance of SHSs [179, 20]. Theoretical and computational work has followed, confirming the extent to which even trace amounts of these contaminants can influence fluid slip [24, 226, 227]. Indeed, ambient levels of surfactants, often impossible to avoid or control even in experimental settings, are known to play a central role altering the behavior of numerous small-scale multiphase flows [2]. The advection of interfacial surfactant produced by the fluid motion triggers the appearance of concentration gradients, which in turn generate Marangoni stresses opposing the flow, ultimately tending to effectively immobilize the interface.

Even though the underlying physical mechanism behind this increase of drag is clear, modelling it in the case of realistic SHSs textures presents serious challenges. The concentration gradients that induce Marangoni stresses appear in the streamwise direction, when stagnation points at the downstream ends of the interfaces prevent surfactants from being further advected by the flow. This is the reason why the initial theoretical studies on the subject [205, 227] to consider the case of infinite SHS gratings transverse to the flow, since this is the simplest two-dimensional geometry that presents stagnation points and can thus capture this effect. In practice, however, gratings tend to be oriented in a longitudinal fashion, since this geometry yields comparatively higher slip both in the absence [166] and in the presence [179] of surfactants. Since infinite longitudinal gratings have no stagnation points and thus can not lead to accumulation of surfactants, including these effects into a model requires considering gratings

of finite length. Such a situation would necessarily involve a three-dimensional velocity field, which in turn complicates the theoretical analysis and has so far prevented models inclusive of surfactants from being developed for realistic grating geometries.

In this Letter, we introduce a theory based on matched asymptotic expansions that accounts for the three-dimensional nature of the field in the case of finite longitudinal gratings. Our theory is valid for an arbitrary profile of shear stress along the air-water interface of each grating, and we further particularize it with a model for the Marangoni shear induced by surfactants based on scaling arguments. The resulting theory is able to predict the slip and drag of SHS longitudinal gratings in the presence of surfactants, and enables a direct comparison, for the first time, between theory and experiments in realistic geometries. We perform experiments without any added surfactants using SHSs in microfluidic channels, which yield a trend in the slip velocity that agrees with our model and with numerical simulations. In addition, our theory allows for a coarse estimation of the unknown physicochemical parameters of the surfactant that is predominantly present inside PDMS microchannels.

Our study considers steady, laminar flow driven by a mean pressure gradient $\hat{G}$ across a thin channel of half-height $\hat{h}$. The bottom of the channel is lined with a pattern of slender, yet finite, parallel rectangular gratings in a longitudinal configuration. Each of these gratings supports a gas-liquid interface that we assume remains flat and flush with the channel floor . Due to the periodicity of the array in the streamwise and spanwise directions, we limit to a unit cell consisting of one grating and its surrounding ridges, as depicted in Figure 6.1a. The streamwise, wall-normal, and spanwise directions are denoted by the coordinates $\hat{x}$, $\hat{y}$ and $\hat{z}$, respectively. Note that throughout the analysis we use hats to designate all dimensional quantities, while dimensionless ones are expressed without hats.

We start by leveraging the disparity of scales between the length $\hat{L}$ and the half-height $\hat{h}$ of the unit cell (see Figure 6.1a), and define a small parameter $\varepsilon = \hat{h}/\hat{L} \ll 1$. Unlike in the typical Hele-Shaw flow approximation [228], here we do not assume that the spanwise length scale (the pitch $\hat{P}$) is also much larger than $\hat{h}$, since in microfluidic applications with longitudinal

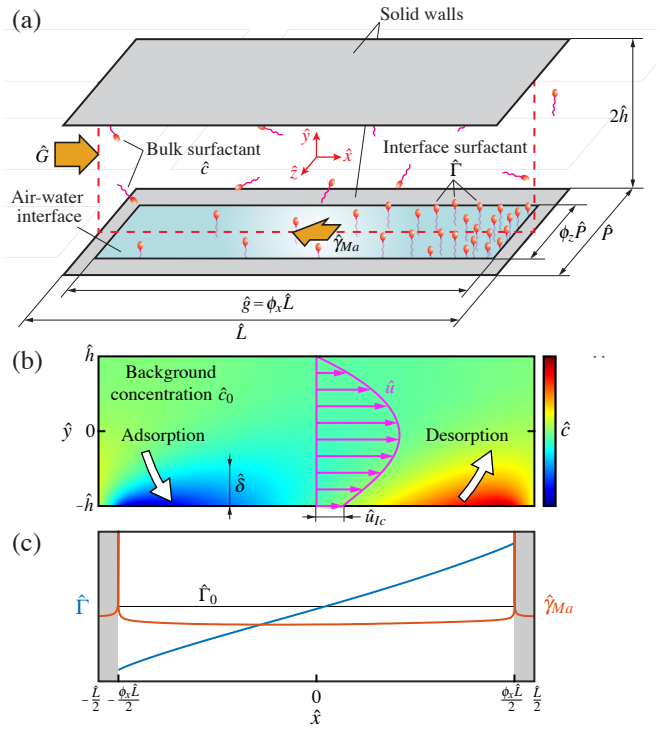

Figure 6.1: (a) Unit cell of the SHS, periodic in $\hat{x}$ and $\hat{z}$. The coordinate origin is taken at the center of the unit cell. (b) Longitudinal cross section at $\hat{z} = 0$, showing the typical distribution of bulk surfactant, with adsorption/desorption regions at the upstream/downstream ends, respectively. (c) Interface concentration and shear stress at the plastron, for the same $\hat{z} = 0$ cross section.

gratings the values of both $\hat{h}$ and $\hat{P}$ lie in the order of tens of micrometers, with $\hat{L}$ typically ranging in the millimeter or centimeter scale [14, 15, 229, 17]. Consequently, we define the nondimensional coordinates $x = \hat{x}/\hat{L}$, $y = \hat{y}/\varepsilon\hat{L}$ and $z = \hat{z}/\varepsilon\hat{L}$. It then follows from the incompressibility condition $\hat{\boldsymbol{\nabla}} \cdot \hat{\boldsymbol{u}} = 0$ that the flow is approximately unidirectional, with the dominant streamwise velocity component scaling as $\hat{u} \sim \hat{U}$ while the wall-normal and spanwise components scale as $\hat{v} \sim \varepsilon\hat{U}$ and $\hat{w} \sim \varepsilon\hat{U}$, respectively. The velocity scale $\hat{U}$ of the flow is naturally defined from the imposed mean pressure gradient as $\hat{U} = \hat{h}^2\hat{G}/\hat{\mu}$, with $\hat{\mu}$ the dynamic viscosity of the fluid. At leading order in ε, the Navier–Stokes equations describing the flow

simplify (Section 6.3.1) to

$$\frac{\partial^2 u}{\partial y^2} + \frac{\partial^2 u}{\partial z^2} = \frac{\partial p}{\partial x}, \tag{6.1a}$$

$$\frac{\partial p}{\partial y} = \frac{\partial p}{\partial z} = 0, \tag{6.1b}$$

where $u(x, y, z) = \hat{u}/\hat{U}$ and $p(x) = \hat{p}/(\hat{G}\hat{L})$ are the dimensionless streamwise velocity and pressure. The unidirectional nature of this leading-order flow is only a good approximation far from the downstream and upstream edges of the plastron, specifically, in regions where $|x \pm \phi_x/2| \gg \varepsilon$, with ϕ_x the streamwise gas fraction as shown in Fig. 6.1a. Therefore, the asymptotic expansion in ε is singular, as is typically found in the thin-gap approximation [222]. Since we consider slender gratings with $\varepsilon \ll 1$, the regions of validity represent most of the domain and useful approximations of both local and integrated flow quantities can be obtained.

Equations (6.1) are complemented with no-slip boundary conditions $u = 0$ at solid walls and ridges. Additionally, the surfactant-laden interface imposes a tangential Marangoni shear stress $\hat{\gamma}_{Ma}$ on the fluid that is determined by the local gradient of surfactant, which is in turn coupled to the flow through a transport equation. It can be shown from the full boundary condition that, under mild assumptions (see Section 6.3.2), this stress is only dependent on x at leading order in ε, and thus we take the remaining nondimensional boundary condition at the air–water interface as $\partial_y u|_I = \gamma_{Ma}(x)$, with $\gamma_{Ma}(x) = \hat{\gamma}_{Ma}/(\hat{\mu}\hat{U}/\varepsilon\hat{L})$ and where the subindex I denotes the particularization of a field to the air-water interface.

Note that, while Eqs. (6.1) also describe the infinite-grating problem, in the case of finite gratings described here the pressure gradient is not constant throughout the whole domain, and the specific functional form of $p(x)$ must be determined from two integral constraints (see Section 6.3.2). First, the volumetric flow rate $Q = \int_{-\phi_z P/2}^{\phi_z P/2} \int_{-1}^{1} u(x, y, z)\, dy\, dz$ must be constant through every cross-section of the domain, in order to satisfy mass conservation. Second, the pressure drop across the whole unit cell must be congruent with the imposed mean pressure gradient, such that $\int_{-1/2}^{1/2} p(x)\, dx = 1$. These two conditions lead to a final expression for the

flow field given by

$$u(x,y,z) = \begin{cases} \left[\frac{2P+3Q_d^\infty(1-\phi_x)\langle\gamma_{Ma}\rangle}{2P+3Q_d^\infty(1-\phi_x)} - \frac{3Q_d^\infty(\langle\gamma_{Ma}\rangle-\gamma_{Ma}(x))}{2P+3Q_d^\infty}\right] u_P(y) \\ \quad + \left[\frac{2P(1-\langle\gamma_{Ma}\rangle)}{2P+3Q_d^\infty(1-\phi_x)} + \frac{2P(\langle\gamma_{Ma}\rangle-\gamma_{Ma}(x))}{2P+3Q_d^\infty}\right] u_d^\infty(y,z) & \text{if } |x| < \dfrac{\phi_x}{2}, \\ \left[\frac{2P+3Q_d^\infty(1-\phi_x\langle\gamma_{Ma}\rangle)}{2P+3Q_d^\infty(1-\phi_x)}\right] u_P(y) & \text{if } \dfrac{\phi_x}{2} < |x| \le \dfrac{1}{2}, \end{cases} \tag{6.2}$$

where $u_P(y) = (1-y^2)/2$ is the nondimensional plane Poiseuille profile and $u_d^\infty(y,z)$ is the deviation from $u_P(y)$ in the infinite-grating case. In other words, $u(y,z) = u_P(y) + u_d^\infty(y,z)$ in the case of $\phi_x = 1$ and $\gamma_{Ma}(x) = 0$, with $u_d^\infty(y,z)$ known from previous studies [164, 230]. Also, P denotes the normalized pitch $P = \hat{P}/\hat{h}$ (see Fig. 6.1a) and Q_d^∞ the contribution of u_d^∞ to the flow rate in the infinite-grating problem [i.e. $Q_d^\infty = \int_{-\phi_z P/2}^{\phi_z P/2}\int_{-1}^{1} u_d^\infty(y,z)\,dy\,dz$], which is itself dependent on P and ϕ_z. The quantity $\langle\gamma_{Ma}\rangle$ is the average Marangoni shear across the plastron $\langle\gamma_{Ma}\rangle = \frac{1}{\phi_x}\int_{-\phi_x/2}^{\phi_x/2}\gamma_{Ma}(x)\,\mathrm{d}x$, and can only take values between 0 (in the case of a clean, free-slip interface) and 1 (for a fully immobilized, no-slip interface). All terms in Eq. (6.2) are now either prescribed or known from the well-studied infinite-grating problem, and thus we have arrived to an approximation of the three-dimensional flow as a linear combination of two known, simpler flow fields. The expression still holds for an arbitrary shear stress profile at the interface, and not necessarily one induced by surfactants, as long as $\gamma_{Ma}(x)$ remains a function of only x. Eq. (6.2) could also be applied to other configurations in which the infinite-grating problem is known, like double-sided SHS [230] or more complicated arbitrary patters [231], and it also remains a valid leading-order flow field for any value of ϕ_x, provided $\varepsilon \ll 1$.

The final step is to find an expression for $\gamma_{Ma}(x)$, which has so far been treated as a prescribed profile, as a function of the underlying surfactant dynamics. With our choice of nondimensionalization, the (linearized) governing equations describing the transport of soluble

surfactant (Section 6.3.1) are given by

$$u\frac{\partial c}{\partial x}+v\frac{\partial c}{\partial y}+w\frac{\partial c}{\partial z}=\frac{1}{\varepsilon Pe}\left(\varepsilon^2\frac{\partial^2 c}{\partial x^2}+\frac{\partial^2 c}{\partial y^2}+\frac{\partial^2 c}{\partial z^2}\right), \tag{6.3a}$$

$$\frac{\partial(u\Gamma)}{\partial x}+\frac{\partial(w\Gamma)}{\partial z}=\frac{1}{\varepsilon Pe_I}\left(\varepsilon^2\frac{\partial^2 \Gamma}{\partial x^2}+\frac{\partial^2 \Gamma}{\partial z^2}\right)+\frac{Bi}{\varepsilon}\left(c_I-\Gamma\right), \tag{6.3b}$$

$$\left.\frac{\partial c}{\partial y}\right|_I=Da\left(c_I-\Gamma\right), \tag{6.3c}$$

$$\left.\frac{\partial u}{\partial y}\right|_I=\gamma_{Ma}(x)=\varepsilon kMa\frac{\partial \Gamma}{\partial x}. \tag{6.3d}$$

Equations (6.3a) and (6.3b) describe the advection and diffusion of the bulk surfactant concentration c and of the interface surfactant concentration Γ, respectively. The adsorption and desorption kinetics governing the exchange between the two species is modeled through the flux boundary condition (6.3c), whereas the Marangoni boundary condition (6.3d) relates the fluid shear stress at the interface with the gradient of surfactant concentration. Note also that Eqs. (6.3b) to (6.3d) are defined only at the air-water interface.

In addition, Eqs. (6.3) introduce six nondimensional numbers. The bulk and interface Péclet numbers are defined as $Pe=\hat{h}\hat{U}/\hat{D}$ and $Pe_I=\hat{h}\hat{U}/\hat{D}_I$, respectively, where $\hat{D}$ and $\hat{D}_I$ are the diffusivities of the two species. The Marangoni number $Ma=n_s\hat{R}\hat{T}\hat{\Gamma}_m/(\hat{\mu}\hat{U})$ depends on the maximum packing concentration at the interface $\hat{\Gamma}_m$, the ideal gas constant $\hat{R}$, the temperature $\hat{T}$ and a parameter n_s quantifying the effects of salinity. Moreover, the Biot $Bi=\hat{h}\hat{\kappa}_d/\hat{U}$ and Damköhler $Da=\hat{h}\hat{\kappa}_a\hat{\Gamma}_m/\hat{D}$ [1] numbers parametrize the effect of kinetics, with $\hat{\kappa}_a$ and $\hat{\kappa}_d$ the adsorption and desorption rate constants. Finally, the normalized concentration $k=\hat{\Gamma}_0/\hat{\Gamma}_m=\hat{\kappa}_a\hat{c}_0/\hat{\kappa}_d$ is a measure of the degree of saturation of the interface, since $\hat{\Gamma}_0=k\hat{\Gamma}_m$ is a scale for the typical interface concentration and $\hat{c}_0$ is the background bulk concentration present in the liquid. These six dimensionless groups, in addition to four geometrical parameters that we choose as ϕ_x, ϕ_z, P and $g=\hat{g}/\hat{h}=\phi_x/\varepsilon$, fully describe the problem.

A scaling analysis of Eqs. (6.3), similar to the one performed in [24] for the case of transverse

[1] Other conventions [24, 222] for the choice of nondimensional groups use the parameter $\chi=\hat{\kappa}_d\hat{h}/(\hat{\kappa}_a\hat{\Gamma}_m)$ instead of the Damköhler number Da. Note that $\chi=Bi\,Pe/Da$.

gratings, leads to a semi-empirical expression for $\langle\gamma_{Ma}\rangle$ that can then be combined with the flow field (6.2) to obtain the final theory (see Section 6.3.3). These scaling arguments hinge on the assumption that the normalized concentration is sufficiently low (i.e. $k \ll 1$), which justifies the choice of linearized equations in (6.3) and is typically the case in situations in which surfactants are not artificially added. Furthermore, the stress at the interface (and thus the gradient of surfactant as well) is assumed to remain approximately constant (i.e $\gamma_{Ma}(x) \approx \langle\gamma_{Ma}\rangle$), a condition that usually holds in small-scale applications in which the flow is not fast enough to reach the so-called stagnant-cap regime [24].

To test our theory, we select the centerline slip velocity $u_{Ic} = u(x, y = -1, z = 0)$ [2] as a way to quantify the degree of slip and drag reduction of a given SHS. The main reason for this choice is that, as opposed to the local slip length $\lambda(x, z) = u_I / \partial_y u|_I$, the experimental measurement of u_{Ic} does not require the estimation of velocity gradients at the interface [18], ensuring a higher accuracy in the already challenging evaluation of the flow field at the air–water interface. The final expression that our model provides for u_{Ic} is

$$u_{Ic} = \left[\frac{\dfrac{1}{Pe_I} + a_2 \dfrac{Bi\, g^2}{(1+\delta Da)}}{\dfrac{1}{Pe_I} + a_1\, k\, Ma\, u_{Ic}^{\text{clean}} + a_2 \dfrac{Bi\, g^2}{(1+\delta Da)}} \right] u_{Ic}^{\text{clean}}, \tag{6.4}$$

where the parameter $\delta = \hat{\delta}/\hat{h}$ denotes the diffusive boundary layer thickness of the bulk concentration close to the interface (Fig. 6.1b), which we model as $\delta(g, Pe) = a_3(1 + a_4\, Pe/g)^{-1/3}$ following further scaling analysis of Eq. (6.3a). The quantity u_{Ic}^{clean} is the centerline slip velocity of the *clean* problem, i.e. taking $\gamma_{Ma}(x) = \langle\gamma_{Ma}\rangle = 0$ in (6.2). This leads to $u_{Ic}^{\text{clean}} = 2P u_{Ic}^{\infty}/[2P + 3Q_d^{\infty}(1 - \phi_x)]$, with u_{Ic}^{∞} the centerline slip velocity of the infinite-grating problem which, like Q_d^{∞}, is fully determined [164, 232]. It is worth noting that other local and global quantities like the effective slip length λ_e can also be readily obtained from our model

[2] Note that the assumption of a roughly constant shear stress $\gamma_{Ma}(x) \approx \langle\gamma_{Ma}\rangle$, when introduced in Eq. (6.2), implies that our model considers u_{Ic} to be also constant along x. In the simulations and experiments, however, it is necessary to choose a specific value of x to evaluate u_{Ic} . We take this value to be $x = 0$, the center of the grating in the streamwise direction.

(Section 6.3.2).

The parameters a_1, a_2, a_3 and a_4 in (6.4) are empirical coefficients that arise in the scaling analysis of Eqs. (6.3). In order to estimate them, we performed 155 finite-element simulations of the full, three-dimensional governing equations, spanning a wide range of dimensionless groups to ensure a proper coverage of the large parameter space. Fitting (6.4) to the results for u_{Ic} obtained from these simulations yielded $a_1 \approx 0.345$, $a_2 \approx 0.275$, $a_3 \approx 5.581$ and $a_4 \approx 3.922$, which are values of order one as expected from scaling coefficients. Additionally, the computation of the full governing equations allowed to corroborate the validity of our modeling assumptions (see Section 6.3.4).

Equipped with a theory, we aimed to compare the values of u_{Ic} obtained from (6.4) with experimental measurements. To this end, we employed micro-particle image velocimetry (µ-PIV) in microfluidic channels, using a confocal microscope (Leica SP8 Resonant Scanning) in a setup similar to the one in [179]. The devices were fabricated with polydimethylsiloxane (PDMS) using photolithography and soft lithography techniques (details in Section 6.3.5), and their outline is shown in Fig. 6.2a and 6.2b. The SHS consists of longitudinal gratings of pitch $\hat{P} = 60\,\mu\text{m}$ and spanwise gas fraction of $\phi_z = 2/3$. A good approximation of a periodic array is achieved with a chamber of width $\hat{W} = 2\,\text{mm}$ that results in 33 parallel gratings across the spanwise direction. The nominal half-height of the channel is $\hat{h} = 60\,\mu\text{m}$, although due to the PDMS casting process this value varies slightly between experiments, and thus we incorporate its deviation into the uncertainty analysis. The depth of the gratings is chosen as $\hat{d} = 25\,\mu\text{m}$, enough to ensure a stable plastron for the duration of each experiment. Since previous work [179, 24] highlighted the grating length as the most relevant geometric parameter that could be adjusted to maximize slip, we test gratings of $\hat{g} = 15\,\text{mm}$, $\hat{g} = 25\,\text{mm}$, $\hat{g} = 35\,\text{mm}$ and $\hat{g} = 45\,\text{mm}$. The values of ϕ_x are such that the length of the solid ridges remains constant with a value of $(1 - \phi_x)\hat{g}/\phi_x = 20\,\mu\text{m}$.

Motivated by previous observations [179] of strong Marangoni stresses in the absence of any added surfactant, we used clean de-ionized water without any additives in our experiments. We

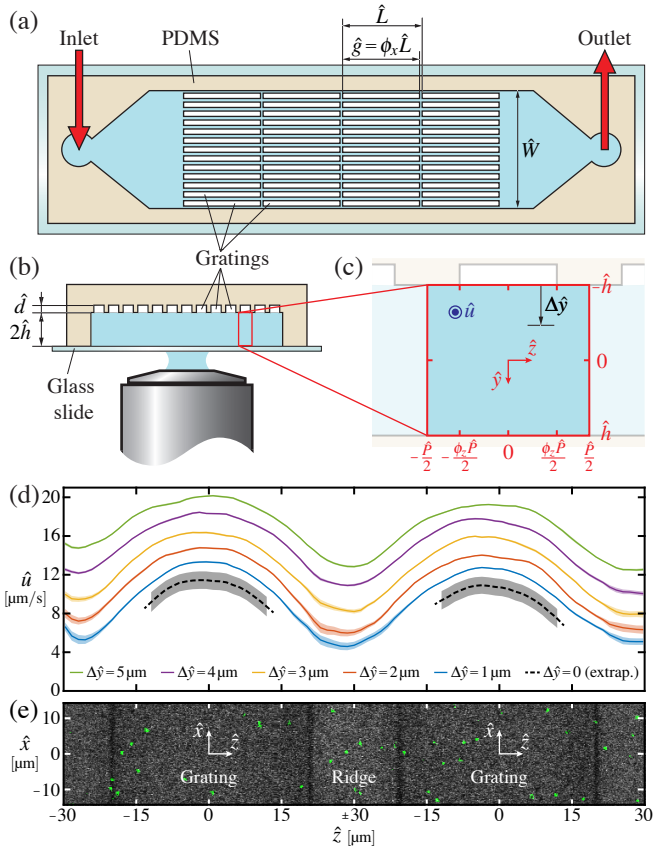

Figure 6.2: Schematics of the (a) top view and (b) cross section of the microfluidic devices used in the experiments. (c) Cross section of a unit cell, such as the one displayed in Fig. 6.1a. The coordinate $\Delta\hat{y}$ denotes the distance from the air-water interface. (d) Velocity profiles resulting from μ-PIV at different distances from the interface, bounded by the experimental standard error (see Section 6.3.5). The dashed line denotes the linearly extrapolated slip velocity. (e) Confocal microscopy snapshot of the gratings, with μ-PIV particles appearing in green.

washed the μ-PIV beads (ThermoFisher FluoSpheres carboxylate 0.5-μm diameter) in order to avoid contamination from the surfactant included in their solution [226], and we followed a basic cleaning protocol (Section 6.3.5) for the syringes (Hamilton Gastight) and tubing (Tygon S3) used to drive the flow through the device. Our goal was to quantify the effects on SHSs of natural contaminants present in typical experimental settings, and also to evaluate the performance of our model in their prediction. This is especially relevant in microfluidics, where PDMS is an extremely popular substrate despite having a role in the release of surface-active molecules [233, 199].

The flow was driven using a syringe pump (KD Legato 111) with a net constant flow rate of

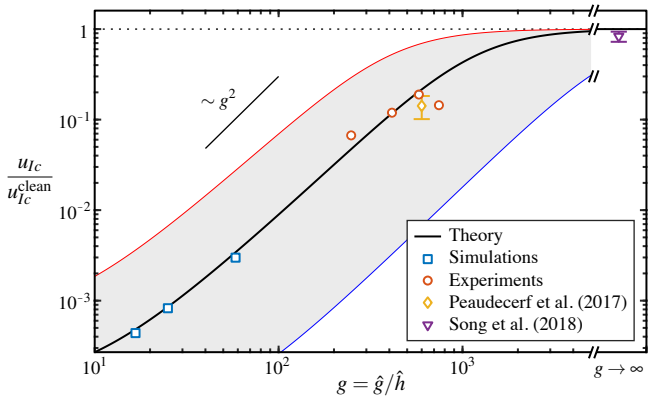

Figure 6.3: Theoretical prediction from our model (6.4) using best estimates of the unknown surfactant parameters, as well as data points obtained from simulations and experiments from both this study and previous literature.

$\hat{Q}_{\text{TOT}} = 1.152\,\mu\text{L}\,\text{min}^{-1}$, ensuring a fixed cross-sectional mean velocity $\langle \hat{u} \rangle_{yz} = \hat{Q}_{\text{TOT}}/(2\hat{h}\hat{W})$ within the chamber. The value of $\langle \hat{u} \rangle_{yz}$ provides a coarse estimate of $\hat{U} \approx 3\langle \hat{u} \rangle_{yz}$ (Section 6.3.2), which is exactly valid only if $\langle \gamma_{Ma} \rangle = 1$ yet useful to estimate the dimensionless groups of the problem. Under these conditions, we measured velocity profiles over two consecutive gratings [3] at different distances from the interface, as displayed in Figs. 6.2d and 6.2e for a grating length of $\hat{g} = 45\,\text{mm}$. A noticeable increase in the fluid velocity can be observed over the gratings, with the flow over the solid ridges appearing to gradually converge towards the expected no-slip condition at the wall. From these vertically spaced profiles, the local velocity at the centerline was extrapolated to the interface using a least-squares linear fit, thereby obtaining $\hat{u}_{Ic}$.

The main challenge in comparing these measurements of $\hat{u}_{Ic}$ to the predictions from our model is the absence of information regarding the type and amount of surfactant present in the channels. Despite this uncertainty, it is possible to obtain a coarse estimate using the theory and previous experimental results (see 6.3.6), finally allowing to compare the slip velocities obtained from theory and experiments (Figure 6.3). Results from simulations are also plotted, but are restricted to values of $g < 60$ due to constraints in our computational capacity. The results show a good agreement of (6.4), with both the simulations and the experiments showing

[3] We avoid imaging gratings too close to the channel lateral side walls to prevent effects related to the loss of periodicity. Specifically, we discard 5 gratings on each side of the channel.

a trend compatible with the simplified $u_{Ic} \sim g^2$ scaling obtained from the dominant balance of Equation (6.4). Furthermore, the estimate of surfactant properties that we obtained from different experimental results [179] appears to be valid for these new results as well, which highlights that the uncontrolled contamination due to surfactants in these two settings is similar. Furthermore, Fig. 6.3 displays theoretical results for a range of values of $\hat{\kappa}_a$ (keeping $\hat{K}_{eq}$ constant), in order to illustrate the second-order effects due to a finite Da number.

Regarding the possible source of contamination, one of the main candidates is the PDMS substrate of the microfluidic channels, which is known to leach surface-active uncrosslinked oligomer chains [233, 199]. However, PDMS is usually regarded as a purely insoluble surfactant [234, 235]. In this limit case, our theory yields $u_{Ic} = u_{Ic}^{\text{clean}}/(1 + a\, Ma_{\text{ins}}\, u_{Ic}^{\text{clean}})$ (see Section 6.3.3), where a is another scaling coefficient of order one and $Ma_{\text{ins}} = n_s \hat{R}\hat{T}\hat{\Gamma}_0 \hat{h}/(\hat{\mu}\hat{D})$, with $\hat{\Gamma}_0$ an independent parameter unrelated to $\hat{c}_0$ in this insoluble case. It is worth noting that this expression for u_{Ic} does not depend on g, directly contradicting the experimental results in Fig. 6.3 and highlighting the importance of at least a certain degree of solubility of the contaminant to replicate the observed behavior. Incidentally, studies have reported the detection of PDMS chains in solution after PDMS is set in contact with water [236, 237]. Furthermore, the levels of concentration reported in [237], in combination with the typical oligomer chain lengths found in [236], leads to concentrations $\hat{c}_0 \sim O(10^{-4} - 10^{-2})$ mol m^{-3}, compatible with our crude estimation. The background concentration $\hat{c}_0$ is also found to vary with the flow velocity [237], suggesting that more sophisticated models could be necessary for finer quantitative predictions.

With the results described here, we have provided important insights about the slip and drag of superhydrophobic surfaces in realistic conditions. The novel theory accounting for laminar flows over finite streamwise gratings has enabled, for the first time, the direct comparison between theory and experiments measuring slip over realistic SHS patterns. It has also provided a powerful tool for the quantification of SHS performance with general sources of shear stress at the air-water interface. Furthermore, our full model for surfactant-contaminated gratings has been key to obtain a coarse estimate of the properties of the surfactants naturally present in

PDMS channels, something crucially important due to the heavy prevalence of this material in microfluidic applications. The model is in good agreement with simulations and experiments, and reveals the importance of considering a finite solubility of the contaminant in order to accurately describe the texture performance.

6.3 Supplementary Material

6.3.1 Full set of governing equations

We consider a steady fluid flow at low Reynolds number, within the unit cell depicted in Figure 6.1a. The three-dimensional velocity field is denoted by $\hat{\boldsymbol{u}} = \hat{u}\,\boldsymbol{e}_x + \hat{v}\,\boldsymbol{e}_y + \hat{w}\,\boldsymbol{e}_z$, where $\boldsymbol{e}_x$, $\boldsymbol{e}_y$ and $\boldsymbol{e}_z$ are unit vectors in the streamwise, wall-normal and spanwise directions (see Fig.6.1a). The scalar fields $\hat{p}$ and $\hat{c}$ represent the pressure and the bulk surfactant concentration, respectively. The governing equations describing the conservation of mass, momentum, and surfactant in the bulk fluid are, in dimensional form,

$$\frac{\partial \hat{u}}{\partial \hat{x}} + \frac{\partial \hat{v}}{\partial \hat{y}} + \frac{\partial \hat{w}}{\partial \hat{z}} = 0, \tag{6.5a}$$

$$\hat{\mu}\left(\frac{\partial^2 \hat{u}}{\partial \hat{x}^2} + \frac{\partial^2 \hat{u}}{\partial \hat{y}^2} + \frac{\partial^2 \hat{u}}{\partial \hat{z}^2}\right) = \frac{\partial \hat{p}}{\partial \hat{x}}, \tag{6.5b}$$

$$\hat{\mu}\left(\frac{\partial^2 \hat{v}}{\partial \hat{x}^2} + \frac{\partial^2 \hat{v}}{\partial \hat{y}^2} + \frac{\partial^2 \hat{v}}{\partial \hat{z}^2}\right) = \frac{\partial \hat{p}}{\partial \hat{y}}, \tag{6.5c}$$

$$\hat{\mu}\left(\frac{\partial^2 \hat{w}}{\partial \hat{x}^2} + \frac{\partial^2 \hat{w}}{\partial \hat{y}^2} + \frac{\partial^2 \hat{w}}{\partial \hat{z}^2}\right) = \frac{\partial \hat{p}}{\partial \hat{z}}, \tag{6.5d}$$

$$\hat{u}\frac{\partial \hat{c}}{\partial \hat{x}} + \hat{v}\frac{\partial \hat{c}}{\partial \hat{y}} + \hat{w}\frac{\partial \hat{c}}{\partial \hat{z}} = \hat{D}\left(\frac{\partial^2 \hat{c}}{\partial \hat{x}^2} + \frac{\partial^2 \hat{c}}{\partial \hat{y}^2} + \frac{\partial^2 \hat{c}}{\partial \hat{z}^2}\right). \tag{6.5e}$$

At the interface, the interfacial surfactant concentration $\hat{\Gamma}$ follows a conservation law. An adsorption–desorption flux couples $\hat{\Gamma}$ to the bulk concentration. Marangoni boundary conditions link the interfacial shear stress to the concentration gradient. The corresponding equations,

defined only at the air–water interface, read

$$\frac{\partial(\hat{u}_I\hat{\Gamma})}{\partial\hat{x}} + \frac{\partial(\hat{w}_I\hat{\Gamma})}{\partial\hat{z}} = \hat{D}_I\left(\frac{\partial^2\hat{\Gamma}}{\partial\hat{x}^2} + \frac{\partial^2\hat{\Gamma}}{\partial\hat{z}^2}\right) + \hat{\mathcal{S}}(\hat{c}_I,\hat{\Gamma}), \tag{6.5f}$$

$$\hat{D}\left.\frac{\partial\hat{c}}{\partial\hat{y}}\right|_I = \hat{\mathcal{S}}(\hat{c}_I,\hat{\Gamma}), \tag{6.5g}$$

$$\hat{\mu}\left.\frac{\partial\hat{u}}{\partial\hat{y}}\right|_I = \hat{\mathcal{N}}(\hat{\Gamma})\frac{\partial\hat{\Gamma}}{\partial\hat{x}}, \tag{6.5h}$$

$$\hat{\mu}\left.\frac{\partial\hat{w}}{\partial\hat{y}}\right|_I = \hat{\mathcal{N}}(\hat{\Gamma})\frac{\partial\hat{\Gamma}}{\partial\hat{z}}, \tag{6.5i}$$

where $\hat{\mathcal{N}}(\hat{\Gamma})$ is a possibly nonlinear term quantifying the dependence of the surface tension with $\hat{\Gamma}$, and depends on the specific model of equilibrium isotherm chosen [2]. The term $\hat{\mathcal{S}}(\hat{c}_I,\hat{\Gamma})$ represents the adsorption-desorption kinetics, and must be compatible with the choice of isotherm. Here, we use a model derived from the Frumkin isotherm [201, 200], which leads to

$$\hat{\mathcal{S}}(\hat{c}_I,\hat{\Gamma}) = \hat{\kappa}_a\hat{c}_I(\hat{\Gamma}_m - \hat{\Gamma}) - \hat{\kappa}_d\hat{\Gamma}e^{A\hat{\Gamma}/\hat{\Gamma}_m}, \tag{6.5j}$$

$$\hat{\mathcal{N}}(\hat{\Gamma}) = n_s\hat{R}\hat{T}\left(\frac{\hat{\Gamma}_m}{\hat{\Gamma}_m - \hat{\Gamma}} + A\frac{\hat{\Gamma}}{\hat{\Gamma}_m}\right). \tag{6.5k}$$

The above equations are complemented with the imposition of a mean background level of bulk concentration

$$\frac{1}{2\hat{h}\hat{P}\hat{L}}\int_{-\hat{P}/2}^{\hat{P}/2}\int_{-\hat{h}}^{\hat{h}}\int_{-\hat{L}/2}^{\hat{L}/2}\hat{c}\,\mathrm{d}\hat{x}\,\mathrm{d}\hat{y}\,\mathrm{d}\hat{z} = \hat{c}_0, \tag{6.5l}$$

as well as with streamwise and spanwise periodicity conditions for variables defined in the bulk fluid,

$$\hat{\boldsymbol{u}}(\hat{\boldsymbol{x}}) = \hat{\boldsymbol{u}}(\hat{\boldsymbol{x}} + \alpha\hat{L}\boldsymbol{e}_x + \beta\hat{P}\boldsymbol{e}_z) \ \text{ for any integers } \alpha,\ \beta, \tag{6.5m}$$

$$\hat{c}(\hat{\boldsymbol{x}}) = \hat{c}(\hat{\boldsymbol{x}} + \alpha\hat{L}\boldsymbol{e}_x + \beta\hat{P}\boldsymbol{e}_z) \ \text{ for any integers } \alpha,\ \beta, \tag{6.5n}$$

which in the case of the pressure also includes a mean pressure drop such that

$$\hat{p}(\hat{\boldsymbol{x}}) = \hat{p}(\hat{\boldsymbol{x}} + \alpha\hat{L}\boldsymbol{e}_x + \beta\hat{P}\boldsymbol{e}_z) + \alpha\hat{G}\hat{L} \quad \text{for any integers } \alpha,\ \beta, \tag{6.5o}$$

and where $\hat{\boldsymbol{x}} = \hat{x}\,\boldsymbol{e}_x + \hat{y}\,\boldsymbol{e}_y + \hat{z}\,\boldsymbol{e}_z$ is the position vector. The remaining equations are the boundary conditions

$$\hat{\boldsymbol{u}} = \boldsymbol{0} \quad \text{on all solid surfaces (no slip and no penetration)}, \tag{6.5p}$$

$$\hat{v} = 0 \quad \text{on the air–water interface (no penetration)}, \tag{6.5q}$$

$$\frac{\partial\hat{c}}{\partial\hat{y}} = 0 \quad \text{on all solid surfaces (no flux)}, \tag{6.5r}$$

$$\frac{\partial\hat{\Gamma}}{\partial\hat{x}} = 0 \quad \text{at } \hat{x} = \pm\phi_x\hat{L} \text{ when } |\hat{z}| \leq \phi_z\hat{P} \text{ (no flux)}, \tag{6.5s}$$

$$\frac{\partial\hat{\Gamma}}{\partial\hat{z}} = 0 \quad \text{at } \hat{z} = \pm\phi_z\hat{P} \text{ when } |\hat{x}| \leq \phi_x\hat{L} \text{ (no flux)}. \tag{6.5t}$$

We normalize Equations (6.5a)-(6.5t) following

$$\begin{gathered} x = \hat{x}/\hat{L},\ y = \hat{y}/(\varepsilon\hat{L}),\ z = \hat{z}/(\varepsilon\hat{L}) \\ u = \hat{u}/\hat{U},\ v = \hat{v}/(\varepsilon\hat{U}),\ w = \hat{w}/(\varepsilon\hat{U}),\ p = \hat{p}/(\hat{G}\hat{L}) \\ c = \hat{c}/\hat{c}_0,\ \Gamma = \hat{\Gamma}/\hat{\Gamma}_0, \end{gathered} \tag{6.6}$$

where $\hat{U} = \hat{h}^2\hat{G}/\hat{\mu}$ and $\hat{\Gamma}_0 = \hat{\kappa}_a\hat{c}_0\hat{\Gamma}_m/\hat{\kappa}_d$ are the natural scales for the velocity and the interfacial

surfactant. Applying this normalization to Equations (6.5a)-(6.5k) results in

$$\frac{\partial u}{\partial x}+\frac{\partial v}{\partial y}+\frac{\partial w}{\partial z}=0, \tag{6.7a}$$

$$\left(\varepsilon^2\frac{\partial^2 u}{\partial x^2}+\frac{\partial^2 u}{\partial y^2}+\frac{\partial^2 u}{\partial z^2}\right)=\frac{\partial p}{\partial x}, \tag{6.7b}$$

$$\varepsilon^2\left(\varepsilon^2\frac{\partial^2 v}{\partial x^2}+\frac{\partial^2 v}{\partial y^2}+\frac{\partial^2 v}{\partial z^2}\right)=\frac{\partial p}{\partial y}, \tag{6.7c}$$

$$\varepsilon^2\left(\varepsilon^2\frac{\partial^2 w}{\partial x^2}+\frac{\partial^2 w}{\partial y^2}+\frac{\partial^2 w}{\partial z^2}\right)=\frac{\partial p}{\partial z}, \tag{6.7d}$$

$$u\frac{\partial c}{\partial x}+v\frac{\partial c}{\partial y}+w\frac{\partial c}{\partial z}=\frac{1}{\varepsilon Pe}\left(\varepsilon^2\frac{\partial^2 c}{\partial x^2}+\frac{\partial^2 c}{\partial y^2}+\frac{\partial^2 c}{\partial z^2}\right). \tag{6.7e}$$

$$\frac{\partial(u_I\Gamma)}{\partial x}+\frac{\partial(w_I\Gamma)}{\partial z}=\frac{1}{\varepsilon Pe_I}\left(\varepsilon^2\frac{\partial^2\Gamma}{\partial x^2}+\frac{\partial^2\Gamma}{\partial z^2}\right)+\frac{Bi}{\varepsilon}\mathcal{S}(c_I,\Gamma), \tag{6.7f}$$

$$\left.\frac{\partial c}{\partial y}\right|_I=Da\,\mathcal{S}(c_I,\Gamma), \tag{6.7g}$$

$$\left.\frac{\partial u}{\partial y}\right|_I=\varepsilon kMa\,\mathcal{N}(\Gamma)\frac{\partial\Gamma}{\partial x}, \tag{6.7h}$$

$$\left.\varepsilon^2\,\frac{\partial w}{\partial y}\right|_I=\varepsilon kMa\,\mathcal{N}(\Gamma)\frac{\partial\Gamma}{\partial z}, \tag{6.7i}$$

$$\mathcal{S}(c_I,\Gamma)=c_I(1-k\Gamma)-\Gamma e^{kA\Gamma}, \tag{6.7j}$$

$$\mathcal{N}(\Gamma)=\left(\frac{1}{1-k\Gamma}+kA\Gamma\right). \tag{6.7k}$$

The parameters appearing in Equations (6.5a)-(6.7k) are detailed in Tables 6.1 and 6.2, as well as the values that they take in our experiments. Since, as explained in the main text, the surfactant type and concentration in the liquid are unknown, only an estimate can be obtained in some cases (see Section 6.3.6 for details). We choose $g=\hat{g}/\hat{h}$, $P=\hat{P}/\hat{h}$, ϕ_x and ϕ_z as the four independent geometric parameters of the problem, noting that ε can then be obtained as $\varepsilon=\phi_x/g$.

Quantity	Symbol	Units	Value (or best estimate) in experiments
Background bulk concentration	$\hat{c}_0$	$\mathrm{mol\,m^{-3}}$	$3 \cdot 10^{-4}$ †
Adsorption rate constant	$\hat{\kappa}_a$	$\mathrm{m^3\,mol^{-1}\,s^{-1}}$	$8.95 \cdot 10^{1}$ †
Desorption rate constant	$\hat{\kappa}_d$	$\mathrm{s^{-1}}$	$7.5 \cdot 10^{-1}$ †
Maximum packing concentration	$\hat{\Gamma}_m$	$\mathrm{mol\,m^{-2}}$	$3.9 \cdot 10^{-6}$ ‡
Bulk surfactant diffusivity	$\hat{D}$	$\mathrm{m^2\,s^{-1}}$	$7 \cdot 10^{-10}$ ‡
Interface surfactant diffusivity	$\hat{D}_I$	$\mathrm{m^2\,s^{-1}}$	$7 \cdot 10^{-10}$ ‡
Salinity parameter	n_s	-	2 ‡
Interaction coefficient	A	-	-2.4 ‡
Ideal gas constant	$\hat{R}$	$\mathrm{J\,mol^{-1}\,K^{-1}}$	8.314
Temperature	$\hat{T}$	K	296
Dynamic viscosity	$\hat{\mu}$	$\mathrm{kg\,m^{-1}\,s^{-1}}$	$8.9 \cdot 10^{-4}$
Velocity scale	$\hat{U}$	$\mathrm{m\,s^{-1}}$	$2.4 \cdot 10^{-4}$
Channel half height (see Fig. 6.1a)	$\hat{h}$	m	$6 \cdot 10^{-5} \pm 3 \cdot 10^{-6}$
Pitch (see Fig. 6.1a)	$\hat{P}$	m	$6 \cdot 10^{-5}$
Grating width (see Fig. 6.1a)	$\phi_z \hat{P}$	m	$4 \cdot 10^{-5}$
Grating length (see Fig. 6.1a)	$\hat{g}$	m	$(1.5, 2.5, 3.5, 4.5) \cdot 10^{-2}$
Ridge size in x (see Fig. 6.1a)	$(1-\phi_x)\hat{g}/\phi_x$	m	$2 \cdot 10^{-5}$

Table 6.1: Parameters appearing in the dimensional equations (6.5a)-(6.6) and in the geometry of the domain (Fig. 6.1a), alongside with their values in the simulations and experiments. The symbol ‡ indicates that the quantity is estimated as the value for the well-characterized SDS, since its order of magnitude does not change appreciably for other substances. The symbol † denotes values that have been coarsely estimated combining our theory and the experimental results in [179] (see Section 6.3.6 for details).

Number	Definition	Range in simulations	Best estimate in experiments
Normalized concentration	$k = \hat{\kappa}_a \hat{c}_0 / \hat{\kappa}_d = \hat{\Gamma}_0 / \hat{\Gamma}_m$	$2.7 \cdot 10^{-5}$ – $5.4 \cdot 10^{-2}$	$4 \cdot 10^{-2}$
Marangoni number	$Ma = n_s \hat{R} \hat{T} \hat{\Gamma}_m / (\hat{\mu} \hat{U})$	$3.1 \cdot 10^{3}$ – $2.3 \cdot 10^{7}$	$9 \cdot 10^{4}$
Péclet number	$Pe = \hat{h} \hat{U} / \hat{D}$	$1.5 \cdot 10^{-2}$ – $1.2 \cdot 10^{5}$	$2 \cdot 10^{1}$
Interface Péclet number	$Pe_I = \hat{h} \hat{U} / \hat{D}_I$	$1.7 \cdot 10^{-1}$ – $6 \cdot 10^{2}$	$2 \cdot 10^{1}$
Biot number	$Bi = \hat{h} \hat{\kappa}_d / \hat{U}$	$8.6 \cdot 10^{-3}$ – $2.5 \cdot 10^{2}$	$2 \cdot 10^{-1}$
Damköhler number	$Da = \hat{h} \hat{\kappa}_a \hat{\Gamma}_m / \hat{D}$	$2.5 \cdot 10^{1}$ – $6.4 \cdot 10^{3}$	$3 \cdot 10^{1}$
Normalized grating length	$g = \hat{g} / \hat{h} = \phi_x / \varepsilon$	1.54 – 58.33	$2.5 \cdot 10^{2}$ – $7.5 \cdot 10^{2}$
Normalized pitch	$P = \hat{P} / \hat{h}$	0.92 – 2	1
Streamwise gas fraction	ϕ_x	0.833 – 0.994	0.9986 – 0.9995
Spanwise gas fraction	ϕ_z	0.667 – 0.980	2/3

Table 6.2: Characteristic dimensionless numbers governing the full problem.

6.3.2 Derivation of the theory for the flow field

Assumption of a spanwise constant interface shear stress

Note that, although $\varepsilon \ll 1$ and $k \ll 1$ in the conditions considered in our study (see Section 6.3.3), the product $\varepsilon k Ma$ appearing in Eqs. (6.7h) and (6.7i) is typically not small, since the Marangoni number is expected to be large $Ma \gg 1$ (see estimates in Table 6.2) and the term $\mathcal{N}(\Gamma) \approx 1$ as long as k and $k|A|$ remain small. In fact, Equation (6.7h) implies that only when $\varepsilon k Ma \gtrsim 1$ the Marangoni stresses at the interface are non-negligible, as it is observed experimentally [17, 18, 179, 20]. Since $\varepsilon \ll 1$, it is possible to assume that $\varepsilon k Ma \gtrsim 1 \gg \varepsilon^2$, and in that case it follows from (6.7i) that $\partial_z \Gamma \approx 0$ at leading order in ε. As detailed in the main text, the asymptotic expansion leading to Eqs. (6.7h) and (6.7i) is singular, and thus the approximation $\partial_z \Gamma \approx 0$ is valid only in regions far from the upstream and downstream stagnation points, i.e. for $|x \pm \phi_x/2| \gg \varepsilon$. Indeed, our finite-element simulations of the full problem confirm that this approximation remains valid in all the cases that were considered. The Marangoni shear $\gamma_{Ma}(x) = \partial_y u|_I$ is thus also assumed to be constant in the spanwise direction and only dependent on x, following Eq. (6.7h).

Velocity field

At leading order in the small parameter ε, the equations (6.7b)-(6.7d) for the flow field lead to

$$\frac{\partial^2 u}{\partial y^2} + \frac{\partial^2 u}{\partial z^2} = \frac{\partial p}{\partial x}, \tag{6.8a}$$

$$\frac{\partial p}{\partial y} = \frac{\partial p}{\partial z} = 0. \tag{6.8b}$$

It is clear from Eq. (6.8b) that p, and thus also $\partial_x p$, will only depend on x. Since the solution u only depends on x through the right-hand-side of Eq. (6.8a), we pose a piecewise solution

$$u(x,y,z) = \begin{cases} u_1(x,y,z) & \text{if } |x| < \phi_x/2, \\ u_2(x,y,z) & \text{if } \phi_x/2 \leq |x| \leq 1/2. \end{cases} \tag{6.9}$$

Taking into account the boundary conditions, the function u_1 satisfies the mixed boundary-value problem given by

$$\begin{aligned} \frac{\partial^2 u_1}{\partial y^2} + \frac{\partial^2 u_1}{\partial z^2} &= \frac{\partial p}{\partial x}(x), \\ u_1 &= 0 \ \text{ if } y = 1 \text{ or if } y = -1 \text{ and } |z| \geq \phi_z P, \\ \frac{\partial u_1}{\partial y} &= \gamma_{Ma}(x) \ \text{ if } y = -1 \text{ and } |z| < \phi_z P. \end{aligned} \tag{6.10}$$

We then introduce the Poiseuille profile $u_P(y) = (1-y^2)/2$ and, by virtue of the linearity of the problem, decompose the solution following $u_1 = -\left[\partial_x p(x)\right] u_P(y) - \left[\gamma_{Ma}(x) + \partial_x p(x)\right] u_d^\infty$. The resulting problem for u_d^∞ is homogeneous, yielding

$$\begin{aligned} \frac{\partial^2 u_d^\infty}{\partial y^2} + \frac{\partial^2 u_d^\infty}{\partial z^2} &= 0, \\ u_d^\infty &= 0 \ \text{ if } y = 1 \text{ or if } y = -1 \text{ and } |z| \geq \phi_z P, \\ \frac{\partial u_d^\infty}{\partial y} &= -1 \ \text{ if } y = -1 \text{ and } |z| < \phi_z P. \end{aligned} \tag{6.11}$$

The problem given by Eqs. (6.11) has been solved in closed form [164, 232], and highlights that $u_d^\infty(y,z)$ is simply the deviation from the Poiseuille profile in the infinite-grating problem.

The function u_2 satisfies

$$\begin{aligned} \frac{\partial^2 u_2}{\partial y^2} + \frac{\partial^2 u_2}{\partial z^2} &= \frac{\partial p}{\partial x}(x), \\ u_2 &= 0 \quad \text{if } y = \pm 1, \end{aligned} \tag{6.12}$$

with the solution given by $u_2 = -\left[\partial_x p(x)\right] u_P(y)$. Consequently, the following linear combination of $u_P(y)$ and $u_d^\infty(y,z)$ solves Eqs. (6.8):

$$u(x,y,z) = \begin{cases} \left[-\dfrac{\partial p}{\partial x}(x)\right] u_P(y) - \left[\gamma_{Ma}(x) + \dfrac{\partial p}{\partial x}(x)\right] u_d^\infty(y,z) & \text{if } |x| < \phi_x/2, \\ \left[-\dfrac{\partial p}{\partial x}(x)\right] u_P(y) & \text{if } \phi_x/2 \le |x| \le 1/2. \end{cases} \tag{6.13}$$

In order to determine the pressure gradient term in Eq. (6.13), we first pose a piecewise pressure field

$$p(x) = \begin{cases} p_1(x) & \text{if } |x| < \phi_x/2, \\ p_2(x) & \text{if } \phi_x/2 \le |x| \le 1/2. \end{cases} \tag{6.14}$$

Integrating the continuity equation (6.7a) across any cross section of the domain evidences that the volumetric flow rate $Q = \int_{-\phi_z P/2}^{\phi_z P/2} \int_{-1}^{1} u(x,y,z)\, dy\, dz$ remains constant in x. Further integrating the piecewise solution (6.13) and invoking Eq. (6.14), we obtain two expressions for the flow rates

$$\begin{aligned} Q_1 &= \int_{-\phi_z P/2}^{\phi_z P/2} \int_{-1}^{1} u_1(x,y,z)\, dy\, dz = \left[-\frac{\partial p_1}{\partial x}(x)\right] \frac{2P}{3} - \left[\gamma_{Ma}(x) + \frac{\partial p_1}{\partial x}(x)\right] Q_d^\infty, \\ Q_2 &= \int_{-\phi_z P/2}^{\phi_z P/2} \int_{-1}^{1} u_2(x,y,z)\, dy\, dz = \left[-\frac{\partial p_2}{\partial x}\right] \frac{2P}{3}, \end{aligned}$$

where $2P/3$ and $Q_d^\infty(\phi_z, P)$ are the flow rates given by $u_P(y)$ and $u_d^\infty(y,z)$, respectively. Note that, since Q_2 must be constant in x, the term $\partial_x p_2$ is necessarily independent of x as well.

Equating $Q_1 = Q_2$ yields a relationship between the two pressure gradients,

$$\frac{\partial p_1}{\partial x}(x) = \left[\frac{2P}{2P + 3Q_d^\infty}\right] \frac{\partial p_2}{\partial x} - \left[\frac{3Q_d^\infty}{2P + 3Q_d^\infty}\right] \gamma_{Ma}(x). \tag{6.16}$$

The last condition that must be satisfied by the solution is the fixed pressure drop across the domain given by Eq. (6.5o). The nondimensional version of this equation, taking $\alpha = 1$ and $\beta = 0$ in (6.5o), leads to $p(x) = p(x + 1) + 1$. This equation can be made specific to $x = -1/2$ and recast into an integral equation for the gradient

$$\int_{-1/2}^{1/2} \frac{\partial p}{\partial x}(x)\, \mathrm{d}x = -1$$

which, after applying the decomposition (6.14), leads to

$$\int_{-1/2}^{-\phi_x/2} \frac{\partial p_2}{\partial x}\, \mathrm{d}x + \int_{-\phi_x/2}^{\phi_x/2} \frac{\partial p_1}{\partial x}(x)\, \mathrm{d}x + \int_{\phi_x/2}^{1/2} \frac{\partial p_2}{\partial x}\, \mathrm{d}x = -1. \tag{6.17}$$

Substituting (6.16) into (6.17), we arrive at

$$\begin{aligned} \frac{\partial p_1}{\partial x}(x) &= -\frac{2P + 3Q_d^\infty(1 - \phi_x)\langle\gamma_{Ma}\rangle}{2P + 3Q_d^\infty(1 - \phi_x)} + \frac{3Q_d^\infty}{2P + 3Q_d^\infty}(\langle\gamma_{Ma}\rangle - \gamma_{Ma}(x)), \\ \frac{\partial p_2}{\partial x} &= -\frac{2P + 3Q_d^\infty(1 - \phi_x\langle\gamma_{Ma}\rangle)}{2P + 3Q_d^\infty(1 - \phi_x)}, \end{aligned} \tag{6.18}$$

which can finally be introduced in (6.13) to produce the closed form solution for the flow field Equation (6.2) in the main text. The term $\langle\gamma_{Ma}\rangle$ in (6.18) represents the average value of $\gamma_{Ma}(x)$ at the interface, i.e. $\langle\gamma_{Ma}\rangle = \frac{1}{\phi_x}\int_{-\phi_x/2}^{\phi_x/2} \gamma_{Ma}(x)\, \mathrm{d}x$.

Once the leading-order velocity field (6.13) is fully determined from known parameters, the relevant quantities characterizing the performance of the SHS can be readily obtained. The local centerline slip velocity $u_{Ic} = u(x, y = -1, z = 0)$ is

$$u_{Ic}(x) = 2P \left[\frac{(1 - \langle\gamma_{Ma}\rangle)}{2P + 3Q_d^\infty(1 - \phi_x)} + \frac{(\langle\gamma_{Ma}\rangle - \gamma_{Ma}(x))}{2P + 3Q_d^\infty}\right] u_{Ic}^\infty, \tag{6.19}$$

with $u_{Ic}^{\infty}(\phi_z, P) = u_d^{\infty}(y = -1, z = 0)$. With the additional assumption of a uniform shear stress $\gamma_{Ma}(x) = \langle\gamma_{Ma}\rangle$, justified in Section 6.3.3, Eq. (6.19) further simplifies to

$$u_{Ic} = \left[\frac{2Pu_{Ic}^{\infty}}{2P + 3Q_d^{\infty}(1-\phi_x)}\right](1 - \langle\gamma_{Ma}\rangle) := u_{Ic}^{\text{clean}}(1 - \langle\gamma_{Ma}\rangle), \tag{6.20}$$

where we define $u_{Ic}^{\text{clean}}(\phi_x, \phi_z, P)$ as the centerline slip velocity for the finite-grating clean case (i.e. $\gamma_{Ma}(x) = \langle\gamma_{Ma}\rangle = 0$). Equation (6.20) leads directly to Equation (6.4) of the main text after the introduction of a model for $\langle\gamma_{Ma}\rangle$. Another common, global measure of SHS performance is the increase in flow rate with respect to that of a Poiseuille flow. Our theory predicts

$$\begin{aligned} Q_d &= \int_{-\phi_z P/2}^{\phi_z P/2}\int_{-1}^{1}[u(x,y,z) - u_P(y)]\,\mathrm{d}y\,\mathrm{d}z = \left[\frac{2P\phi_x Q_d^{\infty}}{2P + 3Q_d^{\infty}(1-\phi_x)}\right](1 - \langle\gamma_{Ma}\rangle) \\ &:= Q_d^{\text{clean}}(1 - \langle\gamma_{Ma}\rangle), \end{aligned} \tag{6.21}$$

where we again introduce $Q_d^{\text{clean}}(\phi_x, \phi_z, P)$ by definition as the increase in flow rate for the finite-grating, clean problem. Perhaps the most common global quantity sought in theoretical SHS studies is the effective slip length, i.e. the quantity λ_e such that a unit cell (Fig. 6.1a), in which the mixed boundary conditions on $y = -1$ are substituted by $u = \lambda_e \partial_y u$, yields the same increase Q_d in flow rate. Such a flow yields a solution $u_{\lambda_e}(y) = u_P(y) + \lambda_e(1-y)/(2+\lambda_e)$ and thus an increase in flow rate of $2P\lambda_e/(2+\lambda_e)$ which, when equated to Q_d, yields an expression for the slip length

$$\lambda_e = \frac{Q_d}{2P - Q_d} = \frac{2\phi_x Q_d^{\infty}(1 - \langle\gamma_{Ma}\rangle)}{2P + [3 - \phi_x(4 - \langle\gamma_{Ma}\rangle)]\,Q_d^{\infty}}. \tag{6.22}$$

6.3.3 Scaling theory for the surfactant transport

Full problem

The analysis of the surfactant transport equations is similar to that in [24], but we fully describe it here in order to achieve an exhaustive characterization of the differences between the two-dimensional and three-dimensional cases. The first key assumption of our model for

the surfactant transport problem given by Equations (6.7e)-(6.7k) is that the concentration of surfactant is low enough to ensure a dilute regime in which $k \ll 1$. We expect this assumption to be the case for most situations in which surfactants are not artificially added, for instance, when unwanted contaminants are naturally present in water [24]. Additionally, since the interaction parameter A is typically not large in absolute value, with $|A| \lesssim 20$ [201], it is possible to assume that $k|A| \ll 1$ as well. The nonlinear terms [Eqs. (6.7j) and (6.7k)] in the governing equations can then be linearized, leading to $\mathcal{S}(c_I, \Gamma) = c_I - \Gamma + O(k) + O(k|A|)$ and $\mathcal{N}(\Gamma) = 1 + O(k) + O(k|A|)$. Consequently, at leading order in k and $k|A|$, Equations (6.7f)-(6.7k) can be simplified, yielding Equations (6.3) in the main text.

Applying an integral average to Eq. (6.3b) along the spanwise direction, we obtain

$$\frac{\partial \langle u_I \Gamma \rangle_z}{\partial x} = \frac{\varepsilon}{Pe} \frac{\partial^2 \langle \Gamma \rangle_z}{\partial x^2} + \frac{Bi}{\varepsilon} (\langle c_I \rangle_z - \langle \Gamma \rangle_z), \tag{6.23}$$

where the spanwise average across the plastron of an arbitrary integrable function $f(z)$ is defined as $\langle f \rangle_z = \frac{1}{\phi_z P} \int_{-\phi_z P/2}^{\phi_z P/2} f(z)\, \mathrm{d}z$, and where the terms in (6.3b) associated with derivatives in z vanish due to the no-slip ($w = 0$) and no-flux ($\partial_z \Gamma = 0$) boundary conditions at the edges $z = \pm \phi_z P/2$ of the plastron. If Equation (6.23) is further integrated from $x = -\phi_x/2$ to $x = \phi_x/2$ and equivalent boundary conditions $u = 0$ and $\partial_x \Gamma = 0$ are applied at $x = \pm \phi_x/2$, we have that

$$\int_{-\phi_x/2}^{\phi_x/2} (\langle c_I \rangle_z - \langle \Gamma \rangle_z)\, \mathrm{d}z = 0, \tag{6.24}$$

and thus by virtue of the mean value theorem an equilibrium condition $\langle c_I \rangle_z = \langle \Gamma \rangle_z$ must occur at some coordinate along the interface, which we call x_0. Downstream from x_0, the flow advection promotes the accumulation of interfacial surfactant, which in turn triggers a net desorption flux and an increase in bulk surfactant with respect to the background level. Upstream from x_0, the situation is the opposite, with a deficit of Γ and c_I with respect to the equilibrium values and a net adsorption flux. Figures 6.1b and 6.1c depict this physical scenario with the two distinct regions along the interface.

The second main assumption is to consider the interfacial concentration Γ as approximately linear. In this case, Eq. (6.24) implies that the equilibrium point must be approximately at the center of the interface (i.e. $x_0 \approx 0$), and thus the bulk concentration at x_0 is approximately the background concentration and we have $\langle c \rangle_z(x_0) = \langle \Gamma \rangle_z(x_0) \approx 1$. Consequently, this assumption allows to scale the concentrations at both ends of the interface $x = \pm\phi_x/2$ as

$$c(x = \pm\phi_x/2) \sim 1 \pm \Delta c, \tag{6.25a}$$

$$\Gamma(x = \pm\phi_x/2) \sim 1 \pm \Delta\Gamma, \tag{6.25b}$$

with Δc and $\Delta\Gamma$ the characteristic variation of the concentrations (see Figures 6.1b and 6.1c). Additionally, note that an approximately linear Γ also implies [Eq. (6.7h)] that the Marangoni shear at the interface is taken as approximately constant (i.e. $\gamma_{Ma}(x) \approx \langle \gamma_{Ma} \rangle$). This assumption is expected to hold as long as the flow is not in the so-called stagnant cap regime [24], characterized by a strongly nonuniform interfacial concentration. Such a regime is reached when advection at the interface overcomes both diffusion and kinetic effects [222], that is, when $\varepsilon Pe_I \gg 1$ and either $Bi/\varepsilon \ll 1$ or $Da \gg 1$ [see Eq. (6.5f)]. Given the typical parameter values in small-scale flows like the ones considered in this study (see Section 6.3.6 and Table 6.2), we conclude that for long gratings $\varepsilon Pe_I \lesssim 1$, justifying this assumption. At any rate, we perform an analysis a posteriori using the results of the numerical simulations (see Section 6.3.4), confirming the approximately linear profile of Γ in all cases considered.

Using these two key assumptions, it is possible to use scaling arguments on Equations (6.3) to obtain an expression for $\langle \gamma_{Ma} \rangle$ as a function of the nondimensional groups of the problem. We start by scaling the terms in Eq. (6.3d) as $\partial_y u|_I \sim \langle \gamma_{Ma} \rangle$ and $\partial_x \Gamma \sim \Delta\Gamma/\phi_x$, leading to

$$\Delta\Gamma \sim \frac{\phi_x \langle \gamma_{Ma} \rangle}{\varepsilon k Ma}. \tag{6.26}$$

Next, we evaluate the terms in Eq. (6.7j) at the interface ends $x = \pm\phi_x/2$. We take $\partial_y c|_I \sim [1 - (1 \pm \Delta c_I)]/\delta \sim \mp\Delta c_I/\delta$ and $(c_I - \Gamma) \sim [1 \pm \Delta c_I - (1 \pm \Delta\Gamma)] \sim \pm(\Delta c_I - \Delta\Gamma)$, where $\delta = \hat{\delta}/\hat{h}$

is the characteristic boundary layer thickness of the bulk concentration (Fig. 6.1b). We arrive at

$$\Delta c_I \sim \frac{\delta Da}{(1+\delta Da)} \frac{\phi_x \langle \gamma_{Ma} \rangle}{\varepsilon k Ma}. \tag{6.27}$$

Finally, Equation (6.23) is integrated from $x = -\phi_x/2$ to $x = x_0$, leading to

$$\langle u_I \Gamma \rangle_z(x_0) = \frac{\varepsilon}{Pe} \frac{\partial \langle \Gamma \rangle_z}{\partial x}(x_0) + \frac{Bi}{\varepsilon} \int_{-\phi_x/2}^{x_0} (\langle c_I \rangle_z - \langle \Gamma \rangle_z) \, \mathrm{d}x, \tag{6.28}$$

whose terms we scale as $\langle u_I \Gamma \rangle_z(x_0) \sim u_{Ic}$, $\partial_x \langle \Gamma \rangle_z(x_0) \sim \Delta\Gamma/\phi_x$, and $\int_{-\phi_x/2}^{x_0} (\langle c_I \rangle_z - \langle \Gamma \rangle_z) \, \mathrm{d}x \sim \phi_x(\Delta c_I - \Delta\Gamma)$. Making use of Equations 6.26 and 6.27 and introducing $g = \hat{g}/\hat{h} = \phi_x/\varepsilon$, we arrive at

$$u_{Ic} \sim \frac{\langle \gamma_{Ma} \rangle}{k Ma} \left(\frac{1}{Pe_I} + \frac{Bi \, g^2}{(1+\delta Da)} \right),$$

which, after introducing empirical coefficients for each term, yields

$$u_{Ic} = \frac{\langle \gamma_{Ma} \rangle}{a_1 k Ma} \left(\frac{1}{Pe_I} + a_2 \frac{Bi \, g^2}{(1+\delta Da)} \right). \tag{6.29}$$

Making use of the theory for the flow field [Eq. (6.20)], we substitute $u_{Ic} = (1 - \langle \gamma_{Ma} \rangle) u_{Ic}^{\mathrm{clean}}$ into (6.29) and obtain the final expression for $\langle \gamma_{Ma} \rangle$ as a function of the parameters of the problem,

$$\langle \gamma_{Ma} \rangle = \frac{a_1 \, k \, Ma \, u_{Ic}^{\mathrm{clean}}}{\dfrac{1}{Pe_I} + a_1 \, k \, Ma \, u_{Ic}^{\mathrm{clean}} + a_2 \dfrac{Bi \, g^2}{(1+\delta Da)}}. \tag{6.30}$$

Equation (6.30) can now be introduced in (6.20) to obtain the formula for the slip velocity (6.4) from the main text. Similarly, combining Eq. (6.30) with (6.21) and (6.22), expressions for the increase in flow rate and effective slip length can be reached.

The only yet undetermined part of the model is an expression for the boundary layer thickness δ, which we seek through scaling of the conservation law for the bulk surfactant (6.3a). In situations with $\varepsilon Pe \gg 1$, streamwise advection must balance wall-normal diffusion $u \partial_x c \sim \frac{1}{\varepsilon Pe} \partial_{yy} c$, which is only possible if c varies over a small length scale $\delta \ll 1$ [222]. We take

$\partial_x c \sim \Delta c_I/\phi_x$, $\partial_{yy} c \sim \Delta c_I/\delta^2$ and the velocity inside the boundary layer as $u \sim u_{Ic} + \langle\gamma_{Ma}\rangle\delta$. In the case of an interface close to immobilization, i.e. $u_{Ic} \sim 0$ and $\langle\gamma_{Ma}\rangle \sim 1$, these scalings indicate that $\delta \sim (Pe/g)^{-1/3}$ when $\varepsilon Pe \gg 1$. In the opposite case of $\varepsilon Pe \ll 1$, Equation (6.3a) is dominated by diffusion, and thus the characteristic length scale of variation of c in the wall-normal direction is the whole half height of the domain, implying $\delta \sim 1$. We choose

$$\delta = a_3(1 + a_4 Pe/g)^{-1/3} \tag{6.31}$$

to satisfy these two extremes, with a_3 and a_4 empirical parameters. It is also possible to obtain a similar expression with an exponent of $-1/2$ instead, by assuming that the boundary layer is essentially shear-free (i.e. $u_{Ic} \sim 1$ and $\langle\gamma_{Ma}\rangle \sim 0$). In practice, the overall value of quantities like u_{Ic} are only weakly dependent on the specific functional form of δ, so we only consider the expression (6.31). Additionally, in the case of interest of long gratings $\varepsilon \ll 1$ in small-scale flows we typically have $Pe/g \lesssim 1$ (Section 6.3.6) and thus the boundary layer is approximately independent of Pe or g.

Purely insoluble surfactant

All previous theoretical expressions can also be obtained in the case of a purely insoluble surfactant, i.e. taking $\mathcal{S}(c_I, \Gamma) = 0$ in (6.7g) and neglecting Equations (6.7e) and (6.7j) altogether. In this case, $\hat{\Gamma}_0$ is an independent parameter that can not be linked to $\hat{c}_0$, since the latter is undefined. The value of k is now simply $k = \hat{\Gamma}_0/\hat{\Gamma}_m$, although we assume $k \ll 1$ still holds and leads to $\mathcal{N}(\Gamma) \approx 1$. Furthermore, since $\varepsilon Pe_I \lesssim 1$ remains valid we can still assume a regime away from the stagnant cap and thus an approximately linear profile for Γ. The same steps taken for the scaling of Eqs. (6.3d) and (6.23) can be followed to arrive at

$$\langle\gamma_{Ma}\rangle = \frac{a\, Ma_{\text{ins}}\, u_{Ic}^{\text{clean}}}{1 + a\, Ma_{\text{ins}}\, u_{Ic}^{\text{clean}}},$$
$$u_{Ic} = \frac{u_{Ic}^{\text{clean}}}{1 + a\, Ma_{\text{ins}}\, u_{Ic}^{\text{clean}}},$$

with $Ma_{\text{ins}} = k\,Ma\,Pe_I = n_s\hat{R}\hat{T}\hat{\Gamma}_0\hat{h}/(\hat{\mu}\hat{D}_I)$, and a another empirical parameter.

6.3.4 Finite-element simulations

We solve numerically the full governing equations (6.5a)-(6.5t) of the problem in dimensional form, performing a total of 155 simulations. The objectives of such a computational study are to (i) determine the values of the empirical parameters a_1, a_2, a_3 and a_4 present in our model [Section 6.3.3], (ii) confirm the modeling assumptions of an (approximately) spanwise constant [Section 6.3.2] and streamwise linear profile [Section 6.3.3] for the interfacial concentration Γ, and (iii) test the performance of the theory against simulations of realistic microchannels in conditions representative of our experiments [Section 6.3.5].

We implemented the three-dimensional simulations using the finite-element software COMSOL Multiphysics 5.5®. The simulation domain is one half of the SHS unit cell depicted in Fig. 6.1a, with $\hat{z}$ spanning only between $\hat{z} = 0$ and $\hat{z} = \hat{P}/2$ due to the spanwise symmetry of the solution. The volume is meshed with tetrahedral elements, concentrating the finest regions around the upstream and downstream edges of the interface $\hat{x} = \pm\phi_x\hat{L}/2$ since it is in those areas where the most abrupt variations of the solution occur. Across all the simulations, the minimum element size (understood as the diameter of a sphere circumscribing the smallest element) is set to $1.5 \cdot 10^{-9}$ m.

The solution of the governing equations is achieved with a combination of the Creeping Flow module for the flow equations [Eqs. (6.5a)-(6.5d)] and the Dilute Species Transport module for the transport of bulk surfactant [Eq. (6.5e)]. The conservation law for the interfacial surfactant [Eq. (6.5f)] is implemented through a General Form Boundary PDE, using (6.5j) as source term. The Marangoni boundary conditions (6.5h) and (6.7i) are enforced through a Weak Contribution constraint, as is the condition that fixes the mean bulk concentration (6.5l).

The system of nonlinear equations is solved through a Newton-type iterative method using the PARDISO direct solver for the linear system at each iteration. We set a relative tolerance of 10^{-5} as a convergence criterion for the solution, which is satisfied by all of our simulations. The

pressure, bulk concentration and interfacial concentration are discretized using linear elements, and the velocity field uses either quadratic or linear elements, depending on the computational demands of each specific simulation.

Although we do not pursue an exhaustive investigation of the parameter space as in [24], we vary the problem parameters to ensure that each of the distinct terms that are pre-multiplied by an empirical factor in (6.30) varies its value over a few orders of magnitude. The ranges of variation of each dimensional quantity in the simulations, as well as of the corresponding nondimensional numbers, is indicated in Tables 6.1 and 6.2. A small number of simulations were chosen with the same parameters as those estimated in the experiments, in order to achieve a direct comparison (see Fig. 6.3 in the main text). However, due to constraints in computational power, the value of the grating length $\hat{g}$ could not be matched with that of the microfluidic devices.

The parameters a_1, a_2, a_3 and a_4 are obtained through least-squares fitting using the MATLAB function `lsqnonlin`. We use the relative error between the centerline slip velocities computed in the simulations and those predicted by the theory (6.4) to define the error, i.e. $\mathrm{ERR} = \sum(u_{Ic}^{\mathrm{theory}} - u_{Ic}^{\mathrm{sim}})^2$. Using this approach, we find $a_1 = 0.345$, $a_2 = 0.275$, $a_3 = 5.581$, and $a_4 = 3.922$. As illustrated in Fig. 6.4, the agreement between simulations and theory, using this set of empirical coefficients, is excellent over more than four orders of magnitude.

6.3.5 Experimental methods

The experimental setup is centered around the custom-built PDMS (Sylgard 184) microfluidic device depicted in Figures 6.2a and 6.2b, which is fabricated from a master mold obtained by photolithography. The chip is bonded to a 0.1 mm-thick glass coverslip (Bellco Glass 1916-25075) through untreated adhesion, and a 40X water objective is used to image the interior of the channels through the coverslip using a confocal microscope (Leica SP8 Resonant Scanning). The device is placed inside a stage top chamber (Okolab H101-K-FRAME) that ensures a precise temperature control, which we set to $\hat{T} = 296\,\mathrm{K}$ throughout all experiments. The

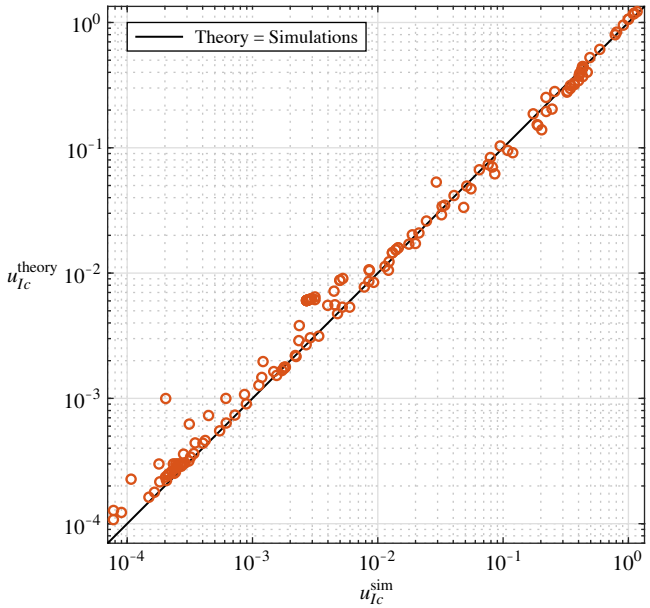

Figure 6.4: Agreement between the 155 numerical simulations and the corresponding predictions from our model, with the scaling coefficients $a_1 = 0.345$, $a_2 = 0.275$, $a_3 = 5.581$, and $a_4 = 3.922$ obtained from least-squares fitting.

fluid is initially contained in a glass syringe (Hamilton Gastight), and driven by a syringe pump (KD Legato 111) at a constant flow rate through plastic tubing (Tygon S3) into and out of the microfluidic channel. We use the barrel of a plastic syringe (BD Luer-Lok) as an outlet reservoir open to the room, in order to establish an ambient pressure level at the end of the fluid circuit. Furthermore, the overall magnitude of the pressure inside the channel is adjusted varying the height of the outlet reservoir with an vertical translation stage (Thorlabs VAP10), in order to ensure that the air-water interface in the observed channels remains flat and thus plastron curvature effects can be safely neglected. The tolerance in the maximum deflection of the interface (at the centerline $z = 0$) with respect to its edges ($z = \pm\phi_z P$) is estimated to be of $\pm 1\,\mu\text{m}$.

Due to the extreme difficulty of removing all traces of surface-active contaminants even in controlled experimental conditions [179], we do not attempt an exhaustive cleaning protocol with that aim. Nevertheless, we follow standard cleaning procedures on all syringes and tubing, ensuring that they are rinsed with DI water with at least twice their volume before they are

used. In addition, we follow a specific cleaning protocol for the µ-PIV particles (ThermoFisher FluoSpheres carboxylate 0.5-µm diameter), since they typically contains surfactants to prevent particle agglomeration [226]. We use a centrifuge (Eppendorf 5418) to separate the beads from the buffer solution, which is discarded and replenished with clean 18 MΩ DI water, and we repeat the process three times. These cleaning procedures ensure that the traces of surfactants responsible for the non-negligible Marangoni stresses that we observe in the experiments are the result of contamination that would naturally occur in typical small-scale flows through microfluidic devices, and not as a byproduct of the specific experimental methods used in this study.

The µ-PIV analysis is performed using the open-source MATLAB toolbox `PIVlab`. The acquisition window has an approximate size of 125 µm × 125 µm, which is sufficient to cover the span of two pitches (see Fig. 6.2e) at the center of the grating in the streamwise direction (i.e. $x = 0$). We image the motion of the µ-PIV particles during time intervals of between 20 s and 60 s at different distances from the interface, with frame rates between 20 fps and 28 fps. Next, we compute the time average of the obtained velocity field, as well as the average in the streamwise x direction, to obtain the final velocity profiles depicted in Figure 6.2d. In order to calculate the value of $\hat{u}_{Ic}$, we perform a linear least-squares fit, typically using between 3 and 5 velocity profiles to obtain an extrapolated slip velocity, from which we extract its value at $z = 0$. This linear fit is performed in MATLAB with a custom script that takes into account uncertainties in both the distance $\Delta\hat{y}$ from the interface and the uncertainty in $\hat{u}$ inherent to the measurement and the averaging in the x direction.

6.3.6 Estimate of plausible surfactant parameters

The main challenge in comparing experimental measurements of $\hat{u}_{Ic}$ to the predictions from our model is the absence of information regarding the type and amount of surfactant present in the channels. Some parameters in the problem are known from the experimental conditions, and hence we fix those as $n_s = 2$ [200], $\hat{R} = 8.314\,\mathrm{J\,mol^{-1}\,K^{-1}}$, $\hat{T} = 296\,\mathrm{K}$ and

$\hat{\mu} = 8.9 \cdot 10^{-4}\,\mathrm{kg\,m^{-1}\,s^{-1}}$. Others can be accurately estimated, since most surfactants have diffusivities (both $\hat{D}$ and $\hat{D}_I$) bounded between 10^{-10} and 10^{-9} $\mathrm{m^2\,s^{-1}}$ and values $\hat{\Gamma}_m$ between 10^{-6} and 10^{-5} $\mathrm{mol\,m^{-2}}$ [201]. We thus use as a reference surfactant the well-studied sodium dodecyl sulfate (SDS), setting $\hat{D} = \hat{D}_I = 7 \cdot 10^{-10}\,\mathrm{m^2\,s^{-1}}$ and $\hat{\Gamma}_m = 3.9 \cdot 10^{-6}\,\mathrm{mol\,m^{-2}}$ as good approximations of these two parameters. However, the typical values of the background bulk concentration $\hat{c}_0$ and the rate constants $\hat{\kappa}_a$ and $\hat{\kappa}_d$ have a much wider range [201], making them difficult to estimate.

Despite the uncertainty, it is possible to obtain a coarse approximation of these quantities by combining the expression (6.4) with previous results [179] obtained in similar conditions. First, note that for arbitrarily long gratings (i.e. $g \to \infty$), Eq. (6.4) indicates that the slip velocity converges to the clean-case value $u_{Ic} \to u_{Ic}^{\mathrm{clean}}$. On the other hand, for intermediate lengths in which (6.4) is still converging to this plateau, the dominant balance of terms results in a simplified approximation $u_{Ic} \approx a_2 Bi\, g^2/[a_1 kMa(1+\delta Da)]$. Moreover, the bounds in the value of $\hat{D}_I$ result in a thick boundary layer $\delta \approx a_3$, since $Pe/g = O(10^{-2}) \ll 1$ when $\hat{h}$, $\hat{U}$ and $\hat{g}$ take values typical of microfluidic applications. Similarly, the value of $\hat{\kappa}_a\hat{\Gamma}_m$ is generally large enough to guarantee $\hat{\kappa}_a\hat{\Gamma}_m > 10^{-5}\,\mathrm{m\,s^{-1}}$ [201], which suggests that in these small-scale flows we have $Da \gg 1$. This means that $(1 + Da\,\delta) \approx a_3 Da$, yielding a final estimate of

$$k\hat{K}_{eq} \approx \frac{a_2 g^2}{a_1 a_3 Ma}\left(\frac{\hat{D}}{\hat{u}_{Ic}\hat{\Gamma}_m}\right), \tag{6.33}$$

where $\hat{K}_{eq}$ is the ratio of rate constants $\hat{K}_{eq} = \hat{\kappa}_a/\hat{\kappa}_d$, which can be regarded as an equilibrium constant. The right-hand side of (6.33) is fully determined from the parameters that are already known or estimated, as well as from the values $\hat{h} = 50\,\mu\mathrm{m}$, $\hat{g} = 30\,\mathrm{mm}$, $\hat{U} \approx 3\langle\hat{u}\rangle_{yz} = 261\,\mu\mathrm{m\,s^{-1}}$ and $\hat{u}_{Ic} = 12.18 \pm 3.48\,\mu\mathrm{m\,s^{-1}}$ from [179]. We then obtain bounds for k individually, leveraging the fact that for non-negligible shear stress at the interface (as in the case of [179]), we must have that $kMa \lesssim 1$ (see Section 6.3.2). Since we are also assuming $k \ll 1$ and, furthermore, value of k close to 1 would result in a short-time collapse of the plastron in experiments (not observed in [179]), we have that $g/Ma \lesssim k \lesssim 10^{-1}$. Combining these two estimates we can

arrive at an estimated range of possible surfactants with different values of k and $\hat{K}_{eq}$ (see Figure 6.3). Given that in our experiments $Da \gg 1$, the surfactant concentrations remain close to equilibrium [Eq. (6.3c)], and hence the specific values of $\hat{\kappa}_a$ and $\hat{\kappa}_d$ are expected to be weakly relevant individually as long as $\hat{K}_{eq}$ remains constant. Consequently, we choose the value of $\hat{\kappa}_a = 89.5\,\mathrm{m^3\,mol^{-1}\,s^{-1}}$ from SDS and deduce $\hat{\kappa}_d$ in a way compatible with the estimate of the equilibrium constant, setting $\hat{\kappa}_d = \hat{\kappa}_a/\hat{K}_{eq} = 0.75\,\mathrm{s^{-1}}$, which also yields the closest values to the measured experimental results. These values indicate that the surfactant responsible for the loss of slip is likely weakly soluble compared to SDS (for which $\hat{\kappa}_d \approx 500\,\mathrm{s^{-1}}$).

6.4 Acknowledgements

We thank David Bothman, Benjamin Lopez and Rachel Schoeppner for their vital technical assistance. This work has been financially supported by ARO MURI W911NF-17-1-0306, ONR MURI N00014-17-1-2676 and the California NanoSystems Institute through a Challenge Grant. We acknowledge the use of the NRI-MCDB Microscopy Facility and the Resonant Scanning Confocal supported by the NSF MRI grant DBI-1625770. A portion of this work was performed in the Microfluidics Laboratory within the California NanoSystems Institute, supported by the University of California Santa Barbara, and the University of California, Office of the President.

Chapter 7

Analysis of the role of UV light in the sunlight inactivation of the SARS-CoV-2 virus

Recently, Ratnesar-Shumate et al [238] reported rapid sunlight inactivation of SARS-CoV-2 in simulated saliva and in complete growth medium (gMEM). Independently and essentially simultaneously, Sagripanti & Lytle [239] introduced a theory for sunlight inactivation of SARS-CoV-2, building on their earlier work for similar viruses [240]. To the best of our knowledge, these data and theory have yet to be compared; when establishing this comparison, the experimentally reported sunlight inactivation in [238] is several times faster than predicted by theory, suggesting that additional experiments and hypotheses may be needed to fully elucidate the mechanism of SARS-CoV-2 sunlight inactivation.

Briefly, the theory of Sagripanti & Lytle [239, 240] considers direct photochemical damage to viral RNA, which is maximal for UVC (wavelengths between 200-280 nm). The effectiveness of UVC is expressed as the exposure that produces one e-fold reduction in infectious virion concentration (i.e. to 37% of the initial value) at a wavelength of 254 nm, which is written as D_{37} [240]. Since larger D_{37} implies slower inactivation, D_{37} is effectively an inverse sensitivity. Based

on genome size, for Coronaviridae, Lytle & Sagripanti estimated D_{37} between 2.5-3.9 J/m2, and $D_{37} = 3.0\,\mathrm{J\,m^{-2}}$ for SARS-CoV-2 [239]; this value is used in the calculations presented here. Although no UVC reaches the Earth's surface, longer UV wavelengths can still affect viral RNA, albeit with decreased sensitivity. To account for this, Lytle & Sagripanti [240] introduced an action spectrum, expressed as the ratio between sensitivity at a given wavelength λ and the UVC sensitivity at 254 nm. Writing this relative sensitivity as $r(\lambda)$, and expressing the spectral irradiance at a given wavelength as $E_{e,\lambda}(\lambda)$, one can evaluate an equivalent UVC irradiance (in $\mathrm{W\,m^{-2}}$) as

$$E_{\mathrm{equiv}} = \int r(\lambda) E_{e,\lambda}(\lambda)\,\mathrm{d}\lambda. \tag{7.1}$$

Because $r(\lambda)$ drops to around 10^{-4} by a wavelength of 320 nm, this integral is performed only over the UVB spectrum (280 to 315 nm). In the calculations reported here, the $r(\lambda)$ is the one compiled by Lytle & Sagripanti [240], the irradiance spectra of Ratnesar-Shumate et al. [238] are used for $E_{e,\lambda}$, and the integral is performed numerically. The infectious virion concentration V would decay with time t as

$$V(t) = V(0)\exp\left[-(k_0 + E_{\mathrm{equiv}}/D_{37})\,t\right], \tag{7.2}$$

where k_0 is the inactivation rate in the dark, which is negligible in the experiments of Ratnesar-Shumate et al. [238].

As shown in Figure 7, the experimentally observed inactivation rates from [238] are significantly faster than the theoretical ones from Equation (7.2). Furthermore, achieving a good fit to the data would require a UVB sensitivity that is beyond the largest values reported for any virus, to the best of our knowledge [240]. As a matter of fact, the experimentally-observed inactivation in simulated saliva is over 8 times faster than would have been expected from the theory. Even in gMEM, inactivation is over 3 times faster than expected from theory. Although one might attempt to explain this significant difference in inactivation rates by considering the difference in light attenuation within each medium, this effect alone would still lead

to slower inactivation relative to theory, contrary to what has been reported by the experiments of Ratnesar-Shumate et al. [238], and therefore is not sufficient to explain the disagreement between theory and experiments.

This discrepancy suggests that additional hypotheses should be tested for the sunlight inactivation mechanism. Other mechanisms of sunlight inactivation are known to exist for other viruses, beside direct nucleic acid damage, as reviewed by Nelson et al. [241]. For example, sunlight in the UVA wavelength range may interact with sensitizer molecules in the medium, yielding photo-produced reactive intermediates that can damage the virus [242]. If sensitivity to wavelengths other than UVB were to be found, sunlight could mitigate outdoor transmission over a broader range of latitudes and daytimes than previously expected. Furthermore, inexpensive and energy-efficient wavelength-specific light sources might be used to augment air filtration systems at relatively low risk for human health, especially in high-risk settings such as hospitals and public transportation.

Overall, these results point to the need for additional experiments to separately test the effects of specific illumination wavelengths and of medium composition.

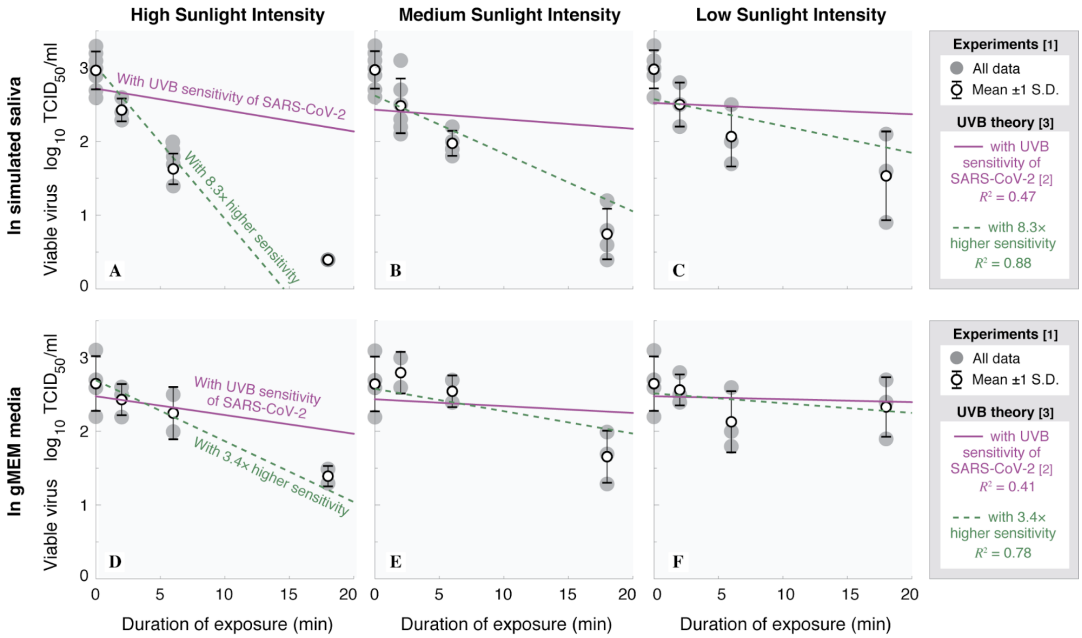

Figure 7.1: SARS-CoV-2 TCID50 versus length of exposure to different simulated sunlight intensities and in different suspension media: (A–C) in simulated saliva; (D–F) in gMEM; (A and D) high simulated sunlight intensity; (B and E) medium simulated sunlight intensity; and (C and F) low simulated sunlight intensity. Data of Ratnesar-Shumate et al. [238] are plotted with grey dots and means at each time point with open circles; error bars are standard deviations. Solid lines indicate the UVB-inactivation theory of Lytle and Sagripanti [240] with SARS-CoV-2 inverse sensitivity $D_{37} = 3.0\,\mathrm{J\,m^{-2}}$, from Sagripanti and Lytle [239]. Dotted lines indicate the UVB-inactivation theory of Lytle and Sagripanti [240] with D37 from a fit to all data for a given medium. Abbreviations: gMEM, complete growth medium; SARS-CoV-2, severe acute respiratory syndrome coronavirus 2; TCID50, 50% tissue culture infectious dose.

Chapter 8

UVA radiation as a potential significant contributor to the sunlight inactivation of SAS-CoV-2

8.1 Abstract

Past experiments demonstrated SARS-CoV-2 inactivation by simulated sunlight; models have considered exclusively mechanisms involving UVB acting directly on RNA. However, UVA inactivation has been demonstrated for other enveloped RNA viruses, through indirect mechanisms involving the suspension medium. We propose a model combining UVB and UVA inactivation for SARS-CoV-2, which improves predictions by accounting for effects associated with the medium. UVA sensitivities deduced for SARS-CoV-2 are consistent with data for SARS-CoV-1 under UVA only. This analysis calls for experiments to separately assess effects of UVA and UVB in different media, and for including UVA in inactivation models.

8.2 Background

Predicting the loss of infectivity of SARS-CoV-2 in various environmental conditions is important to mitigate the current COVID-19 pandemic. Laboratory studies found that although the virus persists at least for several hours in darkness and at room temperature [243], simulated sunlight induces rapid inactivation [238, 244]. This is consistent with epidemiological studies on effects of UV [245], which is the wavelength band assumed to be responsible for inactivation [241].

Ratnesar-Shumate et al. [238] examined SARS-CoV-2 in simulated saliva and in complete growth medium (gMEM). The suspensions were applied to stainless steel surfaces and exposed to simulated sunlight. Inactivation increased with light intensity, and was faster in simulated saliva than in gMEM. Schuit et al. [244] aerosolized SARS-CoV-2 in the same two suspension media as in [238], varying humidity and sunlight intensity. They found weak dependence on humidity, but strong sensitivity to sunlight and medium. In both studies [238, 244], the combination of sunlight and simulated saliva caused faster inactivation than was observed for sunlight and growth medium, although no significant difference between the two media was observed in darkness.

A model of SARS-CoV-2 sunlight inactivation would be highly valuable. Lytle & Sagripanti [240] modeled sunlight inactivation for viruses of interest to biodefense; noting that UVC radiation does not reach the Earth's surface, they assumed an inactivation mechanism relying on UVB-induced damage to viral RNA (or DNA). Their model predicts inactivation rates from a given UVB irradiance spectrum and genome size. Sagripanti & Lytle [239] later calculated inactivation rates for SARS-CoV-2, for several worldwide locations at different times of the year. As will be shown later in Figure 8.2, the experimentally observed inactivation rates in [238, 244] are significantly faster than predicted by the model in [240, 239]. In addition, the observed dependence on the medium composition is not consistent with this medium-independent model.

Besides direct nucleic acid damage, other mechanisms of sunlight inactivation are possible,

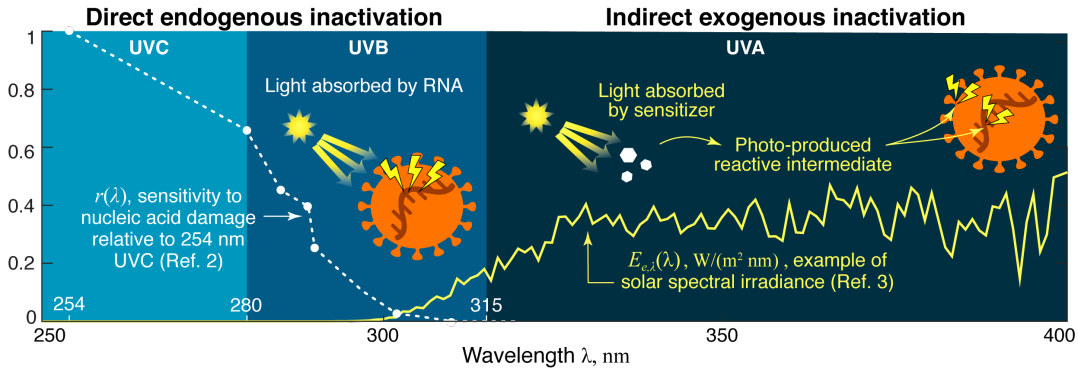

Figure 8.1: UV spectrum and possible mechanisms of inactivation.

as reviewed by Nelson et al. [241] and illustrated in Figure 8.1. UV inactivation is first characterized as either endogenous or exogenous, that is, affecting the interior or the exterior of the virus. Second, inactivation can be either direct or indirect, that is, able to immediately damage the virus, or relying on an intermediate step. Indirect inactivation involves sensitizer molecules, generally provided by the medium, whose interaction with UV yields photo-produced reactive intermediates that can damage the virus [242].

It is generally expected that UVB acts on viruses through a direct, endogenous pathway [241], as has been modeled by [240, 239]. Inactivation by UVA has been established for viruses in presence of sensitizers, through an exogenous, indirect pathway, for example by damaging the virus's envelope and thereby disrupting attachment and entry [241, 242]. Mechanisms that use other pathways (endogenous and indirect, or exogenous and direct) are deemed rare in viruses, since they contain few internal or surface sensitizers that absorb sunlight [241].

To the best of our knowledge, SARS-CoV-2 has not yet been studied under UVA-only; however, Darnell et al. [246] examined SARS-CoV-1 under exposure to either UVC or UVA over 15 minutes in Dulbecco's modified Eagle's medium (DMEM) with supplements. They found a clear effect of UVC, whereas inactivation due to UVA was of the order of measurement uncertainty. Darnell & Taylor [247] later found that UVA irradiation of SARS-CoV-1 in DMEM provided appreciable inactivation after 30 minutes; moreover, adding a photosensitizer

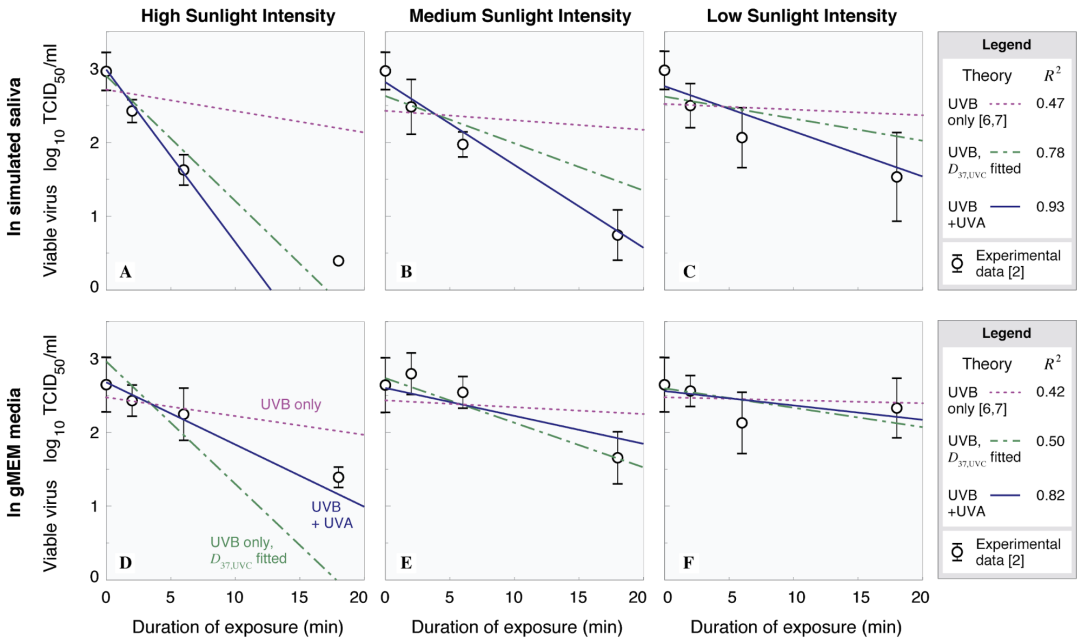

Figure 8.2: Comparison of theories with data for SARS-CoV-2 on stainless steel surfaces. (A, B, C): simulated saliva, (D, E, F): gMEM (complete growth medium). (A, D): high simulated sunlight, (B, E): medium simulated sunlight, (C, F): low simulated sunlight. Purple dotted line: UVB-only theory (Equation 3) with $D|37, \mathrm{UVC} = 3.0\,\mathrm{J\,m^{-2}}$ [240, 239]. Green dot-dashed line: UVB-only theory with $D_{37,\mathrm{UVC}}$ from a fit to all data. Solid line: present model, combining UVB model (with $D_{37,\mathrm{UVC}} = 3.0\,\mathrm{J\,m^{-2}}$) and UVA model, with $D_{37,\mathrm{UVA}}$ from fits using all data for each medium. Symbols: data of Ratnesar-Shumate et al. [238]; for clarity, averages at each time are plotted, with error bars showing standard deviation.

inactivated the virus below the limit of detection within 15 minutes.

These existing results point towards a vulnerability of SARS-CoV-2 to UVA in the presence of sensitizers. Since the relative intensities of UVA and UVB vary greatly in sunlight, establishing UVA sensitivity of SARS-CoV-2 is necessary to obtain practically valuable predictions. In addition, since UVA from sunlight is abundant over a broader range of dates and times than UVB, vulnerability to UVA would imply a much greater sunlight inactivation potential than currently expected. This vulnerability could enable disinfection using inexpensive and efficient UVA light sources. This study tested the hypothesis that a model inclusive of UVA could improve agreement with SARS-CoV-2 experiments, with UVA sensitivities consistent with those for other similar viruses.

8.3 Methods

Even without irradiation, the decay in infectious virion concentration over time is traditionally expressed as an exponential with a medium-dependent rate [248]. Here this rate is written as k_0 medium, where "medium" can be either simulated saliva or growth medium [238, 244]. Therefore the infectious virion concentration V changes with time t following the expression

$$V(t) = V(0) \exp\left(-k_0^{\text{medium}} t\right), \tag{8.1}$$

where $V(0)$ is the initial concentration. The value of k_0 medium is obtained from fit to data, and is negligible compared to sunlight effects [238, 244].

To model sunlight inactivation in a general manner, one needs a hypothesis for the inactivation mechanism. As mentioned earlier, Lytle & Sagripanti [240] considered direct photochemical damage to viral RNA, which is maximal for UVC (wavelengths between 200-280 nm). UVC sensitivity was expressed as the exposure, at 254 nm, that produces one e-fold reduction in infectious virion concentration (i.e. to 37% of the initial value), and is written as $D_{37,\text{UVC}}$ [240]. Based on genome size, for Coronaviridae, they estimated $D_{37,\text{UVC}}$ between 2.5-3.9 J/m2, and $D_{37,\text{UVC}}$ = 3.0 J/m2 for SARS-CoV-2 [239]; this value is used in the calculations presented here. Although no UVC reaches the Earth's surface, longer wavelengths can still affect viral RNA, albeit with decreased sensitivity. To account for this, Lytle & Sagripanti [240] introduced a relative sensitivity, expressed as the ratio between sensitivity at a given wavelength λ and the UVC sensitivity at 254 nm [240] (see Figure 8.1). Writing this relative sensitivity as $r(\lambda)$, and expressing the spectral irradiance at a given wavelength as $E_{e,\lambda}(\lambda)$, one can evaluate an "equivalent UVC" irradiance (in W/m2) as

$$E_{\text{UVC, equiv}} = \int r(\lambda) E_{e,\lambda}(\lambda)\, \mathrm{d}\lambda. \tag{8.2}$$

Since $r(\lambda)$ drops to around 10^{-4} by a wavelength of 320 nm, this integral is performed only over the UVB spectrum (280 to 315 nm). In the calculations reported here, the irradiance

spectra of [238, 244] are used for $E_{e,\lambda}(\lambda)$, and the integral is performed numerically. For a dried thin layer on a surface, or for an aerosol particle, one might assume that the medium provides negligible light attenuation; inactivation by direct photochemical damage to RNA would therefore be independent of medium, and the infectious virion concentration would decay as

$$V(t) = V(0) \exp\left[-(k_0^{\text{medium}} + E_{\text{UVC, equiv}}/D_{37,\text{UVC}})\, t\right]. \tag{8.3}$$

Here, an extension of this model is proposed, to account for indirect inactivation of SARS-CoV-2 due to UVA (315 to 400 nm). The integrated energy across the UVA range is considered. Although a specific wavelength may have relatively stronger impact, this a reasonable approach for sunlight, since the solar spectrum is relatively flat in this range (compared to UVB), such that the integrated energy is a proxy for the energy at any one wavelength, as discussed further below.

The UVA energy that produces an e-fold reduction in V is labeled $D_{37,\text{UVA}}$ medium, dependent on the medium, and the irradiance integrated across the UVA range is E_{UVA}. Therefore the hypothesis being tested here is that, under sunlight, the infectious virion concentration is approximated by

$$V(t) = V(0) \exp\left[-(k_0^{\text{medium}} + E_{\text{UVC, equiv}}/D_{37,\text{UVC}} + E_{\text{UVA}}/D_{37,\text{UVA}}^{\text{medium}})\, t\right]. \tag{8.4}$$

Note that this modeling approach is also consistent with established theories of photochemical kinetics [249], which are widely used (including e.g. for photochromic molecules [250]).

Since $D_{37,\text{UVA}}^{\text{medium}}$ is medium-dependent, it is found by fitting experimental data. For experiments that report infectious virion concentrations, nonlinear model fitting in MATLAB is used, on a logarithmic scale. For experiments that only report an overall inactivation rate at each irradiation condition, $D_{37,\text{UVA}}^{\text{medium}}$ is calculated at each condition and averaged over experiments with the same medium.

8.4 Results

The infectious virion concentration data of Ratnesar-Shumate et al. [238] is shown in Figure 8.2, in units of tissue culture infectious dose/ml ($TCID_{50}$/ml). For clarity, instead of plotting all data points, a circle shows the average at each time, and an error bar shows the standard deviation.

The model based only on UVB inactivation [240, 239], embodied by Equation (3) with $D_{37,\mathrm{UVC}} = 3.0\,\mathrm{J\,m^{-2}}$, is shown by the purple dotted line, and had an R^2 (computed across all light intensities) of 0.47 for simulated saliva and 0.42 for gMEM. To test whether this could be improved by a different value of $D_{37,\mathrm{UVC}}$, a fit was sought across all data (since endogenous inactivation is expected to be medium-independent), and is shown by the green dot-dashed line in Figure 8.2. The fit yields $D_{37,\mathrm{UVC}} = 0.53 \pm 0.11\,\mathrm{J\,m^{-2}}$ (where the uncertainty corresponds to the 95% confidence interval), with updated R^2 values of 0.78 and 0.50. This $D_{37,\mathrm{UVC}}$ is at least five times smaller than expected for any coronavirus (2.5 - 3.9 $\mathrm{J\,m^{-1}}$), or for any virus considered by [240]. This suggests that SARS-CoV-2 is more sensitive to sunlight than expected by UVB-induced, endogenous inactivation alone.

The model inclusive of UVA, described by equation (4), is plotted by the solid blue line in Figure 8.2. The value of $D_{37,\mathrm{UVA}}$ is found by fitting separately for each medium, consistently with the exogenous, indirect inactivation hypothesis. This yields $D_{37,\mathrm{UVA}} = 10.0 \pm 1.8\,\mathrm{kJ\,m^{-2}}$ for simulated saliva and $D_{37,\mathrm{UVA}} = 30 \pm 14\,\mathrm{kJ\,m^{-2}}$ for gMEM. The updated values of R^2 (computed across all light intensities) are 0.93 and 0.82 for simulated saliva and gMEM respectively. Applying this theory also to the aerosol data of Schuit et al. [244] gives $D_{37,\mathrm{UVA}} = 34 \pm 11\,\mathrm{kJ\,m^{-2}}$ in simulated saliva and $D_{37,\mathrm{UVA}} = 88 \pm 50\,\mathrm{kJ\,m^{-2}}$ for gMEM; these appreciable uncertainties seem to reflect the relatively small number of replicates available (for comparison, the influenza experiments of [248] yielded a smaller uncertainty, as shown below).

To assess whether these $D_{37,\mathrm{UVA}}$ values are plausible, data for UVA-only inactivation of SARS-CoV-1 was also examined. For DMEM with supplements, [246] implies $D_{37,\mathrm{UVA}} = 14 \pm 10\,\mathrm{kJ\,m^{-2}}$ (data was collected only over 15 minutes, making it difficult to reduce un-

Data source	Virus	Medium	Light source	$D_{37,\mathrm{UVA}}$, $\mathrm{kJ\,m^{-2}}$
[238]	SARS-CoV-2	Simulated saliva dried on stainless steel surface	Simulated sunlight (UVA + UVB)	10 ± 1.8
[238]	SARS-CoV-2	gMEM dried on stainless steel surface	Simulated sunlight (UVA + UVB)	30 ± 14
[244]	SARS-CoV-2	Simulated saliva dried in aerosol	Simulated sunlight (UVA + UVB)	34 ± 11
[244]	SARS-CoV-2	gMEM in aerosol	Simulated sunlight (UVA + UVB)	88 ± 50
[246]	SARS-CoV-1	DMEM with supplements, 1 cm deep	UVA	14 ± 10
[247]	SARS-CoV-1	DMEM without supplements, 1 cm deep	UVA	9.2 ± 4.2
[248]	Influenza	gMEM in aerosol	Simulated sunlight (UVA + UVB)	12 ± 2.0

Table 8.1: Sensitivity to UVA for a given medium and virus. The parameter $D_{37,\mathrm{UVA}}$, computed by fitting the proposed model (Equation 4) with the data in Figure 8.2, indicates the amount of energy required to achieve one e-fold reduction in virion concentration. Smaller $D_{37,\mathrm{UVA}}$ indicates that less energy is required for inactivation, and therefore that the virus has greater sensitivity. DMEM: Dulbecco's modified Eagle's medium; gMEM: complete growth medium.

certainty). For DMEM without supplements, [247] implies $D_{37,\mathrm{UVA}} = 9.2 \pm 4.2\,\mathrm{kJ\,m^{-2}}$. To provide additional context, $D_{37,\mathrm{UVA}}$ was calculated also for influenza, which like SARS-CoV-2 is an enveloped, RNA virus. Data of [248] was used for influenza, which examined a gMEM-based aerosol under simulated sunlight. Using $D_{37,\mathrm{UVC}} = 7.3\,\mathrm{kJ\,m^{-2}}$ from [240], one deduces $D_{37,\mathrm{UVA}} = 12.0 \pm 2.0\,\mathrm{kJ\,m^{-2}}$. These results are summarized in Table 8.1.

8.5 Discussion

These calculations showed that a model based only on a UVB-driven, endogenous direct mechanism is not sufficient to explain SARS-CoV-2's rapid decay and medium sensitivity under simulated sunlight. To account for these discrepancies, a model inclusive also of exogenous, indirect inactivation due to UVA was proposed and tested (Equation 4). This model improved agreement with data across all conditions. Moreover, the UVA sensitivities deduced for SARS-CoV-2 were comparable to those found for SARS-CoV-1 exposed only to UVA, as well as for

influenza.

Greater UVA sensitivity was found on stainless steel surfaces than in aerosols. This could have several possible explanations; for example, surface reflectivity could effectively increase irradiation by up to 40% [251]. However, since the uncertainty from aerosol experiments is larger than for surfaces, more data is needed to confirm significant differences.

These results point to the need for experiments to separately test effects of UVA, UVB, and of medium composition. Key sensitizers may vary between simulated and real saliva, as well as across saliva from different individuals, leading to different inactivation rates. Sensitizers may respond to narrower wavelength ranges than the full UVA band considered in our model. If UVA sensitivity is confirmed, sunlight could mitigate outdoor transmission over a broader range of latitudes and daytimes than previously expected, since UVA is less strongly absorbed by atmospheric ozone than UVB. For example, at midlatitudes, UVA changes approximately by a factor of two between summer and winter, whereas UVB varies by a factor of four [241]. Furthermore, inexpensive and energy-efficient UVA sources might be used to augment air filtration systems at relatively low risk for human health, especially in high-risk settings such as hospitals and public transportation.

8.6 Acknowledgements

This work was supported by the University of California, Santa Barbara [Vice Chancellor for Research COVID-19 Seed Grant] and by the Army Research Office Multi University Research Initiative [W911NF-17-1-0306 to P.L.-F.].

Bibliography

[1] V. G. Levich and V. S. Krylov, *Surface-tension-driven phenomena*, Annual Review of Fluid Mechanics **1** (1969), no. 1 293–316.

[2] H. Manikantan and T. M. Squires, *Surfactant dynamics: hidden variables controlling fluid flows*, Journal of Fluid Mechanics **892** (2020) P1.

[3] A. N. Frumkin and V. G. Levich, *On surfactants and interfacial motion*, Zh. Fiz. Khim. **21** (1947) 1183–1204.

[4] H. A. Stone and L. G. Leal, *The effect of surfactants on drop deformation and breakup*, J. Fluid Mech. (1989).

[5] L. G. Leal, *Flow induced coalescence of drops in a viscous fluid*, Physics of Fluids **16** (2004), no. 6 1833–1851.

[6] J. Lucassen and R. S. Hansen, *Damping of waves on monolayer-covered surfaces: Ii. influence of bulk-to-surface diffusional interchange on ripple characteristics*, Journal of Colloid and Interface Science **23** (1967), no. 3 319–328.

[7] H. C. Mayer and R. Krechetnikov, *Landau-Levich flow visualization: Revealing the flow topology responsible for the film thickening phenomena*, Phys. Fluids (2012).

[8] A. Borhan and C. F. Mao, *Effects of surfactants on the motion of drops through circular tubes*, Phys. Fluids (1992).

[9] M. Bertalmío, L.-T. Cheng, S. Osher, and G. Sapiro, *Variational problems and partial differential equations on implicit surfaces*, Journal of Computational Physics **174** (2001), no. 2 759–780.

[10] J. B. Greer, *An improvement of a recent eulerian method for solving pdes on general geometries*, Journal of Scientific Computing **29** (2006), no. 3 321–352.

[11] J. Xu, Z. Li, J. Lowengrub, and H. Zhao, *A level-set method for interfacial flows with surfactant*, Journal of Computational Physics **212** (Mar., 2006) 590–616.

[12] M. Muradoglu and G. Tryggvason, *A front-tracking method for computation of interfacial flows with soluble surfactants*, Journal of Computational Physics **227** (Feb., 2008) 2238–2262.

[13] K. E. Teigen, P. Song, J. Lowengrub, and A. Voigt, *A diffuse-interface method for two-phase flows with soluble surfactants*, Journal of Computational Physics **230** (Jan., 2011) 375–393.

[14] J. Ou, B. Perot, and J. P. Rothstein, *Laminar drag reduction in microchannels using ultrahydrophobic surfaces*, Phys. Fluids **16** (Dec., 2004) 4635–4643.

[15] J. Ou and J. P. Rothstein, *Direct velocity measurements of the flow past drag-reducing ultrahydrophobic surfaces*, Phys. Fluids **17** (Oct., 2005) 103606.

[16] T. J. Kim and C. Hidrovo, *Pressure and partial wetting effects on superhydrophobic friction reduction in microchannel flow*, Phys. Fluids **24** (2012), no. 11.

[17] G. Bolognesi, C. Cottin-Bizonne, and C. Pirat, *Evidence of slippage breakdown for a superhydrophobic microchannel*, Phys. Fluids **26** (2014), no. 8 082004.

[18] D. Schäffel, K. Koynov, D. Vollmer, H. J. Butt, and C. Schönecker, *Local flow field and slip length of superhydrophobic surfaces*, Phys. Rev. Lett. **116** (2016) 134501.

[19] F. J. Peaudecerf, J. R. Landel, R. E. Goldstein, and P. Luzzatto-Fegiz, *Traces of surfactants can severely limit the drag reduction of superhydrophobic surfaces*, Proc. Nat. Acad. Sci. **114** (2017), no. 28 7254–7259.

[20] D. Song, B. Song, H. Hu, X. Du, P. Du, C.-H. Choi, and J. P. Rothstein, *Effect of a surface tension gradient on the slip flow along a superhydrophobic air-water interface*, Phys. Rev. Fluids **3** (Mar., 2018) 033303.

[21] C. C. de Langavant, A. Guittet, M. Theillard, F. Temprano-Coleto, and F. Gibou, *Level-set simulations of soluble surfactant driven flows*, Journal of Computational Physics **348** (2017) 271 – 297.

[22] R. Egan, A. Guittet, F. Temprano-Coleto, T. Isaac, F. J. Peaudecerf, J. R. Landel, P. Luzzatto-Fegiz, C. Burstedde, and F. Gibou, *Direct numerical simulation of incompressible flows on parallel octree grids*, Journal of Computational Physics **428** (2021) 110084.

[23] F. Temprano-Coleto, F. J. Peaudecerf, J. R. Landel, F. Gibou, and P. Luzzatto-Fegiz, *Soap opera in the maze: Geometry matters in marangoni flows*, Phys. Rev. Fluids **3** (2018) 100507.

[24] J. R. Landel, F. J. Peaudecerf, F. Temprano-Coleto, F. Gibou, R. E. Goldstein, and P. Luzzatto-Fegiz, *A theory for the slip and drag of superhydrophobic surfaces with surfactant*, Journal of Fluid Mechanics **883** (2020) A18.

[25] P. Luzzatto-Fegiz, F. Temprano-Coleto, F. J. Peaudecerf, J. R. Landel, Y. Zhu, and J. A. McMurry, *UVB radiation alone may not explain sunlight inactivation of SARS-CoV-2*, The Journal of Infectious Diseases (02, 2021). jiab070.

[26] P. Luzzatto-Fegiz, F. Temprano-Coleto, F. J. Peaudecerf, J. R. Landel, Y. Zhu, and J. A. McMurry, *Uva radiation could be a significant contributor to sunlight inactivation of sars-cov-2*, bioRxiv (2020).

[27] Z. He, Z. Dagan, and C. Maldarelli, *The influence of surfactant adsorption on the motion of a fluid sphere in a tube*, J. Fluid Mech. (1990).

[28] W. J. Milliken, H. A. Stone, and L. G. Leal, *The effect of surfactants on the transient motion of newtonian drops*, Phys. Fluids (1992).

[29] R. J. LeVeque and Z. Li, *The immersed interface method for elliptic equations with discontinuous coefficients and singular sources 31:1019–1044, 1994*, SIAM J. Numer. Anal. **31** (1994) 1019–1044.

[30] C. D. Eggleton and K. J. Stebe, *An adsorption-desorption-controlled surfactant on a deforming droplet*, J. Colloid and Interface Sci. (1998).

[31] M. A. Drumright-Clarke and Y. Renardy, *The effect of insoluble surfactant at dilute concentration on drop breakup under shear with inertia*, Phys. Fluids. **16** (2004) 14–21.

[32] A. James and J. Lowengrub, *A surfactant-conserving volume-of-fluid method for interfacial flows with insoluble surfactant*, Journal of Computational Physics **201** (Dec., 2004) 685–722.

[33] K. E. Teigen, X. Li, J. Lowengrub, F. Wang, and A. Voigt, *A diffuse-interface approach for modelling transport, diffusion and adsorption/desorption of material quantities on a deformable interface*, Commun. Math Sci. (2009).

[34] H. A. Stone, *A simple derivation of the time-dependent convective-diffusion equation for surfactant transport along a deforming interface*, Phys. Fluids (1989).

[35] P. Cermelli, E. Fried, and M. E. Gurtin, *Transport relations for surface integrals arising in the formulation of balance laws for evolving fluid interfaces*, J. Fluid Mech. (2005).

[36] R. Clift, G. J. R., and M. E. Weber, Bubbles, Drops and Particles. Academic Press, 1978.

[37] C.-H. Chang and E. I. Franses, *Adsorption dynamics of surfactants at the air/water interface: a critical review of mathematical models, data, and mechanisms*, Colloids and Surfaces A: Physicochemical and Engineering Aspects **100** (1995) 1 – 45.

[38] S.-Y. Lin, Y.-C. Lee, M.-W. Yang, and H.-S. Liu, *Surface equation of state of non-ionic C_mE_n surfactants*, Langmuir (2008).

[39] J. Strain, *Tree methods for moving interfaces*, J. Comput. Phys. **151** (1999) 616–648.

[40] C. Min and F. Gibou, *A second order accurate level set method on non-graded adaptive Cartesian grids*, Journal of Computational Physics **225** (July, 2007) 300–321.

[41] M. Sussman, P. Smereka, and S. Osher, *A level set approach for computing solutions to incompressible two-phase flow*, J. Comput. Phys. **114** (1994) 146–159.

[42] C. Min and F. Gibou, *Robust second-order accurate discretizations of the multi-dimensional Heaviside and Dirac delta functions*, Journal of Computational Physics **227** (Nov., 2008) 9686–9695.

[43] A. Guittet, M. Theillard, and F. Gibou, *A stable projection method for the incompressible Navier–Stokes equations on arbitrary geometries and adaptive Quad/Octrees*, Journal of Computational Physics **292** (2015) 215 – 238.

[44] J. W. Purvis and J. E. Burkhalter, *Prediction of critical Mach number for store configurations*, AIAA J. **17** (1979) 1170–1177.

[45] Y. T. Ng, C. Min, and F. Gibou, *An efficient fluid–solid coupling algorithm for single-phase flows*, Journal of Computational Physics **228** (Dec., 2009) 8807–8829.

[46] J. Papac, F. Gibou, and C. Ratsch, *Efficient symmetric discretization for the Poisson, heat and Stefan-type problems with Robin boundary conditions*, J. Comput. Phys. **229** (2010) 875–889.

[47] C. Min and F. Gibou, *Geometric integration over irregular domains with application to level-set methods*, Journal of Computational Physics **226** (Oct., 2007) 1432–1443.

[48] D. Wang and S. J. Ruuth, *Variable step-size implicit-explicit linear multistep methods for time-dependent partial differential equations*, Journal of Computational Mathematics **26** (2008), no. 6 838–855.

[49] U. M. Ascher, S. J. Ruuth, and B. T. R. Wetton, *Implicit-explicit methods for time-dependent partial differential equations*, SIAM Journal on Numerical Analysis **32** (1995), no. 3 797–823.

[50] T. Aslam, *A partial differential equation approach to multidimensional extrapolation*, J. Comput. Phys. **193** (2004) 349–355.

[51] A. Chorin, *A numerical method for solving incompressible viscous flow problems*, J. Comput. Phys. **2** (1967) 12–26.

[52] C. Min and F. Gibou, *A second order accurate projection method for the incompressible Navier–Stokes equations on non-graded adaptive grids*, Journal of Computational Physics **219** (Dec., 2006) 912–929.

[53] M. Theillard, C. H. Rycroft, and F. Gibou, *A multigrid method on non-graded adaptive octree and quadtree cartesian grids*, Journal of Scientific Computing **55** (Apr, 2013) 1–15.

[54] F. Losasso, F. Gibou, and R. Fedkiw, *Simulating water and smoke with an octree data structure*, ACM Trans. Graph. (SIGGRAPH Proc.) (2004) 457–462.

[55] R. J. LeVeque and Z. Li, *Immersed interface methods for Stokes flow with elastic boundaries or surface tension*, SIAM Journal on Scientific Computing **18** (1997), no. 3 709–735.

[56] J. Brackbill, D. Kothe, and C. Zemach, *A continuum method for modeling surface tension*, Journal of Computational Physics **100** (1992) 335–354.

[57] Y. Sui, H. Ding, and P. D. Spelt, *Numerical simulations of flows with moving contact lines*, Annual Review of Fluid Mechanics **46** (2014), no. 1 97–119.

[58] M. Muradoglu and G. Tryggvason, *Simulations of soluble surfactants in 3D multiphase flow*, Journal of Computational Physics **274** (2014) 737 – 757.

[59] K. D. O'Hare, P. L. Spedding, and J. Grimshaw, *Evaporation rate of the ethanol and water components comprising a binary liquid mixture*, Developments in Chem. Engineering and Mineral Processing (1992).

[60] H. Ghahremani, A. Moradi, J. Abedini-Torghabeh, and S. M. Hassani, *Measuring surface tension of binary mixtures of water + alcohols from the diffraction pattern of surface ripples*, Der Chemica Sinica (1992).

[61] R. Krechetnikov and G. M. Homsy, *Surfactant effects in the Landau-Levich problem*, J. Fluid Mech. (2005).

[62] D. M. Campana, S. Ubal, M. D. Giavedoni, and F. A. Saita, *Numerical prediction of the film thickening due to surfactants in the Landau–Levich problem*, Phys. Fluids (2010).

[63] C. Burstedde, L. C. Wilcox, and O. Ghattas, *`p4est`: Scalable algorithms for parallel adaptive mesh refinement on forests of octrees*, SIAM Journal on Scientific Computing **33** (2011), no. 3 1103–1133.

[64] M. Mirzadeh, A. Guittet, C. Burstedde, and F. Gibou, *Parallel level-set methods on adaptive tree-based grids*, Journal of Computational Physics **322** (2016) 345–364.

[65] A. Guittet, M. Theillard, and F. Gibou, *A stable projection method for the incompressible Navier-Stokes equations on arbitrary geometries and adaptive quad/octrees*, Journal of Computational Physics (2015).

[66] J. H. Ferziger and M. Peric, Computational Methods for Fluid Dynamics. Springer-Verlag Berlin Heidelberg, 2002.

[67] K. Shahbazi, P. F. Fischer, and C. R. Ethier, *A high-order discontinuous Galerkin method for the unsteady incompressible Navier-Stokes equations*, Journal of Computational Physics **222** (2007), no. 1 391 – 407.

[68] V. Girault, B. Riviere, and M. F. Wheeler, *A discontinuous Galerkin method with nonoverlapping domain decomposition for the Stokes and Navier-Stokes problems*, Mathematics of Computation **74** (2005) 53–84.

[69] C. Peskin, *Flow patterns around heart valves: A numerical method*, J. Comput. Phys. **10** (1972) 252–271.

[70] M.-C. Lai and C. S. Peskin, *An immersed boundary method with formal second-order accuracy and reduced numerical viscosity*, Journal of Computational Physics **160** (2000), no. 2 705 – 719.

[71] E. Fadlun, R. Verzicco, P. Orlandi, and J. Mohd-Yusof, *Combined immersed-boundary finite-difference methods for three-dimensional complex flow simulations*, Journal of Computational Physics **161** (2000), no. 1 35 – 60.

[72] M. Sussman, P. Smereka, and S. Osher, *A level set approach for computing solutions to incompressible two-phase flow*, J. Comput. Phys. **114** (1994) 146–159.

[73] S. Osher and J. Sethian, *Fronts Propagating with Curvature-Dependent Speed: Algorithms Based on Hamilton-Jacobi Formulations*, Journal of Computational Physics **79** (1988) 12–49.

[74] Y. T. Ng, C. Min, and F. Gibou, *An efficient fluid–solid coupling algorithm for single-phase flows*, Journal of Computational Physics **228** (Dec., 2009) 8807–8829.

[75] M. Vinokur, *On one-dimensional stretching functions for finite difference calculations*, Journal of Computational Physics **50** (1983), no. 2 215–234.

[76] E. J. Avital, N. D. Sandham, and K. H. Luo, *Stretched cartesian grids for solution of the incompressible Navier-Stokes equations*, International Journal for Numerical Methods in Fluids **33** (2000), no. 6 897–918.

[77] M. Berger and J. Oliger, *Adaptive mesh refinement for hyperbolic partial differential equations*, J. Comput. Phys. **53** (1984) 484–512.

[78] L. H. Howell and J. B. Bell, *An adaptive mesh projection method for viscous incompressible flow*, SIAM Journal on Scientific Computing **18** (1997), no. 4 996–1013.

[79] M. Sussman, A. Almgren, J. Bell, P. Colella, L. Howell, and M. Welcome, *An adaptive level set approach for incompressible two-phase flows*, J. Comput. Phys. **148** (1999) 81–124.

[80] M. Berger and P. Colella, *Local adaptive mesh refinement for shock hydrodynamics*, J. Comput. Phys. **82** (1989) 64–84.

[81] F. Sousa, C. Lages, J. Ansoni, A. Castelo, and A. Simao, *A finite difference method with meshless interpolation for incompressible flows in non-graded tree-based grids*, Journal of Computational Physics **396** (2019) 848 – 866.

[82] J. A. Benek, J. Steger, and F. C. Dougherty, *A flexible grid embedding technique with applications to the Euler equations*, 6th Computational Fluid Dynamics Conference, AIAA, 373–382. (1983).

[83] R. E. English, L. Qiu, Y. Yu, and R. Fedkiw, *An adaptive discretization of incompressible flow using a multitude of moving cartesian grids*, Journal of Computational Physics **254** (2013) 107 – 154.

[84] D. DeZeeuw and K. G. Powell, *An adaptively refined cartesian mesh solver for the Euler equations*, Journal of Computational Physics **104** (1993), no. 1 56 – 68.

[85] S. Karman, *SPLITFLOW: A 3D unstructured cartesian/prismatic grid CFD code for complex geometries*, in 33rd Aerospace Sciences Meeting and Exhibit, 1995.

[86] J. Melton, Automated three-dimensional cartesian grid generation and euler flow solutions for arbitrary geometries. PhD thesis, Univerty of California, Davis, 1996.

[87] J. Melton, M. Berger, M. Aftosmis, and M. Wong, *3d applications of a cartesian grid Euler method*, in 33rd Aerospace Sciences Meeting and Exhibit, 1995.

[88] J. Melton, F. Enomoto, and M. Berger, *3D automatic cartesian grid generation for Euler flows*, in 11th Computational Fluid Dynamics Conference, AIAA-93-3386-CP, 1993.

[89] R. Finkel and J. Bentley, *Quad trees a data structure for retrieval on composite keys*, Acta Informatica **4** (1974), no. 1 1–9.

[90] D. Meagher, *Geometric modeling using octree encoding*, Computer Graphics and Image Processing **19** (1982), no. 2 129 – 147.

[91] W. J. Coirier, *An adaptively-refined, cartesian, cell-based scheme for the Euler and Navier-Stokes equations*, tech. rep., NASA, 1994.

[92] A. Khokhlov, *Fully threaded tree algorithms for adaptive refinement fluid dynamics simulations*, Journal of Computational Physics **143** (1998), no. 2 519 – 543.

[93] F. Harlow and J. Welch, *Numerical calculation of time-dependent viscous incompressible flow of fluid with free surface*, Phys. Fluids **8** (1965) 2182–2189.

[94] S. Popinet, *Gerris: A tree-based adaptive solver for the incompressible Euler equations in complex geometries*, J. Comput. Phys. **190** (2003) 572–600.

[95] F. Losasso, F. Gibou, and R. Fedkiw, *Simulating water and smoke with an octree data structure*, ACM Trans. Graph. (SIGGRAPH Proc.) (2004) 457–462.

[96] C. Min and F. Gibou, *A second order accurate projection method for the incompressible Navier-Stokes equation on non-graded adaptive grids*, J. Comput. Phys. **219** (2006) 912–929.

[97] J. Strain, *Semi-Lagrangian methods for level set equations*, Journal of Computational Physics **151** (1999) 498–533.

[98] D. Xiu and G. Karniadakis, *A semi-Lagrangian high-order method for Navier-Stokes equations*, J. Comput. Phys **172** (2001) 658–684.

[99] F. Losasso, R. Fedkiw, and S. Osher, *Spatially Adaptive Techniques for Level Set Methods and Incompressible Flow*, Computers and Fluids **35** (2006) 995–1010.

[100] G. Karypis and V. Kumar, *A parallel algorithm for multilevel graph partitioning and sparse matrix ordering*, Journal of Parallel Distributed Computing **48** (Jan., 1998) 71–95.

[101] S. Aluru and F. E. Sevilgen, *Parallel domain decomposition and load balancing using space-filling curves*, in Proceedings of the Fourth International Conference on High-Performance Computing, HIPC '97, (Washington, DC, USA), pp. 230–, IEEE Computer Society, 1997.

[102] P. M. Campbell, K. D. Devine, J. E. Flaherty, L. G. Gervasio, and J. D. Teresco, *Dynamic octree load balancing using space-filling curves*, Tech. Rep. CS-03-01, Williams College Department of Computer Science, 2003.

[103] M. Griebel and G. W. Zumbusch, *Parallel multigrid in an adaptive PDE solver based on hashing and space-filling curves*, Parallel Computing **25** (1999) 827–843.

[104] H.-J. Bungartz, M. Mehl, and T. Weinzierl, *A parallel adaptive Cartesian PDE solver using space–filling curves*, Euro-Par 2006 Parallel Processing (2006) 1064–1074.

[105] T. Weinzierl and M. Mehl, *Peano—a traversal and storage scheme for octree-like adaptive Cartesian multiscale grids*, SIAM Journal on Scientific Computing **33** (Oct., 2011) 2732–2760.

[106] T. Tu, D. R. O'Hallaron, and O. Ghattas, *Scalable parallel octree meshing for terascale applications*, in Proceedings of the 2005 ACM/IEEE Conference on Supercomputing, SC '05, (Washington, DC, USA), pp. 4–, IEEE Computer Society, 2005.

[107] R. S. Sampath, S. S. Adavani, H. Sundar, I. Lashuk, and G. Biros, *Dendro: Parallel algorithms for multigrid and AMR methods on 2:1 balanced octrees*, in International Conference for High Performance Computing, Networking, Storage and Analysis, 2008. SC 2008., 2008.

[108] C. Burstedde, O. Ghattas, M. Gurnis, G. Stadler, E. Tan, T. Tu, L. C. Wilcox, and S. Zhong, *Scalable adaptive mantle convection simulation on petascale supercomputers*, in Proceedings of the 2008 ACM/IEEE Conference on Supercomputing, SC '08, (Piscataway, NJ, USA), pp. 62:1–62:15, IEEE Press, 2008.

[109] R. S. Sampath and G. Biros, *A parallel geometric multigrid method for finite elements on octree meshes*, SIAM Journal on Scientific Computing **32** (May, 2010) 1361–1392.

[110] J. R. Stewart and H. C. Edwards, *A framework approach for developing parallel adaptive multiphysics applications*, Finite Elements in Analysis and Design **40** (2004), no. 12 1599–1617.

[111] W. Bangerth, R. Hartmann, and G. Kanschat, *Deal.II - a general-purpose object-oriented finite element library*, ACM Trans. Math. Software **33** (2007).

[112] T. Isaac, C. Burstedde, and O. Ghattas, *Low-cost parallel algorithms for 2:1 octree balance*, in Parallel Distributed Processing Symposium (IPDPS), 2012 IEEE 26th International, pp. 426–437, 2012.

[113] T. Isaac, C. Burstedde, L. C. Wilcox, and O. Ghattas, *Recursive algorithms for distributed forests of octrees*, SIAM Journal on Scientific Computing **37** (2015), no. 5 C497–C531.

[114] J. Rudi, A. C. I. Malossi, T. Isaac, G. Stadler, M. Gurnis, P. W. Staar, Y. Ineichen, C. Bekas, A. Curioni, and O. Ghattas, *An extreme-scale implicit solver for complex PDEs: highly heterogeneous flow in earth's mantle*, in Proceedings of the International

Conference for High Performance Computing, Networking, Storage and Analysis, p. 5, ACM, 2015.

[115] A. Müller, M. A. Kopera, S. Marras, L. C. Wilcox, T. Isaac, and F. X. Giraldo, "Strong scaling for numerical weather prediction at petascale with the atmospheric model NUMA." http://arxiv.org/abs/1511.01561, 2015.

[116] C. Min and F. Gibou, *A second order accurate level set method on non-graded adaptive Cartesian grids*, J. Comput. Phys. **225** (2007) 300–321.

[117] R. Egan and F. Gibou, "Numerical simulations of incompressible two-phase flows on distributed quad-/oc-tree grids with fully sharp interface treatment.." In preparation.

[118] A. J. Chorin, *Numerical solution of the Navier-Stokes equations*, Mathematics of computation **22** (1968), no. 104 745–762.

[119] D. Brown, R. Cortez, and M. Minion, *Accurate projection methods for the incompressible Navier-Stokes equations*, J. Comput. Phys. **168** (2001) 464–499.

[120] R. Courant, E. Isaacson, and M. Rees, *On the solution of nonlinear hyperbolic differential equations by finite differences*, Comm. Pure Appl. Math. **5** (1952) 243–255.

[121] I. D. Mishev, *Finite volume methods on Voronoi meshes*, Numerical Methods for Partial Differential Equations **14** (1998), no. 2 193–212.

[122] S. Balay, J. Brown, K. Buschelman, W. D. Gropp, D. Kaushik, M. G. Knepley, L. C. McInnes, B. F. Smith, and H. Zhang, *PETSc web page*, 2014.

[123] S. Balay, J. Brown, , K. Buschelman, V. Eijkhout, W. D. Gropp, D. Kaushik, M. G. Knepley, L. C. McInnes, B. F. Smith, and H. Zhang, PETSc Users Manual. Argonne National Laboratory, 2012.

[124] S. Balay, W. D. Gropp, L. C. McInnes, and B. F. Smith, *Efficient management of parallelism in object oriented numerical software libraries*, in Modern Software Tools in Scientific Computing (B. user Press, ed.), pp. 163—202, 2012.

[125] W. Bangerth, C. Burstedde, T. Heister, and M. Kronbichler, *Algorithms and data structures for massively parallel generic adaptive finite element codes*, ACM Transactions on Mathematical Software **38** (2011), no. 2 14:1–14:28.

[126] J. Towns, T. Cockerill, M. Dahan, I. Foster, K. Gaither, A. Grimshaw, V. Hazlewood, S. Lathrop, D. Lifka, G. D. Peterson, R. Roskies, J. R. Scott, and N. Wilkens-Diehr, *Xsede: Accelerating scientific discovery*, Computing in Science and Engineering **16** (2014), no. 5 62–74.

[127] C. Min and F. Gibou, *Geometric integration over irregular domains with application to level set methods*, J. Comput. Phys. **226** (2007) 1432–1443.

[128] R. Mittal, H. Dong, M. Bozkurttas, F. Najjar, A. Vargas, and A. von Loebbecke, *A versatile sharp interface immersed boundary method for incompressible flows with complex boundaries*, Journal of Computational Physics **227** (2008), no. 10 4825 – 4852.

[129] P. Bagchi, M. Y. Ha, and S. Balachandar, *Direct numerical simulation of flow and heat transfer from a sphere in a uniform cross-flow*, Journal of Fluids Engineering **123** (2001), no. 2 347–358.

[130] J. Kim, D. Kim, and H. Choi, *An immersed-boundary finite-volume method for simulations of flow in complex geometries*, Journal of Computational Physics **171** (2001), no. 1 132 – 150.

[131] T. A. Johnson and V. C. Patel, *Flow past a sphere up to a Reynolds number of 300*, Journal of Fluid Mechanics **378** (1, 1999) 19–70.

[132] G. Constantinescu and K. Squires, *LES and DES investigations of turbulent flow over a sphere at Re = 10,000*, Flow, Turbulence and Combustion **70** (2003), no. 1-4 267–298.

[133] J.-I. Choi, R. C. Oberoi, J. R. Edwards, and J. A. Rosati, *An immersed boundary method for complex incompressible flows*, Journal of Computational Physics **224** (2007), no. 2 757 – 784.

[134] S. Marella, S. Krishnan, H. Liu, and H. Udaykumar, *Sharp interface Cartesian grid method I: An easily implemented technique for 3D moving boundary computations*, Journal of Computational Physics **210** (Nov., 2005) 1–31.

[135] J. Kim and H. Choi, *An immersed-boundary finite-volume method for simulation of heat transfer in complex geometries*, KSME International Journal **18** (2004), no. 6 1026–1035.

[136] J. C. Hunt, A. Wray, and P. Moin, *Eddies, stream, and convergence zones in turbulent flows.*, Center for Turbulence Research Report **CTR-S88** (1988).

[137] H. Park, A numerical study of the effects of superhydrophobic surfaces on skin-friction drag reduction in wall-bounded shear flows. PhD thesis, 2015.

[138] H. Park, H. Park, and J. Kim, *A numerical study of the effects of superhydrophobic surface on skin-friction drag in turbulent channel flow*, Physics of Fluids **25** (2013), no. 11 110815.

[139] J. Jeong and F. Hussain, *On the identification of a vortex*, Journal of Fluid Mechanics **285** (1995) 69–94.

[140] A. Rastegari and R. Akhavan, *On the mechanism of turbulent drag reduction with super-hydrophobic surfaces*, Journal of Fluid Mechanics **773** (2015) R4.

[141] Z. Li and T. Lu, *Singularities and treatments of elliptic boundary value problems*, Mathematical and Computer Modelling **31** (2000), no. 8 97 – 145.

[142] J. R. Philip, *Flows satisfying mixed no-slip and no-shear conditions*, Zeitschrift für angewandte Mathematik und Physik ZAMP **23** (1972), no. 3 353–372.

[143] C. J. Teo and B. C. Khoo, *Analysis of Stokes flow in microchannels with superhydrophobic surfaces containing a periodic array of micro-grooves*, Microfluidics and nanofluidics **7** (2009), no. 3 353.

[144] N. S. V. Rao, S. Kareti, W. Shi, and S. S. Iyengar, *Robot navigation in unknown terrains: introductory survey of non-heuristic algorithms*, ORNL/TM-12410, Oak Ridge National Laboratory, 1993.

[145] P. Modesti and A. Sciomachen, *A utility measure for finding multiobjective shortest paths in urban multimodal transportation networks*, Eur. J. Oper. Res. **111** (1998), no. 3 495 – 508.

[146] D. A. Crowe, B. B. Averbeck, M. V. Chafee, J. H. Anderson, and A. P. Georgopoulos, *Mental maze solving*, J. Cogn. Neurosci. **12** (2000), no. 5 813–827.

[147] E. W. Dijkstra, *A note on two problems in connexion with graphs*, Numer. Math. **1** (Dec, 1959) 269–271.

[148] J. Tsitsiklis, *Efficient algorithms for globally optimal trajectories*, IEEE Trans. Autom. Control **40** (1995) 1528–1538.

[149] T. Nakagaki, H. Yamada, and Á. Tóth, *Maze-solving by an amoeboid organism*, Nature **407** (Sept., 2000) 470–.

[150] O. Steinbock, Á. Tóth, and K. Showalter, *Navigating complex labyrinths: Optimal paths from chemical waves*, Science **267** (1995), no. 5199 868–871.

[151] M. J. Fuerstman, P. Deschatelets, R. Kane, A. Schwartz, P. J. A. Kenis, J. M. Deutch, and G. M. Whitesides, *Solving mazes using microfluidic networks*, Langmuir **19** (2003), no. 11 4714–4722.

[152] P. Lovass, M. Branicki, R. Tóth, A. Braun, K. Suzuno, D. Ueyama, and I. Lagzi, *Maze solving using temperature-induced Marangoni flow*, RSC Adv. **5** (2015) 48563–48568.

[153] K. Suzuno, D. Ueyama, M. Branicki, R. Tóth, A. Braun, and I. Lagzi, *Maze solving using fatty acid chemistry*, Langmuir **30** (2014), no. 31 9251–9255.

[154] K. Suzuno, D. Ueyama, M. Branicki, R. Tóth, A. Braun, and I. Lagzi, *Marangoni flow driven maze solving*, in Advances in Unconventional Computing (A. Adamatzky, ed.), vol. 2: Prototypes, Models and Algorithms, pp. 237–243. Springer International Publishing, Cham, , 2017.

[155] Y. Wang, X. Liu, X. Li, J. Wu, Y. Long, N. Zhao, and J. Xu, *Directional and path-finding motion of polymer hydrogels driven by liquid mixing*, Langmuir **28** (2012), no. 31 11276–11280.

[156] J. B. Grotberg, D. Halpern, and O. E. Jensen, *Interaction of exogenous and endogenous surfactant: spreading-rate effects*, J. Appl. Physiol. **78** (1995), no. 2 750–756.

[157] R. Palaparthi, D. T. Papageorgiou, and C. Maldarelli, *Theory and experiments on the stagnant cap regime in the motion of spherical surfactant-laden bubbles*, J. Fluid Mech. **559** (2006) 1–44.

[158] N. J. Shirtcliffe, G. McHale, M. I. Newton, C. C. Perry, and F. B. Pyatt, *Plastron properties of a superhydrophobic surface*, Appl. Phys. Lett. **89** (Sept., 2006) 104106.

[159] D. Quéré, *Wetting and Roughness*, Ann. Rev. Mater. Res. **38** (Aug., 2008) 71–99.

[160] J. P. Rothstein, *Slip on Superhydrophobic Surfaces*, Ann. Rev. Fluid Mech. **42** (Jan., 2010) 89–109.

[161] M. A. Samaha, H. V. Tafreshi, and M. Gad-el Hak, *Superhydrophobic surfaces: from the lotus leaf to the submarine*, C. R. Mécanique **340** (2012) 18–34.

[162] C. Lee, C.-H. Choi, and C.-J. Kim, *Superhydrophobic drag reduction in laminar flows: a critical review*, Exp. Fluids **57** (2016), no. 12 176.

[163] B. Bhushan, *Plant leaf surfaces in living nature*, in Biomimetics: Bioinspired Hierarchical-Structured Surfaces for Green Science and Technology (B. Bhushan, ed.), pp. 81–107. Springer International Publishing, Cham, 2018.

[164] J. R. Philip, *Flows satisfying mixed no-slip and no-shear conditions*, Z. Angew. Math. Physik **23** (May, 1972) 353–372.

[165] J. R. Philip, *Integral properties of flows satisfying mixed no-slip and no-shear conditions*, Z. Angew. Math. Physik **23** (Nov., 1972) 960–968.

[166] E. Lauga and H. A. Stone, *Effective slip in pressure-driven Stokes flow*, J. Fluid Mech. **489** (2003) 55–77.

[167] C. Cottin-Bizonne, C. Barentin, Charlaix, L. Bocquet, and J. L. Barrat, *Dynamics of simple liquids at heterogeneous surfaces: Molecular-dynamics simulations and hydrodynamic description*, Eur. Phys. J. E **15** (2004), no. 4 427–438.

[168] C. Ybert, C. Barentin, C. Cottin-Bizonne, P. Joseph, and L. Bocquet, *Achieving large slip with superhydrophobic surfaces: Scaling laws for generic geometries*, Phys. Fluids **19** (Dec., 2007) 123601.

[169] M. Sbragaglia and A. Prosperetti, *A note on the effective slip properties for microchannel flows with ultrahydrophobic surfaces*, Phys. Fluids **19** (2007), no. 4 043603.

[170] C. J. Teo and B. C. Khoo, *Analysis of Stokes flow in microchannels with superhydrophobic surfaces containing a periodic array of micro-grooves*, Microfluid Nanofluid **7** (2009) 353–382.

[171] A. M. J. Davis and E. Lauga, *Geometric transition in friction for flow over a bubble mattress*, Phys. Fluids **21** (Jan., 2009) 011701.

[172] D. G. Crowdy, *Analytical formulae for longitudinal slip lengths over unidirectional superhydrophobic surfaces with curved menisci*, J. Fluid Mech. **791** (2016) R7.

[173] H. Park, H. Park, and J. Kim, *A numerical study of the effects of superhydrophobic surface on skin-friction drag in turbulent channel flow*, Phys. Fluids **25** (2013) 110815.

[174] H. Park, G. Sun, and C.-J. Kim, *Superhydrophobic turbulent drag reduction as a function of surface grating parameters*, J. Fluid Mech. **747** (2014) 722–734.

[175] H. Ling, S. Srinivasan, K. Golovin, G. H. McKinley, A. Tuteja, and J. Katz, *High-resolution velocity measurement in the inner part of turbulent boundary layers over super-hydrophobic surfaces*, J. Fluid Mech. **801** (Aug., 2016) 670–703.

[176] E. J. G. Cartagena, I. Arenas, M. Bernardini, and S. Leonardi, *Dependence of the drag over super hydrophobic and liquid infused surfaces on the textured surface and weber number*, Flow Turbul. Combust. **100** (June, 2018) 945–960.

[177] J. W. Gose, K. Golovin, M. Boban, J. M. Mabry, A. Tuteja, M. Perlin, and S. L. Ceccio, *Characterization of superhydrophobic surfaces for drag reduction in turbulent flow*, J. Fluid Mech. **845** (June, 2018) 560–580.

[178] A. Rastegari and R. Akhavan, *The common mechanism of turbulent skin-friction drag reduction with superhydrophobic longitudinal microgrooves and riblets*, J. Fluid Mech. **838** (Mar., 2018) 68–104.

[179] F. J. Peaudecerf, J. R. Landel, R. E. Goldstein, and P. Luzzatto-Fegiz, *Traces of surfactants can severely limit the drag reduction of superhydrophobic surfaces*, Proc. Nat. Acad. Sci. USA **114** (2017) 7254–7259.

[180] Y. Cheng, J. Xu, and Y. Sui, *Numerical study on drag reduction and heat transfer enhancement in microchannels with superhydrophobic surfaces for electronic cooling*, Appl. Therm. Eng. **88** (2015) 71–81. Special Issue for International Heat Transfer Symposium 2014.

[181] L. S. Lam, M. Hodes, and R. Enright, *Analysis of Galinstan-based microgap cooling enhancement using structured surfaces*, Trans. ASME J. Heat Mass Transfer **137** (2015) 091003.

[182] T. L. Kirk, M. Hodes, and D. T. Papageorgiou, *Nusselt numbers for poiseuille flow over isoflux parallel ridges accounting for meniscus curvature*, J. Fluid Mech. **811** (2017).

[183] C. Lee, C.-H. Choi, and C.-J. Kim, *Structured surfaces for a giant liquid slip*, Phys. Rev. Lett. **101** (Aug., 2008) 064501.

[184] R. Truesdell, A. Mammoli, P. Vorobieff, F. van Swol, and C. J. Brinker, *Drag reduction on a patterned superhydrophobic surface*, Phys. Rev. Lett. **97** (2006), no. 4.

[185] B. Gruncell, Superhydrophobic surfaces and their potential application to hydrodynamic drag reduction. PhD thesis, University of Southampton, Jan., 2014.

[186] F. Temprano-Coleto, F. J. Peaudecerf, J. R. Landel, F. Gibou, and P. Luzzatto-Fegiz, *Soap opera in the maze: Geometry matters in marangoni flows*, Phys. Rev. Fluids **3** (Oct., 2018) 100507.

[187] W. Bond and D. A. Newton, *Bubbles, drops and Stokes' law*, Phil. Mag. **5** (1928) 794–800.

[188] A. N. Frumkin and V. G. Levich, *Effect of surface-active substances on movements at the boundaries of liquid phases*, Zhur. Fiz. Khim. **21** (1947) 1183–1204 (in Russian). This work is summarized in the textbook by [189], also translated from Russian.

[189] V. Levich, Physicochemical Hydrodynamics. Prentice Hall, 1962.

[190] R. Palaparthi, D. T. Papageorgiou, and C. Maldarelli, *Theory and experiments on the stagnant cap regime in the motion of spherical surfactant-laden bubbles*, J. Fluid Mech. **559** (2006) 1–44.

[191] H. C. Mayer and R. Krechetnikov, *Landau-Levich flow visualization: Revealing the flow topology responsible for the film thickening phenomena*, Phys. Fluids **24** (May, 2012) 052103.

[192] R. Pereira, I. Ashton, B. Sabbaghzadeh, J. D. Shutler, and R. C. Upstill-Goddard, *Reduced air–sea CO2 exchange in the Atlantic Ocean due to biological surfactants*, Nat. Geosci. **11** (July, 2018) 492–496.

[193] R. A. Kropfli, L. A. Ostrovski, T. P. Stanton, E. A. Skirta, A. N. Keane, and V. Irisov, *Relationships between strong internal waves in the coastal zone and their radar and radiometric signatures*, J. Geophys. Res. **104** (1999), no. C2 3133–3148.

[194] P. Luzzatto-Fegiz and K. R. Helfrich, *Laboratory experiments and simulations for solitary internal waves with trapped cores*, J. Fluid Mech. **757** (2014) 354–380.

[195] O. Manor, I. U. Vakarelski, X. Tang, S. J. O'Shea, G. W. Stevens, F. Grieser, R. R. Dagastine, and D. Y. C. Chan, *Hydrodynamic boundary conditions and dynamic forces between bubbles and surfaces*, Phys. Rev. Lett. **101** (2008) 024501.

[196] A. Maali, R. Boisgard, H. Chraibi, Z. Zhang, H. Kellay, and A. Würger, *Viscoelastic drag forces and crossover from no-slip to slip boundary conditions for flow near air–water interfaces*, Phys. Rev. Lett. **118** (2017) 084501.

[197] M. A. Lewis, *Chronic and sublethal toxicities of surfactants to aquatic animals: A review and risk assessment*, Water Res. **25** (Jan., 1991) 101–113.

[198] M. C. Facchini, S. Decesari, M. Mircea, S. Fuzzi, and G. Loglio, *Surface tension of atmospheric wet aerosol and cloud/fog droplets in relation to their organic carbon content and chemical composition*, Atmos. Environ. **34** (2000), no. 28 4853–4857.

[199] A. Hourlier-Fargette, J. Dervaux, A. Antkowiak, and S. Neukirch, *Extraction of silicone uncrosslinked chains at air-water-polydimethylsiloxane triple lines*, Langmuir **34** (2018) 12244–12250.

[200] A. J. Prosser and E. I. Franses, *Adsorption and surface tension of ionic surfactants at the air–water interface: review and evaluation of equilibrium models*, Colloids Surf. A **178** (2001), no. 1 1–40.

[201] C. H. Chang and E. I. Franses, *Adsorption dynamics of surfactants at the air/water interface: a critical review of mathematical models, data, and mechanisms*, Colloids Surf. A **100** (1995) 1–45.

[202] J. F. Harper, *Stagnant-cap bubbles with both diffusion and adsorption rate-determining*, J. Fluid Mech. **521** (2004) 115–123.

[203] M. J. Rosen and J. T. Kunjappu, Surfactants and interfacial phenomena. John Wiley and Sons, Hoboken, New Jersey, USA, 4 ed., 2012.

[204] A. M. Lévêque, *Les lois de la transmission de chaleur par convection*, in Annales des Mines, ou Recueil de Mémoires sur l'Exploitation des Mines et sur les Sciences et les Arts qui s'y Rapportent, Tome XIII, pp. 201–299, 305–362, 381–415. Dunod, 1928.

[205] J. R. Landel, A. L. Thomas, H. McEvoy, and S. B. Dalziel, *Convective mass transfer from a submerged drop in a thin falling film*, J. Fluid Mech. **789** (2016) 630–668.

[206] C. Schönecker and S. Hardt, *Longitudinal and transverse flow over a cavity containing a second immiscible fluid*, J. Fluid Mech. **717** (FEB, 2013) 376–394.

[207] D. G. Crowdy, *Effective slip lengths for immobilized superhydrophobic surfaces*, J. Fluid Mech. **825** (Aug., 2017) R2.

[208] E. Jones, T. E. Oliphant, P. Peterson, et. al., *SciPy: open source scientific tools for Python*, 2001. [Online; accessed 17 January 2019].

[209] Z. He, C. Maldarelli, and Z. Dagan, *The size of stagnant caps of bulk soluble surfactant on the interfaces of translating fluid droplets*, J. Colloid Interface Sci. **146** (1991) 442–451.

[210] S. B. Pope, Turbulent flows. Cambridge University Press, 2000.

[211] K. G. Nayar, D. Panchanathan, G. H. McKinley, and J. H. Lienhard, *Surface tension of seawater*, J. Phys. Chem. Ref. Data **43** (Nov., 2014) 043103.

[212] R. Schmidt and B. Schneider, *The effect of surface films on the air–sea gas exchange in the Baltic sea*, Mar. Chem. **126** (Sept., 2011) 56–62.

[213] S. Pogorzelski and A. D. Kogut, *Kinetics of marine surfactant adsorption at an air/water interface. Baltic sea studies*, Oceanologia **43** (2001), no. 4 389–404.

[214] D. Langevin, *Rheology of adsorbed surfactant monolayers at fluid surfaces*, Annual Review of Fluid Mechanics **46** (2014), no. 1 47–65.

[215] Z. A. Zell, A. Nowbahar, V. Mansard, L. G. Leal, S. S. Deshmukh, J. M. Mecca, C. J. Tucker, and T. M. Squires, *Surface shear inviscidity of soluble surfactants*, Proceedings of the National Academy of Sciences USA **111** (2014), no. 10 3677–3682.

[216] G. J. Elfring, L. G. Leal, and T. M. Squires, *Surface viscosity and Marangoni stresses at surfactant laden interfaces*, Journal of Fluid Mechanics **792** (2016) 712–739.

[217] A. P. Kotula and S. L. Anna, *Regular perturbation analysis of small amplitude oscillatory dilatation of an interface in a capillary pressure tensiometer*, Journal of Rheology **59** (2015), no. 1 85–117.

[218] D. Langevin and F. Monroy, *Marangoni stresses and surface compression rheology of surfactant solutions. Achievements and problems*, Advances in Colloid and Interface Science **206** (2014) 141 – 149.

[219] D. G. Crowdy, *Perturbation analysis of subphase gas and meniscus curvature effects for longitudinal flows over superhydrophobic surfaces*, J. Fluid Mech. **822** (Aug., 2017) 307–326.

[220] C. Schönecker, T. Baier, and S. Hardt, *Influence of the enclosed fluid on the flow over a microstructured surface in the Cassie state*, J. Fluid Mech. **740** (FEB, 2014) 168–195.

[221] S. E. Game, M. Hodes, and D. T. Papageorgiou, *Effects of slowly varying meniscus curvature on internal flows in the cassie state*, J. Fluid Mech. **872** (2019).

[222] L. G. Leal, Advanced Transport Phenomena: Fluid Mechanics and Convective Transport Processes. Cambridge Series in Chemical Engineering. Cambridge University Press, 2007.

[223] I. N. Sneddon, Mixed boundary value problems in potential theory,. North-Holland Pub. Co.; Wiley, Amsterdam, New York, 1966.

[224] E. S. Asmolov and O. I. Vinogradova, *Effective slip boundary conditions for arbitrary one-dimensional surfaces*, J. Fluid Mech. **706** (2012) 108–117.

[225] E. Lauga, M. Brenner, and H. Stone, Microfluidics: The No-Slip Boundary Condition, pp. 1219–1240. Springer Berlin Heidelberg, Berlin, Heidelberg, 2007.

[226] H. Li, Z. Li, X. Tan, X. Wang, S. Huang, Y. Xiang, P. Lv, and H. Duan, *Three-dimensional backflow at liquid–gas interface induced by surfactant*, Journal of Fluid Mechanics **899** (2020) A8.

[227] T. Baier and S. Hardt, *Influence of insoluble surfactants on shear flow over a surface in cassie state at large péclet numbers*, Journal of Fluid Mechanics **907** (2021) A3.

[228] F. Feuillebois, M. Z. Bazant, and O. I. Vinogradova, *Effective slip over superhydrophobic surfaces in thin channels*, Phys. Rev. Lett. **102** (Jan, 2009) 026001.

[229] P. Tsai, A. M. Peters, C. Pirat, M. Wessling, R. G. H. Lammertink, and D. Lohse, *Quantifying effective slip length over micropatterned hydrophobic surfaces*, Physics of Fluids **21** (2009), no. 11 112002.

[230] C. J. Teo and B. C. Khoo, *Analysis of stokes' flow in microchannels with superhydrophobic surfaces containing a periodic array of micro-grooves*, Microfluid. Nanofluidics **7** (Dec., 2008) 353.

[231] D. Crowdy, *Frictional slip lengths for unidirectional superhydrophobic grooved surfaces*, Physics of Fluids **23** (2011), no. 7 072001.

[232] C. J. Teo and B. C. Khoo, *Flow past superhydrophobic surfaces containing longitudinal grooves: effects of interface curvature*, Microfluid. Nanofluidics **9** (Aug., 2010) 499–511.

[233] A. Hourlier-Fargette, A. Antkowiak, A. Chateauminois, and S. Neukirch, *Role of uncrosslinked chains in droplets dynamics on silicone elastomers*, Soft Matter **13** (2017) 3484–3491.

[234] L. Lee, E. Mann, D. Langevin, and B. Farnoux, *Neutron reflectivity and ellipsometry studies of a polymer molecular layer spread on the water surface*, Langmuir **7** (1991), no. 12 3076–3080.

[235] V. Bergeron and D. Langevin, *Monolayer spreading of polydimethylsiloxane oil on surfactant solutions*, Physical review letters **76** (1996), no. 17 3152.

[236] K. J. Regehr, M. Domenech, J. T. Koepsel, K. C. Carver, S. J. Ellison-Zelski, W. L. Murphy, L. A. Schuler, E. T. Alarid, and D. J. Beebe, *Biological implications of polydimethylsiloxane-based microfluidic cell culture*, Lab Chip **9** (2009) 2132–2139.

[237] S.-S. D. Carter, A.-R. Atif, S. Kadekar, I. Lanekoff, H. Engqvist, O. P. Varghese, M. Tenje, and G. Mestres, *Pdms leaching and its implications for on-chip studies focusing on bone regeneration applications*, Organs-on-a-Chip **2** (2020) 100004.

[238] S. Ratnesar-Shumate, G. Williams, B. Green, M. Krause, B. Holland, S. Wood, J. Bohannon, J. Boydston, D. Freeburger, I. Hooper, K. Beck, J. Yeager, L. A. Altamura, J. Biryukov, J. Yolitz, M. Schuit, V. Wahl, M. Hevey, and P. Dabisch, *Simulated Sunlight Rapidly Inactivates SARS-CoV-2 on Surfaces*, The Journal of Infectious Diseases **222** (05, 2020) 214–222.

[239] J.-L. Sagripanti and C. D. Lytle, *Estimated inactivation of coronaviruses by solar radiation with special reference to covid-19*, Photochemistry and Photobiology **96** (2020), no. 4 731–737.

[240] C. D. Lytle and J.-L. Sagripanti, *Predicted inactivation of viruses of relevance to biodefense by solar radiation*, Journal of Virology **79** (2005), no. 22 14244–14252.

[241] K. L. Nelson, A. B. Boehm, R. J. Davies-Colley, M. C. Dodd, T. Kohn, K. G. Linden, Y. Liu, P. A. Maraccini, K. McNeill, W. A. Mitch, T. H. Nguyen, K. M. Parker, R. A. Rodriguez, L. M. Sassoubre, A. I. Silverman, K. R. Wigginton, and R. G. Zepp, *Sunlight-mediated inactivation of health-relevant microorganisms in water: a review of mechanisms and modeling approaches*, Environ. Sci.: Processes Impacts **20** (2018) 1089–1122.

[242] T. Kohn and K. L. Nelson, *Sunlight-mediated inactivation of ms2 coliphage via exogenous singlet oxygen produced by sensitizers in natural waters*, Environmental Science & Technology **41** (2007), no. 1 192–197. PMID: 17265947.

[243] N. van Doremalen, T. Bushmaker, D. H. Morris, M. G. Holbrook, A. Gamble, B. N. Williamson, A. Tamin, J. L. Harcourt, N. J. Thornburg, S. I. Gerber, J. O. Lloyd-Smith, E. de Wit, and V. J. Munster, *Aerosol and surface stability of sars-cov-2 as compared with sars-cov-1*, New England Journal of Medicine **382** (2020), no. 16 1564–1567.

[244] M. Schuit, S. Ratnesar-Shumate, J. Yolitz, G. Williams, W. Weaver, B. Green, D. Miller, M. Krause, K. Beck, S. Wood, B. Holland, J. Bohannon, D. Freeburger, I. Hooper, J. Biryukov, L. A. Altamura, V. Wahl, M. Hevey, and P. Dabisch, *Airborne SARS-CoV-2 Is Rapidly Inactivated by Simulated Sunlight*, The Journal of Infectious Diseases **222** (06, 2020) 564–571.

[245] T. Carleton, J. Cornetet, P. Huybers, K. C. Meng, and J. Proctor, *Global evidence for ultraviolet radiation decreasing covid-19 growth rates*, Proceedings of the National Academy of Sciences **118** (2021), no. 1.

[246] M. E. Darnell, K. Subbarao, S. M. Feinstone, and D. R. Taylor, *Inactivation of the coronavirus that induces severe acute respiratory syndrome, sars-cov*, Journal of Virological Methods **121** (2004), no. 1 85–91.

[247] M. Darnell and D. Taylor, *Evaluation of inactivation methods for severe acute respiratory syndrome coronavirus in noncellular blood products*, Transfusion **46** (2006), no. 10 1770–1777.

[248] M. Schuit, S. Gardner, S. Wood, K. Bower, G. Williams, D. Freeburger, and P. Dabisch, *The Influence of Simulated Sunlight on the Inactivation of Influenza Virus in Aerosols*, The Journal of Infectious Diseases **221** (11, 2019) 372–378.

[249] M. Hippler, *Photochemical kinetics: Reaction orders and analogies with molecular beam scattering and cavity ring-down experiments*, Journal of Chemical Education **80** (2003), no. 9 1074.

[250] E. Chevallier, A. Mamane, H. A. Stone, C. Tribet, F. Lequeux, and C. Monteux, *Pumping-out photo-surfactants from an air–water interface using light*, Soft Matter **7** (2011) 7866–7874.

[251] Y. Namba, *Specular Spectral Reflectance Of A1S1304 Stainless Steel At Near-Normal Incidence*, in Scattering in Optical Materials II (S. Musikant, ed.), vol. 0362, pp. 93 – 103, International Society for Optics and Photonics, SPIE, 1983.